

JSR A

E-ISSN:2687-6167
Number 59
December 2024

JOURNAL OF
SCIENTIFIC REPORTS A

Journal of Scientific Reports-A, December 2024, Number 59



Sultan Hassanul Ulama University, Jember, Indonesia
Jember Campus, Tawang Road, 67101, 67101 Jember
Phone: 0371-44111-62
E-mail: jsra@sigmail.com
jsra.com

Digital Open Access

gity of
SCIENCE



Owner

On Behalf of Kütahya Dumlupınar University
Prof. Dr. Süleyman KIZILTOPRAK (Rector),
On Behalf of Institute of Graduate Studies
Assoc. Prof. Dr. Eray ACAR (Director)

Editorial Board

Önder UYSAL	Kütahya Dumlupınar University
Fatih ŞEN	Kütahya Dumlupınar University
Oktay ŞAHBAZ	Kütahya Dumlupınar University
Nevzat BEYAZIT	Ondokuz Mayıs University
Onur KARAMAN	Akdeniz University
Cafer ÖZKUL	Kütahya Dumlupınar University
Levent URTEKİN	Ahi Evran University
Ümran ERÇETİN	Kütahya Dumlupınar University
Ceren KARAMAN	Akdeniz University
Durmuş ÖZDEMİR	Kütahya Dumlupınar University
Fatih Yavuz ILGIN	Erzincan Binali Yıldırım University
Güray KAYA	Kütahya Dumlupınar University
Pelin Çağım TOKAT BİRGİN	Kütahya Dumlupınar University
Nataliia BALYTSKA	Zhytomyr State Technological University
Natalia ZUIEVSKA	National Technical University of Ukraine 'Igor Sikorsky Kyiv Polytechnic Institute'
Oksana VOVK	National Technical University of Ukraine 'Igor Sikorsky Kyiv Polytechnic Institute'
Nodor SULASHVILI	The University of Georgia
Csoknyai TAMAS	Budapest University of Technology and Economics
Tibor POOS	Budapest University of Technology and Economics
Sait ALTUN	Kütahya Dumlupınar University
Sevgi KARACA	Kütahya Dumlupınar University
Ramazan BAYAT	Kütahya Dumlupınar University
Muhammed BEKMEZCİ	Kütahya Dumlupınar University
Ayşenur AYGÜN	Kütahya Dumlupınar University
Safa DÖRTERLER	Kütahya Dumlupınar University
Seyfullah ARSLAN	Kütahya Dumlupınar University
Büşra TUTUMLU	Kütahya Dumlupınar University
Merve ARSLAN	Kütahya Dumlupınar University
Bahadır YÖRÜR	Kütahya Dumlupınar University
Naciye Nur ARSLAN	Kütahya Dumlupınar University

Journal of Scientific Reports-A started its publication life in 2000 as name of Journal of Science and Technology of Dumlupınar University and is a national peer-reviewed journal published regularly four times a year in March, June, September and December. The language of the journal is English. Articles submitted to the journal are evaluated by at least two referees who are experts in the subject and selected by the editorial board. All articles submitted to the journal are evaluated by the double-blind method. Articles submitted to our journal for review should not be previously published, accepted for publication and in the process of being evaluated for publication in another journal. All responsibility for the articles published in the journal belongs to the author(s).

The journal aims to share scientific studies carried out in the fields of science and engineering at national and international level with scientists and the public. Original research articles, review articles and short notes in science and engineering disciplines are accepted for the journal. Original research articles are expected to contain theoretical and experimental results and should not be published in other journals. In the review articles, it is expected that scientific, technological and current developments on a specific subject are reflected by using an extensive bibliography and made a satisfying evaluation of these. Short notes should be brief writings prepared to announce the first findings of an original study.

Editorial Policy

The journal is open access and the article evaluation period is between 1-2 months.

Correspondence Address: Kütahya Dumlupınar Üniversitesi Evliya Çelebi Yerleşkesi Fen Bilimleri Enstitüsü
43270 KÜTAHYA

E-mail: joursra@gmail.com

Phone: 0 274 443 19 42

Webpage: gsjsra.com

Fax: 0 274 265 20 60

Section Editors

Civil Engineering Prof. Dr. M. Çağatay KARABÖRK	Kütahya Dumlupınar University
Mechanical Engineering Prof. Dr. Ramazan KÖSE	Kütahya Dumlupınar University
Electrical-Electronics Engineering Assist. Prof. Kadir VARDAR	Kütahya Dumlupınar University
Computer Engineering Assoc. Prof. Doğan AYDIN	Kütahya Dumlupınar University
Industrial Engineering Assist. Prof. Üyesi Kerem CİDDİ	Kütahya Dumlupınar University
Mining Engineering Assist. Prof. Uğur DEMİR	Kütahya Dumlupınar University
Geology Engineering Assist. Prof. Muzaffer ÖZBURAN	Kütahya Dumlupınar University
Metallurgical and Materials Engineering Prof. Dr. İskender IŞIK	Kütahya Dumlupınar University
Food Engineering Prof. Dr. Muhammet DÖNMEZ	Kütahya Dumlupınar University
Environmental Engineering Assoc. Prof. Dr. Nevzat BEYAZIT	Ondokuz Mayıs University
Mathematics Assist. Prof. Cansu KESKİN	Kütahya Dumlupınar University
Physics Assoc. Prof. Huriye Sanem AYDOĞU	Kütahya Dumlupınar University
Chemistry Assoc. Prof. Bülent ZEYBEK	Kütahya Dumlupınar University
Biology Assist. Prof. Nüket Akalın BİNGÖL	Kütahya Dumlupınar University
Biochemistry Assoc. Prof. Derya KOYUNCU ZEYBEK	Kütahya Dumlupınar University
Occupational Health and Safety Prof. Dr. Cem ŞENSÖĞÜT	Kütahya Dumlupınar University
Software Engineering Assist. Prof. Şerif Ali SADIK	Kütahya Dumlupınar University

Advisory Board

Şükrü ASLAN	Sivas Cumhuriyet University/ Turkey
Erdal ÇELİK	Ankara Yıldırım Beyazıt University/ Turkey
Cemal PARLAK	Ege University/ Turkey
Muhammet DÖNMEZ	Kütahya Dumlupınar University/ Turkey
İhsan ÖZKAN	Konya Technical University/ Turkey
Ercan ARPAZ	Kocaeli University/ Turkey
Yavuz GÜL	Sivas Cumhuriyet University/ Turkey
Ataç BAŞÇETİN	İstanbul Technical University/ Turkey
Taner ERDOĞAN	Kocaeli University/ Turkey
Derek ABBOTT	University of Adelaide/ Australia
Kristian ALMSTRUP	Copenhagen University Hospital/ Denmark
Josette Camilleri	University of Birmingham/ UK
Yan-Ru LOU	Fudan University/ China
Ken HAENEN	Hasselt University/ Belgium
Fanming JIN	Shanghai Jiao Tong University/ China
Suneel KODAMBAKA	Florida International University/ USA
Hyoyoung LEE	Sungkyunkwan University/ Republic of Korea
Vinod TIWARI	Banaras Hindu University/ India
Sabine WURMEHL	Leibniz Institute/ Germany
Kai XIAO	Oak Ridge National Laboratory/ USA
Shahid ADEEL	Government College University/ Pakistan
J. Marty ANDERIES	Arizona State University/ USA
Ayaga BAWAH	University of Ghana/ Ghana
Lilong CHAI	University of Georgia/ USA
Idiano D'ADAMO	Sapienza University of Rome/ Italy
Sanjit DEB	Texas Tech University/ USA
Caroline HACHEM-VERMETTE	University of Calgary/ Canada
Marlia Mohd HANAFIAH	The National University of Malaysia/ Malaysia
Nick HOLDEN	University College Dublin/ Ireland
Chang-Wei HU	Sichuan University/ China
Masashi KATO	Nagoya University/ Japan
Tafadzwanashe MABHAUDHI	University of KwaZulu-Natal/ South Africa
Mubarak MUJAWAR	Universiti Teknologi Brunei/ Brunei
Nidhi NAGABHATLA	United Nations University CRIS/ Belgium
Gunnar SEIDE	Maastricht University/ Netherlands
Jonathan Wong	Hong Kong Baptist University/ Hong Kong
Yenchun Jim WU	National Waiwan Normal University/ Taiwan
Jie ZHUANG	University of Tennessee/ USA

JOURNAL OF SCIENTIFIC REPORTS-A
E-ISSN: 2687-6167

CONTENTS

RESEARCH ARTICLES

Buckling behavior of simply supported tapered square plates 1-9
Safa UZUN*, Mustafa Haluk SARAÇOĞLU, Gökhan GÜÇLÜ, Fethullah USLU

On (k,3)-arcs derived by Ceva configurations in PG(2,5) 10-18
Elif ALTINTAŞ KAHRİMAN*, Ayşe BAYAR

An experimental investigation of reducing the wake length at a low speed by passive flow control and biomimetic application 19-31
Sefa ŞAHİN, Ahmet Selim DURNA, Cem KOLBAKIR*

Reinforcement learning for energy optimization in IoT based landslide early warning systems 32-57
Seyfullah ARSLAN*, Safa DÖRTERLER, Fırat AYDEMİR

Comparison of regression and tree-based methods for the prediction of zero-inflated claim data 58-69
Aslıhan ŞENTÜRK ACAR

Investigation of glass fiber reinforced aluminum honeycomb panel repair performance according to aviation standards 70-86
Akın ÇALLI*, Orkun TUNÇKAN

REVIEW ARTICLE

Cellulose and its derivatives as biodegradable materials: A review 87-104
Muhammed Zakir TUFAN*, Cengiz ÖZEL

The golden discovery of camelina sativa: a pivotal study of its unique components and its multiple uses in various applications in science and industry 105-118
Rayane MAHIOUS, Ebru HALVACI, Ayşenur AYGUN, Fatih ŞEN*



Contents lists available at *Dergipark*

Journal of Scientific Reports-A

journal homepage: <https://dergipark.org.tr/tr/pub/jsr-a>



E-ISSN: 2687-6167

Number 59, December 2024

RESEARCH ARTICLE

Receive Date: 29.01.2024

Accepted Date: 29.07.2024

Buckling behavior of simply supported tapered square plates

Sefa Uzun^{a*}, Mustafa Halûk Saraçoğlu^b, Gökhan Güçlü^c, Fethullah Uslu^d

^aKütahya Dumlupınar University, Department of Civil Engineering, Kütahya, 43100, Türkiye, ORCID: 0009-0008-9450-1063

^bKütahya Dumlupınar University, Department of Civil Engineering, Kütahya, 43100, Türkiye, ORCID: 0000-0003-3842-5699

^cKütahya Dumlupınar University, Department of Civil Engineering, Kütahya, 43100, Türkiye, ORCID: 0000-0003-2931-9501

^dKütahya Dumlupınar University, Department of Civil Engineering, Kütahya, 43100, Türkiye, ORCID: 0000-0001-8057-5119

Abstract

Buckling is one of the important design parameters for the design of plate structures. The critical buckling loads and buckling coefficients for a series of different tapered plates are investigated. Buckling analyses of square plates are performed by changing different types of thickness variation by using ANSYS finite element software. Plates are assumed to be thin plate. The loading types and taper ratio of the simply supported square plates considerably affect the critical buckling loads. The analysis results are compared with existing literature findings and presented graphically and in tabular form. It is concluded that the analyses results are in good harmony with the literature results. The graphics proposed in this study could be useful for designers. The novelty of this study is the presentation of new straightforward formulas that provide critical buckling load coefficients separately for designers, specifically for simply supported tapered plates under uniaxial and biaxial axial loading conditions.

© 2023 DPU All rights reserved.

Keywords: Tapered plate; finite element method; critical buckling load; buckling coefficient

1. Introduction

Plates are plane structural elements whose one dimension is smaller than the other two dimensions. They utilized various areas such as structural, mechanical, marine, and aerospace engineering. These types of structural elements generally bear loads perpendicular to their plane and are also subjected to many different types of loads. In the design of plate structures, in-plane buckling loads must be taken into account, as well as other loads acting on the plate.

Tapered plates are utilized as structural elements in certain applications to achieve objectives such as weight reduction and to enhance architectural designs. Researchers have made significant studies about the buckling of variable thickness plates in the past [1-4]. Based on findings from these studies, tapered plates provide various benefits

in engineering and design, including improved performance in buckling, reduced weight, optimized stiffness, enhanced aesthetics, efficient material use, and versatile functional capabilities.

* Corresponding author. Tel.: 0 274 4434151
E-mail address: sefa.uzun@dpu.edu.tr

Researchers used different solution methods to calculate the critical buckling load of the plates with variable thickness. Klein developed a simple formulation for the buckling of bi-axially loaded simply supported plates that are tapered in thickness and in plan simultaneously in his report. He also presented some design curves as the result of the study [5]. Pope gives an analysis for the buckling of tapered rectangular plates in thickness. The considered plates are loaded under uniform loads in the direction of taper with different boundary conditions [6]. Harik et al., presented a semi-numerical and a semi-analytical method for the analysis of rectangular plates with varying rigidities. Investigated plates are subjected to different in-plane loads and results were presented for different boundary conditions [7]. Nerantzaki and Katsikadelis applied the analog equation method in the buckling analysis of plates of variable thickness and demonstrated that the obtained numerical results from the method were effective in his study [8]. Saeidifar et al. studied the numerical calculation of buckling loads for an elastic rectangular plate with variable thickness in one direction. In the study, the numerical examples have been presented and, also compared to some numerical results from the literature [9]. Viswanathan et al. investigated the buckling of rectangular plates of variable thickness under uniaxial in-plane load using the quintic spline approximation technique. The thickness of the plates they examined varies linearly, exponentially, and sinusoidally in one direction [10].

The finite element method, which is frequently used in studies, has also been preferred by researchers in the problem of plate buckling. Hassan and Kurgan carried out a study on the modeling and buckling analysis of rectangular plates in ANSYS [11]. Kacimi et al. have investigated the critical shear buckling stresses for simply supported plates. The plates are loaded with different ratios of shear loads. Results are also compared with analytical ones in the study [12]. Uslu et al. have studied the buckling of perforated square plates by using ANSYS software [13]. Baran and Balkan have investigated the thermal buckling of plates. In the study, they discussed the response of thermal buckling conditions under different orientation angles [14]. Deniz has studied the buckling behavior of composite plates with curved surface experimentally. In the study he evaluates the results at the view of the critical buckling load versus the hole diameter and fiber orientations [15].

In this study, the buckling behavior of simply supported tapered square plates is investigated by using finite element software. For this purpose, by tapering different thickness models simply supported on all four edges square plates were formed with a series, and the critical buckling loads of these plates under uniaxial and bi-axial loadings were calculated. For designers, simple formulas that give the critical buckling load coefficients of simply supported tapered square plates are developed for both loading cases separately.

2. Formulation of the problem

According to the classical plate theory or thin plate theory assumptions, the ratio of the short side of the plate to its thickness should be greater than 10 and less than 100. When this ratio is less than 10, it is necessary to use first order shear deformation theory or higher order theories, where different effects are also taken into account. If this ratio is greater than 100, then the structural element will need to be defined as a membrane.

According to [16], the methods used for uniform thickness plates can also be applied in the calculations of the variable thickness plates if the rigidities of the plates change slightly. Otherwise, more detailed methods should be used.

The geometry and loading condition of a thin square tapered plate is given in Fig. 1. The square tapered plate is simply supported at four edges. The square tapered plate is subject to uniaxial buckling load. This load is an in-plane compressive N load acting on and normal to the edges $x = 0$ and $x = a$. The governing equation of the plate is given

in Equation 1[17].

$$D \left[\frac{\partial^4 w}{\partial x^4} + 2 \frac{\partial^4 w}{\partial x^2 \partial y^2} + \frac{\partial^4 w}{\partial y^4} \right] + N \frac{\partial^2 w}{\partial x^2} = 0 \quad (1)$$

In this equation $D = D(x, y) = \frac{Eh^3(x, y)}{12(1-\nu)^2}$ is the variable flexural stiffness of the tapered plate, $h = h(x, y)$ is the variable thickness, ν is Poisson's ratio, E is Young's modulus, $w(x, y)$ is the transverse deflection, and N is the distributed normal buckling load.

If the solution of the above equation which is a linear partial differential equation with constant coefficients is turned into a two-harmonic equation, it becomes as follows:

$$w_0 = \sum_m \sum_n a_{mn} \sin \frac{m\pi x}{a} \sin \frac{n\pi y}{b} \quad (2)$$

In this equation, m represents the half wave in longitudinal direction and n represents the half wave in transverse direction. The function $w(x, y)$ satisfies the simply supported boundary condition for the displacement. Bending moment M_n can be described as follows:

$$M_n = -D \left[\left(\frac{m\pi}{a} \right)^2 + \nu \left(\frac{n\pi}{b} \right)^2 \right] \sin \frac{m\pi x}{b} \sin \frac{n\pi y}{b} \quad (3)$$

In a simply supported on four edges square plate, the bending moment at the edges of the plate is $M_n = 0$. If this situation is substituted into the $w(x, y)$ equation, the following expression is obtained:

$$\left\{ D \left[\left(\frac{m\pi}{a} \right)^4 + 2 \left(\frac{m\pi}{a} \right)^2 \left(\frac{n\pi}{b} \right)^2 + \left(\frac{n\pi}{b} \right)^4 \right] - N \left(\frac{m\pi}{a} \right)^2 \right\} \sin \frac{m\pi x}{b} \sin \frac{n\pi y}{b} = 0. \quad (4)$$

When the equation is simplified, the following expression is obtained:

$$N = \frac{\pi^2 a^2 D}{m^2} \left(\frac{m^2}{a^2} + \frac{n^2}{b^2} \right)^2 \quad (5)$$

When the denominator of one of the terms in Equation 5 becomes equal to zero, the critical buckling load, which is the smallest value of N , occurs. In this equation m must be chosen so as to make the equation minimum [12]. This critical value is obtained, by taking $n = 1$ in the equation. Hence the Equation 5 becomes as in Equation 6.

$$N_{cr} = k \frac{\pi^2 D}{a^2} \quad (6)$$

The bending rigidity of the tapered rectangular plate D can be defined by using the function as in Equation 7.

$$D = D_m \left[\left(\frac{h_0 + h_1}{2} \right) \left(h_0 + \frac{h_1 - h_0}{a} x \right)^{-3} \right] \quad (7)$$

In the equation D_m is the bending rigidity value at the middle section of the plate at $x = a/2$. The critical buckling coefficient can be stated in terms of D_m in Equation 8.

$$k = \frac{a^2 N_{cr}}{\pi^2 D_m} \quad (8)$$

The critical buckling coefficient k , defined in terms of D_m , is independent of the thickness variation direction. This coefficient for the plates with a small taper ratio h_1/h_0 will be almost the same as the uniform thickness plates [4].

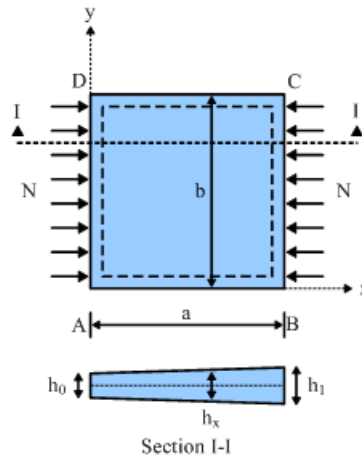


Fig. 1. Geometry and loading condition of tapered square plate.

3. Finite element software

Buckling analyses were conducted using the well-established finite element software ANSYS. Initially, the material properties and geometric parameters were defined within the ANSYS package. Subsequently, the finite element mesh was generated by selecting an appropriate element from the library. Following mesh creation, the plate thickness variation was implemented using APDL (Ansys Parametric Design Language) within the program. Boundary conditions and loads were then specified, and both static and buckling analyses were performed accordingly. The choice of element from the library plays a crucial role in determining result accuracy and computational efficiency. In this study, the SHELL181 element was utilized.

The SHELL181 element is specifically designed for analyzing thin plate structures. The reliability and accuracy of the SHELL181 element for buckling analysis have been validated through numerous studies in the literature [11]. It features four nodes positioned at the corners, with each node having six degrees of freedom: translations in the x, y, and z directions, and rotations about the x, y, and z axes. SHELL181 is well-suited for applications involving linear,

large rotation, and/or large strain nonlinear behavior [18]. Various element properties can be adjusted using key option (KEYOPT) settings in the software. This element is suitable for conducting both bending and buckling analyses of plates. The geometry of the SHELL181 element is illustrated in Fig. 2.

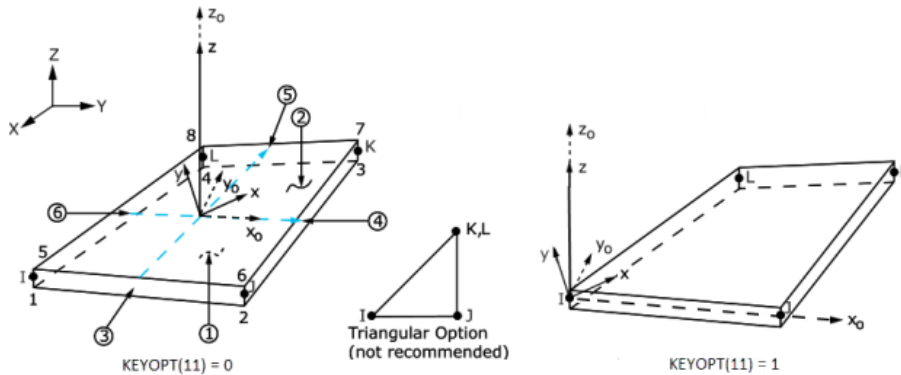


Fig. 2. SHELL181 finite element [11].

4. Material, model and loading conditions

The numerical analyses employ structural steel material. The Young's modulus and Poisson's ratios of the structural steel are 2.10^5 MPa, and 0.30, respectively.

The dimensions of the square tapered plates used in the numerical analyses are $a = 1000$ mm and $b = 1000$ mm, respectively. The plate thickness varies linearly along the x-axis as shown in Fig. 1. In this study, h_0 (thickness at the $x = 0$) is constant and equals to 10 mm. And h_1 (thickness at the $x = a$) varies according to the taper ratio. According to the thin plate assumptions, taper ratio h_1 / h_0 is up to a maximum of 10. In this study, the taper ratio varies from 1 to 10 in increments of 0.125. The boundary conditions of the square tapered plate are given in the Table 1. In the Table 1, u , v , and w denote the deflections at the x, y, and z directions.

Analyses are performed for tapered square plates with different in-plane loadings as uniaxial and biaxial as shown in Fig. 3. In uniaxial loading, in-plane loads of uniform compressive forces N per unit length is subjected parallel to the tapered direction x. In biaxial loading, in-plane loads of the same uniform compressive forces N per unit length is subjected perpendicular to the tapered direction x in addition to the uniaxial buckling loadings.

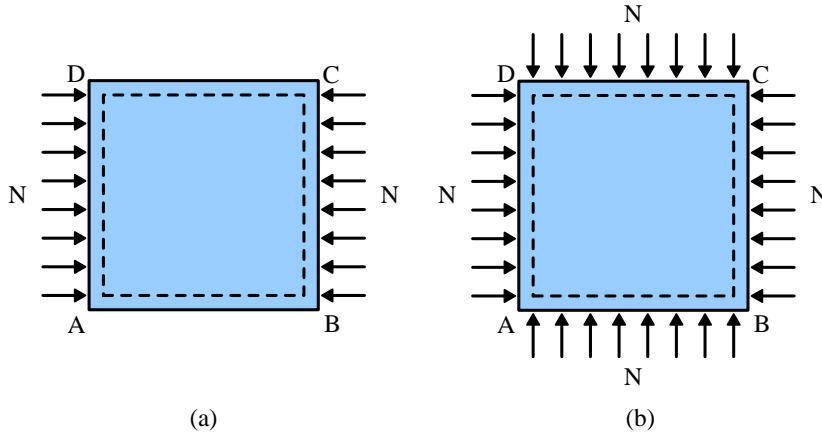


Fig. 3. The loading conditions of the square tapered plate: (a) uniaxial load and (b) biaxial load.

Table 1. Boundary conditions of the square tapered plate.

Edge or Point	Boundary Condition 1	Boundary Condition 2
Edge AB	$w(x,0) = 0$	$\frac{\partial w(x,0)}{\partial x} = 0$
Edge BC	$w(a,y) = 0$	$\frac{\partial w(a,y)}{\partial y} = 0$
Edge CD	$w(x,a) = 0$	$\frac{\partial w(x,a)}{\partial x} = 0$
Edge DA	$w(0,y) = 0$	$\frac{\partial w(0,y)}{\partial y} = 0$
Point A	$v(0,0) = 0$	-
Point B	$v(a,0) = 0$	-
Midpoint of edge AB	$u\left(\frac{a}{2},0\right) = 0$	-

5. Results and discussion

The buckling coefficients obtained by finite element models for simply supported square tapered plates with different taper ratios, along with the corresponding values from Wittrick and Ellen [4], are listed in Table 2. As shown in Table 2, the results from the finite element model closely match those from Wittrick and Ellen.

Table 2. The verification of the buckling coefficients of uniaxial loaded tapered square plates.

h_1/h_0	$k^{Wittrick}$	k^{ANSYS}	$k^{Difference}(\%)$
-----------	----------------	-------------	----------------------

1.125	3.966	3.982	0.41
1.250	3.882	3.900	0.47
1.500	3.638	3.662	0.65
1.750	3.364	3.393	0.86
2.000	3.100	3.132	1.03

The calculated buckling coefficients for tapered plates under uniaxial and biaxial loadings are provided in Table 3. As seen from Table 3, the buckling coefficient decreases as the taper ratio increases. For a given taper ratio, the uniaxial buckling coefficient is roughly twice as large as the biaxial buckling coefficient. Figure 4 illustrates the buckling coefficients for both loading cases obtained from the numerical models. As shown in Fig. 4, the buckling coefficient decreases as the taper ratio increases for both uniaxial and biaxial loadings. Additionally, the uniaxial and biaxial buckling coefficients become closer to each other as the taper ratio increases.

Table 3. The buckling coefficients of simply supported tapered square plates under uniaxial and biaxial loadings

h_1/h_0	Buckling Coefficient		h_1/h_0	Buckling Coefficient		h_1/h_0	Buckling Coefficient	
	Uniaxial	Biaxial		Uniaxial	Biaxial		Uniaxial	Biaxial
1.000	3.998	1.999	4.125	1.713	1.158	7.250	0.957	0.736
1.125	3.965	1.991	4.250	1.664	1.134	7.375	0.939	0.724
1.250	3.882	1.970	4.375	1.618	1.110	7.500	0.922	0.714
1.375	3.770	1.940	4.500	1.574	1.087	7.625	0.905	0.703
1.500	3.642	1.905	4.625	1.532	1.065	7.750	0.889	0.693
1.625	3.508	1.866	4.750	1.491	1.044	7.875	0.874	0.683
1.750	3.373	1.825	4.875	1.453	1.023	8.000	0.858	0.673
1.875	3.240	1.783	5.000	1.416	1.003	8.125	0.844	0.664
2.000	3.111	1.740	5.125	1.381	0.984	8.250	0.830	0.655
2.125	2.988	1.697	5.250	1.347	0.965	8.375	0.816	0.646
2.250	2.871	1.655	5.375	1.315	0.947	8.500	0.802	0.637
2.375	2.760	1.614	5.500	1.284	0.930	8.625	0.790	0.628
2.500	2.655	1.574	5.625	1.254	0.913	8.750	0.777	0.620
2.625	2.555	1.535	5.750	1.226	0.897	8.875	0.765	0.612
2.750	2.461	1.497	5.875	1.199	0.881	9.000	0.753	0.604
2.875	2.373	1.461	6.000	1.172	0.866	9.125	0.741	0.596
3.000	2.289	1.425	6.125	1.147	0.851	9.250	0.730	0.588
3.125	2.210	1.391	6.250	1.123	0.837	9.375	0.719	0.581
3.250	2.136	1.358	6.375	1.099	0.823	9.500	0.708	0.574
3.375	2.065	1.326	6.500	1.077	0.809	9.625	0.698	0.566
3.500	1.998	1.296	6.625	1.055	0.796	9.750	0.688	0.560
3.625	1.935	1.266	6.750	1.034	0.783	9.875	0.678	0.553
3.750	1.875	1.238	6.875	1.013	0.771	10.000	0.668	0.546
3.875	1.818	1.210	7.000	0.994	0.759			
4.000	1.764	1.184	7.125	0.975	0.747			

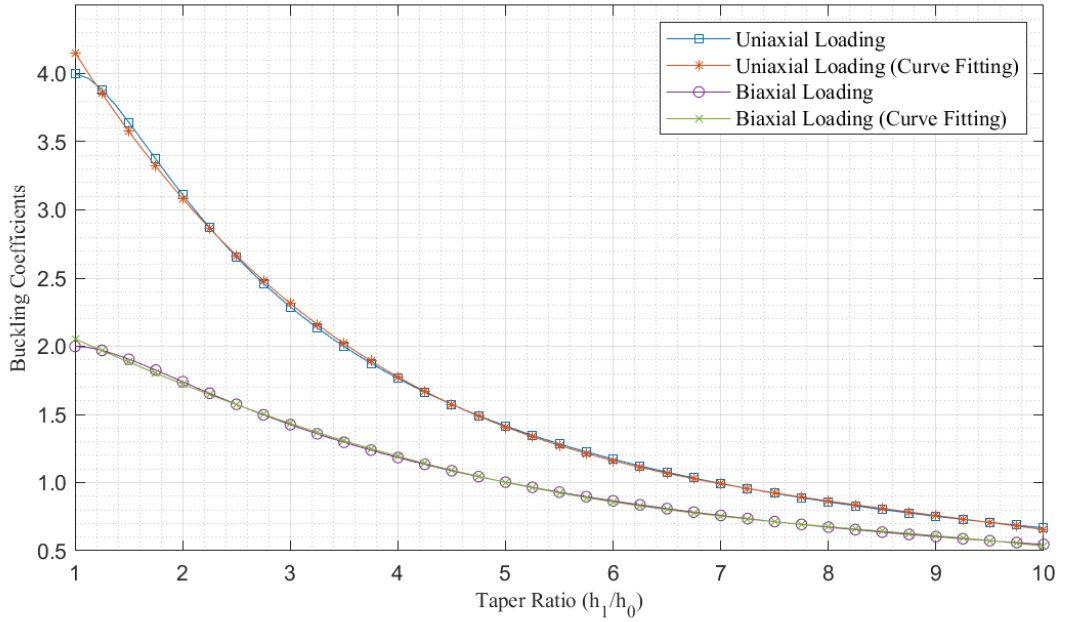


Fig. 4. The buckling coefficients for uniaxial and biaxial loadings.

MATLAB was used to fit curves to the numerical results, as depicted in Fig. 4. The formulas of these fitted curves are given by Equation 9 and Equation 10 for uniaxial and biaxial loadings, respectively. These formulas can be utilized in the design of simply supported tapered square plates.

$$k_u = 0.0003741 \left(\frac{h_1}{h_0}\right)^4 - 0.0153 \left(\frac{h_1}{h_0}\right)^3 + 0.2328 \left(\frac{h_1}{h_0}\right)^2 - 1.668 \left(\frac{h_1}{h_0}\right) + 5.603 \quad (9)$$

$$k_b = -0.0001848 \left(\frac{h_1}{h_0}\right)^4 + 0.002808 \left(\frac{h_1}{h_0}\right)^3 + 0.00918 \left(\frac{h_1}{h_0}\right)^2 - 0.3763 \left(\frac{h_1}{h_0}\right) + 2.419 \quad (10)$$

6. Conclusion

The critical buckling coefficient of tapered square plate under uniaxial and biaxial loadings are calculated by using general purpose finite element software. Plate is simply supported in all four edges. The plates are tapered in only x direction and these non-uniform plates with linear thickness variations are loaded in-plane in the direction of thickness variations. The key findings from the research can be summarized as below:

- While creating the simply supported steel plate models, the thickness at the ($x=0$) AD edge of the plate was taken as constant h_0 .
- Plates have a small taper ratio of h_1 / h_0 along the x-axis.
- Plate thickness varies slightly, linearly and the taper ratio varies from 1 to 10.

- Formulas have been developed separately for the critical buckling load coefficients for uniaxial and biaxial loading cases.
- Curves for design are presented for uniaxial and biaxial loadings.
- In tapered plates, it has been determined that when the thickness ratio or the slope increases by a very small amount the critical buckling load change more rapidly.
- While the difference in buckling coefficient between uniaxial and biaxial loading is approximately 2 for uniform thickness, this difference decreases to 0.122 as the taper ratio increases.

In future research, different parameters could be used for the critical buckling investigation of non-uniform plates under in plane loads. These parameters could be aspect ratios, materials, boundary conditions, thickness functions, etc.

Acknowledgements

There is no conflict of interest with any person/institution in the prepared article.

Funding

No funding was received to assist with the preparation of this manuscript.

References

- [1] S. S. Hwang, "Stability of plates with piecewise varying thickness," *J. Appl. Mech.*, vol. 40, no. 4, pp. 1127–1129, 1973
- [2] P. V. Navaneethakrishnan, "Buckling of nonuniform plates: spline method," *J. Eng. Mech.*, vol. 114, no. 5, 1988.
- [3] C. M. Wang, G. M. Hong, and T. J. Tan, "Elastic buckling of tapered circular plates," *Comput. Struct*, vol. 55, no. 6, pp. 1055–1061, 1995.
- [4] W. H. Wittrick and C. H. Ellen, "Buckling of tapered rectangular plates in compression," *Aeronautical Quarterly*, vol. 13, no. 4, pp. 308–326, Nov. 1962, doi: 10.1017/s0001925900002547.
- [5] B. Klein, "The buckling of tapered plates in compression compressive buckling under varying loading of simply supported plates simultaneously tapered in plan form and in thickness," *Aircraft Engineering and Aerospace Technology*, vol. 28, no. 12, pp. 427–430, 1956, doi: 10.1108/eb032774.
- [6] G. G. Pope, "The buckling of plates tapered in thickness," 1963.
- [7] I. E. Harik, X. Liu, and R. Ekambaram, "Elastic stability of plates with varying rigidities," *Computers and Structures*, vol. 38, no. 2, pp. 161–168, 1991.
- [8] M. S. Nerantzaki and J. T. Katsikadelis, "Buckling of plates with variable thickness—an analog equation solution," *Eng Anal Bound Elem*, vol. 18, no. 2, pp. 149–154, Sep. 1996.
- [9] M. Saeidifar, S. N. Sadeghi, and M. R. Saviz, "Analytical solution for the buckling of rectangular plates under uni-axial compression with variable thickness and elasticity modulus in the y-direction," *Proc Inst Mech Eng C J Mech Eng Sci*, vol. 224, no. 1, pp. 33–41, Aug. 2009, doi: 10.1243/09544062JMES1562.
- [10] K. K. Viswanathan, P. V. Navaneethakrishnan, and Z. A. Aziz, "Buckling analysis of rectangular plates with variable thickness resting on elastic foundation," in *IOP Conference Series: Earth and Environmental Science*, Institute of Physics Publishing, 2015. doi: 10.1088/1755-1315/23/1/012006.
- [11] A. Hassan and N. Kurgan, "Modeling and buckling analysis of rectangular plates in ANSYS," *International Journal of Engineering and Applied Sciences*, vol. 11, no. 1, pp. 310–329, May 2019, doi: 10.24107/ijeas.531011.
- [12] A. Kacimi, G. Ikhenazen, F. Mohri, M. Saidani and M. Kilardj, "Linear and nonlinear stability analysis of thin rectangular plates subjected to local in-plane shearing," *Structural Engineering International*, vol. 33, no. 4, pp. 689–698, 2023, doi: 10.1080/10168664.2023.2208143.
- [13] F. Uslu, M.H. Saraçoğlu and U. Albayrak, "Buckling of Square and Circular Perforated Square Plates under Uniaxial Loading," *Journal of Innovations in Civil Engineering and Technology*, vol. 4, no. 2, pp. 61–75, 2022.
- [14] F. Baran and D. Balkan, "Thermal buckling analysis of laminated plates with variable angle fiber orientation," *Niğde Ömer Halisdemir University Journal of Engineering Sciences*, vol. 12, no. 3, pp. 912–918, 2023, doi: 10.28948/ngumuh.1241416.
- [15] M. E. Deniz, "Buckling behavior of curved composite plates with a central circular hole," *Dicle University Journal of Engineering*, vol. 8, no. 1, pp. 203–212, 2017.
- [16] Timoshenko, S., Woinowsky-Krieger, S., *Theory of Plates and Shells*. McGraw-Hill, Inc., 1959.
- [17] D. Çıraklı, M.H. Saraçoğlu, U. Albayrak, "The effect of layer thicknesses on buckling behavior in foam core sandwich plates with various materials," *International Journal of Technological Sciences*, vol. 15, no. 3, pp. 111–117, Dec 2023, doi: 10.55974/utbd.1373786.
- [18] A. Swanson Analysis System Inc., "ANSYS User's manual." 2005.



E-ISSN: 2687-6167

Number 59, December 2024

RESEARCH ARTICLE

Receive Date: 01.10.2024

Accepted Date: 03.11.2024

On $(k,3)$ -arcs derived by Ceva configurations in $PG(2,5)$

Elif Altıntaş Kahrıman^{a,*}, Ayşe Bayar^b

^a*Haliç University, Faculty of Engineering, Software Engineering, İstanbul, 34000, Turkey,*

ORCID: 0000-0002-3454-0326

^b*Eskişehir Osmangazi University, Faculty of Science, Department of Mathematics and Computer Sciences, Eskişehir, 26000, Turkey,*

ORCID: 0000-0002-2210-5423

Abstract

In this study, we investigate complete $(k,2)$ -arcs and $(k,3)$ -arcs derived from a Ceva configuration in the projective plane of order five by implementing an algorithm in C#. Our results indicate the existence of a complete $(6,2)$ -arc that has no points in common with the $(7,3)$ -arc formed by the Ceva configuration. Furthermore, we identify eight different complete $(10,3)$ -arcs that include a Ceva configuration. Additionally, we explore cyclic order Ceva configurations, denoted as C_1, C_2, C_3 , and C_4 , all of which have a common center. The vertices of each configuration C_i are on the sides of the preceding configuration C_{i-1} , with i ranging from 2 to 4. We determine different thirty-two complete $(10,3)$ -arcs and different two complete $(6,2)$ -arcs by constructing cyclic order Ceva configurations C_1, C_2, C_3, C_4 with a common center in $PG(2,5)$.

© 2023 DPU All rights reserved.

Keywords: projective plane; $(k,3)$ -arc; Ceva configuration

1. Introduction

In projective geometry, arcs are very important and have many uses in combinatorics and related domains. A k -arc is defined as a set K of k points (where $k \geq 3$) that are not all located on the same line in a finite projective plane π (which need not be Desarguesian). A $(p + 2)$ -arc is referred to as a hyperoval. The highest value of k can be achieved only when p is even, while $k \geq p + 2$ if the plane π has an order of p . Ovals are commonly referred to in the literature, with Hirschfeld being a notable source [1]. Research on arcs in projective planes is extensive, particularly regarding full $(k,2)$ -arcs that create complete quadrangles, leading to Fano planes in the projective plane, as analyzed in [2, 3]. The identification and classification of Fano subplanes in a projective plane of order nine, related to parts of a left nearfield of order nine, are described in [4].

Fano configurations in 5-dimensional projective spaces over $GF(2)$ are discovered in [5]. In the projective planes of order nine and twenty-five, the simplest Cartesian Group techniques for classifying $(k,3)$ -arcs are outlined in

references [6, 7]. The research by Altıntaş investigates $(k,2)$ -arcs in the projective plane of order five, coordinated by elements from $GF(5)$, using an arc-finding algorithm developed in C# [8]. Complete (k,n) -arcs, $n=2,3,4$ related to Desargues configuration are determined in [9].

One of the conclusions that eluded Euclid is Ceva's Theorem, which will be stated and examined from now on. It appears nowhere in his thirteen volumes of the Elements. Giovanni Ceva established the theory that bears his name circa 1678. The outcome was published in his work *De Lineis Rectis*, also known as *The Straight Line*. In addition, he addressed various additional geometric results and rediscovered Menelaus' Theorem. According to the Ceva Theorem, if we draw segments from a triangle's vertices to the interior points of its opposite sides, the segments will only be concurrent that is, share a common point if and only if the ratios taken cyclically that the cevians on the opposite sides determine multiply out to 1 [10].

In the recent Benyi-Curgus generalization of the theorems of Ceva and Menelaus [11], both the collinearity of points and the concurrence of straightlines specified by six points on the edges of a triangle are characterized. Both Menelaus's and Ceva's theorems have intriguing applications in projective and Euclidean geometries.

Theorems of Ceva and Menelaus are well-known conclusions. However, these theorems characterize a projective property through an affine property: concurrency in Ceva's theorem and collinearity in Menelaus' theorem. Benitez aims to get over this, therefore. In particular, the cross ratio a projective quantity is used in the study to characterize the concurrence of the cevians [12]. One can express Menelaus' theorem in a projective form by using the dual of this latter characterization. Nicolae discusses the Ceva-Menelaus transformation of a line into four curves. This proved to be a parabola, a hyperbola, or a bean ellipse. The triangle's three straight lines are tangent to each of the conics. Furthermore, in the study the harmonic transform for a ceviana has no envelope since it is a beam of straight lines flowing through a point is discovered [13].

Menelaus and Ceva theorems in projective planes $P_2(F)$, where F is the field of characteristic not equal to two, were given by Kelly B. Funk [14]. Menelaus and Ceva 6-figures were first introduced in Moufang projective planes by Kaya and Çiftçi in [15]. Menelaus and Ceva's 6-figures in fibered geometry were examined in [16] with multiple degrees of membership of the points and lines of the basic geometry. Intuitionistic fuzzy projective Menelaus and Ceva's conditions in the intuitionistic fuzzy projective plane with base plane that is projective plane are given by Akça et al. [17].

The primary goal of this work is to examine $(k,3)$ -arcs in $PG(2,5)$ that are associated with the Ceva configuration. In Section 2, we present specific terms that are important for our research. The projective plane of order five over $GF(5)$ is constructed in Section 3 together with its lines, points, and incidence relation. A Ceva configuration is then determined in this projective plane. In Section 4, we introduce our algorithm and method to find all the results that related to (k,n) -arcs derived by a Ceva configuration in $PG(2,5)$. It is demonstrated that eight distinct complete $(10,3)$ -arcs exist, each containing a Ceva configuration and a complete $(6,2)$ -arc formed by the remaining points, utilizing the algorithm implemented in C#. Also, cyclic order Ceva configurations C_1, C_2, C_3, C_4 derived from the Ceva configuration C_1 are defined in $PG(2,5)$. We give the examples related to the complete $(10,3)$ -arcs and complete $(6,2)$ -arcs derived by the cyclic order Ceva configurations C_1, C_2, C_3, C_4 with the common center. In the last section, we give our results.

2. Preliminaries

This section offers a review of important definitions and theorems concerning projective planes, along with an outline of certain properties of arcs in these planes.

Definition 1. A projective plane (N, D, \circ) consists of a set N of points, and a set D of subsets of N , called lines, such that every pair of points is contained in exactly one line, every two different lines intersect in exactly one point, and there exist four points, no three of which are collinear.

Definition 2. The vector space $V(n+1, q)$ is $(n+1)$ -dimensional and consists of vectors with coordinates from the finite field $GF(q)$. The projective space $PG(n, q)$ is defined as the collection of points, each corresponding to a line that passes through the origin in $V(n+1, q)$. Specifically, this means that each point in $PG(n, q)$ can be represented as $P(x)$, where x is any non-zero vector in $V(n+1, q)$. If K is the finite field $GF(q)$, also denoted as F_q , then the n -dimensional projective plane is referred to as $PG(n, K)$ or $PG(n, q)$. In this context, q represents the order of $PG(n, q)$. The number of points in this projective plane can be determined using the formula

$$\theta(n) = \frac{q^{n+1}-1}{q-1}.$$

(x_1, x_2, \dots, x_n) represents a point in N , where x_1, x_2, \dots, x_n are not all zero, and $(\lambda x_1, \lambda x_2, \dots, \lambda x_n) \equiv (x_1, x_2, \dots, x_n)$, $\lambda \in K \setminus \{0\}$. Similarly, the notation $[a_1, a_2, \dots, a_n]$ denotes any line in D , where a_1, a_2, \dots, a_n are not all zero. The relationship $[\mu a_1, \dots, \mu a_n] \equiv [a_1, \dots, a_n]$ holds for $\mu \in K \setminus \{0\}$. The projective plane P_2K is characterized as a point-line geometry (N, D, \circ) defined by K . The incidence relation is given by $\circ: (x_1, \dots, x_n) \circ [a_1, \dots, a_n]$ if and only if $a_1x_1 + a_2x_2 + a_3x_3 + \dots + a_nx_n = 0$.

Let p denote a prime number and r a positive integer. The projective plane of order $q = p^r$ over the finite field $K = GF(p^r)$, where p^r represents the number of elements, is expressed as $P_2K = PG(2, p^r)$ [18].

Definition 4. Let P be a projective plane. In P , a 6-figure is a sequence of 6 distinct points $(A_1A_2A_3, A_1'A_2'A_3')$ such that $A_1A_2A_3$ is a triangle, and $A_1' \in A_2A_3, A_2' \in A_3A_1, A_3' \in A_1A_2$. $A_1, A_2, A_3, A_1', A_2', A_3'$ are called vertices of this 6-figure. If the lines $A_1A_1', A_2A_2', A_3A_3'$ are concurrent, $(A_1A_2A_3, A_1'A_2'A_3')$ is called a Ceva 6-figure [15].

Definition 5. In a projective plane, a (k, n) -arc K is defined as a set of k points such that any line intersects K at exactly n points, with no line intersecting the set at more than n points, where $n \geq 2$ [19].

Definition 6. A line l in a projective plane is defined as an μ -secant of a (k, n) -arc K if it intersects K at μ points. Let τ_i represent the total number of i -secants to K . The notations σ_i or $\sigma_i(Q)$ denote the count of i -secants to the set K that pass through a point Q , which is part of $P \setminus K$. A point Q is classified as an index zero point if the condition $\sigma_n(Q) = 0$ holds [20].

If no $(k+1, n)$ -arc contains a (k, n) -arc, then the (k, n) -arc is considered complete [20].

Definition 7. The points out of a (k, n) -arc K in P which passes through it i -secant of K is called a point of index i [20].

3. The Projective plane of order 5

The study considers $PG(2,5)$, which is built over $GF(5)$ using the irreducible polynomial $f(x) = x^3 + 2x^2 + x - 1$. The elements of $GF(5)$ with thirty one points and thirty one lines are 0, 1, 2, 3, and 4. In the projective plane order five, every line consists of six points, and each point is associated with six lines that pass through it [21].

The projective plane of order five has a point set N defined as $N = \{N_i | i = 1, 2, \dots, 31\}$ where

$$\begin{aligned} N_1 &= (0, 0, 1), & N_2 &= (1, 1, 1), & N_3 &= (1, 2, 2), & N_4 &= (1, 4, 2), & N_5 &= (1, 4, 3), \\ N_6 &= (1, 3, 4), & N_7 &= (1, 0, 3), & N_8 &= (1, 3, 1), & N_9 &= (1, 2, 4), & N_{10} &= (1, 0, 4), \end{aligned}$$

$$\begin{aligned}
 N_{11} &= (1, 0, 1), & N_{12} &= (1, 2, 1), & N_{13} &= (1, 2, 3), & N_{14} &= (1, 3, 0), & N_{15} &= (0, 1, 3), \\
 N_{16} &= (1, 1, 3), & N_{17} &= (1, 3, 3), & N_{18} &= (1, 3, 2), & N_{19} &= (1, 4, 0), & N_{20} &= (0, 1, 4), \\
 N_{21} &= (1, 1, 0), & N_{22} &= (0, 1, 1), & N_{23} &= (1, 1, 2), & N_{24} &= (1, 4, 4), & N_{25} &= (1, 0, 2), \\
 N_{26} &= (1, 4, 1), & N_{27} &= (1, 2, 0), & N_{28} &= (0, 1, 2), & N_{29} &= (1, 1, 4), & N_{30} &= (1, 0, 0), \\
 N_{31} &= (0, 1, 0).
 \end{aligned}$$

Table 1 presents the incidence relation between the points and the lines in the projective plane $PG(2,5)$. In this table, each row corresponds to a specific line, denoted as D_i , where i ranges from 1 to 31. For each line D_i , the table lists the points on that line.

Table 1. The points and lines based on incidence relation.

D_1	N_2	N_3	N_{17}	N_{22}	N_{24}	N_{30}
D_2	N_3	N_4	N_{18}	N_{23}	N_{25}	N_{31}
D_3	N_4	N_5	N_{19}	N_{24}	N_{26}	N_1
D_4	N_5	N_6	N_{20}	N_{25}	N_{27}	N_2
D_5	N_6	N_7	N_{21}	N_{26}	N_{28}	N_3
D_6	N_7	N_8	N_{22}	N_{27}	N_{29}	N_4
D_7	N_8	N_9	N_{23}	N_{28}	N_{30}	N_5
D_8	N_9	N_{10}	N_{24}	N_{29}	N_{31}	N_6
D_9	N_{10}	N_{11}	N_{25}	N_{30}	N_1	N_7
D_{10}	N_{11}	N_{12}	N_{26}	N_{31}	N_2	N_8
D_{11}	N_{12}	N_{13}	N_{27}	N_1	N_3	N_9
D_{12}	N_{13}	N_{14}	N_{28}	N_2	N_4	N_{10}
D_{13}	N_{14}	N_{15}	N_{29}	N_3	N_5	N_{11}
D_{14}	N_{15}	N_{16}	N_{30}	N_4	N_6	N_{12}
D_{15}	N_{16}	N_{17}	N_{31}	N_5	N_7	N_{13}
D_{16}	N_{17}	N_{18}	N_1	N_6	N_8	N_{14}
D_{17}	N_{18}	N_{19}	N_2	N_7	N_9	N_{15}
D_{18}	N_{19}	N_{20}	N_3	N_8	N_{10}	N_{16}
D_{19}	N_{20}	N_{21}	N_4	N_9	N_{11}	N_{17}
D_{20}	N_{21}	N_{22}	N_5	N_{10}	N_{12}	N_{18}
D_{21}	N_{22}	N_{23}	N_6	N_{11}	N_{13}	N_{19}
D_{22}	N_{23}	N_{24}	N_7	N_{12}	N_{14}	N_{20}
D_{23}	N_{24}	N_{25}	N_8	N_{13}	N_{15}	N_{21}
D_{24}	N_{25}	N_{26}	N_9	N_{14}	N_{16}	N_{22}
D_{25}	N_{26}	N_{27}	N_{10}	N_{15}	N_{17}	N_{23}
D_{26}	N_{27}	N_{28}	N_{11}	N_{16}	N_{18}	N_{24}
D_{27}	N_{28}	N_{29}	N_{12}	N_{17}	N_{19}	N_{25}
D_{28}	N_{29}	N_{30}	N_{13}	N_{18}	N_{20}	N_{26}
D_{29}	N_{30}	N_{31}	N_{14}	N_{19}	N_{21}	N_{27}
D_{30}	N_{31}	N_1	N_{15}	N_{20}	N_{22}	N_{28}
D_{31}	N_1	N_2	N_{16}	N_{21}	N_{23}	N_{29}

4. An algorithm for constructing (k,n) -arcs related to the Ceva configuration in the projective plane of order five

In this section, we present an algorithm used to construct (k, n) –arcs, and to identify $(k, 3)$ –arcs based on secant distributions in $PG(2,5)$.

Method: Finding (k, n) –arcs

Step 1: To identify the points and lines of $PG(2,5)$, we utilize the irreducible polynomial $f(x) = x^3 + 2x^2 + x - 1$. By applying this polynomial, we determine thirty-one points and thirty-one lines within the projective plane, as detailed in Table 1.

Step 2: Consider a Ceva Configuration in given projective plane of order five. In Ceva configuration, a center point and six other points form a $(7,3)$ -arc denoted by C in $PG(2,5)$, which is incomplete.

Step 3: There are 6 points not on the lines spanned by the points of Ceva configuration.

Step 4: The complete $(k, 3)$ –arcs are investigated by adding these six points to $(7, 3)$ –arc.

We present the following algorithm, implemented in C#, designed to identify complete $(k,3)$ -arcs within $PG(2,5)$:

Steps of Algorithm

$A \leftarrow \text{Read}(\text{Excel File})$

$B \leftarrow \text{Read}(\text{Text File})$

$C \leftarrow A$

while $s(C) > 0$

$B_i \leftarrow \text{input}(b), \{b | b \in C, b \notin B, i = s(B) + 1\}$

$j = 1$

while $j \leq s(B)$

for $k = (j+1)$ to $s(B)$

$m \leftarrow \text{the index of row on } B_j, B_k$

$D \leftarrow A_{mn}; \{A_{mn} | A_{mn} \neq B_j, A_{mn} \neq B_k, n = 1, \dots, 10\}$

Remove a from A ; $\{a | a \in A, a \in D\}$

$C \leftarrow c; \{c | c \in A, c \notin C\}$

end for

$j = j + 1$

end while

end while

Theorem 1. Let C be a Ceva configuration in $PG(2,5)$. If the given algorithm is applied to the points of Ceva configuration to find $(k,3)$ - arcs, there is a $(6,2)$ - arc constructing with the remaining points.

Proof. Let C be Ceva configuration in $PG(2,5)$. If we apply the algorithm to C , six points are remained in $PG(2,5)$. Since all points of a projective plane lie on a pencil of lines through a single point, the points of a Ceva configuration are on a pencil of lines through a point. So, five line through any point outside C contains one point of the Ceva configuration, while one line contains two points of C . Since any three points from the remaining set are not collinear, it follows that this set of remaining points forms a $(6,2)$ -arc.

Theorem 2. There exist eight distinct complete $(10,3)$ -arcs that include a Ceva configuration in $PG(2,5)$.

Proof. Let C represent a Ceva configuration. By utilizing the algorithm outlined in Theorem 1 on C , we can get a $(6,2)$ -arc. Each point in this $(6,2)$ -arc lies on six lines, of which five intersect the Ceva configuration C at a single point, while one line intersects it at two points. Consequently, there are three lines that intersect the configuration and pass through the points of the $(6,2)$ -arc, which qualify as 2-secant lines. Choosing one remaining point from each of

these 2-secant lines and adding them to the (7,3)-arc formed by the Ceva configuration results in eight distinct complete (10,3)-arcs.

Theorem 3. Let C_1 , be a Ceva configuration in $PG(2,5)$. Then the cyclic order of Ceva configurations C_1, C_2, C_3, C_4 can be constructed having the same center such that the vertices of Ceva configuration C_i , are the points on the sides of the Ceva configuration $C_{i-1}, i=2,3,4$.

Proof. Let C_1 be the Ceva configuration $(A_1A_2A_3, A_1'A_2'A_3')$ with the center M in $PG(2,5)$. Let the vertices of C_2 with the center M be A_1', A_2' , and A_3' . If we define the points A_1'', A_2'' , and A_3'' as the intersection points $MA_1' \cap A_2'A_3'$, $MA_2' \cap A_1'A_3'$, and $MA_3' \cap A_1'A_2'$, respectively, C_2 is obtained as the Ceva configuration $(A_1'A_2'A_3', A_1''A_2''A_3'')$ with the center M. In the same way that we obtained C_2 from C_1 , we can now define a Ceva configuration C_3 as $(A_1''A_2''A_3'', A_1'''A_2'''A_3''')$ such that the vertices of C_3 are the points on the sides of C_2 where A_1''', A_2''' , and A_3''' as the intersection points $MA_1'' \cap A_2''A_3''$, $MA_2'' \cap A_1''A_3''$, and $MA_3'' \cap A_1''A_2''$. Similarly, the Ceva configuration C_4 is constructed by using the side points and the center M of C_3 . C_4 can be found as $(A_1'''A_2'''A_3''', A_1A_2A_3)$ where A_1''''', A_2''''' , and A_3''''' are the intersection points $MA_1''' \cap A_2'''A_3'''$, $MA_2''' \cap A_1'''A_3'''$, and $MA_3''' \cap A_1'''A_2'''$, respectively. Since the vertices of C_5 are the points A_1, A_2, A_3 on the sides of C_4 , C_5 configuration is the same as C_1 . Thus, C_1, C_2, C_3, C_4 are cyclic order of Ceva configurations $C_i, i=1,2,3,4$ in $PG(2,5)$.

Corollary. Let C_1, C_2, C_3, C_4 be cyclic order of Ceva configurations $C_i, i=1,2,3,4$ in $PG(2,5)$. Then there are thirty two (10,3)- arcs which is defined by C_1, C_2, C_3 , and C_4 .

Proof. Let C_1, C_2, C_3, C_4 be cyclic order of Ceva configurations $C_i, i=1,2,3,4$ in $PG(2,5)$. Since there are eight different complete (10,3) –arcs containing a Ceva configuration in $PG(2,5)$ from Theorem 2, thirty two different complete (10,3)-arcs are constructed from the Ceva configurations C_1, C_2, C_3 , and C_4 .

Now, by taking cyclic order Ceva configurations C_1, C_2, C_3, C_4 derived from the Ceva configuration $C_1 = (N_3N_2N_6, N_5N_{21}N_{24})$ in $PG(2,5)$, we give all complete (10,3)–arcs with tables and complete (6,2)–arcs for each Ceva configurations $C_i, i = 1,2,3,4$.

Example 1. Let C_1 be (7,3)-arc defined by the Ceva configuration $(N_3N_2N_6, N_5N_{21}N_{24})$ with the center point N_{29} . By implementing this algorithm to C_1 , it is seen that $C_1 = \{N_2, N_3, N_5, N_6, N_{21}, N_{24}, N_{29}\}$ is (7,3)-arc but incomplete arc. In this projective plane, the points on the lines spanned by (7,3)-arc are deleted in $PG(2,5)$, then $N_4, N_8, N_{12}, N_{13}, N_{18}, N_{18}, N_{19}$ points are remained. Since six lines pass through each of these points in $PG(2,5)$, five of them intersect the Ceva configuration in one point, and one of them intersect the Ceva configuration in two points. In Table 2, 1–secant and 2–secant lines of the Ceva configuration passing through the remaining points out of (7, 3)–arc are given in $PG(2,5)$.

Table 2. The secant lines of the Ceva configuration.

Point	1-secant lines	2-secant lines
N_4	$D_2, D_6, D_{12}, D_{14}, D_{19}$	D_3
N_8	$D_6, D_7, D_{10}, D_{16}, D_{18}$	D_{23}
N_{12}	$D_{10}, D_{11}, D_{14}, D_{22}, D_{27}$	D_{20}
N_{13}	$D_{11}, D_{12}, D_{15}, D_{21}, D_{28}$	D_{23}
N_{18}	$D_2, D_{16}, D_{17}, D_{26}, D_{28}$	D_{20}
N_{19}	$D_{17}, D_{18}, D_{21}, D_{27}, D_{29}$	D_3

When the algorithm applied to C_1 and the remaining points, eight complete (10,3)-arcs are obtained and given in Table 3.

Table 3. The complete (10,3)-arcs containing the Ceva configuration C_1 .

The incomplete (7,3)-arc C_1	The complete (10,3)-arcs
$C_1 \cup \{N_4, N_8, N_{12}\}$	$\{N_2, N_3, N_4, N_5, N_6, N_8, N_{12}, N_{21}, N_{24}, N_{29}\}$
$C_1 \cup \{N_4, N_8, N_{18}\}$	$\{N_2, N_3, N_4, N_5, N_6, N_8, N_{18}, N_{21}, N_{24}, N_{29}\}$
$C_1 \cup \{N_4, N_{12}, N_{13}\}$	$\{N_2, N_3, N_4, N_5, N_6, N_{12}, N_{13}, N_{21}, N_{24}, N_{29}\}$
$C_1 \cup \{N_4, N_{13}, N_{18}\}$	$\{N_2, N_3, N_4, N_5, N_6, N_{13}, N_{18}, N_{21}, N_{24}, N_{29}\}$
$C_1 \cup \{N_8, N_{12}, N_{19}\}$	$\{N_2, N_3, N_5, N_6, N_8, N_{12}, N_{19}, N_{21}, N_{24}, N_{29}\}$
$C_1 \cup \{N_8, N_{18}, N_{19}\}$	$\{N_2, N_3, N_5, N_6, N_8, N_{18}, N_{19}, N_{21}, N_{24}, N_{29}\}$
$C_1 \cup \{N_{12}, N_{13}, N_{19}\}$	$\{N_2, N_3, N_5, N_6, N_{12}, N_{13}, N_{19}, N_{21}, N_{24}, N_{29}\}$
$C_1 \cup \{N_{13}, N_{18}, N_{19}\}$	$\{N_2, N_3, N_5, N_6, N_{13}, N_{18}, N_{19}, N_{21}, N_{24}, N_{29}\}$

Let's start by taking the points N_5, N_{21}, N_{24} on the sides of $C_1 = (N_3N_2N_6, N_5N_{21}N_{24})$ as the vertices of a new Ceva configuration $C_2 = (N_5N_{21}N_{24}, N_1N_{10}N_{15})$ having the same center point N_{29} . If we apply the algorithm to C_2 , then the remaining points are $N_7, N_{17}, N_{20}, N_{13}, N_{18}, N_{19}$. Six lines pass through each of these points. Five of them intersect C_2 in one points, and one is the remaining line, which intersect C_2 in two points. If one remaining point is chosen from each of these 2-secant lines and added to C_2 , eight different complete (10,3)-arcs are obtained as following Table 4. And also these remaining points $N_7, N_{17}, N_{20}, N_{13}, N_{18}, N_{19}$ construct (6,2)-arcs according to Theorem 1.

Table 4. The complete (10,3)-arcs containing the Ceva configuration C_2 .

The incomplete (7,3)-arc C_2	The complete (10,3)-arcs
$C_2 \cup \{N_7, N_{17}, N_{20}\}$	$\{N_1, N_5, N_7, N_{10}, N_{15}, N_{17}, N_{20}, N_{21}, N_{24}, N_{29}\}$
$C_2 \cup \{N_7, N_{17}, N_{28}\}$	$\{N_1, N_5, N_7, N_{10}, N_{15}, N_{17}, N_{21}, N_{24}, N_{28}, N_{29}\}$
$C_2 \cup \{N_7, N_{20}, N_{27}\}$	$\{N_1, N_5, N_7, N_{10}, N_{15}, N_{20}, N_{21}, N_{24}, N_{27}, N_{29}\}$
$C_2 \cup \{N_7, N_{27}, N_{28}\}$	$\{N_1, N_5, N_7, N_{10}, N_{15}, N_{21}, N_{24}, N_{27}, N_{28}, N_{29}\}$
$C_2 \cup \{N_{17}, N_{20}, N_{30}\}$	$\{N_1, N_5, N_{10}, N_{15}, N_{17}, N_{20}, N_{21}, N_{24}, N_{29}, N_{30}\}$
$C_2 \cup \{N_{17}, N_{28}, N_{30}\}$	$\{N_1, N_5, N_{10}, N_{15}, N_{17}, N_{21}, N_{24}, N_{28}, N_{29}, N_{30}\}$
$C_2 \cup \{N_{20}, N_{27}, N_{30}\}$	$\{N_1, N_5, N_{10}, N_{15}, N_{20}, N_{21}, N_{24}, N_{27}, N_{29}, N_{30}\}$
$C_2 \cup \{N_{27}, N_{28}, N_{30}\}$	$\{N_1, N_5, N_{10}, N_{15}, N_{21}, N_{24}, N_{27}, N_{28}, N_{29}, N_{30}\}$

Let C_3 and C_2 be taken instead of C_2 and C_1 , respectively. Then new Ceva configuration C_3 is $(N_1N_{10}N_{15}, N_{11}N_{23}N_{31})$ with the same center point N_{29} . If we apply the algorithm to C_3 , then the remaining points are $N_4, N_8, N_{12}, N_{13}, N_{18}, N_{19}$. If one remaining point is chosen from each of these 2-secant lines and added to C_3 , eight different complete (10,3)-arcs are obtained as following Table 5.

Table 5. The complete (10,3)-arcs containing the Ceva configuration C_3 .

The incomplete (7,3)-arc C_3	The complete (10,3)-arcs
$C_3 \cup \{N_7, N_{17}, N_{20}\}$	$\{N_1, N_5, N_7, N_{10}, N_{15}, N_{17}, N_{20}, N_{21}, N_{24}, N_{29}\}$
$C_3 \cup \{N_7, N_{17}, N_{28}\}$	$\{N_1, N_5, N_7, N_{10}, N_{15}, N_{17}, N_{21}, N_{24}, N_{28}, N_{29}\}$
$C_3 \cup \{N_7, N_{20}, N_{27}\}$	$\{N_1, N_5, N_7, N_{10}, N_{15}, N_{20}, N_{21}, N_{24}, N_{27}, N_{29}\}$
$C_3 \cup \{N_7, N_{27}, N_{28}\}$	$\{N_1, N_5, N_7, N_{10}, N_{15}, N_{21}, N_{24}, N_{27}, N_{28}, N_{29}\}$

$C_3 \cup \{N_{17}, N_{20}, N_{30}\}$	$\{N_1, N_5, N_{10}, N_{15}, N_{17}, N_{20}, N_{21}, N_{24}, N_{29}, N_{30}\}$
$C_3 \cup \{N_{17}, N_{28}, N_{30}\}$	$\{N_1, N_5, N_{10}, N_{15}, N_{17}, N_{21}, N_{24}, N_{28}, N_{29}, N_{30}\}$
$C_3 \cup \{N_{20}, N_{27}, N_{30}\}$	$\{N_1, N_5, N_{10}, N_{15}, N_{20}, N_{21}, N_{24}, N_{27}, N_{29}, N_{30}\}$
$C_3 \cup \{N_{27}, N_{28}, N_{30}\}$	$\{N_1, N_5, N_{10}, N_{15}, N_{21}, N_{24}, N_{27}, N_{28}, N_{29}, N_{30}\}$

Now, let C_4 and C_3 be taken instead of C_3 and C_2 , respectively. Then new Ceva configuration C_4 is $(N_{11}N_{23}N_{31}, N_3N_2N_6)$ with the same center point N_{29} . If we apply the algorithm to C_4 , then the remaining points are $N_7, N_{17}, N_{20}, N_{27}, N_{28}, N_{30}$. If one remaining point is chosen from each of these 2–secant lines and added to C_4 , eight different complete $(10,3)$ –arcs are obtained as following Table 6.

Table 6. The complete $(10,3)$ –arcs containing the Ceva configuration C_4 .

The completion of $(7,3)$ –arc C_4	The complete $(10,3)$ –arcs
$C_4 \cup \{N_7, N_{17}, N_{20}\}$	$\{N_2, N_3, N_6, N_7, N_{11}, N_{17}, N_{20}, N_{23}, N_{29}, N_{31}\}$
$C_4 \cup \{N_7, N_{17}, N_{27}\}$	$\{N_2, N_3, N_6, N_7, N_{11}, N_{17}, N_{23}, N_{27}, N_{29}, N_{31}\}$
$C_4 \cup \{N_7, N_{20}, N_{30}\}$	$\{N_2, N_3, N_6, N_7, N_{11}, N_{20}, N_{23}, N_{29}, N_{30}, N_{31}\}$
$C_4 \cup \{N_7, N_{27}, N_{30}\}$	$\{N_2, N_3, N_6, N_7, N_{11}, N_{23}, N_{27}, N_{28}, N_{29}, N_{31}\}$
$C_4 \cup \{N_{17}, N_{20}, N_{28}\}$	$\{N_2, N_3, N_6, N_{11}, N_{17}, N_{20}, N_{23}, N_{28}, N_{29}, N_{31}\}$
$C_4 \cup \{N_{17}, N_{27}, N_{28}\}$	$\{N_2, N_3, N_6, N_{11}, N_{17}, N_{23}, N_{27}, N_{28}, N_{29}, N_{31}\}$
$C_4 \cup \{N_{20}, N_{28}, N_{30}\}$	$\{N_2, N_3, N_6, N_{11}, N_{20}, N_{23}, N_{28}, N_{29}, N_{30}, N_{31}\}$
$C_4 \cup \{N_{27}, N_{28}, N_{30}\}$	$\{N_2, N_3, N_6, N_{11}, N_{23}, N_{27}, N_{28}, N_{29}, N_{30}, N_{31}\}$

5. Conclusion

In this work, it is determined that $(k,2)$ –arcs and $(k,3)$ –arcs obtained from a Ceva configuration in $PG(2,5)$ by giving the algorithm implemented in C#. The following conclusions are found in $PG(2,5)$:

1. There is a complete $(6,2)$ –arc that does not contain any common points with the $(7,3)$ –arc determined by a Ceva configuration.
2. There are eight different complete $(10,3)$ –arcs containing a Ceva configuration.
3. There are cyclic order Ceva configurations C_1, C_2, C_3, C_4 having the same center such that the vertices of the Ceva configuration C_i , are the points on the sides of the Ceva configuration $C_{i-1}, i=2,3,4$.
4. Related to the cyclic order Ceva configurations C_1, C_2, C_3, C_4 , there are two different complete $(6,2)$ –arcs and thirty-two different complete $(10,3)$ –arcs.

These findings show that there is a significant relationship between arcs and Ceva configurations in the projective planes.

Author Contributions

Ayşe Bayar led the conceptualization and development of the theoretical framework and provided insights during the conceptualization phase, and supervised the entire paper, ensuring the accuracy of the theoretical framework, in addition to editing the manuscript for clarity. Elif Altıntaş Kahrıman performed the (k,n) –arcs analysis, contributed to

the methodology by applying the algorithm, wrote the majority of the original manuscript. All authors commented on the final form of the manuscript.

Acknowledgements

This study did not receive any specific funding or financial assistance from governmental, commercial, or nonprofit organizations.

References

- [1] J.W.P. Hirschfeld and J.A. Thas, "General Galois Geometries," *Springer Monographs in Mathematics*. Springer-Verlag London, 2016.
- [2] A. Bayar, Z. Akca, E. Altıntas, and S. Ekmekci, S. "On the complete arcs containing the quadrangles constructing the Fano planes of the left near field plane of order 9," *New Trend Math. Sci.*, 4(4), 266-266, 2016. <http://dx.doi.org/10.20852/ntmsci.2016.113>
- [3] S. Ekmekci, A. Bayar, E. Altıntas, and Z. Akca, "On the Complete (k,2)- Arcs of the Hall Plane of Order 9," *IJARCSSE*, 6 (10), 282-288, 2016. ISSN: 2277 128X.
- [4] Z. Akca, S. Ekmekci, and A. Bayar, "On Fano Configurations of the Left Hall Plane of order 9," *Konuralp J. Math.*, 4 (2), 116-123, 2016.
- [5] Z. Akca, and A. Altıntas, "A Note on Fano Configurations in the Projective Space PG(5,2)," *Konuralp J. Math.*, 9(1), 190-192, 2021.
- [6] Z. Akca, "A numerical computation of (k, 3)-arcs in the left semifield plane order 9", *Int. Electron. J. Geom.*, 4(2), 13-21, 2011.
- [7] Z. Akca, and I. Günaltılı, I. "On the (k, 3)- arcs of CPG (2,25,5)," *Anadolu Univ J Sci Technol J Theor Sci*, 1(0), 21-27, 2012.
- [8] E. Altıntas, and A. Bayar, "Complete (k,2)-Arcs in the Projective Plane Order 5," *HSJG*, 5(1), 11-14, 2023. e-ISSN 2687-4261.
- [9] E. Altıntaş Kahrıman, A. Bayar, "Some Geometric Structures Related to Desargues Configuration in PG(2,5)," *Estuscience-Se*, 25(3):511-518, September 2024. <https://doi.org/10.18038/estubtda.1525364>
- [10] O.H. Rodriguez, and J. Fernández, "Heuristic Conversations On Ceva's Theorem", 2016.
- [11] V. Danos, and L. Regnier, "The structure of multiplicatives," *Arch Math Logic*, 28, 181-203, 1989. <https://doi.org/10.1007/BF01622878>
- [12] J. Benitez, "A unified proof of Ceva and Menelaus' theorems using projective geometry," *JGG*, 11(1):39-44, 2007. ISSN 1433-8157
- [13] V. Nicolae, "On The Ceva's And Menelaus's Theorems." *Rom. J. Phys.*, [S.l.], v. 5, n. 2, p. 43-50, 2020. ISSN 2537-5229.
- [14] B.K. Funk, "Ceva and Menelaus in projective geometry," University of Louisville, 42 p, 2008.
- [15] S. Çiftçi, R. Kaya, and J.C. Ferrar, "On Menelaus and Ceva 6-figures in Moufang projective planes," *Geom. Dedicata*, vol. 19, no. 3, pp. 295-296, 1985.
- [16] A. Bayar, and S. Ekmekçi, "On the Menelaus and Ceva 6-figures in the fibered projective planes," *Abstr. Appl. Anal.*, 1-5, 2014. 10.1155/2014/803173
- [17] Z. Akça, A. Bayar, and S. Ekmekçi, "On the intuitionistic fuzzy projective Menelaus and Ceva's conditions," *Commun. Fac. Sci. Univ. Ank. Ser. A1 Math. Stat.*, 69(1), 891-899, 2020. <https://doi.org/10.31801/cfsuasmas.567753>.
- [18] J.W.P. Hirschfeld, and J.A. Thas, "General Galois Geometries," *The Charendon Press*, Oxford, 1991.
- [19] J.W.P. Hirschfeld, and J.F. Voloch, "Group-arcs of prime order on cubic curves," *Finite Geometry and Combinatorics*, 191, 177-185, 2015.
- [20] J.W.P. Hirschfeld, and E.V.D. Pichanick "Bounded for arcs of arbitrary degree in finite Desarguesian Planes" *J Comb Des.*, 24(4), 184-196, 2016.
- [21] B.A. Qassim, "The construction for the arcs (8,4)-from the two arcs (7,4)-in PG (2,q), q=5," *J. Phys. Conf. Ser.*, 1664012039, 2020.



Contents lists available at *Dergipark*

Journal of Scientific Reports-A

journal homepage: <https://dergipark.org.tr/pub/jsr-a>



E-ISSN: 2687-6167

Number 59, December 2024

RESEARCH ARTICLE

Receive Date: 05.07.2024

Accepted Date: 29.07.2024

An experimental investigation of reducing the wake length at a low speed by passive flow control and biomimetic application

Sefa Şahin^a, Ahmet Selim Durna^b, Cem Kolbakır^{c,*}

^aDepartment of Aerospace Engineering, University of Samsun, Samsun, Türkiye ORCID: 0000-0002-2920-5849

^bDepartment of Aerospace Engineering, University of Samsun, Samsun, Türkiye ORCID: 0000-0002-9824-6660

^cDepartment of Aerospace Engineering, University of Samsun, Samsun, Türkiye ORCID: 0000-0002-3355-6289

Abstract

This study explores the use of biomimetic designs in passive flow control to reduce wake length at low speed, aiming to enhance aerodynamic efficiency. Inspired by nature's optimization of fluid dynamics in birds and marine life, this research investigates the applicability of these biological principles to improve aerospace engineering designs, particularly for low Reynolds number flows relevant to Unmanned Aerial Vehicles (UAVs). The experimental setup involved a smoke visualization wind tunnel to examine flow patterns around several wing models. These models incorporated bio-inspired elements, mimicking shark skin riblets and humpback whale tubercles, strategically positioned to delay flow separation and minimize wake length. The wing models, designed using 3D modeling software and printed via a 3D printer, were tested at various angles of attack in a smoke visualization wind tunnel by measuring their wake length via image processing. Experiments were carried out in two stages; types of protrusion were investigated on the first stage and the position of a selected protrusions examined in the second stage. The findings indicate significant differences in wake length reduction across the models, with certain biomimetic adaptations, especially optimized triangular protrusions inspired by shark skin, showing notable improvements in aerodynamic performance at higher angles of attack. Among different models in the first stage, Model B was the most effective model in aerodynamic performance with a drag reduction effect of 18% compared to the reference model NACA 0018. In the second stage experiments, Model B-15 showed the most effective aerodynamic result by reducing the wake length by 30% in the range of $\alpha=0^\circ-20^\circ$, while the reduction for Model B-20 was 26%. The results offer valuable insights into the design of efficient, low-speed flight vehicles, suggesting that biomimetics could lead to innovative designs with higher performance and energy efficiency. This research emphasizes the potential of integrating biomimetic principles into passive flow control strategies.

* Corresponding author. Tel.: +90-362-313-0055 | 2134

E-mail address: cem.kolbakir@samsun.edu.tr

© 2023 DPU All rights reserved.

Keywords: biomimetics; experimental aerodynamics; passive flow control; smoke visualization; riblet; drag reduction

1. Introduction

The use of a solution inspired by living and/or inanimate objects is called bio-inspiration. It has been widely used in building design, especially in art, since the early times of humanity. It was first mentioned in 1957 by Otto Schmitt, under a scientific approach put forward to solve the problems of humans regarding systems, processes, and models in nature. It has taken its place in the literature as “biomimetic” in 1969 [1]. Although its initial application was primarily seen in architectural designs, today its usage in engineering problems has become widespread, evolving into a recognized branch of science. Its application in the field of aerodynamics started back in the 1500s with Da Vinci and has been systematically investigated over the last 40 years, and the most common examples of its application are in aircraft designed by being inspired by the body and wing structure of living things capable of flying [2].

Aviation was inspired not only by the structure of flying creatures but also by birds, insects, plants and sea creatures. The body and fin formations of sea creatures, along with their similar structure to creatures in the air, draw attention. Studies on the leaf and spiny structures of plants also show formations to reduce drag or allow the fluid to slide on a hydrophobic surface [3]. Observing birds in general, it has been proven that the wing structures, the arrangement of the feathers on the front and rear wings, and the protrusions on wing tips are used to reduce drag and achieve lower energy consumption [3,4]. Due to the movements of living things in nature, it is logical to create new designs inspired by nature, especially in small-sized aircraft like micro UAVs. The low-speed interactions that take place in living things are at where aerodynamic effects are observed, which makes development in this field reasonable. Another example is a bomber aircraft designed with inspiration from the wings, body, and tail structures of birds shown in Fig. 1 (a). Gopinathan and colleagues focused on the influence of the wavy pattern structure on whale fins experimentally. They studied under different conditions, depending on whether the wave amplitude structure is constant or variable, and its effect on the tapering wing structure. It has been observed that for wing models with different amplitude waves and a sweep angle of 30° , the tubercles increase the lift to drag coefficient performance (C_L / C_D) of swept-back wings by enhancing C_L / C_D ratio in the pre-stall angles of attack region [4]. As a similar example, humpback whale’s wavy fin is used in the wind turbine blade and iceboat mast to support sail could be seen in Fig. 1 (b). In the Fig. 1 (c), the protruding structure (riblets) of the shark's body is used to cover the aircraft. These applications increase aerodynamic performance by connecting the flow to the wing [5].

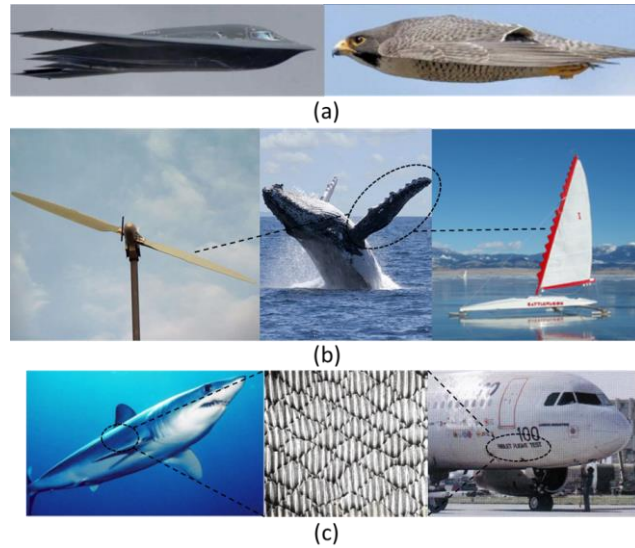


Fig.1. Biomimetic example (a) for wing and fuselage structure a B-2 Bomber inspired by stooping peregrine falcon [6] (b) wind turbine blade inspired by the fin structure of humpback whales (left) and iceboat with leading-edge tubercles on the mast supporting a sail (right) [7,8] (c) trials of shark-inspired riblets on an airplane covered with a plastic film of the same microscopic texture [3,9].

Protruding surfaces are based on the principle of preventing the flow from stalling by providing vortex formation at low speed. Due to the formation of the pressure difference, the flow attaches to the surface more, reducing drag, increasing lift, and ensuring its continuity.

The study of Stark et al. [10] examined the effect of leading-edge tubercles on the wake behaviour around a marine rudder with a NACA 0015 profile at $Re=2.26 \times 10^6$. The improvement in the lift coefficient reaches up to 19%. The study of Zhang et al. [11] used a novel leading-edge protuberance method at $Re=2 \times 10^5$ with the aim of examining the control effectiveness and associated flow physics. The lift coefficient and lift-to-drag ratio were improved by the protuberance, with increases of 54.5% and 67.7%, respectively, and decreased drag and moment coefficients, by as much as 6.70% and 11.1%. The study of Asghar et al. [12] employed a bioinspired passive flow control strategy in the leading-edge region of a propeller blade. Specific tubercle configurations exhibited improvements in efficiency of up to 6%. The study of Domel et al. [13] showed that riblets provide improvements in lift-to-drag ratio ranging from 1.2% and 4.2%. It is important to note that the flow regime considered in this study ($Re \approx 4 \times 10^4$) is relevant for many systems. The interest in low Re (10^3 - 10^5) related to renewable energy (wind turbine) and aviation has increased. Unmanned and micro air vehicles are gaining importance with developing technology (military and civil). In the low Reynolds number regime, the strong effect of viscous forces leads to earlier stalling of the wing profile compared to the high Reynolds number regime [14]. Inspired by riblets, their designed surface structure provided improvements in lift-to-drag ratio comparable to those best reported. This outperforms currently available designs at low angles of attack, with improvements of up to 323%. Additionally, this study introduces a new perspective to the literature by applying 2D bump geometry to optimize biomimetics. In their study using the PIV technique, they observed that a short separation bubble developed behind both the riblet and the 2D bump geometry, helping to provide greater suction and therefore lift for these foils compared to the control. Also, as understood from the CFD results they performed by positioning

the riblet on a flat plate showed that the separation bubble and streamwise vortices created when the riblet is placed correctly on an airfoil will help increase lift force and reduce drag. Güler et al. [15] numerically investigated the aerodynamic performance of NACA 0018 by adding riblets on the side of suction at $Re=1 \times 10^5$. Their results revealed a 4.5% enhancement in the C_L/C_D ratio and a 37% increase in lift coefficient, due to the reduction in trailing edge separation and laminar separation bubble. The study of Han et al. [16] has demonstrated that the biomimetic shark-skin coating, fabricated using the bio-replicated forming method, achieves a significant drag reduction efficiency, reaching up to 8.25% relative to the flat surface. The study of Viswanath [17] presents experimental effects of riblets applied to wings, airfoils, and aircraft or wing-body designs. Optimized riblets achieved a skin friction drag reduction of 5–8% on 2D airfoils. In wing-body configurations, an overall drag reduction of approximately 2–3% is expected.

While research on aerodynamic effects using biomimetics is not a recent subject, its application to low-speed vehicle studies is relatively rare. However, the advances in technology are increasing the focus on low-speed applications [4,11,12,13,15]. Despite the aforementioned studies, using the smoke visualization technique in a low-speed wind tunnel, especially at low Reynolds numbers to observe the effects of biomimetic applications are quite rare. One of the known studies belongs to Seyhan et al. [18]. In the study, flow around a NACA 0015 airfoil with leading-edge tubercles was investigated using force measurements and smoke visualization at the range of $\alpha=0^\circ-30^\circ$. Tests were performed at a low Reynolds number, specifically $Re=6.3 \times 10^4$. The improvement in aerodynamic performance observed as a result of the experiment is due to the presence of stall cell creation with the counter-rotating vortex couples and three-dimensional spanwise flow pattern induced by leading-edge tubercles in the post-stall regime. Present study, seeks to evaluate the aerodynamics of passive control methods, such as protrusions, biomimetics, and surface shapes, through the application of smoke visualization techniques. Various bio-inspired airfoil geometries such as 2D bumps, optimized triangular prisms, and shark skin-inspired protrusions (riblets) were analyzed by smoke visualization and by comparing their wake length.

2. Models and experimental setup

Experiments were conducted at the Aerodynamics Laboratory of the University of Samsun. The first component of the experimental setup is the smoke visualization wind tunnel, which is the TecQuipment Modular Air Flow Bench (AF17). The dimensions of the test section are $260 \times 260 \times 40$ mm and airflow speed varies from 0.8 to 35 m/s. The produced models are securely positioned in the test section center and then angle of attack is adjusted by means of a digital protractor measuring with an accuracy of 0.01° . LED lighting is installed along the edges of the test section, which aids in clear visualization of smoke lines, flow separations, and vortex formations during the experiments. Smoke generated by a smoke generator passes through a smoke rake into the test section. To ensure homogeneous smoke distribution, a specially designed smoke rake with needles is used. This smoke rake disperses smoke lines in a dense and thin structure, enhancing the accuracy of observations and the interpretability of results. Additional information about the smoke rake can be found in Jurnal et al. [19]. The second component of the experimental setup is the ViCount Compact Smoke Generator branded oil-based smoke generator. The experiment equipment is shown in Fig. 2. For the experiments, the wing models were designed using a computer-aided 3D modeling software and printed via a 3D printer. Polylactic Acid (PLA) printing material with a precision of 0.2 mm was utilized, using a printer with dimensions of $220 \times 220 \times 250$ mm. The models have 100 mm chord and 40 mm span, making contact with the walls of the test section at both ends.

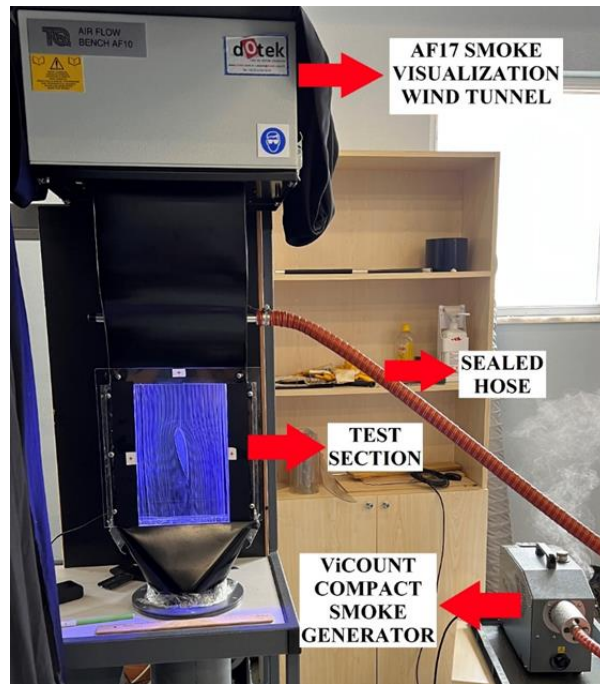


Fig. 2. Components of experimental setup.

All experiments were performed at angles of attack (α) of 0° , 4° , 8° , 12° , 14° , 16° and 20° . The experiments were carried out in two stages. Initially, five different wing structures -NACA 0018, Model A, Model B, Bump Model, and Riblet Wing Model- were tested. At the end of the first stage, the second stage experiments were conducted using Model B, which exhibited the greatest reduction in wake length across all α during the first stage. Thus, in the second stage, variations of Model B were tested and changes in wake length were evaluated through image processing. The protrusions on the models were placed at the maximum thickness of the wing and their height was adjusted to 2 mm. NACA 0018, served as a reference for measurements, while other models (Model A, Model B, Bump Model, and Riblet Wing Model) were produced and tested based on the work of Domel et al. [13], as mentioned previously. The “bump” on Bump Model was designed by scaling the upper half of the NACA 0018 airfoil geometry and placing it on the airfoil. The bump has an induced angle $\alpha=3^\circ$. Model A, inspired from shark skin riblets, consists of optimized triangular prisms protrusions on NACA 0018 airfoil. The width of the triangular profile was set to 2 mm. These same features applied to Model B, except the triangles were 4 mm wide. The Riblet Wing Model has six riblets protrusions inspired by structure of shark skin itself. The angle between the wing model and riblets is defined as tilted angle, θ . Unlike the studies of Domel et al. [13], the upper surface of the riblet was designed as a flat surface and the riblets tilted at a much higher angle ($\theta = 40^\circ$) to overcome the production difficulties. Additionally, for the second stage experiment, six models consisting of different vertical distance variations of Model B (ranging from $0.25c$ to the leading edge with decrements of $0.05c$) were designed. Refer to Fig. 3 for images of the designed models and positive tilted angle θ for riblets. Finally, a SONY DSC-RX10MIII camera was set up in front of the smoke visualization wind tunnel to capture images during the experiment. The models at the determined angles of attack are tested multiple times with long exposure to ensure possible mishaps and the accuracy of the experiment. It has been observed that there is no difference between the images taken. The experiments are carried out and processed under the same

conditions and measurement features. Image processing was carried out via MATLAB. A non-dimensional distance reference measurement location was selected based on the $0.1c$ distance from the trailing edge of the wing. Since the models itself are infinite wings, there are no wing-tip effects and only 3D effects are caused by the protrusions. Number of pixels between two streamlines at the wake were measured, then calculated in terms of non-dimensionalized distance x/c . The results of repeated image processing are the same and the accuracy of the measurements taken is provided with precision. Additional information about the image processing can be found in Jurnal et al. [20].

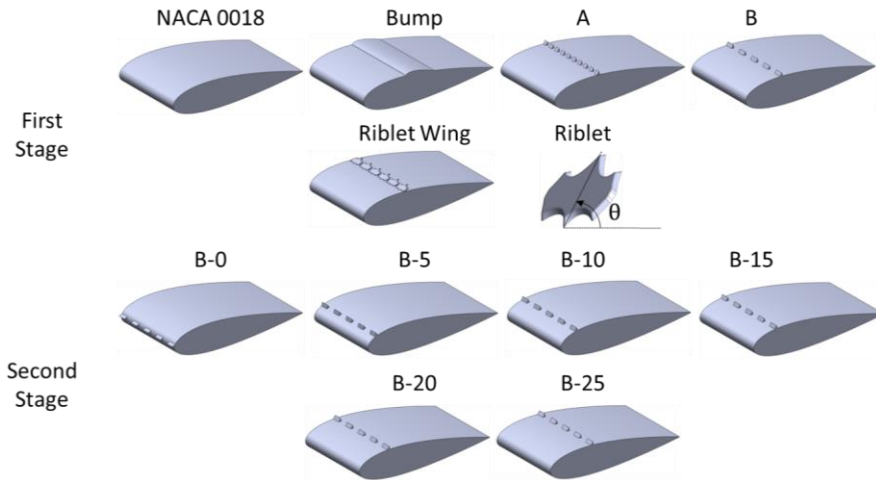


Fig. 3. Designed models and positive tilted angle θ for riblet.

3. Results and discussions

Models were tested using smoke visualization wind tunnel and performed at low Reynolds number. Some processed images of the first stage experiments -NACA 0018, Model A, Bump Model, Model B and Riblet Wing Model- are arranged side by side in Fig. 4 according to their α . The results of the experiment, show the variation of dimensionless wake length according to an α for the five models, as depicted in Fig. 5. The visualization results show that boundary layer separation is clearly visible from the streaklines as the α increases. From Fig. 4, for $\alpha=0^\circ$, it is seen that the wake lengths of the other models, except the Riblet Wing, are very similar to each other. Streaklines attached around the models without any separation, but in the Riblet Wing, the flow passing the riblets started to disperse, and then a laminar separation bubble formed on the wing. As seen in Fig. 5, it prevented the flow from attaching to the wing, thus increasing the wake length. Streaklines on NACA 0018 between $\alpha=8^\circ$ - 12° , the separation occurs from the trailing edge to the leading edge and the wake length increases in this process. In this range, Model A and Model B induce turbulence in the flow thanks to their triangular prism protrusions. The streaklines captured by the protrusions are clearly visible for Model A at $\alpha=12^\circ$, and for Model B at $\alpha=8^\circ$ and 12° . This effect seems to be more dominant in Model B than in Model A. The reason for this is that the width of the triangular prisms on Model B are twice as large as those on Model A. Due to its narrow width in Model A, it fails to suppress turbulence development, thus unable to reattach the flow behind the wing, resulting in no change in wake length. In Model B, due to its greater width, it allows turbulence to develop and effectively retains the flow around the wing, resulting in a lower wake length. When Fig. 4 in the Bump Model analyzed, the effect of inducing turbulence and retaining the flow can be clearly observed at $\alpha=8^\circ$ and 12° . When compared in Fig. 5, the Bump Model provides a similar aerodynamic performance increase to the Model B. This effect of the Bump Model on attaching the streamlines to the wing is due to the rounded structure at the leading edge of the bump. At $\alpha=16^\circ$, Model A, Model B, and the Bump Model cannot fully utilize the advantages

provided by their protrusions because the flow separation shifts towards the leading edge, causing the separated flow to bypass the protrusions without following the surface, indicating a loss of flow interaction. However, it is understood that a slight pressure change is created due to their protruding structures and that they still accelerate the flow and contribute to turbulence. The effect of the high θ can be seen in the Riblet Wing. The incoming flow continues to contact the riblets and still has control in the wake region. However, as seen in Fig. 5, the wake length is higher than other models due to the high θ . Compared to NACA 0018 with $\alpha=20^\circ$, other models have a lower and similar wake length. The protrusions do not disturb the flow and provide a lower wake length even if separated earlier. Thus, NACA 0018 has a higher wake length than other models. This shows that the effect of the pressure change at $\alpha=16^\circ$ continues. The effects of α can be seen in Fig. 5. Starting from $\alpha=4^\circ-8^\circ$, wake length differences between the wings began to appear. Differences before the $\alpha=4^\circ-8^\circ$ are not very noticeable. Models with similar wake lengths at $\alpha=4^\circ$ differed with the increasing angle of attack immediately afterwards. This also indicates that the protrusions located in the same position provide similar control at low α , but at higher α such as 14° , it is observed that the B-30 model dominates in control.

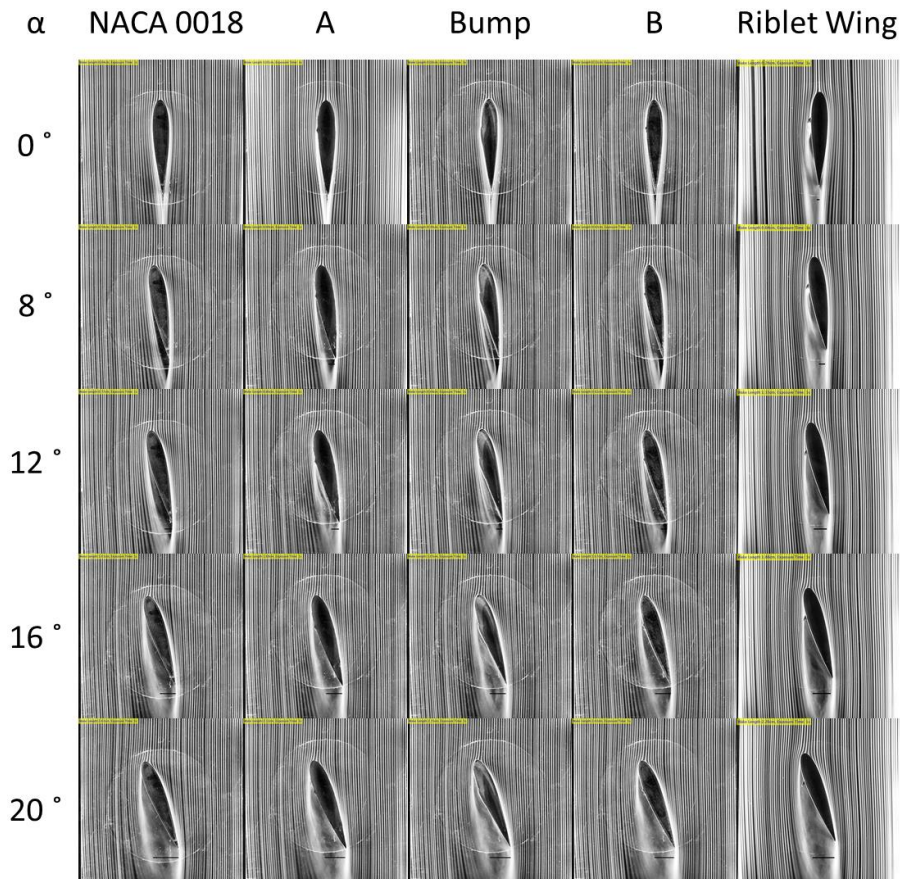


Fig. 4. Processed images of first stage models at different angles of attack.

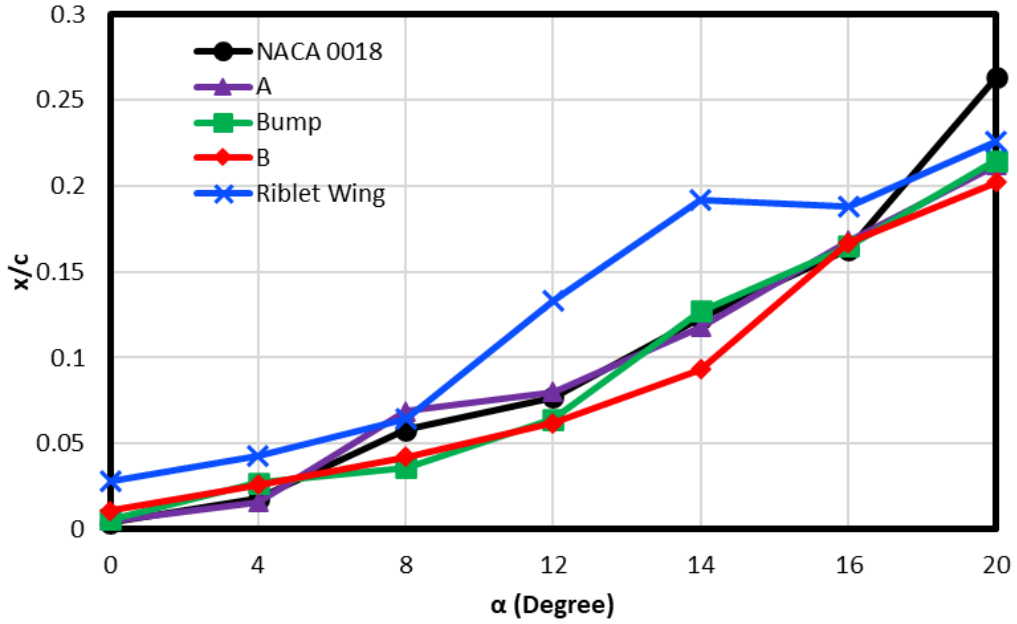


Fig. 5. Variation of dimensionless wake length according to α of 5 models in first stage experiments.

In Riblet Wing Model, a higher tilt angle was applied compared to previous studies in the literature [13]. Riblets resulted in an increase in the wake length at all angles of attack except $\alpha=20^\circ$. It has been observed that the reason for these wake increases is the laminar separation bubble effect, particularly noticeable at $\alpha=0^\circ$ and 4° , as shown in Fig. 6. As mentioned by Genc and colleagues [21], in a low Reynolds number regime, as in this study, laminar separation bubble can induce an early stall by separating the flow from the wing.

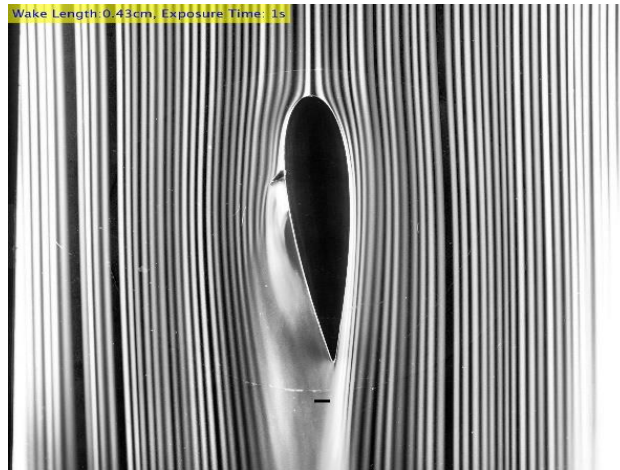


Fig. 6. Laminar separation bubble formation on Riblet Wing Model at 4° angle of attack.

Results of Model A generally were close to NACA 0018, as seen in Fig. 5. Results indicate a reduction in wake length by an average of 4% between $\alpha=12^\circ$ - 20° and 7% between $\alpha=14^\circ$ - 20° . Bump Model, inspired by the work of Domel et al. [13], reduced wake length by an average of 11% between $\alpha=8^\circ$ - 20° . Despite an initial increase in wake length up to $\alpha=5^\circ$, Bump Model was able to decrease wake length and increase aerodynamic performance within the $\alpha=4^\circ$ - 14° range. This result aligns with the drag coefficient trend observed in the study of Domel et al. [13], indicating consistency between wake length measurement, as depicted in Fig. 5, and drag coefficient. This alignment underscores the robustness of the findings, demonstrating compatibility between qualitative and quantitative data. However, since the bump already has an $\alpha=3^\circ$, it is more prone to stall. Consequently, Bump Model exhibited a larger wake length after $\alpha=14^\circ$.

Among all models in the first stage experiments, Model B positively impacted performance by reducing wake length, according to Fig. 5. It exhibited the least wake length and decreased it by an average of 24% between $\alpha=8^\circ$ - 14° and 18% between $\alpha=8^\circ$ - 20° . This shows protrusions on Model B were effective in delaying the stall. According to the experimental study by Jacobs and Sherman [22], which has a Reynolds number ($Re=41,400$) that is quite similar to this study, the stall angle of NACA 0018 is about 9° . The stall angle of Model B occurs after $\alpha=14^\circ$, indicating that it delays the stall. Therefore, as seen in Fig. 3, Model B was chosen for the second stage of the experiments instead of Model A, Bump Model and Riblet Wing. Variations of Model B were created to better examine the effects of protrusion.

Some processed images of second stage models -B-15, B-20 and B-25- from the flow visualization experiments, compared with Model B and NACA 0018, are arranged side by side according to their α in Fig. 7. Variation of dimensionless wake length according to angle of attack is given in Fig. 8. As seen in Fig. 7, at $\alpha=0^\circ$, the flow remains attached to the surface of the wing in all models. When $\alpha=8^\circ$, it is clearly seen that the flow in NACA 0018 begins to separate from the trailing edge, but has not entered the stall yet. A similar situation is also seen in the Model B-25. In the B-10, B-15, B-20 and B-30, it is seen that the flow is attached to the wing with the effect of the protruding structure. This ensured that the wake length was longer than NACA 0018, as seen in Fig. 8. At $\alpha=12^\circ$, it was observed that the B-10 and B-15 exhibited a sudden increase in wake length. In the NACA 0018, it is observed that the flow begins to separate from a location further behind where the protrusions of B-10 and B-15 are located. When the B-10 and B-15 models are examined in Fig. 7 and 8; it is seen that at low α , while the flow is attached to the wing, it loses its control effect between $\alpha=8^\circ$ - 12° and the height of the protrusion that the flow contacts increases the flow separation area and increases the wake length. At $\alpha=16^\circ$, it is evident that the passive flow control characteristics of the B-15 and B-25 become dominant at high angles. It is observed that the protrusions provide the flow to bring it closer to the wing. At $\alpha=20^\circ$, the two models that are still effective appear to be B-15 and B-30. The control effects of protruding models on wake length continue, although they weaken. When analyzed in general, it has been observed that protrusions positioned close to the leading edge are effective at high α , while protrusions positioned further back are effective at low α . B-15, on the other hand, appears to play an effective role at both high and low α among the protruding models positioned in the 0-0.3c range. For other α that are not included in the images in Fig. 7, evaluation can be made in Fig. 8. The protruding models, which were similar at $\alpha=0^\circ$ and 4° and provided a slightly lower wake length than NACA 0018, behaved differently as the α increased. Compared to the NACA 0018, while the B-25 initially experiences an increase in wake length, it provides a decrease at $\alpha=12^\circ$ and 14° . It was determined that the B-25 model triggered leading edge separation at low α (4° - 8°), but suppressed this separation by providing flow control by showing the protrusion effect at increasing α (12° - 14°). At the following α , wake length increased dramatically. While B-15 provides more effective control at low α such as 4° and 8° , it increases wake length at 12° and 14° . Subsequently, it manages to achieve lower wake length again at 16° and 20° . When B-10 and B-20 are analyzed, it is seen that B-10 is effective up to 8° and B-20 has control superiority between $\alpha=8^\circ$ - 12° . Between 14° - 20° , B-10 was again superior to B-20 in terms of control over wake length.

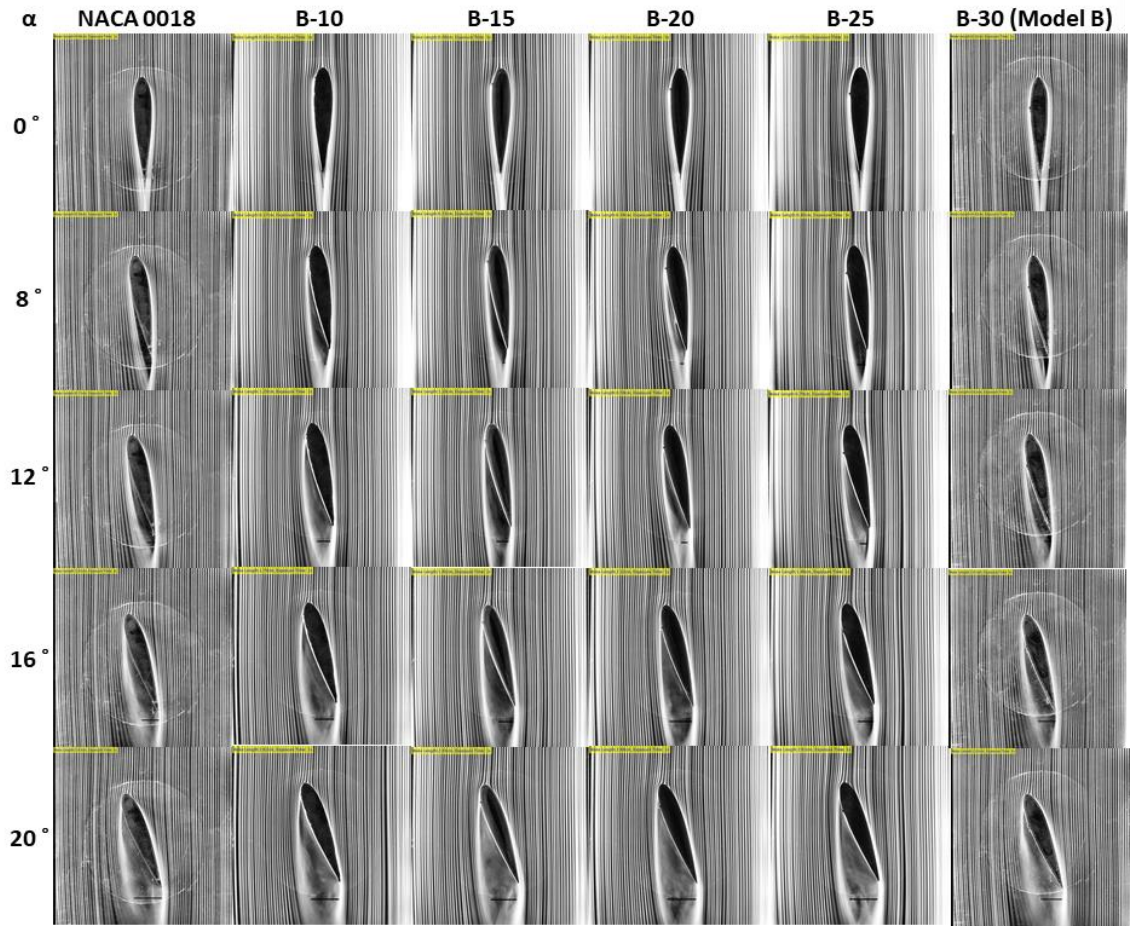


Fig. 7. Processed images of second stage models at different angles of attack.

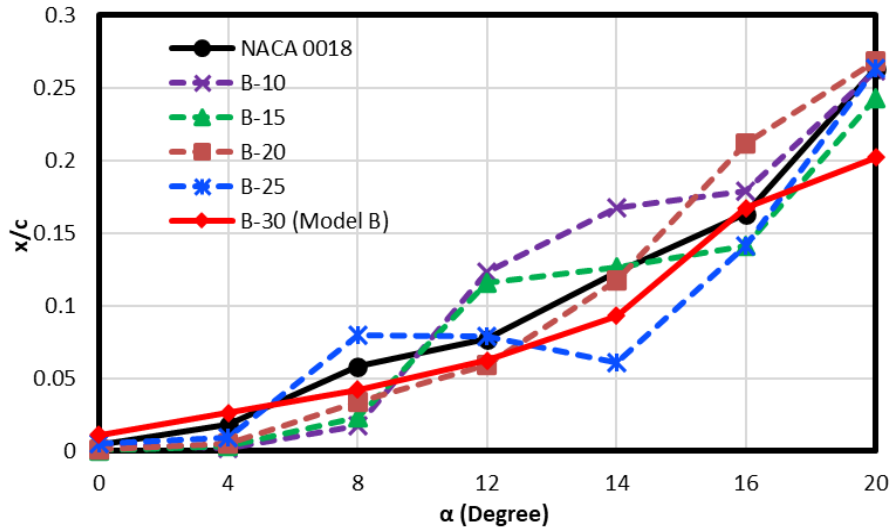


Fig. 8. Variation of dimensionless wake length according to α for second stage experiments.

Among the models presented in Fig. 3, Model B-0 and B-5 were the least effective results compared to NACA 0018. Model B-0 increased the wake length at all angles of attack except $\alpha=4^\circ$ and a similar trend was observed in Model B-5 except $\alpha=4^\circ$ and $\alpha=20^\circ$. Therefore, B-0 and B-5 were excluded from Fig. 7 and 8. The aerodynamic performance of Model B-10, with the protrusions placed at $0.1c$, is presented in Fig. 8. While the reduction in wake length in the range of $\alpha=0^\circ-8^\circ$ is an average of 45%, this reduction decreases to only 4% in $\alpha=0^\circ$ and 20° range. Model B-15 provided the most effective performance increase compared to NACA 0018 among all tested models. Wake length was reduced by an average of 30% in $\alpha=0^\circ-20^\circ$. It reduced the wake length by an average of 81% in $\alpha=0^\circ-8^\circ$ and by an average of 6% in $\alpha=14^\circ-20^\circ$. The performance provided by the Model B-15 started to decrease again towards later models. Similar to the Model B-15, Model B-20 demonstrated high performance gains by reducing wake length. It reduced the wake length by an average of 26% in the α range of $0^\circ-20^\circ$, and provided an uninterrupted reduction of an average of 43% in the α range of $0^\circ-14^\circ$. The Model B-25 shows a wake length reduction of an average of 7% in the $0^\circ-20^\circ$ range, similar to the Model B-10. It is effective between $\alpha=12^\circ-20^\circ$ and it reduces the wake length by an average of 15%. As seen in Fig. 8 for the Model B-25, it is quite interesting that even if the angle increases $\alpha=8^\circ-14^\circ$, the wake length remains almost constant between $\alpha=8^\circ-12^\circ$ and then decreases $\alpha=12^\circ-14^\circ$.

4. Conclusion

Experimental studies based on biomimetics in passive flow control in smoke visualization in the wind tunnel was used to examine changes in wake length at low Reynolds numbers ($Re=3.5 \times 10^4$). Most of the studies in the literature are carried out with high Reynolds numbers. To the authors' knowledge there is no study has been conducted, in the fields of biomimetics, using the smoke visualization technique in a low-speed wind tunnel, especially at lower Reynolds numbers. To the authors' knowledge, studies using smoke visualization techniques in a low-speed wind tunnel, especially at low Reynolds numbers to observe the effects of biomimetic applications are quite rare. In the experiments carried out, positive effects of biomimetics and aerodynamics were observed. The study aims to understand the effect of bioinspired protruding sections and their effects on aerodynamic performance by investigating the wake length. It has been found that by causing the turbulence in the flow, the flow attaches to the wing, delaying the stall, and increasing aerodynamic performance due to the reduced wake length. Protruding structures cause

turbulence in low-speed flow, creating effects such as the flow attached to the wing, delaying stall, and improving aerodynamic performance due to the reduction in drag force. It has been observed that the protruding structure placed in the appropriate position of the wing is effective at both low and high α . We noticed that results obtained with wake length measurement methods in this study agree quite well with experimental results obtained by Domel et al. [13].

In the first stage of the experiments, 5 different models with protrusions at the thickest cross section of the airfoils were tested and evaluated by their post-stall performance. Riblet Wing Model, as a complete application of biomimetics compared to Model B, Model B is indisputably superior to the Riblet Wing Model. It can be said that the tilted angle and design of Domel et al. [13] are quite functional for riblet design. While there was no change in the wake length for Model A post-stall compared to reference NACA 0018, it was decreased by an average of 11% for Bump Model and 18% for Model B. Performance difference between Model A and B is interesting. The difference between the two models is that the widest of the triangular prisms has been increased from 2 mm to 4 mm. This creates a difference in the sequence frequency of the protruding structures. However, while this seemingly simple difference made almost no difference compared to the Reference Model NACA 0018 in one case (Model A), it provided a superior aerodynamic performance increase in the other (Model B).

Second stage experiments continued with Model B and its variations. Among the all models, Model B-15 was the design that showed the most effective aerodynamic performance. It reduced the wake length by an average of 30% in the $\alpha=0^\circ-20^\circ$ range compared with NACA 0018. Model B-20, reduced its wake length by an average of 26% in the $\alpha=0^\circ-20^\circ$ range. The Riblet Wing Model increased the wake length at all angles except $\alpha=20^\circ$. When the α increases, the flow separation approaches the leading edge. At a low α , flow separation occurs near the trailing edge, and at a high α , flow separation occurs closer to the leading edge. As can be seen from these results, the positions of the placed protrusions provide control over this phenomenon. As seen in the Model B-15 and Model B-20, this positioning is effective at both low and high α .

In future studies, when the Riblet structure, the effects of placing it on the wing at different tilted angles and the frequency of its arrangement can be investigated. The effect of the Bump Model, different wing models can be tried as bumps (such as NACA 0012 and NACA 2412). Hot wire tests can be performed in both experimental stages, taking into account these visual and wake length measurements. Thus, the results obtained from this experiment can be confirmed with more quantitative results.

Acknowledgements

The research work is supported by TÜBİTAK 2209-A (project number: 1919B012102223).

References

- [1] J. F. V Vincent et al., "Biomimetics: its practice and theory Biomimetics: its practice and theory," pp. 471–482, 2009, doi: 10.1098/rsif.2006.0127.
- [2] J. B. Anders, "Biomimetic flow control," *Fluids 2000 Conf. Exhib.*, no. June, 2000, doi: 10.2514/6.2000-2543.
- [3] J. B. R. Rose, S. G. Natarajan, and V. T. Gopinathan, Biomimetic flow control techniques for aerospace applications: a comprehensive review, *Springer*, vol. 20, no. 3. Netherlands, 2021 doi: 10.1007/s11157-021-09583-z.
- [4] V. T. Gopinathan, J. Bruce Ralphin Rose, and M. Surya, "Investigation on the effect of leading edge tubercles of sweptback wing at low reynolds number," *Mech. Ind.*, vol. 21, no. 6, 2020, doi: 10.1051/meca/2020095.
- [5] D. W. Bechert, G. Hoppe, and W. E. Reif, "On the drag reduction of the shark skin," *AlAA 23rd Aerosp. Sci. Meet.* 1985, 1985, doi: 10.2514/6.1985-546.
- [6] W. A. Akpan, C. M. Orazulume, E. J. Oduobuk, E. Engineering, I. State, and A. I. State, "Aerodynamics of Birds' Flight: Analysis and Applications," *International Journal of Applied Science and Research*, pp. 156–177, 2023.
- [7] D. T. H. New and B. F. Ng, Flow Control Through Bio-inspired Leading-Edge Tubercles: Morphology, Aerodynamics, Hydrodynamics and Applications. 2020. doi: 10.1007/978-3-030-23792-9.

- [8] F. E. Fish, P. W. Weber, M. M. Murray, and L. E. Howle, "Marine applications of the biomimetic humpback whale flipper," *Mar. Technol. Soc. J.*, vol. 45, no. 4, pp. 198–207, 2011, doi: 10.4031/MTSJ.45.4.1.
- [9] Z. Han et al., "Biomimetic multifunctional surfaces inspired from animals," *Adv. Colloid Interface Sci.*, vol. 234, pp. 27–50, 2016, doi: 10.1016/j.cis.2016.03.004.
- [10] C. Stark and W. Shi, "The influence of leading-edge tubercles on the hydrodynamic performance and propeller wake flow development of a ducted propeller," *Proc. Int. Offshore Polar Eng. Conf.*, pp. 2837–2844, 2021.
- [11] M. M. Zhang, G. F. Wang, and J. Z. Xu, "Experimental study of flow separation control on a low-Re airfoil using leading-edge protuberance method," *Exp. Fluids*, vol. 55, no. 4, 2014, doi: 10.1007/s00348-014-1710-z.
- [12] A. Asghar, R. E. Perez, P. W. Jansen, and W. D. E. Allan, "Application of leading-edge tubercles to enhance propeller performance," *AIAA J.*, vol. 58, no. 11, pp. 4659–4671, 2020, doi: 10.2514/1.J058740.
- [13] A. G. Domel, M. Saadat, J. C. Weaver, H. Haj-Hariri, K. Bertoldi, and G. V. Lauder, "Shark skin-inspired designs that improve aerodynamic performance," *J. R. Soc. Interface*, vol. 15, no. 139, pp. 1–9, 2018, doi: 10.1098/rsif.2017.0828.
- [14] J. G. Leishman, *Introduction to Aerospace Flight Vehicles*. Embry-Riddle Aeronautical University, 2022.
- [15] E. Güler, T. Durhasan, İ. Karasu, and H. Akbıyık, "Passive Flow Control around NACA 0018 Airfoil Using Riblet at Low Reynolds Number," *Iğdır Üniversitesi Fen Bilim. Enstitüsü Derg.*, vol. 11, no. 3, pp. 2208–2217, Sep. 2021, doi: 10.21597/jist.897982.
- [16] X. Han, D. Y. Zhang, X. Li, and Y. Y. Li, "Bio-replicated forming of the biomimetic drag-reducing surfaces in large area based on shark skin," *Chinese Sci. Bull.*, vol. 53, no. 10, pp. 1587–1592, May 2008, doi: 10.1007/s11434-008-0219-3.
- [17] P. R. Viswanath, "Aircraft viscous drag reduction using riblets," 2002.
- [18] M. Seyhan, M. Sarioglu and Y. E. Akansu, "Influence of Leading-Edge Tubercle with Amplitude Modulation on NACA 0015 Airfoil," *AIAA JOURNAL*, vol.59, no.10, pp.3965-3978, 2021
- [19] G. Jurnal, C. Kose, C. Kolbakir, A. S. Durna, and B. Karadag, "Improvement of smoke rakes and the image processing for the flow visualization experiments," in *11th Ankara International Aerospace Conference*, September 2021, 2021, pp. 1–7.
- [20] G. Jurnal, T. Çobanoğlu, C. Kolbakir, and A. S. Durna, "Flow Control Using Plasma Actuator On The Airfoils With Various Camber And Thickness Dimensions," in *ULIBTK'24 Uluslararası Katılımlı 23. Isı Bilimi ve Tekniği Kongresi*, 2023, pp. 1–10.
- [21] M. S. Genç, I. Karasu, and H. Hakan Açikel, "An experimental study on aerodynamics of NACA2415 aerofoil at low Re numbers," *Exp. Therm. Fluid Sci.*, vol. 39, pp. 252–264, 2012, doi: 10.1016/j.expthermflusci.2012.01.029.
- [22] E. N. Jacobs and A. Sherman, "Airfoil section characteristics as affected by variations of the Reynolds number," *Tech. rep.*, Washington. D.C Natl. Advis. Comm. Aeronaut., no. 586, pp. 227–259, 1939.



Contents lists available at *Dergipark*

Journal of Scientific Reports-A

journal homepage: <https://dergipark.org.tr/pub/jsr-a>



E-ISSN: 2687-6167

Number 59, December 2024

RESEARCH ARTICLE

Receive Date: 20.11.2024

Accepted Date: 27.12.2024

Reinforcement learning for energy optimization in IoT based landslide early warning systems

Seyfullah Arslan^{a,*}, Safa Dörterler^b, Fırat Aydemir^c

^a*Kütahya Dumlupınar University, Faculty of Engineering, Computer Engineering Dept., 43100, Kütahya, Türkiye
ORCID: 0000-0002-2573-273X*

^b*Kütahya Dumlupınar University, Faculty of Engineering, Computer Engineering Dept., 43100, Kütahya, Türkiye
ORCID: 0000-0001-8778-081X*

^c*Kütahya Dumlupınar University, Faculty of Engineering, Computer Engineering Dept., 43100, Kütahya, Türkiye
ORCID: 0000-0002-8965-1429*

Abstract

This study introduces a novel energy management model based on Deep Reinforcement Learning for IoT-based landslide early warning systems, aiming to achieve energy neutrality and enhance system resilience, efficiency, and sustainability. Unlike traditional energy optimization methods, the proposed model employs a Deep Q-Network (DQN) to dynamically optimize the duty cycle of sensor nodes by leveraging real-time energy availability. By adaptively balancing energy harvesting and consumption, sensor nodes can maintain continuous operation even under highly variable environmental conditions, maximizing their performance during high-energy periods while preserving battery life when energy is limited. Extensive simulations using real-world solar radiation data demonstrate the model's superior capability in extending system longevity and operational stability compared to existing approaches. Addressing critical energy management challenges in landslide monitoring systems, this work enhances system reliability, scalability, and adaptability, offering a robust foundation for broader IoT applications deployed in energy-limited and dynamic environments. The proposed method represents a significant improvement over conventional techniques, as it autonomously optimizes energy resources to ensure the continuous and sustainable operation of IoT ecosystems. © 2023 DPU All rights reserved.

* Corresponding author. Tel.: +90 (274) 443 42 68; fax: +90 (274) 265 20 13 - 14.
E-mail address: seyfullah.arslan@dpu.edu.tr
<http://dx.doi.org/10.1016/j.cviu.2017.00.000>

Keywords: Reinforcement learning; internet of things; energy management optimization; landslide early warning systems

1. Introduction

Landslides are one of the serious natural disasters that cause significant loss of life and property worldwide. The 2020 Gjerdrum landslide in Norway led to fatalities, the displacement of dozens of families, and millions of dollars in economic loss [1]. In regions such as South Asia, landslides frequently result in severe casualties and infrastructure destruction, particularly during heavy monsoon rains, further compounding the economic and social impact [2]. These disasters occur in mountainous and sloping areas and are triggered by sudden rainfall, groundwater movements, and weak soil structures [3]. Dense settlements and infrastructure projects in the regions where these disasters occur further increase the impact of landslides. Early warning systems have been developed to prevent loss of life and economic damages caused by landslides [4]. These systems identify the risk of landslides in advance, providing the opportunity to evacuate people living in affected areas to safe areas. However, the reliability of these systems depends on sensor networks that can provide accurate and continuous data [5]. Sensors used in landslide early warning systems must be capable of long-term operation, especially under harsh environmental conditions and energy constraints [6]. Therefore, energy management of sensors poses a significant challenge.

In recent years, Internet of Things (IoT)-based sensor networks have been employed extensively in landslide early warning systems [7]. However, most of the sensors in these networks have limited battery life, which has increased the importance of energy harvesting techniques [8]. Energy harvesting sensors can sustain long-term operation by collecting energy from solar, wind, and environmental vibrations [9]. However, the irregular and unpredictable dynamics of energy harvesting are one of the main factors limiting the effectiveness of such systems. Energy-harvesting sensors must efficiently utilize the harvested energy and sustain their duty cycles without power outages [10]. However, intelligent energy management algorithms are needed to optimize energy consumption.

Reinforcement Learning (RL) has significant potential for application in the field of energy management and duty cycle optimization. The RL algorithms can potentially enable energy-neutral operation (ENO) through autonomous optimization of sensor nodes' energy harvesting and consumption processes [11]. In particular, Deep Reinforcement Learning (DRL) algorithms facilitate the expeditious adaptation of sensors to environmental alterations and enhance energy efficiency [12]. The RL algorithms utilized in these studies guarantee uninterrupted system operation by establishing a balance between the energy collection and consumption processes [13].

The objective of this paper is to present a novel energy management model for IoT-based landslide early warning systems. The proposed model uses a reinforcement learning algorithm to optimize the battery levels of solar-powered sensor nodes and increase their continuous operation capability. This study introduces a system to enhance the energy efficiency of IoT nodes in landslide early warning systems. Furthermore, a Deep Q-Networks (DQN) based reinforcement learning algorithm is developed to optimize the energy consumption of nodes. This algorithm aims to achieve energy-neutral operation by balancing the energy collection and consumption of nodes.

Real-world solar radiation data is used to evaluate the performance of the developed system, and the energy harvesting process is simulated. Furthermore, the impact of the system on extending the battery life and improving the reliability of landslide early warning systems is analyzed. Simulation results show that the proposed model improves energy efficiency and ensures the uninterrupted operation of sensors.

The main contributions of this study are as follows:

- In early warning systems of natural disasters such as landslides, IoT nodes are provided to operate continuously without energy interruption.
- The proposed model addresses a significant gap in achieving energy-neutral operation under dynamic and unpredictable environmental conditions, which has been a critical limitation in prior studies.
- Energy consumption and harvesting processes are dynamically balanced using a reinforcement learning algorithm, specifically a Deep Q-Network (DQN), to adaptively respond to real-time variations in energy availability.

- Unlike conventional approaches, this model ensures uninterrupted operation of IoT nodes by preventing overcharging or depleting battery levels, which enhances both system longevity and reliability.
- Simulations with real-world solar radiation data validate the model's ability to self-adapt, demonstrating superior performance in extending battery life and maintaining operational stability compared to existing techniques.
- The system introduces an autonomous and scalable solution to energy management challenges in harsh and energy-limited environments, providing a robust framework for broader IoT applications beyond landslide monitoring.
- Using reinforcement learning, the model allows IoT nodes to intelligently optimize their duty cycles, enhancing energy efficiency without manual intervention.
- The proposed approach lays a foundation for future advancements in reinforcement learning-based energy management systems, addressing key challenges such as energy variability, scalability, and operational sustainability.

In conclusion, this study addresses energy management challenges in energy-harvesting IoT-based landslide early warning systems and introduces an approach to enhance their effectiveness. By optimizing energy harvesting and consumption processes, the model ensures uninterrupted sensor operation and supports the development of reliable early warning systems for natural disasters like landslides.

This paper consists of 5 sections in total. The second section, "Related Work," provides a comprehensive review of previous work on landslide early warning systems and energy harvesting technologies. The third section, "Materials and Methods," presents details of the proposed reinforcement learning-based energy management model. This section describes the methods developed to improve energy efficiency for IoT nodes and the model's training process. The fourth section, "Results and Discussion," discusses the simulation results and the performance of the model. The last section, "Conclusion," contains the study's overall conclusions and recommendations for future research.

2. Related work

Landslide early warning systems are highly essential in curbing devastating effects of natural disasters on human lives. These systems give early warning of future events of landslides, hence prompting the relocation of people in landslide-prone areas. Events of landslides are caused by various natural factors: excessive rainfall, soil moisture, fault movement, and rockfalls [14]. Accurate forecasting of these events will involve selecting the right sensors, efficient data processing, and optimization of decision-making processes. The research area of the landslide forecasting has witnessed a remarkable development in a number of techniques and methodologies over the last ten years. Some of these techniques include machine learning, artificial neural networks, data mining, geographic information systems, numerical modeling, and hybrid approaches.

Machine learning has been successfully used to solve complex problems in areas such as optimization [15-17], data classification [18-20], object recognition [21], [22], medical diagnosis [23], [24], educational technologies [22], voice analysis [25], [26], image analysis [27], [28], and decision support systems [29-31]. Recently, energy optimization and efficient resource management in wireless sensor networks (WSNs) and Internet-of-Things (IoT) systems have gained increasing attention to enhance network lifetime and reduce energy consumption. Ali et al. propose a novel ARSH-FATI-based Cluster Head Selection (ARSH-FATI-CHS) algorithm integrated with ranked-based clustering to address the energy efficiency challenges in WSNs [32]. Their approach dynamically balances exploration and exploitation during the cluster head selection process, taking into account residual energy, communication distance, and workload parameters. Simulation results demonstrate that the ARSH-FATI-CHS algorithm outperforms traditional techniques, such as particle swarm optimization (PSO), achieving approximately 25% improvement in network lifetime. This study highlights the importance of advanced metaheuristic algorithms in reducing communication energy and prolonging the lifespan of sensor nodes in WSNs, which are fundamental components in IoT ecosystems. In addition, Ali et al. provide a comprehensive survey on energy optimization techniques for Multiprocessor System-on-Chip (MPSoC) architectures in IoT and consumer electronics systems [33]. They emphasize the critical role of workload mapping and scheduling approaches, such as Dynamic Voltage and Frequency

Scaling (DVFS), Dynamic Power Management (DPM), and inter-processor communication reduction, in achieving substantial energy savings. The study also underscores the significance of combining coarse-grained software pipelining techniques with DVFS to improve performance and energy efficiency. By evaluating the integration of MPSoCs in IoT systems, the authors offer insightful directions for future research, particularly in balancing computational performance and energy consumption.

Researchers have used various machine learning techniques, including supervised and unsupervised learning, to analyze extensive datasets from areas with high landslide risk. Artificial neural networks have achieved success in landslide risk prediction by using parameters such as soil moisture, rainfall, slope, and soil type. Thirugnanam et al. developed a landslide early warning system [34]. They divided early warning systems into six phases which are data collection, transmission, modeling, analysis, prediction, and warning. In the data collection and transmission phase, they used various rain, humidity, and slope meter sensors to collect their data in a center with the developed IoT system. These data from the field are analyzed in real time, and landslides are successfully predicted with the developed machine learning algorithm. In addition, the researchers took into account that the data transmission stops and the system does not work correctly in case of various IoT sensors not working, malfunctioning, battery depletion, etc. In such cases, they predicted the data that could not come from the sensors with machine learning algorithms and ensured the security of the system. In another study, Hemalatha et al. developed a landslide early warning system by collecting the parameters affecting landslides in real time with rainfall, humidity, water pressure, and motion sensors [35]. They trained their model with current-PWP and 24-PWP algorithms based on the Support Vector Regression method. The continuity of the warning system depends on the parameters coming from the sensors and the system sensors operate 24/7 depending on electricity. In case of a power outage, sensors powered by solar energy ensure the continuity of the system. They also used machine learning algorithms to predict sensor values as a second measure. Collini et al. used various machine learning methods by analyzing 341 landslide events in Florence, Italy, and obtained the most successful results with the XGBoost model [36]. In another study, Ng et al. developed landslide prediction models using meteorological and topographic data collected from landslide-free and prone areas [37]. Their results turned out to be more successful when using the random forest model. Data collection and analysis are one of the key components in this developed system that uses machine learning methods. A commodity of a large amount of historical and real-time data is being modeled and made meaningful in this process to produce forecasts and determine early warning systems. These data have been used for the development of various models of forecasting using different machine learning and deep learning algorithms, such as Logistic regression, Support Vector Machine, Random Forest, and Convolutional Neural Network.

Another important technique that is normally used in the prediction of landslide risks includes data mining. Different machine learning algorithms analyze sensors or geographic information system data, such as soil type, measurement of moisture, GPS data, condition of weather, and variation in position for the prediction of risk from landslides. Franceschini et al. have generated a landslide inventory by applying methods of data mining and open-source websites with diverse geological and hydrological data in Italy [38]. Based on this aspect of the study, web pages revealed the use of predefined descriptive keywords in crawling web pages related to landslide events between 2010 and 2019, whereas those showing relevance were collected in an inventory. Subsequently, this was linked to several geographical databases that showed factors affecting landslides, such as population density, slope, rainfall, and geological structure. The relationships between these yielded a risk map related to areas prone to landslides and hence predicted future landslide events. As a result, the authors were then able to portray the usability of automated data mining methods in developing a landslide inventory and the usefulness of associating those methods with various geographical factors when conducting landslide risk analysis. Qian collected and analyzed data from many different sources and created a disaster emergency management system based on data mining [39]. They showed that this big data platform collected from various sources was successfully used as a disaster emergency management system and was more successful than traditional methods. Another study obtained images of 26 deep mountains and valleys in China. There were 146 landslide disasters in the locations where these images were obtained. Various machine learning algorithms classified these landslides according to landslide types and the results were compared with each

other. As a result, solutions are presented to prevent landslide disasters and ensure the sustainability of rural industries by using remote sensing technologies and IoT sensors [40]. Pennington et al. introduced a global landslide event reporting tool using photo data from social media and various sources and artificial intelligence algorithms [41]. This tool detects landslide events by collecting data from social media platforms such as Twitter and using natural language processing and machine learning techniques. With the system developed by the authors, landslide events were monitored with an accuracy rate of 76%, and useful and valuable information was provided to emergency teams and decision-makers. Many countries around the world have created national and regional landslide databases by collecting data from various social media and news sources to investigate the impact of landslide disasters, document damage and loss of life, identify dangerous areas, etc. [42-47]. These databases are then processed and analyzed with various artificial intelligence applications to mitigate the effects of the disaster or to develop early warning systems to warn decision-makers and the public before the disaster occurs [41].

Geographic Information Systems (GIS) are an important tool for real-time monitoring of natural disasters locally and globally and for emergency response. GISs collect data through aerial and satellite images [48-50], radars [48], [51], [52] and various sensors [53-55]. At the same time, GIS technology has been successfully used in the early detection and prevention of landslides [51]. In recent years, many studies have been conducted on the use of GIS and have shown the effectiveness of GIS in detecting landslides. Can et al. created a geographic information system into which citizens can voluntarily upload photos of landslides [56]. They further proposed the CNN architecture to automate the detection of landslide photos from image data in the system and evaluate the accuracy of the landslide events. The CNN architecture proposed detects landslide photos automatically, which will help the rapid assessment of the quality of data when a manual evaluation of data is time-consuming and costly. It therefore means that the CNN architecture could identify photos of landslides with 94% accuracy, which can be applied to community-based emergency response systems. Goniewicz et al. presented how geographic information systems technologies can be used in disaster risk analysis, emergency management, and post-disaster recovery and reconstruction processes [51]. As a result, they exemplified several illustrations of geographic information systems technology for disaster and emergency management and went forward to show that the use of such technologies was an important tool in disaster and emergency management. Yang et al. developed a web-based emergency response and visualization system using Cesium Digital Earth technology [49]. The system will be designed in such a way that it will be able to implement a geographic information system that can help the emergency responders take appropriate actions a lot faster and more potentially during natural disasters. Moreover, a landslide scenario example was used to design how the systems will be employed and the effectiveness they will have.

Yet another technique is the numerical modeling technique. In this technique, landslide risk is estimated by simulating factors such as soil moisture, precipitation, slope, and soil type [57]. The numerical modeling techniques can also be combined with GIS data and machine learning techniques [58]. Similarly, Park et al. proposed a combination of statistical and physically based approaches for the development of a landslide early warning system [59]. It was a study within some regions in South Korea that needed to estimate landslide risk and develop early warning systems based on two different landslide modeling approaches. The first model represents a heuristic approach based on the statistical analysis of past landslides, while the second one is a physically based model that considers precipitation, soil moisture content, and other factors in predicting occurrences of landslide events. Whereas the statistical model offers information related to the analysis of past events, the physical model provides the estimate of landslide risk considering current conditions. Thus, it brings about a more efficient landslide early warning system by combining these two models into one space for both approaches to landslide early warning systems.

Meanwhile, in another research finding, Harilal et al. have also proposed a system for early warning against landslides by issuing warnings for the onset of rainfall conditions that exceed a certain threshold [57]. Landslide probabilities could then be determined based on the geographical characteristics and daily rainfall data latitude provided by the Indian meteorological service. It was then compared with real-time rainfall data, and automatically, in the case of increased risk of landslide, a warning message was generated. The performance of the system was also evaluated. Since then, it found that the rainfall threshold determination for developing a real-time landslide early

warning system yielded successful results. Salvatici et al. discussed in their paper [60] the application of physically based models for regional-scale predictions of rainfall-induced shallow landslides. Causes, mechanisms of occurrence, characteristics of shallow landslides, and estimation of shallow landslide probabilities in light of precipitation, moisture, slope, soil properties, and vegetation cover were studied. The model performance is assessed in the paper by comparisons to measurements made at a site known for its accuracy. The results proved that the model makes good predictions of shallow landslide probability and can be used as an uncomplicated early warning system.

Another methodology that could be used either for the detection of areas where landslides occur or to forecast landslide disasters is hybrid approaches. The data obtained by image processing, satellite images, aerial photographs, drone images, or various sensors are rendered meaningful through different techniques. Using artificial neural networks, possible scenarios of natural disasters that may happen in the future can be created by analyzing variously obtained data. These high-resolution satellite images identify the landslides. Characteristics of landslide features can be identified by applying techniques of image processing to these images. The occurrence of the landslide can also be identified by image processing methods, which in turn identifies the factors that cause the occurrence of it to help determine damages caused by landslides and take measures for the safety of the local people. Interferometric synthetic aperture radar and Google Earth imagery were used to develop a landslide early warning system by Nhu et al. in their study [61]. The data they obtained was used to develop a geographic information system, in which those data were classified using machine learning algorithms. For the learning process of landslide susceptibility mapping, they used AdaBoost, Decision Tree, and hybridized versions of these two machine learning algorithms and obtained the most successful results from the AdaBoost model. Thus, they have shown that data obtained with image processing techniques and machine learning algorithms can be used efficiently for the detection of landslides.

A literature synthesis reveals that the principal structure of landslide disaster early warning systems is as follows: data collection, data transmission, modeling, analysis, prediction, and warning. Data is collected through various sensors such as rain gauges, moisture meters, slope meters, groundwater level meters, strain gauges, and geophones in the data collection phase. Data transmission is provided using GPRS, internet, telephone connections, telemetry, Wi-Fi, and various IoT systems. The collected data is then analyzed using various methods to make landslide predictions, and the warning system is activated. Data collection and transmission are among the most critical components of this system. However, if we consider the system as a chain in this way, the system will not work if there is a problem with any link in the chain. Sensors, which are one of the critical components of the system, may be damaged in harsh environmental conditions, or suitable conditions may not be provided for the battery conditions of the sensors, power outages may occur, and the data collection/transmission component will be adversely affected, and the modeling, analysis, and prediction component will not work. Therefore, without data, no output will be produced, and the system will become unusable. Researchers have taken various measures and developed alternative solutions to keep the system running in these and similar situations. Thirugnanam et al. proposed a solution with machine learning algorithms [34]. With the proposed solution, they predicted the data that could not be received from the sensors. They used the previous values of these parameters to predict the changes in slope, which are frequently seen in landslide events and sent them as input to other system components. Harilal et al. [57], Hariharan et al. [62], Guntha et al. [63], and Guntha and Ramesh [63] used multiple meteorological and meteorological data sensors to maintain the system. Huang et al. [64], Fathani et al. [65], Hemalatha et al. [66], and Harilal et al. [57] used multiple data transmission links to overcome data transmission problems. Fathani et al. [65], Hemalatha et al. [66], and Harilal et al. [57] used multiple thresholds in case of data flow problems.

Studies on energy management and energy harvesting of sensors offer essential solutions for wireless sensor networks and IoT applications. Researchers have developed different methods to ensure sensors' energy independence and guarantee the continuity of data collection/transmission processes, especially in harsh environmental conditions. In addition to these methods, reinforcement learning and energy harvesting strategies stand out. Zhang and Lin used RL algorithms to optimize energy-neutral operations in hybrid energy-harvesting wireless body area networks, TBANs [67]. In the work here, energy efficiency is improved by using DQN. Murad et al. optimized the automatic management of energy harvesting IoT nodes with the Proximal Policy Optimization algorithm and gave more

autonomous energy management [68]. Omidkar et al. used Q-learning in optimizing spectrum and power allocation in energy harvesting-enabled device-to-device (D2D) communications [69]. Chu et al. optimized power control in multiple access systems with reinforcement learning and improved the system's energy efficiency [70]. Finally, Aoudia et al. developed a reinforcement learning-based energy management algorithm called RLMan [71]. This algorithm optimizes the energy consumption of nodes in wireless sensor networks and dynamically adjusts the power usage based on the state of charge of the node's energy storage device. The algorithm achieved high performance under time-varying energy resource conditions and increased packet transmission rates by up to 70%.

The literature presents significant progress in energy management and harvesting techniques, with various studies proposing innovative methods to improve energy efficiency and ensure the continuous operation of IoT systems. Techniques such as reinforcement learning, dynamic duty cycling, and adaptive power optimization have shown promise in enhancing system performance. However, their original contributions to balancing energy harvesting and consumption remain limited. Many existing approaches focus on optimizing either energy collection or energy consumption independently rather than integrating both processes into a unified and adaptive framework. Additionally, while reinforcement learning algorithms such as Q-learning, DQN, and Proximal Policy Optimization have been applied, their scalability, real-time adaptability, and performance under dynamic and unpredictable environmental conditions are not consistently validated with real-world data. The effectiveness of current methods for achieving energy-neutral operations (ENO) in IoT devices, especially under tough conditions, remains uncertain.

The proposed model aims to fill the critical gaps identified in the literature by introducing a reinforcement learning-based energy management approach that is designed for IoT-based landslide early warning systems. A Deep Q-Network (DQN) is exploited to address the key limitation of the previous methods in achieving an energy-neutral operation under dynamic and unpredictable environmental conditions. Model can be used for dynamically balancing energy-harvesting and power-consumption processes at IoT nodes, adapting to any real-time variations in energy availability. Thus, model guarantees faultless operation and prolongs the operating life of a system by avoiding overcharging or deep depletions of the batteries. Besides, in-depth simulations for real-world solar radiation have also confirmed the good self-adaptability features of the model, showing superior performances compared to traditional approaches. Proposed model enhances the dependability and scalability of the landslide monitoring system and gives the basic foundation for general IoT applications in energy-limited environments.

This paper discusses the most important challenge of any landslide early warning system, how to ensure the long-term energy independency of IoT sensors with continuing their operation. The strategy proposed in this paper seeks to optimize a combined reinforcement learning-energy harvesting model in a coherent, self-adjusting framework that furnishes an integrated solution to a problem that was separately solved by earlier works dealing specifically with either energy harvesting or consumption policies, respectively. With dynamic optimization of energy harvesting and consumption, continuity for data collection and transmission has been provided in changing environmental conditions or in case of a power outage. In this way, model ensures enhancement in the reliability, scalability, and adaptability features with significant contributions to IoT-based natural disaster management systems and beyond.

3. Material and methods

This section describes the material used and methods adopted to develop and validate the reinforcement learning-based approach for optimizing energy management in IoT nodes for the proposed landslide early warning system.

3.1. Reinforcement learning framework and Deep Q-Network (DQN)

This work implements reinforcement learning to enhance energy efficiency in IoT-based landslide early warning systems. RL is a learning process whereby an agent develops a strategy that maximizes its cumulative rewards through interactions with the environment [72]. Accordingly, with respect to each instance, the agent perceives its current state, performs an appropriate action, and obtains a reward as feedback. These rewards contribute to the agent's long-

term strategy that involves maximizing the total expected rewards. This total discounted reward, which the agent will try to maximize, is described in Equation 1.

$$R_t = \sum_{t'=t}^T \gamma^{t'-t} r_{t'} \quad (1)$$

In this equation, R_t represents the cumulative discounted reward at time step t , with γ serving as the discount factor that reduces the influence of future rewards on current decision-making, with $0 \leq \gamma \leq 1$. The term $r_{t'}$ denotes the instantaneous reward received at each time step, and T is the time step at which the task concludes. By adjusting γ , the agent can balance the trade-off between immediate and future rewards, optimizing its long-term strategy. The agent's objective is to learn a policy that selects actions yielding the highest expected rewards in each state.

To achieve optimal action selection, the Q-learning algorithm estimates an optimal action-value function $Q^*(s, a)$, defined through the Bellman equation. This Equation allows the agent to determine the most suitable action in a given state by considering the maximum expected reward obtainable in the subsequent state. The Bellman equation is formulated in Equation 2 [73].

$$Q^*(s, a) = E_{s' \sim E} [r + \gamma \max_{a'} Q^*(s', a') | s, a] \quad (2)$$

In Equation 2, $Q^*(s, a)$ represents the optimal action-value function for a given state-action pair (s, a) . The expectation operator E represents the expected value over all possible outcomes. The variable s' denotes the subsequent state, and E represents the environment governing state transitions. The term r signifies the immediate reward, while γ is the discount factor that scales down the importance of future rewards. Finally, $\max_{a'} Q^*(s', a')$ identifies the maximum Q-value for the next state s' across all possible actions a' . This equation enables the agent to leverage information about future states to make optimal decisions at each step.

Applying Q-learning in large and complex state spaces presents significant challenges [74]. To address this, Deep Q Networks (DQN) are utilized in this study to approximate the Q-function in high-dimensional state spaces using neural networks [75]. DQN leverages deep neural networks to enhance the learning process, allowing the agent to make efficient decisions in complex environments [76]. In DQN, a loss function $L_i(\theta_i)$ is defined and iteratively optimized, as shown in Equation 3.

$$L_i(\theta_i) = \mathbb{E}_{s, a \sim p(\cdot)} [(y_i - Q(s, a; \theta_i))^2] \quad (3)$$

In Equation 3, $L_i(\theta_i)$ denotes the loss function at iteration i , where θ_i represents the network's weight parameters for that iteration. The behavior distribution $p(s, a)$ indicates the probability distribution over the agent's experiences in state s and action a . The target value y_i at each iteration i is given by $y_i = E_{s' \sim E} [r + \gamma \max_{a'} Q^*(s', a') | s, a]$, which depends on the expected reward and the maximum estimated Q-value from the previous iteration's parameters θ_{i-1} . This loss function guides weight parameter updates, enhancing the Q-function approximation's accuracy in each iteration.

The gradient of the loss function concerning the weights is computed to update the network parameters, as defined in Equation 4.

$$\nabla_{\theta_i} L_i(\theta_i) = \mathbb{E}_{s, a \sim p(\cdot); s' \sim E} [(r + \gamma \max_{a'} Q(s', a'; \theta_{i-1}) - Q(s, a; \theta_i)) \nabla_{\theta_i} Q(s, a; \theta_i)] \quad (4)$$

In Equation 4, $\nabla_{\theta_i} L_i(\theta_i)$ represents the gradient of the loss function at iteration i concerning the weight parameters θ_i . The terms s and a indicate the current state-action pair, while $s' \sim E$ specifies that the next state is sampled from the environment E . The expression r denotes the immediate reward obtained, and γ is the discount

factor emphasizing present over future rewards. The term $\max_{a'} Q(s', a'; \theta_{i-1})$ selects the a value that gives the highest Q-value for the next state s' , based on the parameters from the previous iteration. Finally, $(s, a; \theta_i)$ denotes the predicted Q-value for the current state-action pair with the current parameters θ_i .

This gradient optimizes the network's weight parameters by minimizing the difference between predicted and target Q-values. By leveraging this structure, DQN enables the agent to efficiently learn optimal actions in high-dimensional environments, improving its decision-making process and leading to more accurate policy learning.

3.2. Dataset

The present work proposes a model that uses instantaneous battery level, air temperature, and energy harvesting amount to maintain the battery at an optimum level. To avoid randomness, energy harvesting is simulated. A solar radiation dataset, containing hourly radiation data, is used to calculate the energy harvested by a specified solar panel.

The dataset used is taken from the European Commission Photovoltaic Geographic Information System, and it includes measurements taken in Istanbul-Turkey between 2019 and 2020 [77]. There are 17544 data in the dataset used in training. The first 100 hours of the same dataset were used in the testing phase.

The data used has six columns, which include time, G(i), H_sun, T2m, WS10m, and Int. The time column gives the date and time of measurement. G(i): the amount of global radiation on the inclined plane, a unit of W/m². H_sun: solar altitude, unite of degree. T2m: air temperature 2 meters above the ground, its unit is degree Celsius. WS10m total wind speed 10 meters above the ground, its unit is m/s. "Int" takes values 0 or 1; 1 is the value when the solar radiation value is reconstructed. During training, G and values are being used for the state space.

3.3. Proposed model

This study proposes a reinforcement learning model to improve energy efficiency and optimize the battery life of IoT nodes used in landslide early warning systems. The proposed model aims to balance IoT nodes' energy consumption and energy harvesting to prevent batteries from being completely depleted or overcharged. In this way, the reliability of landslide early warning systems will be increased by ensuring the uninterrupted and efficient operation of IoT nodes in the field.

It is not feasible to sustain the continuous energy demands of IoT nodes in regions prone to landslides with conventional energy sources. Therefore, the energy needs of IoT nodes should be met by renewable energy sources such as solar energy. In the proposed model, each IoT node is equipped with a solar panel and a rechargeable battery. The energy harvested through the solar panel charges the battery and meets the energy needs of the node. The architecture of this reinforcement learning-based energy management system for IoT nodes is illustrated in Figure 1.

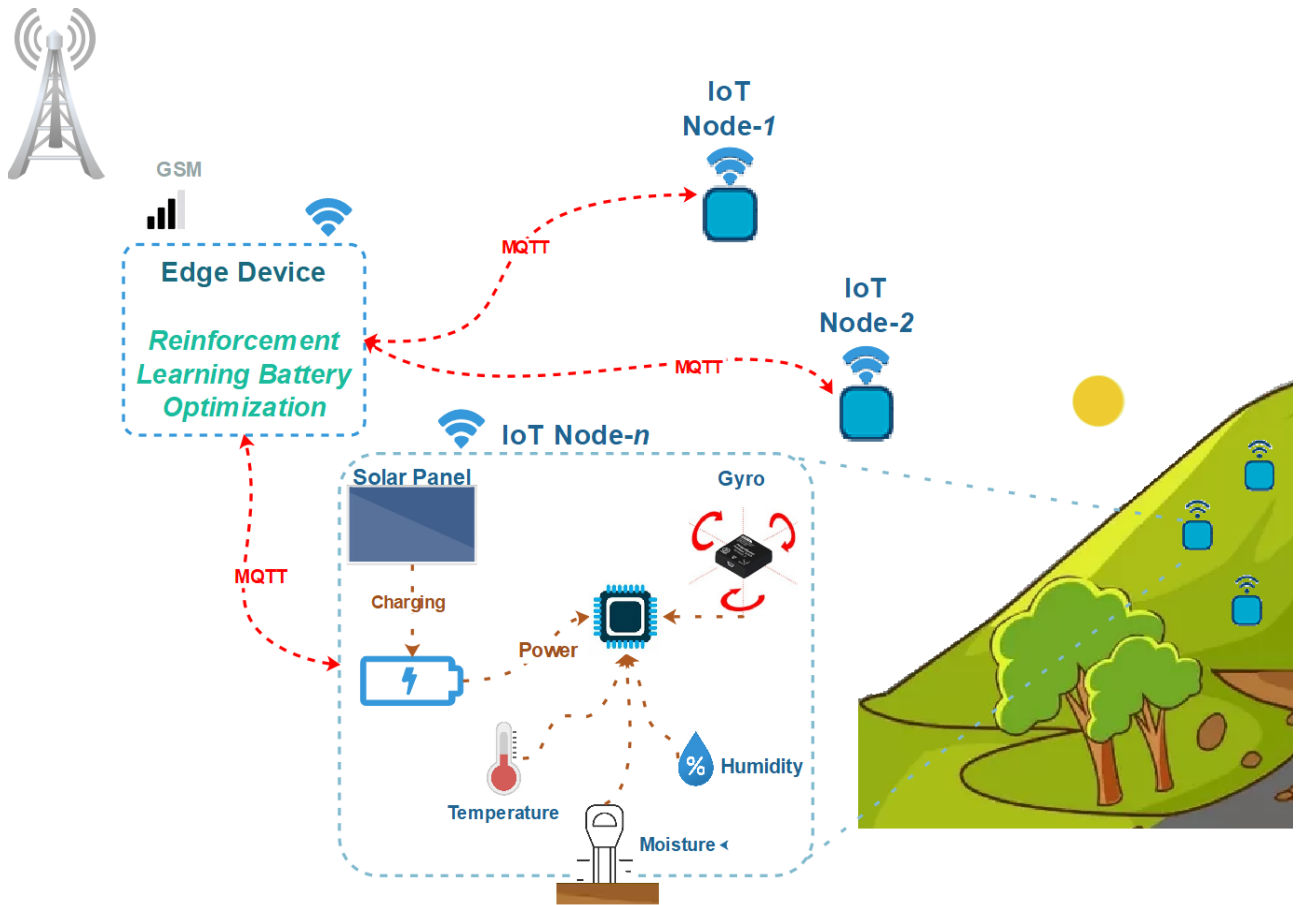


Fig. 1. Architecture of the reinforcement learning-based energy management system for landslide early warning

Figure 1 illustrates the architecture of the IoT-based landslide early warning system that is powered by reinforcement learning-based energy optimization. The formed system includes several IoT nodes equipped with different sensors for monitoring environmental conditions. Each node gathers environmental data such as soil moisture, temperature, and humidity, and sends it wirelessly to a central edge device using the MQTT protocol. The IoT nodes harvest energy through solar panels to meet their energy requirements, with this harvested energy stored in the nodes' batteries.

The reinforcement learning model will analyze data collected to come up with optimum energy consumption by the IoT nodes. The model dynamically adjusts the duty cycle of nodes with consideration of the present level of the battery and how much energy has been harvested. In this way, the system can improve energy efficiency for non-interrupted operation. This architecture is designed to improve energy sustainability in IoT nodes and enhance the reliability of the landslide early warning system.

3.3.1. Reinforcement learning model

The proposed approach is modeled as a Markov Decision Process (MDP) within the reinforcement learning framework. An MDP is defined by the tuple $\langle S, A, P, R, \gamma \rangle$, consisting of four main components: S represents the state space, A represents the action space, P denotes the state transition probabilities, R denotes the reward function, and γ is the discount factor.

In this study, the state space is represented by a three-dimensional vector:

$$s_t = [B_t, T_t, E_{h,t}] \quad (5)$$

$$B_t = \left(\frac{P_{\text{current}}}{B_{\text{max}}} \right) \times 100 \quad (6)$$

The vector s_t , which is provided as input to the trained DQN model, represents the state at time t . Here, B_t indicates the battery level at time t (expressed as a percentage of mAh), which represents the current state of the energy storage in the IoT node and serves as a critical parameter for determining the appropriate duty cycle based on energy availability. T_t represents the ambient temperature at time t (in °C), and $E_{h,t}$ is the amount of harvested energy at time t (in mAh).

The action space encompasses the potential decisions the trained agent can make. In this study, the action space consists of five distinct duty cycle levels.

$$A = \{a_1, a_2, a_3, a_4, a_5\} \quad (7)$$

In the above representation, A defines the state space, and a_1, a_2, a_3, a_4 , and a_5 correspond to 20%, 40%, 60%, 80%, and 100% duty cycles, respectively. By simulating energy consumption under these duty cycles, the battery level is updated according to Equation 8.

$$E_{c,t} = P_{\text{min}} + (P_{\text{max}} - P_{\text{min}}) \times \left(\frac{D(a_t) - D_{\text{min}}}{D_{\text{max}} - D_{\text{min}}} \right) \times \Delta t \quad (8)$$

where $E_{c,t}$ denotes the amount of energy consumed over a given time interval. P_{min} and P_{max} represent the minimum and maximum energy consumption levels of the IoT node, respectively. $D(a_t)$ is the duty cycle action selected for time t , while D_{min} and D_{max} define the minimum and maximum selectable duty cycles, respectively. Following this, the amount of energy harvested from the solar panel during the specified time interval is calculated using Equation 9 to determine the increase in battery level.

$$E_{h,t} = \frac{G_t \times A_p \times \eta_p}{V_s} \times 1000 \times \Delta t \quad (9)$$

In Equation (9), $E_{h,t}$ represents the energy harvested during the time interval t (in mAh). G_t is the solar irradiance at time t (W/m²), A_p is the area of the solar panel (m²), η_p is the efficiency percentage of the solar panel, and V_s is the system voltage (V). The battery level update is performed based on Equations 10 and 11.

$$B_s = B_t - E_{c,t} + E_{h,t} \quad (10)$$

$$B_{t+1} = \min(\max(B_s, 0), B_{\text{max}}) \quad (11)$$

In these equations, B_s represents the total energy available in the battery after accounting for both the energy consumed by the IoT node and the energy harvested through the solar panel. B_{t+1} denotes the battery level in the next time step; if the total harvested energy causes the battery to exceed its maximum capacity, the level is capped at B_{\max} .

The goal of the Reinforcement Learning agent is to maintain the battery level at an optimal level continuously and to be rewarded for the duration it remains at this level. Therefore, the agent is penalized during training for overcharging or discharging. The reward function defined below is used to determine the reward-penalty amounts.

$$d_n = |B_{t+1} - (B_{\max} \times 0.8)| \quad (12)$$

$$O_t = \begin{cases} \left(\frac{B_s - B_{\max}}{B_{\max}} \right) \times \frac{4-k}{4}, & B_s > B_{\max} \\ 0, & \text{otherwise} \end{cases} \quad (13)$$

$$R_t = \begin{cases} 5, & d_n < 500 \\ 5 - 50 \times \left(\frac{d_n}{B_{\max}} + O_t \right), & 500 \leq d_n < 3000 \\ -50, & d_n \geq 3000 \end{cases} \quad (14)$$

Here, d_n represents the energy neutrality distance, which increases as the battery level deviates from the optimal level of 80%. O_t denotes the amount of overcharge. If the battery level at a given time and the total harvested energy in that interval exceed the maximum battery capacity, and the duty cycle selected is less than 100%, the penalty rate increases. In Equation 13, the value k represents the coefficient for the overcharge penalty, indicating the index of the chosen action in the action space, ranging from 0 to 4. The highest penalty is given when the duty cycle is set to 20%. Finally, using the values of d_n and O_t , the total reward R_t is calculated. R_t reflects the balance between energy efficiency and operational performance, penalizing deviations from the optimal battery level and rewarding actions that maintain energy neutrality

3.3.2. Deep Q Network architecture and model training

The proposed model employs the Deep Q-learning (DQN) algorithm as the reinforcement learning method. DQN is an extension of the traditional Q-learning algorithm using deep neural networks, enabling it to operate effectively in high-dimensional state spaces. The DQN network here consists of a three-dimensional input layer that takes the state space as input, three hidden layers of 64, 32, and 8 dimensions, respectively, and a five-dimensional output layer that provides an action from the action space as output. The architecture of the network used in training is shown in Figure 2.

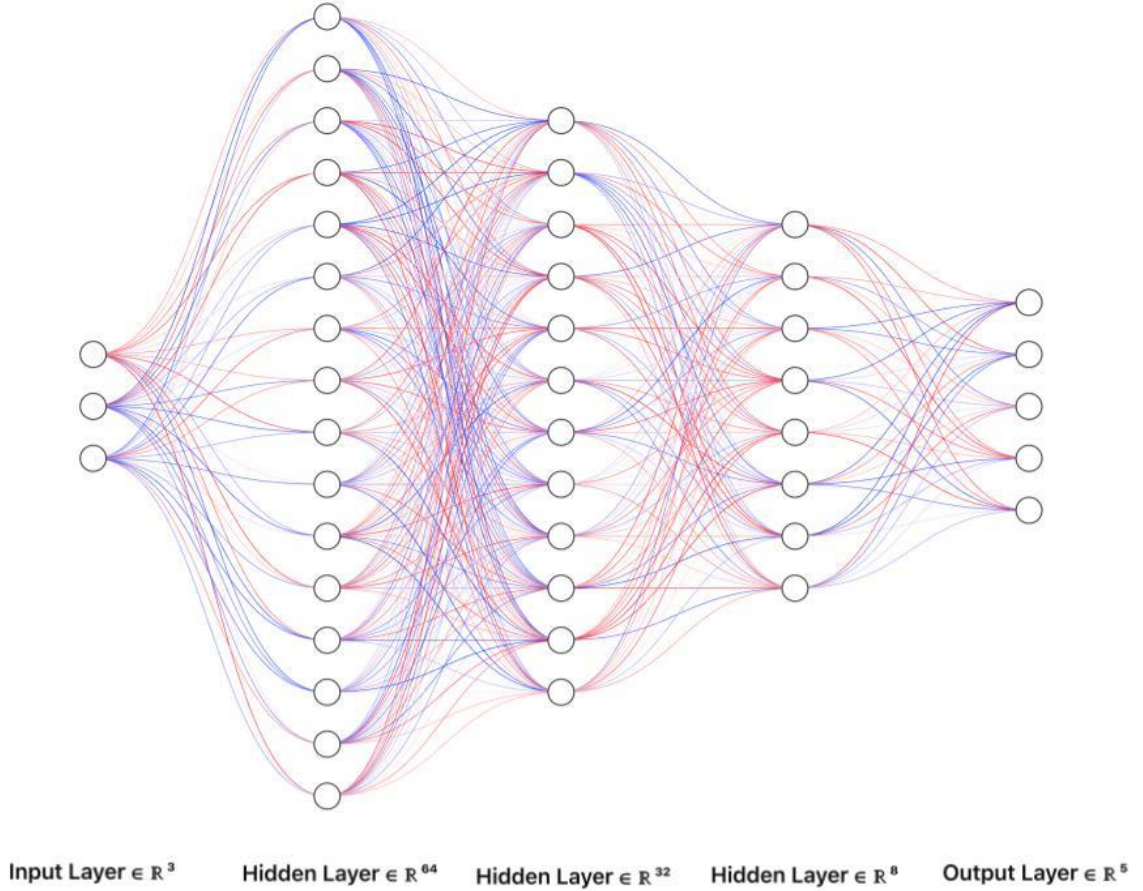


Fig. 2. Architecture of the DQN used in training.

This neural network is used to approximate the $Q(s, a; \theta)$ state-action value function, where θ represents the neural network's weights.

During the training process, the neural network parameters θ are initialized randomly. The Epsilon-Greedy strategy is applied in training, with the epsilon (ϵ) value initially set to 1,0 [78]. A random number between 0 and 1 is then selected and compared with the ϵ value. If the randomly chosen number is less than ϵ , an action is chosen randomly from the action space. Otherwise, the action with the highest Q value, as predicted by the neural network, is selected. At the end of each time step, the value of ϵ is reduced according to Equation 15.

$$\epsilon = \max(\epsilon_{min}, \epsilon \times \epsilon_{decay}) \quad (15)$$

where ϵ_{min} is the minimum allowable epsilon value, and ϵ_{decay} is the decay rate per time step. After these operations, the action a_t is used to select a duty cycle, resulting in the next state s_{t+1} and the reward R_t . The information from this experience is then stored in the experience replay memory. An example of the format for stored data in the replay memory is shown below:

$$(s_t, a_t, R_t, s_{t+1}, \partial) \tag{16}$$

Here, ∂ is a boolean variable indicating whether the training episode ends after this step. Experience data is stored in memory until a specified memory size is reached.

There are two main components in the application of the DQN model. One is the primary model used while the agent continuously interacts with the environment. The other is the target model, which is used to prevent instability caused by rapid changes in the weights of the primary model. The weights of the target model are gradually transferred from the primary model to the target model using a method known as soft update [79].

$$y_j = \begin{cases} R_j, & \text{if } \partial_j = \text{True} \\ R_j + \gamma \times \max_{a'} Q(s_{j+1}, a'; \theta^-), & \text{otherwise} \end{cases} \tag{17}$$

where y_j represents the target Q values, θ^- represents the parameters of the target network and γ represents the the discount factor, which determines the importance of future rewards compared to immediate rewards. A value of γ close to 1 prioritizes long-term rewards, while a lower value focuses on short-term gains, allowing the model to balance immediate performance with sustainable energy neutrality over time. The weights of the target network are adjusted to approach the weights of the main network according to the following assignment:

$$\theta^- \leftarrow \tau \times \theta + (1 - \tau) \times \theta^- \tag{18}$$

Here, τ is the soft update rate, typically a small value like 0,001. The loss function used in the trained model is the Mean Squared Error (MSE), calculated for the specified model as follows:

$$L(\theta) = \frac{1}{N} \sum_i (y_j - Q(s_j, a_j; \theta))^2 \tag{19}$$

Figure 3 presents the pseudocode of the proposed model, which outlines the step-by-step process of the reinforcement learning-based energy optimization framework, including initialization, action selection, energy calculations, reward assignment, and model updates.

```

1 - Initialize the DQN parameters  $\theta$ 
2 - Clone  $\theta$  to  $\theta^-$  (target network)
3 - Initialize replay memory with capacity defined in Replay_buffer_size
4 - Set  $\epsilon$  = Exploration_rate
5 for_each_episode:
6     - Set B_current = B_max
7     - Set done = false
8     - Set total_reward = 0
9     - Set time_step t = 0
10    - Initialize state s_0 = [Irradiation_0, Temperature_0, (B_current/B_max)x100]
11    while_not_done:
12        - Select action a_t randomly with probability  $\epsilon$ 
13        - Otherwise, a_t = argmax_a Q(s_t;  $\theta$ )
14        - duty_cycle = (a_t + 1)  $\times$  (incremental percentage)
15        - E_c = Base_Consumption + (Additional_Consumption  $\times$  a_t)
16        - E_h = ((Irradiation_t  $\times$  A_p  $\times$   $\eta_p$ ) / V_s)  $\times$  1000 (mAh)
17        - B_temp = B_current - E_c + E_h
18        - if B_temp > B_max:
19            - overcharge_penalty_rate = (B_temp - B_max) / B_max
20            - overcharge_penalty_rate = overcharge_penalty_rate  $\times$  ((4 - a_t) / 4)
21            - B_current = B_max
22        else:
23            - overcharge_penalty_rate = 0
24            - B_current = max(B_temp, 0)
25            - if B_current == 0:
26                - done = true
27        - s_(t+1) = [Irradiation_(t+1), Temperature_(t+1), (B_current/B_max)x100]
28        - neutrality_dist = abs(B_current - B_opt)
29        - if neutrality_dist < Threshold_1:
30            - r_t = High_Value
31        - else_if (neutrality_dist >= Threshold_1 and neutrality_dist < Threshold_2):
32            - r_t = Medium_Base_Value - (Additional_Penalty_Factor  $\times$ 
33                (neutrality_dist / B_max) + overcharge_penalty_rate)
34        - else:
35            - r_t = Heavy_Penalty
36        - Store (s_t, a_t, r_t, s_(t+1), done) in replay memory
37        - if replay_memory_size > Batch_size:
38            - Sample a minibatch of transitions
39            - for each sampled transition:
40                if done:
41                    - y_j = r_j
42                else:
43                    - Compute target y_j = r_j + Discount_factor  $\times$  max_a Q(s_(j+1);  $\theta^-$ )
44            - Update  $\theta$  by minimizing the loss between Q(s_j, a_j;  $\theta$ ) and y_j
45            - Soft update target network:  $\theta^- \leftarrow \tau x \theta + (1 - \tau) x \theta^-$ 
46        - s_t = s_(t+1)
47        - total_reward += r_t
48        - Increment t by 1
49        - If done or t reaches the end of the data sequence, break the loop
50    -  $\epsilon$  = max(epsilon_min,  $\epsilon$   $\times$  Decay_Rate)
51    - Optionally save model parameters ( $\theta$  and  $\theta^-$ ) at scheduled intervals

```

Fig. 3. Pseudocode of the proposed model.

4. Results and discussion

This section covers the results from our study on how the RL-based model works in optimizing energy management in IoT nodes to allow for early detection of natural hazards like landslides and outlines some benchmark parameters that had been used for training the RL model and the agent and a simulation environment which was set up with these parameters. Details of the parameters and the values used for training are listed in Table 1.

Table 1. Parameters and configuration for agent training and simulation environment.

Parameter Type	Parameter Name	Parameter Value
Agent	State Space Size	3
Agent	Action Space Size	5
Agent	Exp. Replay Memory Size	1000
Agent	Gamma (γ)	0.95
Agent	Epsilon Decay (ϵ_{decay})	0.9995
Agent	Tau (τ)	0.001
Model	Hidden Layer Activation	ReLU
Model	Output Layer Activation	Linear
Model	Optimizer	Adam
Model	Optimizer Learning Rate	0.001
Model	Loss Function	MSE
Environment	Panel Area (A_p)	0.5 m ²
Environment	Max Battery Level (B_{max})	5000 mAh
Environment	Panel Efficiency (η_p)	0.15
Environment	Optimum Battery Level	4000 mAh
Environment	System Voltage	5 Volt
Training	Batch Size	32
Training	Episode	1000

The variables in Table 1 describe the parameters and configurations used for the training and simulation environment of the reinforcement learning model proposed in the article. State Space Size refers to the three-dimensional data vector that the model receives as input, while Action Space Size defines five different duty cycles that the model can choose from. Exp. Replay Memory Size indicates the amount of experiences retained during the learning process. Gamma value is the discount factor that determines the effect of future rewards on today's rewards. Epsilon Decay regulates how the selection rate of random actions in the epsilon-change strategy decreases over time. Tau defines the soft update of the weights of the target model to the main model. The Hidden Layer Activation and Output Layer Activation functions used in the training of the model specify how the activation between layers will occur during the learning process of the neural network. Optimizer and Optimizer Learning Rate determine the weight

update strategy and speed of the model, while Loss Function is an error measure that evaluates the performance of the model. Parameters such as Panel Area, Panel Efficiency, System Voltage, Max Battery Level and Optimum Battery Level used in the simulation environment describe the physical properties used in energy collection and consumption calculations. Finally, Batch Size and Episode define the amount of data processing in the training process of the model and the total number of training cycles. These parameters allow the proposed model to be configured for energy management optimization.

Training and simulations were performed using the computer hardware specification: AMD Ryzen 5600X, NVIDIA RTX 3060 with CUDA for training acceleration, and RAM 16 GB. The results demonstrated a balance between energy harvesting and consumption, enabling the IoT node to operate continuously within the specified duty cycles. It is observable from Figure 4 that during highly energy-available periods of the year, the battery level remains full. During winter, when energy becomes really scarce, the level of the battery decreases but never to zero. This means the model maintains the IoT node always on by keeping the battery at an optimal level even when energy harvesting is low. In this way, the IoT node can operate continuously without interruption and never allow the battery level to drop to zero.

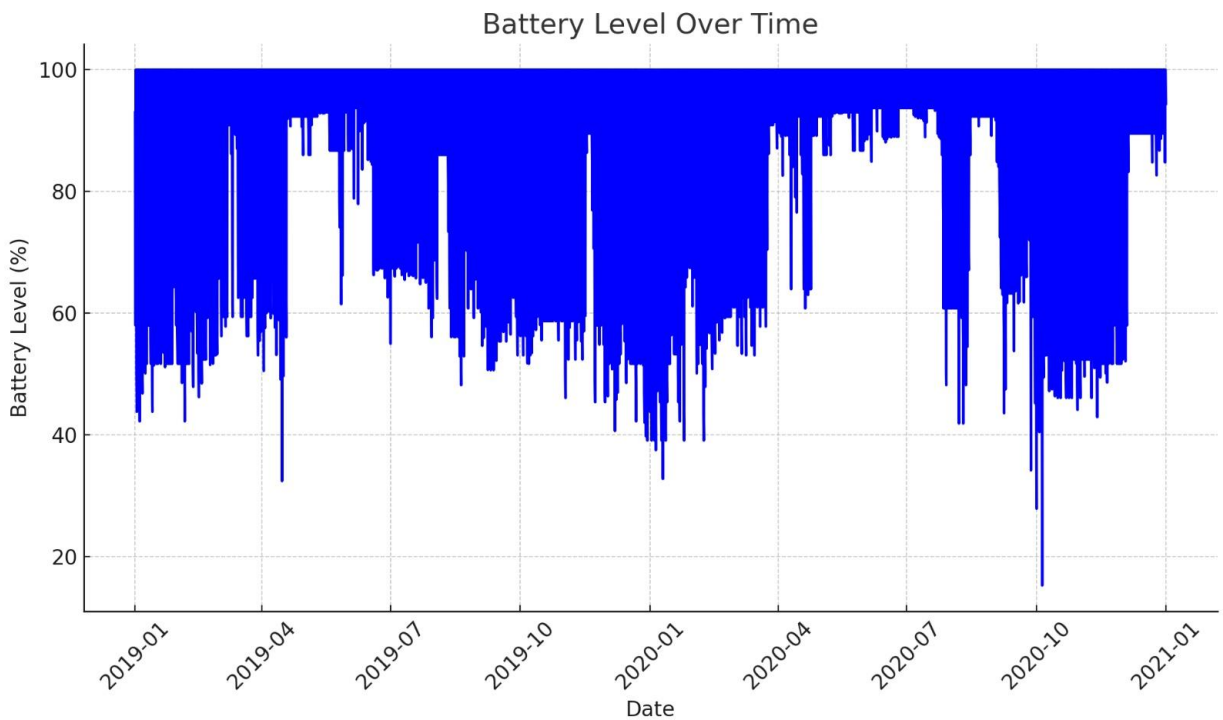


Fig. 4. Variation of battery level over time.

As shown in Figure 5, the energy harvesting data reveal that the model dynamically adjusts the IoT node's operational cycle by considering seasonal variations throughout the year. This allows for maximum energy harvesting during summer months with high solar irradiance. Therefore, the model is able to maintain a higher level of battery and increase its IoT node activity cycle. The model improves system performance by allowing it to operate at a high-duty cycle when the battery level and energy harvesting are high. Conversely, if the energy harvesting during winter

is low, the proposed model optimizes the energy consumption by operating an IoT node on a low-duty cycle. It is an effective adaptiveness for energy neutrality, enabling the system to utilize energy efficiently.

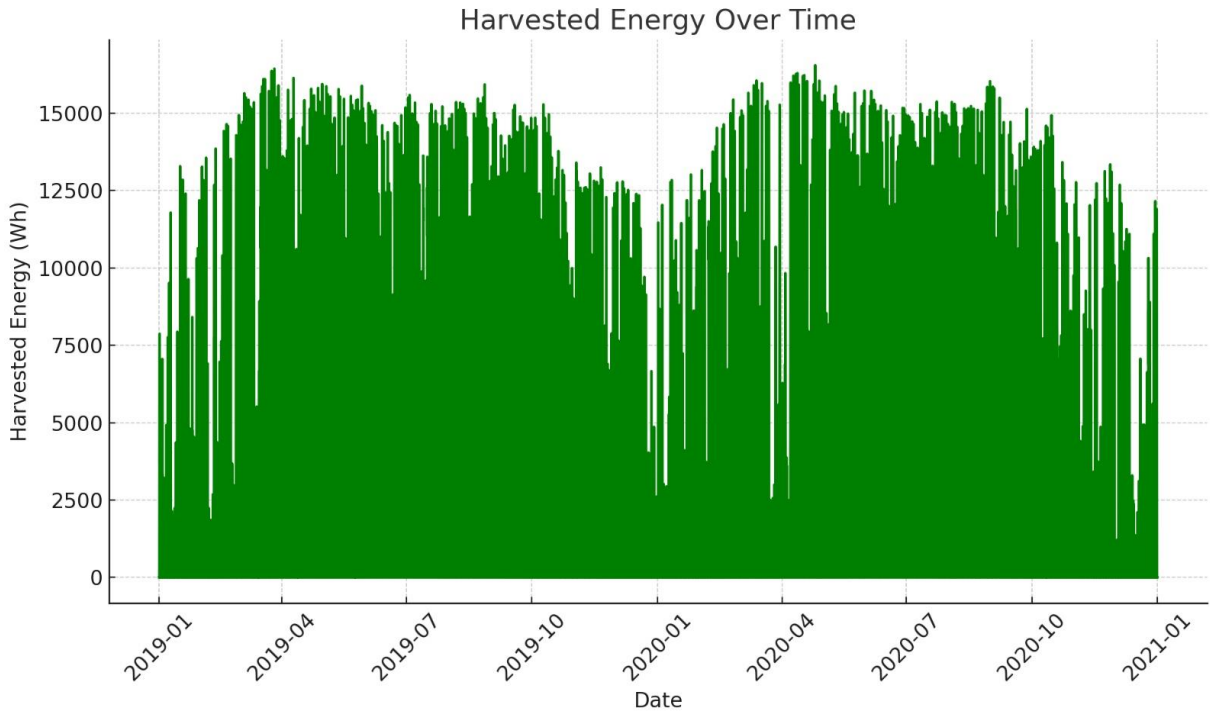


Fig. 5. Variation of harvested energy over time.

Figure 6 illustrates how dynamic and adaptive structure of the model adjusts the duty cycle in response to varying battery levels, ensuring energy neutrality. At lower battery levels (e.g., 20%-40%), the model automatically switches to a reduced duty cycle (20%-40%) to minimize energy consumption and prevent over-discharging. On the other hand, when the battery level increase (e.g., 80%-100%), the model progressively selects higher duty cycles (80%-100%), maximizing performance and data collection while maintaining energy sustainability.

This adaptive behavior highlights the ability to balance energy harvesting and consumption, ensuring uninterrupted operation even during periods of limited energy availability. The figure clearly demonstrates this relationship, with annotations providing additional clarity on the specific duty cycles selected at various battery levels. This feature ensures the IoT node operates efficiently and remains energy-neutral, adapting seamlessly to fluctuations in energy availability

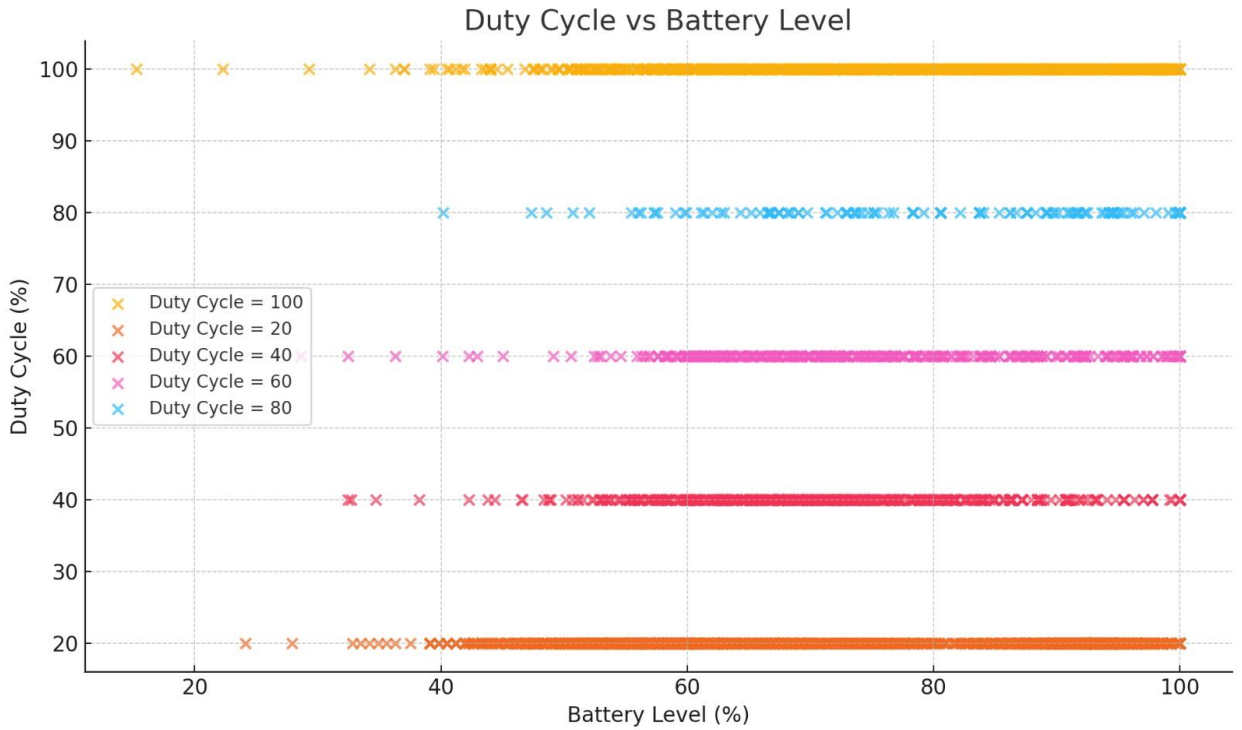


Fig. 6. Relationship between battery level and selected duty cycle.

This adaptive operational strategy is further corroborated in the relationship between total reward and duty cycle as depicted in Figure 7, whereby actions by the agent return higher rewards than random actions. It changes the duty cycle, depending on the battery level, for doing some energy efficiency enhancement. In this way, the IoT node gets operated uninterruptedly. This signifies that decisions made by the model are optimum concerning power management and thereby highest efficiency in the operation of the IoT node.



Fig. 7. Relationship between selected duty cycles and obtained rewards.

In Figure 8, which illustrates the relationship between action types and total reward, the difference between random actions (denoted as Action Type 0) and the actions selected by the trained RL agent (denoted as Action Type 1) is evident. The trained RL agent has achieved significantly higher rewards compared to random actions. This demonstrates that the RL agent makes more informed and optimized decisions regarding the energy management of the IoT node. The model selects appropriate duty cycles at every given time, taking into consideration the battery level and energy harvesting, hence increasing energy efficiency and feeding the continuous operation of the IoT node. It prefers low-duty cycles mainly during the periods of low-energy harvesting to save energy, while during high-energy harvesting periods, it operates the system more efficiently with high-duty cycles. These prove that the model is more successful than random actions and it can select the optimal action for continuous and efficient operation of IoT node.

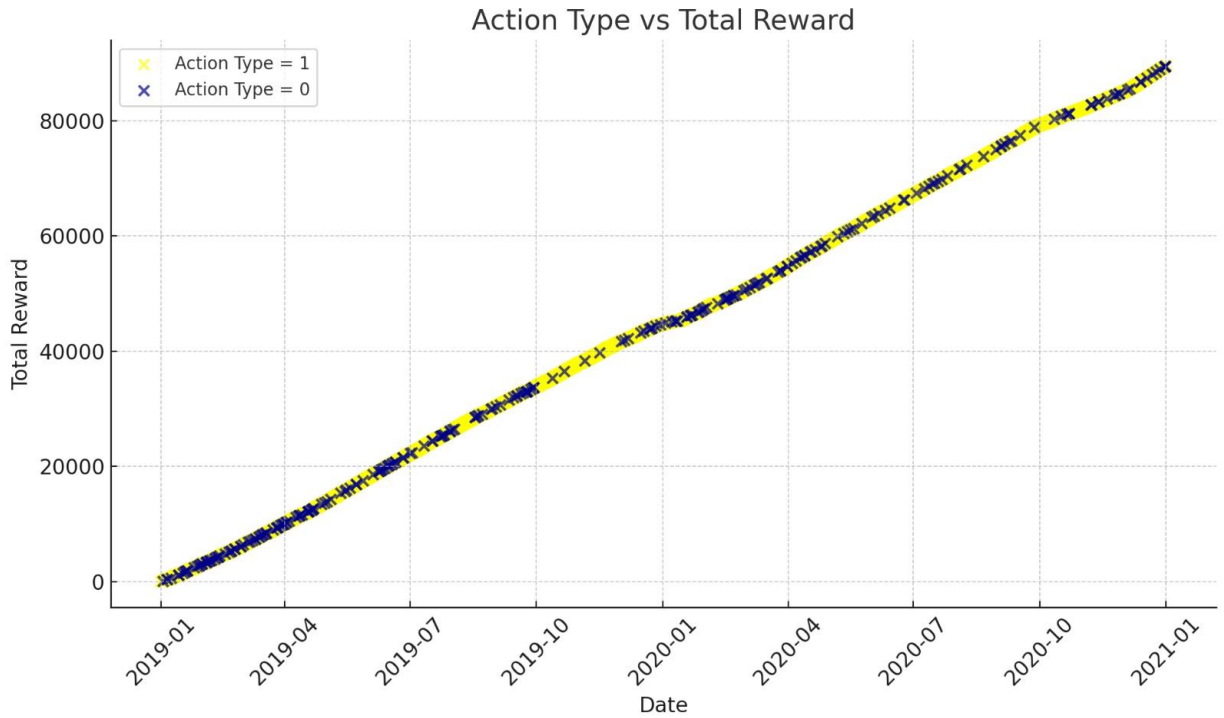


Fig. 8. Total rewards obtained by random actions and those selected by the agent.

Finally, it is observed from Figure 9 that the line that shows the relation between the epsilon value and total reward is such that while the epsilon value decreases, the total reward increases. This indicates that the total reward obtained with randomly determined actions was substantially lower, but higher rewards were achieved when the model chose the actions to be performed. This reflects the effectiveness that the model gained during the learning process.

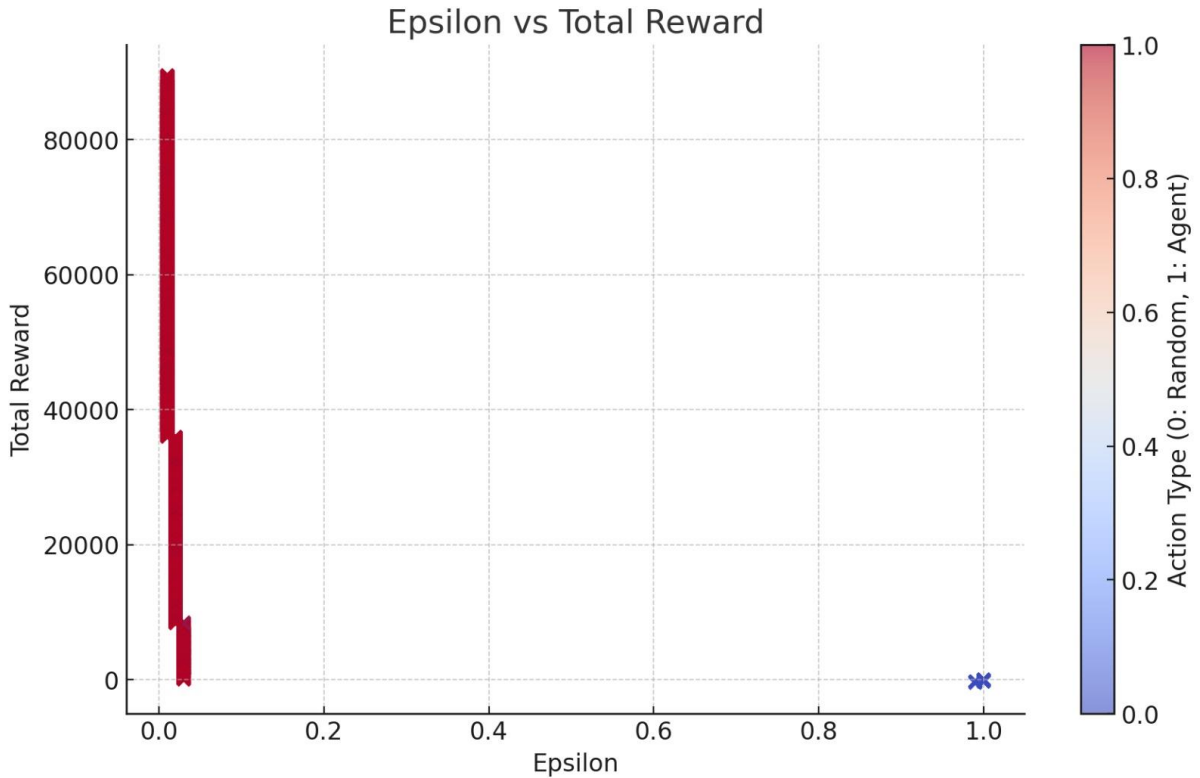


Fig. 9. Relationship between epsilon value and obtained reward.

These results confirm the efficiency of the proposed model based on reinforcement learning towards improving energy efficiency in IoT-based landslide early warning systems and enabling continuous operation. The model helps the IoT node use energy efficiently by keeping the battery level in an optimal state and enhances system reliability. These reflect that a dynamic balance exists between energy harvesting and the duty cycle and that the model effectively presents a sustainable solution for energy management in IoT systems.

Table 2. Uptime comparison with studies in the literature.

Study	Uptime (Seconds)	Uptime (Hours)	Uptime (Days)
Ait Aoudia et al. [80]	23,328,000	6,480	270
Murad et al. [81]	604,800	168	7
Charef et al. [82]	500	0.14	~0.006
Abadi et al. [83]	3,000	0.83	~0.035
Proposed Method	63,158,400	17,544	731

The comparison in the table clearly shows that the proposed model provides a significant superiority over the existing studies in the literature in terms of the working time of the IoT node. The proposed method worked continuously for 17544 hours (731 days, 2 years), exceeding the highest time of 270 days in the table by approximately 2.7 times. These results show that the proposed model offers a more efficient strategy in terms of duty cycle

optimization and battery management, and ensures that the IoT node remains operational for a long time. This is a significant advantage, especially in remote and maintenance-requiring environments where energy collection is limited.

5. Conclusion

This work presents a novel RL-based model to improve energy efficiency and operational sustainability in IoT-based landslide early warning systems. This study will employ the DQN algorithm to achieve energy neutrality by effectively optimizing the balance between energy harvesting and consumption. Our strategy is centered on an optimum level of the battery of IoT sensor nodes in such a way that continuous operational capability would be ensured for those nodes installed or deployed in remote disaster areas where the probability of frequent maintenance is not feasible. Unlike conventional energy management models, our model dynamically adapts to variations in environmental energy availability—solar radiation specifically—through adjustment in the duty cycle of sensor nodes. Thus, when energy harvest is high, the model increases the duty cycle to capture and utilize more data for better system reliability and response. At low energies, the model reduces the duty cycle—a reason being to save the battery life without completely compromising any core functionalities.

However, the study has some limitations that should be addressed in future work. Firstly, while the model was validated using real-world solar radiation data, its performance under other environmental conditions (e.g., wind energy, vibration-based energy harvesting) was not considered. Future research could expand the scope by incorporating multi-source energy harvesting and investigating the impact of environmental variability on system performance. Future studies will also focus on validating the proposed model using different datasets collected from various geographic locations and environmental conditions to further enhance its robustness and applicability.

These results from the simulation verify that the model is effective in ensuring continuity during prolonged operations. We have used real-world solar radiation data to demonstrate that the model's adaptive management can enable IoT nodes to attain high-duty cycles during energy-rich conditions and low-duty cycles during energy-starved conditions. This kind of strategy extends not only the battery lifetime of sensor nodes but also enhances landslide early warning system resilience to keep it operational through seasonal cycles and inclement weather.

As the limitation, this study relied on simulations for validation. While the results are promising, deploying the model in real-world landslide-prone areas and monitoring its long-term performance would provide more robust insights. This can include assessing the model's ability to adapt to hardware failures, unpredictable weather patterns, and sensor inaccuracies.

These features make the proposed RL-based model quite suitable for IoT applications in unpredictable and energy-limited environments. The work also contributes to a wide variety of energy management issues in IoT by showing how reinforcement learning can manage energy resources autonomously in this study. Additionally, further work could focus on the following directions: integrating advanced machine learning techniques, such as hybrid reinforcement learning or transfer learning, to enhance the system's adaptability and decision-making in highly dynamic environments. Developing more energy-efficient hardware for IoT nodes to complement the software-based optimization approaches. Exploring the scalability of the proposed model in larger IoT networks with heterogeneous energy sources and varying duty cycle requirements.

Our findings have proved that the RL approach can be expanded and tailored to accommodate complex demands for energy in IoT systems other than landslide monitoring, providing a foundation for future research focused on RL-based energy management in diverse IoT applications.

Author contributions

S.A., S.D., and F.A. actively participated in conducting the experimental studies and writing the manuscript.

Acknowledgements

This study did not receive any specific funding or financial assistance from governmental, commercial, or nonprofit organizations.

References

- [1] R. Steen, E. Roud, T. M. Torp, and T.-A. Hansen, "The impact of interorganizational collaboration on the viability of disaster response operations: The Gjerdrum landslide in Norway," *Saf Sci*, vol. 173, p. 106459, 2024.
- [2] D. Petley, "Global patterns of loss of life from landslides," *Geology*, vol. 40, no. 10, pp. 927–930, 2012.
- [3] M. T. Chaudhary and A. Piracha, "Natural disasters—origins, impacts, management," *Encyclopedia*, vol. 1, no. 4, pp. 1101–1131, 2021.
- [4] F. Guzzetti *et al.*, "Geographical landslide early warning systems," *Earth Sci Rev*, vol. 200, p. 102973, 2020.
- [5] M. A. Jamshed, K. Ali, Q. H. Abbasi, M. A. Imran, and M. Ur-Rehman, "Challenges, applications, and future of wireless sensors in Internet of Things: A review," *IEEE Sens J*, vol. 22, no. 6, pp. 5482–5494, 2022.
- [6] N. Casagli, E. Intrieri, V. Tofani, G. Gigli, and F. Raspini, "Landslide detection, monitoring and prediction with remote-sensing techniques," *Nat Rev Earth Environ*, vol. 4, no. 1, pp. 51–64, 2023.
- [7] M. Esposito, L. Palma, A. Belli, L. Sabbatini, and P. Pierleoni, "Recent advances in internet of things solutions for early warning systems: A review," *Sensors*, vol. 22, no. 6, p. 2124, 2022.
- [8] J. Singh, R. Kaur, and D. Singh, "Energy harvesting in wireless sensor networks: A taxonomic survey," *Int J Energy Res*, vol. 45, no. 1, pp. 118–140, 2021.
- [9] A. J. Williams, M. F. Torquato, I. M. Cameron, A. A. Fahmy, and J. Sienz, "Survey of energy harvesting technologies for wireless sensor networks," *IEEE Access*, vol. 9, pp. 77493–77510, 2021.
- [10] T. Sanislav, G. D. Mois, S. Zeadally, and S. C. Folea, "Energy harvesting techniques for internet of things (IoT)," *IEEE access*, vol. 9, pp. 39530–39549, 2021.
- [11] S. Shresthamali, M. Kondo, and H. Nakamura, "Multi-objective reinforcement learning for energy harvesting wireless sensor nodes," in *2021 IEEE 14th International Symposium on Embedded Multicore/Many-core Systems-on-Chip (MCSoc)*, IEEE, 2021, pp. 98–105.
- [12] A. Karras, C. Karras, I. Karydis, M. Avlonitis, and S. Sioutas, "An Adaptive, Energy-Efficient DRL-Based and MCMC-Based Caching Strategy for IoT Systems," in *International Symposium on Algorithmic Aspects of Cloud Computing*, Springer, 2023, pp. 66–85.
- [13] E. O. Arwa and K. A. Folly, "Reinforcement learning techniques for optimal power control in grid-connected microgrids: A comprehensive review," *Ieee Access*, vol. 8, pp. 208992–209007, 2020.
- [14] L. M. Highland and P. Bobrowsky, *The landslide handbook-A guide to understanding landslides*, no. 1325. *US Geological Survey*, 2008.
- [15] A. Tekerek and M. Dörterler, "The adaptation of gray wolf optimizer to data clustering," *Politeknik Dergisi*, p. 1, 2020.
- [16] S. Dörterler, "Kanser Hastalığı Teşhisinde Ölüm Oyunu Optimizasyon Algoritmasının Etkisi," *Mühendislik Alanında Uluslararası Araştırmalar VIII*, p. 15, 2023.
- [17] İ. Akgül and V. Kaya, "Learning performance of optimization algorithms in convolutional neural networks: An application," in *INSAC Scientific Researches in Natural and Engineering Sciences*, 1st ed., vol. 1, Duvar, 2022, ch. 11, pp. 215–236.
- [18] N. Yağmur, H. Temurtaş, and İ. Dağ, "Anemi hastalığının yapay sinir ağları yöntemleri kullanılarak sınıflandırılması," *Journal of Scientific Reports-B*, no. 008, pp. 20–34, 2023.
- [19] N. N. Arslan, E. Şahin, and M. Akçay, "Deep learning-based isolated sign language recognition: a novel approach to tackling communication barriers for individuals with hearing impairments," *Journal of Scientific Reports-A*, no. 055, pp. 50–59, 2023.
- [20] V. Kaya, İ. Akgül, and Ö. Tanır, "A novel hybrid model based on machine and deep learning techniques for the classification of microalgae," *Phyton-International Journal of Experimental Botany*, vol. 92, no. 9, pp. 2519-2534, 2023.
- [21] G. Arslan, F. Aydemir, and S. Arslan, "Enhanced license plate recognition using deep learning and block-based approach," *Journal of Scientific Reports-A*, no. 058, pp. 57–82, 2023.
- [22] F. Aydemir and S. Arslan, "A System Design With Deep Learning and IoT to Ensure Education Continuity for Post-COVID," *IEEE Transactions on Consumer Electronics*, 2023.
- [23] S. Dörterler, H. Dumlu, D. Özdemir, and H. Temurtaş, "Hybridization of Meta-heuristic Algorithms with K-Means for Clustering Analysis: Case of Medical Datasets," *Gazi Mühendislik Bilimleri Dergisi*, pp. 1–23.
- [24] E. Şahin, D. Özdemir, and H. Temurtaş, "Multi-objective optimization of ViT architecture for efficient brain tumor classification," *Biomed Signal Process Control*, vol. 91, p. 105938, 2024.
- [25] F. Aydemir and S. Arslan, "Covid-19 pandemi sürecinde çocukların el yıkama alışkanlığının nesnelere interneti tabanlı sistem ile izlenmesi," *Mühendislik Bilimleri ve Araştırmaları Dergisi*, vol. 3, no. 2, pp. 161–168, 2021.
- [26] M. C. Özbacı, H. Şahin, and T. T. Bilgin, "Makine Öğrenmesi Yöntemleri ile GTZAN Veri Kümesine Ait Müzik Türlerinin Sınıflandırılması," *Mühendislik Bilimleri ve Araştırmaları Dergisi*, vol. 6, no. 1, pp. 77–87.
- [27] E. Şahin and M. F. Talu, "WY-NET: A NEW APPROACH TO IMAGE SYNTHESIS WITH GENERATIVE ADVERSARIAL NETWORKS," *Journal of Scientific Reports-A*, no. 050, pp. 270–290, 2022.
- [28] E. Şahin and M. F. Talu, "Automatic Mustache Pattern Production on Denim Fabric with Generative Adversarial Networks," *Computer Science*, vol. 7, no. 1, pp. 1–9, 2022.
- [29] N. Yagmur, İ. Dağ, and H. Temurtaş, "Classification of anemia using Harris hawks optimization method and multivariate adaptive regression

spline,” *Neural Comput Appl*, pp. 1–20, 2024.

- [30] N. Yagmur, I. Dag, and H. Temurtas, “A new computer-aided diagnostic method for classifying anaemia disease: Hybrid use of Tree Bagger and metaheuristics,” *Expert Syst*, p. e13528, 2023.
- [31] İ. Akgül, V. Kaya, E. Karavaş, S. Aydın, and A. Baran, “A Novel Artificial Intelligence-Based Hybrid System to Improve Breast Cancer Detection Using DCE-MRI,” *Bulletin Of The Polish Academy Of Sciences. Technical Sciences*, vol. 72, no. 3, 2024.
- [32] H. Ali, U. U. Tariq, M. Hussain, L. Lu, J. Panneerselvam, and X. Zhai, “ARSH-FATI: A novel metaheuristic for cluster head selection in wireless sensor networks,” *IEEE Syst J*, vol. 15, no. 2, pp. 2386–2397, 2020.
- [33] H. Ali *et al.*, “A survey on system level energy optimisation for MPSoCs in IoT and consumer electronics,” *Comput Sci Rev*, vol. 41, p. 100416, 2021.
- [34] H. Thirugnanam, M. V. Ramesh, and V. P. Rangan, “Enhancing the reliability of landslide early warning systems by machine learning,” *Landslides*, vol. 17, pp. 2231–2246, 2020.
- [35] T. Hemalatha, M. V. Ramesh, and V. P. Rangan, “Effective and accelerated forewarning of landslides using wireless sensor networks and machine learning,” *IEEE Sens J*, vol. 19, no. 21, pp. 9964–9975, 2019.
- [36] E. Collini, L. A. I. Palesi, P. Nesi, G. Pantaleo, N. Nocentini, and A. Rosi, “Predicting and understanding landslide events with explainable AI,” *IEEE Access*, vol. 10, pp. 31175–31189, 2022.
- [37] C. W. W. Ng, B. Yang, Z. Q. Liu, J. S. H. Kwan, and L. Chen, “Spatiotemporal modelling of rainfall-induced landslides using machine learning,” *Landslides*, vol. 18, pp. 2499–2514, 2021.
- [38] R. Franceschini, A. Rosi, F. Catani, and N. Casagli, “Exploring a landslide inventory created by automated web data mining: the case of Italy,” *Landslides*, vol. 19, no. 4, pp. 841–853, 2022.
- [39] X. Qian, “Regional Geological Disasters Emergency Management System Monitored by Big Data Platform,” *Processes*, vol. 10, no. 12, p. 2741, 2022.
- [40] X. Chen, “Early Warning of Regional Landslide Disaster and Development of Rural Ecological Industrialization Based on IoT Sensor,” *Sci Program*, vol. 2022, 2022.
- [41] C. V. L. Pennington *et al.*, “A near-real-time global landslide incident reporting tool demonstrator using social media and artificial intelligence,” *International Journal of Disaster Risk Reduction*, vol. 77, p. 103089, 2022.
- [42] G. Herrera *et al.*, “Landslide databases in the Geological Surveys of Europe,” *Landslides*, vol. 15, pp. 359–379, 2018.
- [43] K. Sassa and P. Canuti, *Landslides-disaster risk reduction*. Springer Science & Business Media, 2008.
- [44] B. Rosser, S. Dellow, S. Haubrock, and P. Glassey, “New Zealand’s national landslide database,” *Landslides*, vol. 14, pp. 1949–1959, 2017.
- [45] C. S. Juang, T. A. Stanley, and D. B. Kirschbaum, “Using citizen science to expand the global map of landslides: Introducing the Cooperative Open Online Landslide Repository (COOLR),” *PLoS One*, vol. 14, no. 7, p. e0218657, 2019.
- [46] M. J. Froude and D. N. Petley, “Global fatal landslide occurrence from 2004 to 2016,” *Natural Hazards and Earth System Sciences*, vol. 18, no. 8, pp. 2161–2181, 2018.
- [47] Q. Han, K. Sassa, and M. Mikoš, “International programme on landslides (ipl): a programme of the icl for landslide disaster risk reduction,” *Understanding and Reducing Landslide Disaster Risk: Volume 1 Sendai Landslide Partnerships and Kyoto Landslide Commitment 5th*, pp. 187–203, 2021.
- [48] A. C. Teodoro and L. Duarte, “The synergy of remote sensing and geographical information systems in the management of natural disasters,” in *Nanotechnology-Based Smart Remote Sensing Networks for Disaster Prevention*. Elsevier, 2022, pp. 217–230.
- [49] Z. Yang, J. Li, J. Hyyppä, J. Gong, J. Liu, and B. Yang, “A comprehensive and up-to-date web-based interactive 3D emergency response and visualization system using Cesium Digital Earth: taking landslide disaster as an example,” *Big Earth Data*, pp. 1–23, 2023.
- [50] M. N. I. Sarker, Y. Peng, C. Yiran, and R. C. Shouse, “Disaster resilience through big data: Way to environmental sustainability,” *International Journal of Disaster Risk Reduction*, vol. 51, p. 101769, 2020.
- [51] K. Goniewicz *et al.*, “Geographic information system technology: review of the challenges for its establishment as a major asset for disaster and emergency management in Poland,” *Disaster Med Public Health Prep*, vol. 15, no. 5, pp. 573–578, 2021.
- [52] C. Nefros, G. Kitsara, and C. Loupasakis, “Geographical Information Systems and Remote Sensing Techniques to Reduce the Impact of Natural Disasters in Smart Cities,” *IFAC-PapersOnLine*, vol. 55, no. 11, pp. 72–77, 2022.
- [53] P. V. Gorsevski, M. K. Brown, K. Panter, C. M. Onasch, A. Simic, and J. Snyder, “Landslide detection and susceptibility mapping using LiDAR and an artificial neural network approach: a case study in the Cuyahoga Valley National Park, Ohio,” *Landslides*, vol. 13, pp. 467–484, 2016.
- [54] N. M. Abdullah, N. Sulaiman, U. Nazir, M. Ismail, S. K. K. A. Latib, and N. P. N. Mahmud, “Geographical Information System (GIS) and Remote Sensing (RS) Applications in Disaster Risk Reduction (DRR) in Malaysia,” *International Journal of Integrated Engineering*, vol. 14, no. 5, pp. 25–37, 2022.
- [55] I. Alcántara-Ayala and R. J. Garnica-Peña, “Landslide Warning Systems in Upper Middle-Income Countries: Current Insights and New Perspectives,” in *Progress in Landslide Research and Technology, Volume 1 Issue 2, 2022*, Springer, 2023, pp. 159–168.
- [56] R. Can, S. Kocaman, and C. Gokceoglu, “A convolutional neural network architecture for auto-detection of landslide photographs to assess citizen science and volunteered geographic information data quality,” *ISPRS Int J Geoinf*, vol. 8, no. 7, p. 300, 2019.
- [57] G. T. Harilal, D. Madhu, M. V. Ramesh, and D. Pullarkatt, “Towards establishing rainfall thresholds for a real-time landslide early warning system in Sikkim, India,” *Landslides*, vol. 16, no. 12, pp. 2395–2408, 2019.
- [58] X. Fan *et al.*, “Prediction of a multi-hazard chain by an integrated numerical simulation approach: the Baige landslide, Jinsha River, China,” *Landslides*, vol. 17, pp. 147–164, 2020.
- [59] J.-Y. Park, S.-R. Lee, D.-H. Lee, Y.-T. Kim, and J.-S. Lee, “A regional-scale landslide early warning methodology applying statistical and physically based approaches in sequence,” *Eng Geol*, vol. 260, p. 105193, 2019.

- [60] T. Salvatici *et al.*, “Application of a physically based model to forecast shallow landslides at a regional scale,” *Natural Hazards and Earth System Sciences*, vol. 18, no. 7, pp. 1919–1935, 2018.
- [61] V.-H. Nhu *et al.*, “Landslide susceptibility mapping using machine learning algorithms and remote sensing data in a tropical environment,” *Int J Environ Res Public Health*, vol. 17, no. 14, p. 4933, 2020.
- [62] B. Hariharan and R. Guntha, “Crowdsourced landslide tracking-lessons from field experiences of landslide tracker mobile app,” in *EGU General Assembly Conference Abstracts*, 2021, pp. EGU21-12711.
- [63] R. Guntha, S. N. Rao, and M. V Ramesh, “Deployment experiences with Amrita Kripa: a user-friendly feature rich crowdsourced humanitarian application,” *Procedia Comput Sci*, vol. 171, pp. 302–311, 2020.
- [64] C. He, N. Ju, Q. Xu, and J. Huang, “Automated data processing and integration of large multiple data sources in geohazards monitoring,” *International Journal of Georesources and Environment-IJGE (formerly Int'l J of Geohazards and Environment)*, vol. 3, no. 1–2, pp. 9–21, 2017.
- [65] T. F. Fathani, D. Karnawati, and W. Wilopo, “An adaptive and sustained landslide monitoring and early warning system,” in *Landslide Science for a Safer Geoenvironment: Volume 2: Methods of Landslide Studies*, Springer, 2014, pp. 563–567.
- [66] T. Hemalatha, M. V. Ramesh, and V. P. Rangan, “Adaptive learning techniques for landslide forecasting and the validation in a real world deployment,” in *Advancing Culture of Living with Landslides: Volume 5 Landslides in Different Environments*, Springer, 2017, pp. 439–447.
- [67] L. Zhang and P. Lin, “Reinforcement learning based energy-neutral operation for hybrid EH powered TBAN,” *Future Generation Computer Systems*, vol. 140, pp. 311–320, 2023.
- [68] A. Murad, F. A. Kraemer, K. Bach, and G. Taylor, “Autonomous management of energy-harvesting iot nodes using deep reinforcement learning,” in *2019 IEEE 13th International Conference on Self-Adaptive and Self-Organizing Systems (SASO)*, IEEE, 2019, pp. 43–51.
- [69] A. Omidkar, A. Khalili, H. H. Nguyen, and H. Shafiei, “Reinforcement-learning-based resource allocation for energy-harvesting-aided D2D communications in IoT networks,” *IEEE Internet Things J*, vol. 9, no. 17, pp. 16521–16531, 2022.
- [70] M. Chu, X. Liao, H. Li, and S. Cui, “Power control in energy harvesting multiple access system with reinforcement learning,” *IEEE Internet Things J*, vol. 6, no. 5, pp. 9175–9186, 2019.
- [71] F. A. Aoudia, M. Gautier, and O. Berder, “RLMan: An energy manager based on reinforcement learning for energy harvesting wireless sensor networks,” *IEEE Transactions on Green Communications and Networking*, vol. 2, no. 2, pp. 408–417, 2018.
- [72] Y. Li, “Deep reinforcement learning: An overview,” *arXiv preprint arXiv:1701.07274*, 2017.
- [73] Y. Fei, Z. Yang, Y. Chen, and Z. Wang, “Exponential bellman equation and improved regret bounds for risk-sensitive reinforcement learning,” *Adv Neural Inf Process Syst*, vol. 34, pp. 20436–20446, 2021.
- [74] J. Clifton and E. Laber, “Q-learning: Theory and applications,” *Annu Rev Stat Appl*, vol. 7, no. 1, pp. 279–301, 2020.
- [75] F. Liu, L. Viano, and V. Cevher, “Understanding deep neural function approximation in reinforcement learning via ϵ -greedy exploration,” *Adv Neural Inf Process Syst*, vol. 35, pp. 5093–5108, 2022.
- [76] T. T. Nguyen, N. D. Nguyen, and S. Nahavandi, “Deep reinforcement learning for multiagent systems: A review of challenges, solutions, and applications,” *IEEE Trans Cybern*, vol. 50, no. 9, pp. 3826–3839, 2020.
- [77] European Commission, “European Commission Photovoltaic Geographic Information System.” Accessed: Nov. 09, 2024. [Online]. Available: https://re.jrc.ec.europa.eu/pvg_tools/en/
- [78] V. Mnih *et al.*, “Human-level control through deep reinforcement learning,” *Nature*, vol. 518, no. 7540, pp. 529–533, 2015.
- [79] T. P. Lillicrap, “Continuous control with deep reinforcement learning,” *arXiv preprint arXiv:1509.02971*, 2015.
- [80] F. Ait Aoudia, M. Gautier, and O. Berder, “RLMan: An Energy Manager Based on Reinforcement Learning for Energy Harvesting Wireless Sensor Networks,” *IEEE Transactions on Green Communications and Networking*, vol. 2, no. 2, pp. 408–417, Jun. 2018, doi: 10.1109/TGCN.2018.2801725.
- [81] A. Murad, F. A. Kraemer, K. Bach, and G. Taylor, “Autonomous management of energy-harvesting iot nodes using deep reinforcement learning,” in *2019 IEEE 13th International Conference on Self-Adaptive and Self-Organizing Systems (SASO)*, IEEE, 2019, pp. 43–51.
- [82] N. Charef, M. Abdelhafidh, A. Ben Mnaouer, K. Andersson, and S. Cherkaoui, “RL-Based Adaptive Duty Cycle Scheduling in WSN-Based IoT Nets,” in *GLOBECOM 2023-2023 IEEE Global Communications Conference*, IEEE, 2023, pp. 3777–3782.
- [83] A. F. E. Abadi, S. A. Asghari, M. B. Marvasti, G. Abaci, M. Nabavi, and Y. Savaria, “RLBEEP: Reinforcement-Learning-Based Energy Efficient Control and Routing Protocol for Wireless Sensor Networks,” *IEEE Access*, vol. 10, pp. 44123–44135, 2022, doi: 10.1109/ACCESS.2022.3167058.



Contents lists available at *Dergipark*

Journal of Scientific Reports-A

journal homepage: <https://dergipark.org.tr/pub/jsr-a>



E-ISSN: 2687-6167

Number 59, December 2024

RESEARCH ARTICLE

Receive Date: 02.09.2024

Accepted Date: 25.12.2024

Comparison of regression and tree-based methods for the prediction of zero-inflated claim data

Aslıhan Şentürk Acar*

*Hacettepe University, Department of Actuarial Sciences, Beytepe, Ankara, Turkey
aslihans@hacettepe.edu.tr, ORCID: 0000-0002-1708-2028

Abstract

Pricing non-life insurance products is based on the prediction of two components; claim frequency and claim severity. In this study we focus on claim frequency data that has a zero-inflated structure. Although zero-modified regression models such as zero-inflated and hurdle models are used for data sets with excess zeros, machine learning (ML) methods are also preferred for this type of data sets in recent years. When the objective is the prediction, ML methods generally provide more accurate results than regression models especially for large and complex datasets. Tree-based ML methods run decision trees as the base of the algorithm and improve performance by using the predictions of multiple trees. Combining the traditional methods with ML methods is a current popular approach for prediction tasks. Objective of this study is to compare the predictive performance of regression methods and tree-based ML methods for zero-inflated claim frequency data using a real insurance dataset. Motor third party liability insurance claim data from an insurance company in Turkey is used for the case study. To predict claim frequency, generalized linear models (GLM), zero-inflated model and hurdle model are used under Poisson distribution as regression models and regression trees, boosting and GLM-Boost that is a combination of GLM and Boosting algorithm are used as ML methods. Predictive performances of candidate models are compared using both average in-sample and average out-of-sample losses. According to the case study results, ML methods performed better predictive performance than zero-modified models. Specially, GLM-Boost method performed best among others and that is a promising result for the approaches that are combinations of GLM and ML methods.

© 2023 DPU All rights reserved.

Keywords: non-life insurance, claim frequency, zero-inflated data, machine learning, predictive modeling

1. Introduction

Actuarial pricing methods in non-life insurance is generally based on generalized linear models due to the ease of implementation and interpretation. Beside the practical usage, GLMs assume a linear relationship between the transformed response and explanatory variables on the basis of link function, need an exponential dispersion family distribution for the response variable, has sensitivity to multicollinearity and don't take into account interactions and

non-linear relationships. Also, GLMs may struggle with high-dimensional data with regards to matrix operations in maximum likelihood estimation. Because of these drawbacks, machine learning methods become popular since they can handle interactions and non-linearities automatically, can control overfitting, have flexibility with data types and are generally robust to outliers. Due to the data driven property of insurance business, machine learning methods became popular also for insurance data modelling in recent years [1-5]. Wuthrich and Buser [1] use various ML methods including regression trees, ensemble methods and neural networks for claim frequency data. Liu et al. [2] compare the predictive performance of AdaBoost algorithm with GLM, neural network and support vector machines to predict claim frequency. Dal Pozzolo [3] used various ML methods to estimate claims in Kaggle competition. Noll et al. [4] used GLM, regression trees, boosting, GLM-Boost and neural network methods to predict claim frequency data. Clemente et al. [5] compared GLM and gradient boosting model for claim frequency data.

Classification and regression trees are simple and visually practical methods that provide basis for other ML methods such as boosting. Boosting is an iterative ensemble learning method that is a combination of many weak learners such as regression trees. For the predictive purposes, boosting algorithm performs well due to the iterative process that combines weak learners into a strong learner by minimizing error. Various boosting algorithms are used to estimate both claim frequency and claim severity data [2, 6-9]. All these studies emphasise the promising performance of boosting algorithms for claim data modelling. In recent years, combination of ML algorithms and traditional methods is also popular for predictive issues in insurance data [1, 4]. One of these methods is GLM-Boost [4] that is a combination of GLM and boosting algorithm.

From the other side, main characteristic of motor insurance claim data is excess zeros due to the No Claim Discount (NCD) system and deductible modification. Policyholders don't report low-cost claims not to pay over-premium in the next policy year or when the claim size is below the deductible amount. Zero-inflated and hurdle models are popular for imbalanced data that is frequently observed property in insurance [10, 11]. Those zero-modified methods are used as an alternative to GLMs for zero-inflated claim frequency data [12, 13].

In this study, we aim to compare predictive performance of traditional GLM, zero-inflated model, hurdle model, regression trees, boosting and GLM-Boost approach for the prediction of a zero-inflated motor insurance claim frequency data. Different from other studies in the literature, zero-inflated and hurdle models are compared with tree-based ML methods for zero-inflated claim frequency data in this study.

In the second part of the paper, statistical methods are summarized, in the third part, dataset is explained and the statistical analysis is performed. The paper ends with the conclusion part.

2. Statistical Models

2.1. Generalized linear models

Generalized linear models are purposed by Nelder and Wedderburn [14]. The distribution of response variable in GLMs can be any distribution from exponential family and the mean of response variable can be a linear function of explanatory variables on different scales depending on the link function.

For $i = 1, 2, \dots, n$ let N_i be the number of claims of policy i . Under GLM, N_i 's are assumed to be independent. Mean function of N_i is defined as,

$$E(N_i) = h^{-1}(\mathbf{x}'_i \boldsymbol{\beta}) \quad (1)$$

where \mathbf{x}'_i and $\boldsymbol{\beta}$ are the vector of covariates and the vector of regression coefficients respectively. $h(\cdot)$ is the link function that specifies the relation between the linear predictor and the response variable.

Under Poisson assumption, distribution of N_i is defined as,

$$N_i \sim Poi(\lambda(x_i) v_i) \tag{2}$$

where, $\lambda(x_i)$ is the regression function and v_i is the exposure for policy i .

2.2. Zero-inflated and hurdle models

Zero-inflated and hurdle models are used to model datasets that have excess zeros. Zero-inflated models are mixed models that consist of a point mass at zero and a positive count distribution. Hurdle models are the combinations of left-truncated count and right-censored hurdle components [15].

Let the probability of observing zero and the probability density function of counts are denoted by π and $f_2(n)$ respectively. Probability function of zero-inflated distribution is defined as,

$$P(N = j) = \begin{cases} \pi + (1 - \pi)f_2(0), & j = 0 \\ (1 - \pi)f_2(j), & j > 0 \end{cases} \tag{3}$$

In hurdle model, let the probability of observing zero is denoted by $f_1(0)$. Probability of observing j claims with hurdle model is defined as follows [16],

$$P(N = j) = \begin{cases} f_1(0), & j = 0 \\ \frac{1-f_1(0)}{1-f_2(0)} f_2(j), & j > 0 \end{cases} \tag{4}$$

2.3. Regression trees

Regression trees are the popular non-parametric, simple and flexible methods for regression tasks. The objective is to construct trees in a way that feature space is partitioned into homogenous subsets. For the partitioning, binary tree growing algorithm can be used. The algorithm is repeated until a stopping rule is applied. For the goodness of binary splits, optimal split is chosen such that deviance loss is minimized. Regression trees are the fundamental methods for other ensemble algorithms that rely on iterative process such as boosting.

Let's assume that there are p explanatory variables and we will split data into M regions (R_1, R_2, \dots, R_M) . In each region, claim frequency parameter is λ_m . So, expected frequency is,

$$\hat{\lambda}(x) = \sum_{m=1}^M \hat{\lambda}_m I(x \in R_m) \tag{5}$$

If we minimize the sum of squares of the difference between the responses and predictions, $\hat{\lambda}_m$ is the average of response in region R_m [17]. For more details about classification and regression trees we refer [1].

2.4. Boosting

In boosting method, forward stage-wise algorithm of Friedman [18] is applied to solve optimization problem by fitting weak learners and adding it to the previous fitted terms sequentially. We try to find optimal parameters by adaptively minimizing loss function in each iteration adding a weak learner to the present predictor. This algorithm is called gradient boosting machine. In our case, weak learners are the regression trees and the objective is to minimize Poisson deviance.

Assume that $L(.)$ is the objective function and we try to minimize in-sample loss over class of functions f given as,

$$\hat{f} = \underset{f}{\operatorname{argmin}} \frac{1}{n} \sum_{i=1}^n L(N_i, f(\mathbf{x}_i), v_i) \quad (6)$$

Let $\hat{f}_{m-1}(\cdot)$ be the minimizer of Eq. (6) and $\hat{g}_m(\mathbf{x})$ is a regression model that acts as base learner in the algorithm. If we define working weights,

$$w_i^{(m)} = v_i e^{\hat{f}_{m-1}(\mathbf{x}_i)} \quad (7)$$

and f functions as the logged frequency ($\log \lambda$), the steps of Poisson regression tree boosting machine with logarithmic link function are given as follows,

1. Choose a constant shrinkage parameter, $\alpha \in (0,1]$. This parameter makes weak learner even weaker.
2. Calculate $\hat{f}_0(\mathbf{x}) = \log \hat{\lambda}_0(\mathbf{x}) = \log \left(\frac{\sum_{i=1}^n N_i}{\sum_{i=1}^n v_i} \right)$
3. For $m=1,2,\dots,M$ repeat,
 - a) Calculate working weights, $w_i^{(m)}$
 - b) Fit a Poisson regression tree to working data (learning dataset)
 - c) Update: $\hat{f}_m(\mathbf{x}) = \hat{f}_{m-1}(\mathbf{x}) + \alpha \hat{g}_m(\mathbf{x})$
4. Obtain the estimator, $\hat{f}(\mathbf{x}) = \hat{f}_M(\mathbf{x})$ [1]

2.5. GLM-Boost

In this method, optimal GLM estimates are used as initial values ($\hat{f}_0(\mathbf{x})$) that is set into the exposure of the boosted regression trees and then boosting algorithm is processed iteratively [4].

3. Case Study

In this study, objective function is the average Poisson deviance loss function that is defined as follows,

$$L(D, \hat{\lambda}) = \frac{1}{n} \sum_{i=1}^n 2N_i \left[\frac{\lambda(\mathbf{x}_i) v_i}{N_i} - 1 - \log \left(\frac{\lambda(\mathbf{x}_i) v_i}{N_i} \right) \right] \geq 0 \quad (8)$$

where D is training data set. We try to minimize this loss function that provides maximum likelihood estimate of λ [4]. For test dataset, we put T instead of D in Eq.(8).

3.1. Data set

Dataset consists of information related to motor third party liability insurance, started/renewed in years 2009-2012. Dataset is taken from a private insurance company in Turkey. Only the policies of private automobiles are taken into account. Response variable is the number of claims in one policy year.

Risk factors do not change during the policy period. For each policy, we have information about policy number, novation number, rider number, rider type, policy year, province where vehicle is registered, no claim discount (ncd) code, age of vehicle, age and gender of policyholder, cubic capacity of vehicle, previous claim number of policy and binary code that indicates whether policy has just started (new) or not (old). Exposure is calculated using policy number and rider numbers in one accounting year. One policy number belongs to only one year, repeated information of the same policy in unknown since policy number changes in each renewal process. Any deductible modification is

not applied in these policies. We made an exposure based calculation of correction factors for each accident quarter, using the Bornhuetter-Ferguson and Cape-Cod methods and multiplied those factors with the observed claim numbers to prevent distortion due to the reporting process.

Provinces are clustered into seven regions where clusters are generated using *k*-means clustering algorithm based on the 2010 year accident statistics of accident numbers, death numbers and injured party numbers for each province. Accident statistics are taken from the web site of Turkish Statistical Institute.

In preliminary analysis of data, we observed some values for age of driver, age of vehicle and previous claim number were pointless. So, we assumed upper limit of 90 for the age of driver, 50 for the age of vehicle and 5 for the previous claim number. All analyses of case study are performed using R Studio software, version 4.3.0.

There are 1,246,990 automobile insurance policies between the years 2009-2012. Explanatory variables are given below,

- Policy year (*year*)
- Previous claim number (*prev_cnum*), number of claim that occurred in previous policy year
- Age of driver (*age*),
- Age of vehicle (*ageveh*)
- Cubic capacity of vehicle (*cc*)
- No claim discount (*ncd*) level of policy, categorical variable with 7 levels where 4 is entrance level, 7 is highest discount and 1 is highest over premium level.
- Region, cluster of provinces where the vehicle is registered. Categorical with 7 levels
- Gender of policyholder, binary variable
- New_old, binary variable that indicates whether the policy is new or renewed (old). (new:0, old:1)

Statistics of continuous features, exposure and claim numbers are given in Table 1,

Table 1. Summary statistics of continuous features, exposure and claim numbers

	Age of policyholder	Age of vehicle	Cubic capacity	Year	Prev_cnum	Exposure	Claim number
Min	18	0	0	2009	0	0.0027	0
Median	42	13	1600	2011	0	1	0
Mean	43.31	13.13	1555	2011	0.0264	0.8317	0.0661
Max	90	50	7000	2012	5	1	8

Data is highly zero inflated since the median value of claim number is zero. Mean exposure value is close to one that shows most of the policies are in force for the whole policy year. Histogram of claim numbers is given in Figure 1. In accordance with Table 1, we see that data has a highly zero-inflated structure.

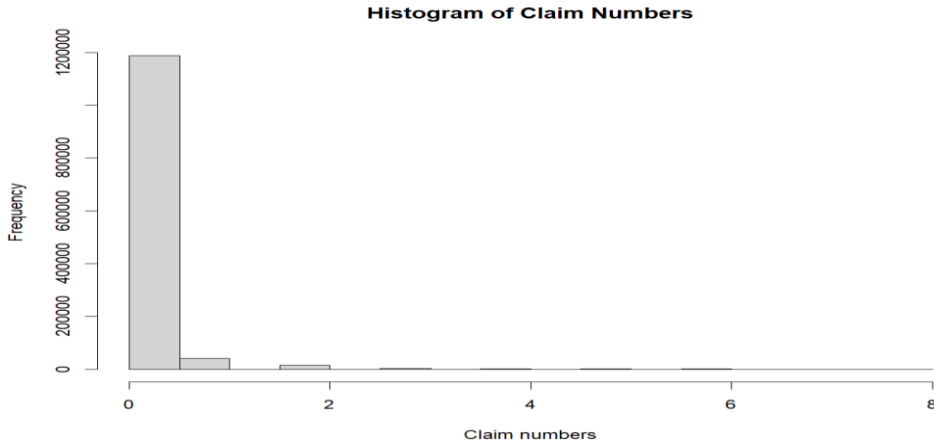


Figure 1. Histogram of claim numbers

Number of policies in each level of categorical variables are given in Table 2,

Table 2. Policy numbers in levels of categorical features

<u>Gender</u>						
Female			Male			
172,264			1,074,726			
<u>New old</u>						
New			Old			
931,168			315,822			
<u>Ncd</u>						
1	2	3	4	5	6	7
1,257	7,499	23,933	452,874	214,223	157,528	389,676
<u>Region</u>						
0	1	2	3	4	5	6
165,754	258,567	93,757	261,859	189,234	84,586	193,233

Most of the policy holders are male, are new in the system, have entrance ncd level (4) and from Region 3. Claim frequency of general portfolio is 0.0795 that is an indication of zero-inflation.

Dummy coding is applied for categorical variables and chose reference level that has the biggest volume. To test the collinearity between the variables we calculated Pearson’s correlation coefficients for continuous features and Cramer’s V measures for categorical variables are given in Table 3 and Table 4.

Table 3. Pearson’s correlation coefficients

	Year	Prev_cnum	Age	Ageveh	Cc
Year	1	0	0.08	0.03	0.02
Prev_cnum	0	1	0	-0.01	0
Age	0.08	0	1	0.11	-0.02

Ageveh	0.03	-0.01	0.11	1	-0.03
Cc	0.02	0	-0.02	-0.03	1

Table 4. Cramer’s V measures

	Region	Ncd	Gender	New_old
Region	1	0.0397	0.0793	0.0603
Ncd	0.0397	1	0.0215	0.4270
Gender	0.0793	0.0215	1	0.0046
New_old	0.0603	0.4270	0.0046	1

Based on correlation coefficients, there is a high correlation between ncd level and new_old status of policies and a slight correlation between the age of driver and the age of vehicle. For now, we will use all the features in the models.

3.2. Analysis

We fit Poisson GLM by assuming the age of driver, age of vehicle and the cubic capacity both continuous and categorical while other features are same in the models. We compared results based on AIC and the significance of the variables. In each case, variables are significant at 95% significance level but AIC is smaller when the variables are categorical. As a result, we used these three variables categorical in regression models. Categories are binned as follows:

Cubic capacity, with 3 levels [0-1300], (1300-1600), (1600-7000]

Age of driver, with 6 levels [18,25], (25,30], (30,40], (40,50], (50,70], (70,90]

Age of vehicle, with 5 levels [0,1], (1,5], (5,10], (10,20], (20,50]

We applied dummy coding for categorical variables. Design matrix has full rank under dummy coding and this means linearly independence of columns [19]. To compare the predictive performance of candidate models, dataset is partitioned into two parts, training dataset (80%) and the test dataset (20%). In-sample loss is calculated on training data set while out-of-sample loss is calculated on test data set using Eq. (8). Reason of using deviance loss function is that this loss function evaluated on a different test dataset provides a good predictive performance indicator [4].

First model is GLM under Poisson distribution with logarithmic link function. We used all explanatory variables in Poisson GLM only taking into account main effects. We call this model as *GLM1*. According to the model results, new_old was not statistically significant with p-value 0.5261. Analysis of deviance table is given in Table 5,

Table 5. Anova results of GLM1

	Df	Deviance	Resid. Df	Resid. Dev
Null			997591	407221
ageglm	5	1824	997586	405396
agevehglm	4	1101	997582	404295
cc	2	188	997580	404106
gender	1	86	997579	404020
region	6	2425	997573	401594
ncd	6	4370	997567	397223
new_old	1	0	997566	397223
prev_cnum	1	197	997565	397026
year	1	7	997564	397019

A decrease in residual deviance from a simple model to a complex model indicates that the additional parameters provide a better fit. Based on deviance results, new_old variable is excluded from the model since there is no difference in residual deviance after new_old variable is added to the model. Summary of refitted model without new_old (GLM2) is given in Table 6,

Table 6. Results of GLM2

Parameter	Estimate	Std. Error	z value	Pr(> z)
Intercept	17.5549	7.5406	2.3280	0.0199
ageglm1	0.3402	0.0173	19.6990	< 2e-16
ageglm2	0.1599	0.0128	12.4940	< 2e-16
ageglm4	0.0259	0.0105	2.4660	0.0136
ageglm5	-0.0608	0.0111	-5.4840	0.0000
ageglm6	-0.0785	0.0297	-2.6410	0.0083
agevehglm1	0.1418	0.0165	8.5850	< 2e-16
agevehglm2	0.1281	0.0113	11.2870	< 2e-16
agevehglm3	0.0516	0.0108	4.7890	0.0000
agevehglm5	-0.0436	0.0126	-3.4590	0.0005
cc1	-0.1138	0.0150	-7.5660	0.0000
cc2	-0.0300	0.0120	-2.4970	0.0125
gendermale	-0.0738	0.0108	-6.8610	0.0000
region1	-0.5689	0.0133	-42.8340	< 2e-16
region2	-0.7020	0.0196	-35.7280	< 2e-16
region3	-0.3588	0.0125	-28.7530	< 2e-16
region4	-0.3691	0.0136	-27.1010	< 2e-16
region5	-0.1587	0.0162	-9.7980	< 2e-16
region6	-0.4954	0.0139	-35.6550	< 2e-16
ncd1	0.2658	0.0816	3.2560	0.0011
ncd2	-0.1077	0.0443	-2.4290	0.0151
ncd3	-0.0877	0.0259	-3.3840	0.0007
ncd5	-0.2886	0.0109	-26.4110	< 2e-16
ncd6	-0.4449	0.0130	-34.2660	< 2e-16
ncd7	-0.6396	0.0106	-60.1430	< 2e-16
prev_cnum	0.3003	0.0203	14.7890	< 2e-16
year	-0.0096	0.0038	-2.5720	0.0101

According to GLM results, all features are statistically significant at 95% confidence level. Mean claim frequency is decreasing after driver's age 50, vehicle's age 20 and at lower cubic capacity when compared to the base level. Claim frequency is higher in female drivers than males and in region 0. While previous claim number increases the claim frequency, policy year has a decreasing effect on it. Comparison of two GLMs based on loss values and AICs is given in Table 7.

Table 7. In-sample losses, out-of-sample losses and AIC values of GLMs

Model	Average in-sample loss	Average out-of-sample loss	AIC
GLM1	0.3979	0.4011	501404
GLM2	0.3979	0.4011	501403

There is not a significant difference based on in-sample and out-of-sample loss of two GLMs. According to AIC values *GLM2* performs better with a small difference. To compare other methods, we use same explanatory variables, *new_old* variable is excluded.

3.2.1. Zero-inflated and hurdle Poisson model

Due to the excess zero structure of claim numbers, we fit both zero-inflated Poisson (ZIP) and hurdle Poisson model to claim numbers. Logistic regression is used for the zero component of the models. First, for the ZIP model, we assumed the probability of excess zero part is independent of exposure and did not use exposure in logit part. Then exposure is used in both parts of the model. Average losses are lower when exposure is used only in count part. Similar with ZIP model, we used exposure only in Poisson part of hurdle model. Average in-sample and out-of-sample losses of models are given in Table 8,

Table 8. Average in-sample and out-of-sample losses of zero-modified models

Model	Average in-sample loss	Average out-of-sample loss
ZIP	0.3980	0.4010
Hurdle Poisson	0.4047	0.4074

Based on average losses, ZIP model shows better predictive performance than the hurdle model. Hurdle model may not capture the complex structure of excess zeros as effective as the zero-inflated model since zero-inflated models incorporate a separate process for zeros. Average portfolio frequencies of predicted claim numbers from ZIP is 0.0794 and hurdle model is 0.0761. In accordance with prediction performances, hurdle model underestimates average portfolio frequency.

3.2.2. Regression trees

We did not make any feature pre-process for regression trees but used age of driver, age of vehicle and the cubic capacity as continuous variables. 5000 policies are assumed at each leaf of the tree. We also fitted tree with 10000 policies at each leaf but deviances were higher. According to the analysis results, optimal cost complexity (cp) parameter that controls the size of the tree is 0.01. We call this regression tree with cp 0.01 as *RT1*. To be an alternative, we also fitted tree with cp=0.00001 value (*RT2*) since smaller cp value provides a larger tree. Average in-sample and out-of-sample loss values are given in Table 9,

Table 9. Average in-sample and out-of-sample losses of regression trees

Model	Average in-sample loss	Average out-of-sample loss
RT1 (cp=0.01)	0.4036	0.4061
RT2 (cp=0.00001)	0.3971	0.4009

According to the model results, when cp is smaller (0.00001), tree is constructed on all explanatory variables except previous claim number. When cp is 0.01, the tree is constructed on only *ncd* level of policy. We can conclude that regression trees perform better predictive performance when they have larger cp value that provides larger tree and more features.

3.2.3. Boosting and GLM-Boost methods

We used regression trees as weak learners for boosting. Similar to regression trees, we assumed cp parameter 0.0001, 50 iterations for the construction of weak learners and 5000 policies at each leaf of the tree. We did not apply shrinkage in the boosting algorithm. We choose depth of the tree as $J=2$ (*Boost2*) and $J=3$ (*Boost3*), that shows the number of levels from the root node to a leaf node. Average loss values of both boosting methods are given in Table 10,

Table 10. Average in-sample and out-of-sample losses of boosting algorithms

Model	Average in-sample loss	Average out-of-sample loss
Boost2 (J=2)	0.3966	0.4001
Boost3 (J=3)	0.3956	0.4000

We can say that predictive performance of boosting algorithm increases when the depth of the tree is higher.

In *GLM-Boost* methods, estimates of *GLM2* model are used as initial values that is set into the exposure of the boosted regression trees. Under the same parameters with *Boost3*, at the end of 50th iteration, average in-sample loss is **0.3955** and out-of-sample loss is **0.3999** that are the smallest loss values among all candidate models. These results support the combination of GLM and boosting approach that iteratively improves the predictive performance of the model is a good alternative for the prediction purposes. In this approach, parameter estimates of best performing GLM are set into the exposure of the regression trees and boosting algorithm works. Combining optimal initial values from GLM and a strong boosting algorithm improves the predictions.

Since average out-of-sample loss is calculated using test data, it is the main indicator for the prediction when compared with in-sample loss. To sum up, average out-of-sample loss of Poisson GLM, ZIP, regression trees and boosting methods are given in Table 11. Although data has a zero-inflated structure, machine learning methods based on regression trees, perform better predictive performance than zero-inflated model. Specially, GLM-Boost approach that combined GLM and boosting is a promising point for the future studies that combine traditional and machine learning methods.

Table 11. Average out-of-sample losses of candidate methods

Model	Average out-of-sample loss
GLM2	0.4011
ZIP	0.4010
RT2	0.4009
Boost3	0.4000
GLM-Boost	0.3999

To see the similarity between the observed claim numbers and predicted (test data) ones, we give statistics in Table 12.

Table 12. Statistics of observed and predicted claim numbers

Model	Min	Median	Mean	Max
Observed	0.00000	0.00000	0.06660	8.00000
GLM2	0.00009	0.06164	0.06603	0.42789
ZIP	0.00009	0.06199	0.06611	0.35541
RT2	0.00009	0.06257	0.06604	0.20690

Boost3	0.00008	0.06062	0.06601	0.45123
GLM-Boost	0.00007	0.06064	0.06605	0.43006

Because of zero-inflated structure of the data set, predictions have distribution around zero. Predictions of each model have mean value close to the mean of observed claim numbers. In general, we can say that the predictions of different models have similar values and that supports the small differences between the average loss values of the models.

4. Conclusion

In this study, we compared the predictive performances of GLM, zero-modified models, regression trees and two boosting approaches using a zero-inflated claim frequency data. Main result of this study is, boosted regression trees and GLM-Boost performed better than both zero-inflated Poisson and hurdle Poisson model in addition to Poisson GLM based on average in-sample and average out-of-sample losses. These results are in accordance with the studies in the literature in that tree-based ML methods (specially boosting) show better predictive performance for claim data when compared with GLM [4, 5]. Although GLMs are easy to implement and interpret, steps such as feature pre-processing, feature selection, interactions affect the predictive performance of the model. Instead, ML methods provide flexibility for these processes and handle interactions and non-linearities automatically. When the predictive accuracy is the subject, ensemble methods provide a good choice since they combine predictions from learners that reduce overfitting and variance. As an ensemble method, boosting strengthens the predictions by sequentially fitting weak learners that are regression trees in this study. GLM-Boost that showed best predictive performance is applied by boosting GLM with regression trees. This approach is a simple example for the combination of a classical regression model and a machine learning method. This type of combinations look bright for the predictive purposes of actuarial data. As a future work, combination of neural networks with a classical regression model can be used to predict claim data [20]. Also, approaches that combine zero-inflated models with boosting can be used to predict imbalanced claim frequency data [21].

A statistical method that shows good predictive performance on a data, may not show the same performance on a different dataset. Additively, average loss values between the predictive models have small differences due to the zero-inflated structure of the data in this study. So, it may be a good idea to perform related models on different datasets that don't have imbalanced distribution and to predict different response variables such as claim amount or probability of a claim.

Acknowledgements

I would like to thank Ronald Richman (actuary) for all his support on the analysis and other theoretical questions.

References

- [1] M. V. Wuthrich and C. Buser, "Data analytics for non-life insurance pricing," *Swiss Finance Institute Research Paper*, no. 16-68, 2023.
- [2] Y. Liu, B.-J. Wang, and S.-G. Lv, "Using multi-class AdaBoost tree for prediction frequency of auto insurance," *Journal of Applied Finance and Banking*, vol. 4, no. 5, p. 45, 2014.
- [3] A. Dal Pozzolo, G. Moro, G. Bontempi, and D. Y. A. Le Borgne, "Comparison of data mining techniques for insurance claim prediction," *Universita degli Studi di Bologna*, 2011.
- [4] A. Noll, R. Salzmann, and M. V. Wuthrich, "Case study: French motor third-party liability claims," *Available at SSRN 3164764*, 2020.
- [5] C. Clemente, G. R. Guerreiro, and J. M. Bravo, "Modelling Motor Insurance Claim Frequency and Severity Using Gradient Boosting," *Risks*, vol. 11, no. 9, p. 163, 2023.
- [6] A. Ferrario and R. Hämmerli, "On boosting: Theory and applications," *Available at SSRN 3402687*, 2019.
- [7] L. Guelman, "Gradient boosting trees for auto insurance loss cost modeling and prediction," *Expert Systems with Applications*, vol. 39, no. 3, pp. 3659-3667, 2012.

- [8] R. Henckaerts, M.-P. Côté, K. Antonio, and R. Verbelen, "Boosting insights in insurance tariff plans with tree-based machine learning methods," *North American Actuarial Journal*, vol. 25, no. 2, pp. 255-285, 2021.
- [9] B. So, "Enhanced gradient boosting for zero-inflated insurance claims and comparative analysis of CatBoost, XGBoost, and LightGBM," *Scandinavian Actuarial Journal*, pp. 1-23, 2024.
- [10] P. Zhang, D. Pitt, and X. Wu, "A new multivariate zero-inflated hurdle model with applications in automobile insurance," *ASTIN Bulletin: The Journal of the IAA*, vol. 52, no. 2, pp. 393-416, 2022.
- [11] I. N. El-Saeiti and G. Alomair, "Comparative Evaluation of Zero-Inflated and Hurdle Models for Balanced and Unbalanced Data: Performance Assessment and Model Fit Analysis," *European Journal of Science, Innovation and Technology*, vol. 3, no. 6, pp. 192-199, 2023.
- [12] K. C. Yip and K. K. Yau, "On modeling claim frequency data in general insurance with extra zeros," *Insurance: Mathematics and Economics*, vol. 36, no. 2, pp. 153-163, 2005.
- [13] J.-P. Boucher, M. Denuit, and M. Guillén, "Risk classification for claim counts: a comparative analysis of various zeroinflated mixed Poisson and hurdle models," *North American Actuarial Journal*, vol. 11, no. 4, pp. 110-131, 2007.
- [14] J. A. Nelder and R. W. Wedderburn, "Generalized linear models," *Journal of the Royal Statistical Society Series A: Statistics in Society*, vol. 135, no. 3, pp. 370-384, 1972.
- [15] J. Mullahy, "Specification and testing of some modified count data models," *Journal of econometrics*, vol. 33, no. 3, pp. 341-365, 1986.
- [16] A. Zeileis, C. Kleiber, and S. Jackman, "Regression models for count data in R," *Journal of statistical software*, vol. 27, no. 8, pp. 1-25, 2008.
- [17] T. Hastie, R. Tibshirani, J. H. Friedman, and J. H. Friedman, "The elements of statistical learning: data mining, inference, and prediction". Springer, 2009.
- [18] J. H. Friedman, "Greedy function approximation: a gradient boosting machine," *Annals of statistics*, pp. 1189-1232, 2001.
- [19] M. V. Wüthrich and M. Merz, "Statistical foundations of actuarial learning and its applications". Springer Nature, 2023.
- [20] M. V. Wüthrich and M. Merz, "Yes, we CANN!," *ASTIN Bulletin: The Journal of the IAA*, vol. 49, no. 1, pp. 1-3, 2019.
- [21] S. C. Lee, "Addressing imbalanced insurance data through zero-inflated Poisson regression with boosting," *ASTIN Bulletin: The Journal of the IAA*, vol. 51, no. 1, pp. 27-55, 2021.



Contents lists available at Dergipark

Journal of Scientific Reports-A

journal homepage: <https://dergipark.org.tr/tr/pub/jsr-a>



E-ISSN: 2687-6167

Number 59, December 2024

RESEARCH ARTICLE

Receive Date: 20.12.2024

Accepted Date: 30.12.2024

Investigation of glass fiber reinforced aluminum honeycomb panel repair performance according to aviation standards

Akın Çallı^{a,*}, Orkun Tunçkan^b

^aEskişehir Technical University, Institute of Graduate Studies, Department of Airframe and Powerplant Maintenance, Eskişehir 26480, Türkiye, ORCID: 0009-0003-7003-8741

^bEskişehir Technical University, Faculty of Aeronautics and Astronautics, Eskişehir 26480, Türkiye, ORCID: 0000-0002-5357-5110

Abstract

Aluminum honeycomb structures are widely used in aviation and aerospace engineering designs due to their high strength/density properties. Although they are resistant to atmospheric conditions and acceptable impacts, they can suffer from corrosion and mechanical damage in some cases. This damage that occurs over time can affect the structural integrity and maintenance-repair process, which in turn can affect the safety and service life of this material. In this study, a different repair technique was tried by giving artificial damage to aluminum honeycomb structures. Repair procedures were carried out in accordance with the maintenance protocols of the manufacturing companies in order to restore the original strength properties of the material. After the repair, various non-destructive testing (NDT) methods, such as visual inspection and ultrasonic testing, were employed to inspect for discontinuities. A bending test was subsequently conducted to evaluate the material's strength, and the results were analyzed. The bending test results indicate that the repaired structures exhibited structural integrity close to their pre-damage state. The results of this study demonstrate that the repaired aluminum honeycomb structures achieved strength levels comparable to the original, undamaged material, meeting aviation industry standards. This highlights the effectiveness and reliability of the developed repair methods for ensuring safety and functionality in aerospace applications.

© 2023 DPU All rights reserved.

Keywords: Honeycomb composite, Aviation material, Glass-fibre reinforced, Aluminum honeycomb.

1. Introduction

The main reason for using composite materials in the aviation industry is to reduce the weight of the aircraft and save fuel. However, composites used in aviation industries have important advantages such as superior corrosion resistance, durability, high temperature tolerance and reduced maintenance requirements, in addition to their lightness.

Since aircraft are often exposed to harsh atmospheric conditions, it is necessary to use materials that are resistant to temperature fluctuations, corrosion and corrosive substances. Honeycomb composites, which are the subject of this study, perform well under such extreme conditions, thus increasing the safety of aircraft structures and extending their operational life [1-6]. The integration of composite materials into aircraft structures has led to transformative advances in design methodologies. Traditional metallic materials require a significant number of fasteners (e.g. bolts and rivets) for assembly, creating significant problems such as increased weight and long production processes. In contrast, composites allow large, geometrically complex components to be manufactured in one piece. Therefore, the need for numerous joints is reduced. Thus, assembly processes are accelerated and structural fit and integrity are ensured. In addition, flight performance is increased because honeycomb structures provide superior aerodynamic properties [7,8]. Another advantage of composite materials is their potential to mitigate the environmental impact associated with aviation. Given the significant contribution of the sector to global carbon emissions, achieving sustainability goals is imperative. At this point, composite materials significantly reduce fuel consumption and therefore carbon emissions by reducing the total weight of the aircraft [9-11].

One of the main reasons for the adoption of composite materials in aviation is that the desired matrix and reinforcement material can be selected during the production process. At the same time, the form of the fiber material can be selected, and structural composites such as honeycomb can be preferred when it is necessary. Therefore, appropriate optimization can be made by taking into account the relevant parameters in the entire production process. For example, multilayer honeycomb composite structures can be designed to exhibit distinct mechanical properties in different areas of an aircraft. Thus, while weight is reduced for non-critical areas, specially designed reinforced structures provide increased strength in parts exposed to high stress. This versatility and depth of possibilities allow aerospace engineers not only to optimize the use of composites such as honeycomb effectively but develop superior structural designs as well [12-17]. However, there are also some disadvantages of composite materials in aviation. For instance, include complex manufacturing processes, high costs, technical difficulties associated with maintenance and repair. In particular, damage detection and repair for composites are more complex and time consuming compared to traditional metallic materials. cFor this reason, it is aimed to increase the flight performance of glass fiber reinforced aluminum honeycomb panels used in aircraft by developing new, fast and efficient maintenance processes [18,19].

1.1. Honeycomb Composite

Honeycomb sandwich composites based on the inherent features of composite materials is subclass out of regular and periodic hexagonal repeating unit cell configuration being the hallmark of cellular materials. The design of materials are designed specifically to fit the particular context in which material is used for. Key factors to consider are corrosion, creep performance, stiffness, strength, fatigue resilience, low mass characteristics and cost. For applications that are very mission critical such as weight be as little in any case the use of flat layers of thin would lead to local buckling.

Honeycomb sandwich composites are widely utilized in structural applications requiring a combination of high strength and low weight. These composites consist of two thin, stiff, and strong outer layers that primarily bear the applied loads. These outer layers are bonded to a relatively thicker, low density core structure positioned between them, with an adhesive layer ensuring the structural integrity of the assembly. Figure 1 provides a schematic representation of a typical composite sandwich structure [20,21].

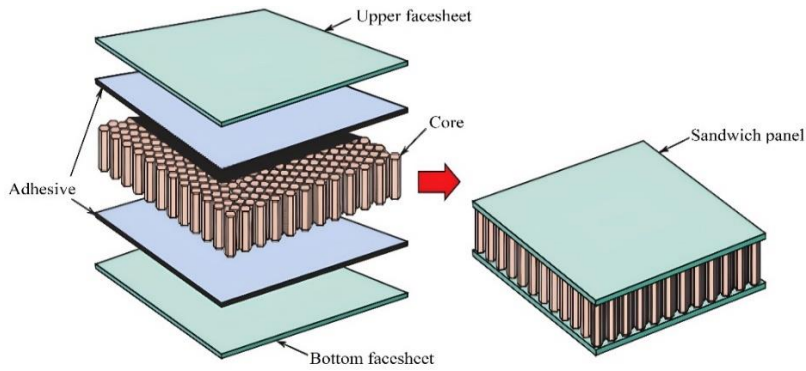


Fig. 1. A general representation of composite sandwich structures.

Composite sandwich structures exhibit outstanding mechanical properties, including low density, a high strength to weight ratio, excellent corrosion resistance and energy absorption capabilities. These advantages make honeycomb structures highly versatile and widely applicable across various engineering disciplines, particularly in the aerospace and marine industries. Due to their anisotropic nature, the mechanical properties of honeycomb structures vary along the three principal directions, as shown in Figure 2 (T, L, and W). In hexagonal configurations, the T direction (through thickness direction) exhibits the highest compressive and tensile strengths, making it the preferred direction for load bearing applications. Conversely, the L (longitudinal) and W (width) directions provide superior shear strength, with the L direction offering greater shear strength and shear modulus compared to the W direction. The cell size in honeycomb structures is the distance between parallel sides of the hexagonal cells. This parameter plays a huge role in the mechanical properties of the structure, as it is the material density and stiffness [22].

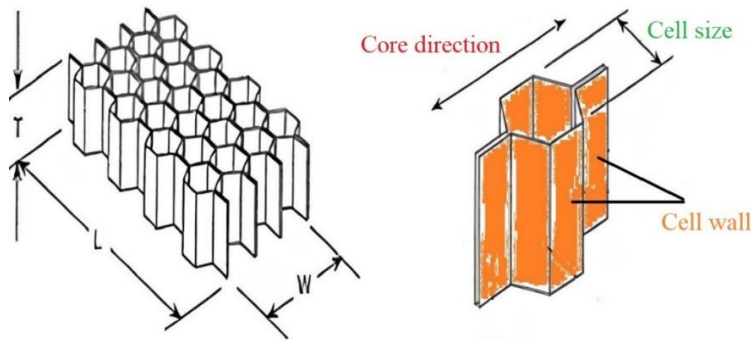


Fig. 2. A general representation of honeycomb core structures.

The face sheets are the outermost layers of sandwich composite structures and they determine all kinds of aspects. The layers are mostly fabricated using a composite of hyper materials. It is shaped to be resistant to bending, shear loading and specific face sheet materials that comprise carbon epoxy, aramid epoxy and glass epoxy for their tailored mechanical properties and matching for the expected operational environment. The sandwich core of a sandwich structure serves not only as the primary load bearing section but is also very important for supporting face sheets fastening. In aerospace, core materials such as aluminum alloys, aramid fibers, nomex honeycomb and high strength alloys of the metal are most commonly used.

The principal advantage of sandwich structures lies in their exceptional contribution to weight reduction, which is

critical in aerospace applications. Figure 3 illustrates a comparison of the strength and stiffness ratios across various sandwich structures. Notably, the structure on the far right demonstrates 37 times greater stiffness and 7 times higher flexural strength compared to a solid aluminum plate, while weighing only 9% of the plate's mass [23,24].

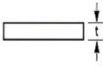
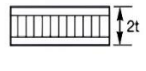
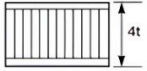
	Core	Core (t) + facesheet (t)	Core (3t) + facesheet (t)
			
Relative stiffness	1	7	37
Relative bending strength	1	3,5	9,2
Relative weight	1	1,03	1,06

Fig. 3. The strength and stiffness ratios of various sandwich structures.

2. Experimental Study

With advancements in aviation technology, new materials, devices, methods and techniques are continuously being developed. In this study, aluminum honeycomb panels widely used as primary structural materials in commercial aircraft and procured from maintenance and repair organizations were utilized. As depicted in Figure 4, the sandwich structure employed in this experiment consists of an aluminum alloy core with a surface coating made of glass fiber reinforced epoxy. The main material used in the study is identified as BMS 4-23 TYPE II, comprising a core made of aluminum alloy 5424 and surface coatings of glass fiber reinforced epoxy.

The 5000 series aluminum alloys, commonly referred to as aluminum-magnesium (Al-Mg) alloys, incorporate magnesium as their primary alloying element. These alloys are known for their medium strength, excellent formability, weldability and corrosion resistance, making them suitable for various aerospace applications. Glass fiber, characterized by high corrosion resistance, liquid impermeability, lightweight properties and good mechanical strength, is widely used in applications such as passenger floor panels and cargo floor panels, where materials must withstand high traffic and load conditions.

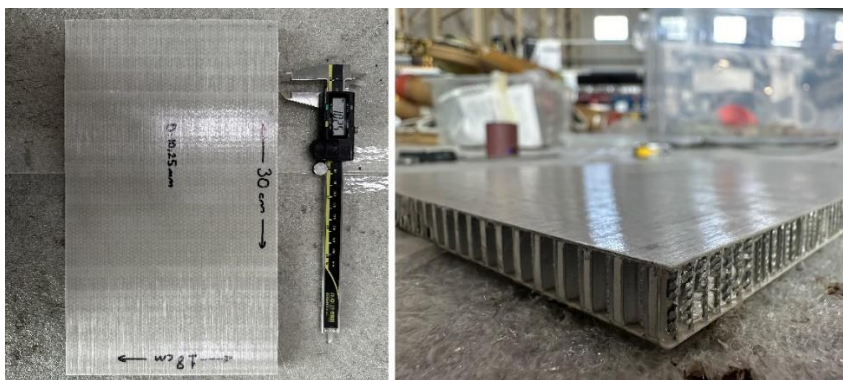


Fig. 4. A sample sandwich structure, featuring an aluminum alloy core, is constructed with glass fiber reinforced epoxy.

2.1. Artificial Damage Induction on the Sample

The sample material used in this study is commonly employed for cabin floor panels and cargo compartment floor panels in aircraft. To simulate real world conditions, artificial damage was introduced to the panel, reflecting the types of damage these components typically encounter during service. In operational environments, impact damage is prevalent, while both impact and hole damage are commonly observed during maintenance activities.

For the purposes of this study, artificial damage was applied with predefined dimensions and depths to facilitate subsequent repair procedures. As illustrated in Figure 5, impact damage was induced using a hammer, while hole damage was created using a drill. These methods were selected to replicate realistic damage scenarios and ensure the effectiveness of the repair techniques under investigation.



Fig. 5. Induction of artificial damage on the samples.

2.2. Application of the Repair Procedure

During the repair phase, the latest revision of the Structural Repair Manual (SRM) provided by Boeing was utilized as a reference. All repair steps were executed by qualified and experienced personnel to ensure adherence to industry standards. Initially, critical information, including the appropriate repair method and the specific materials required, was determined in accordance with the guidelines outlined in the SRM. The repair process commenced with cleaning the sample and removing the damaged layers. As depicted in Figure 6, the removal of the damaged area was conducted based on the shape and extent of the damage. Following this step, the depth of the damage was meticulously measured to guide subsequent repair actions.

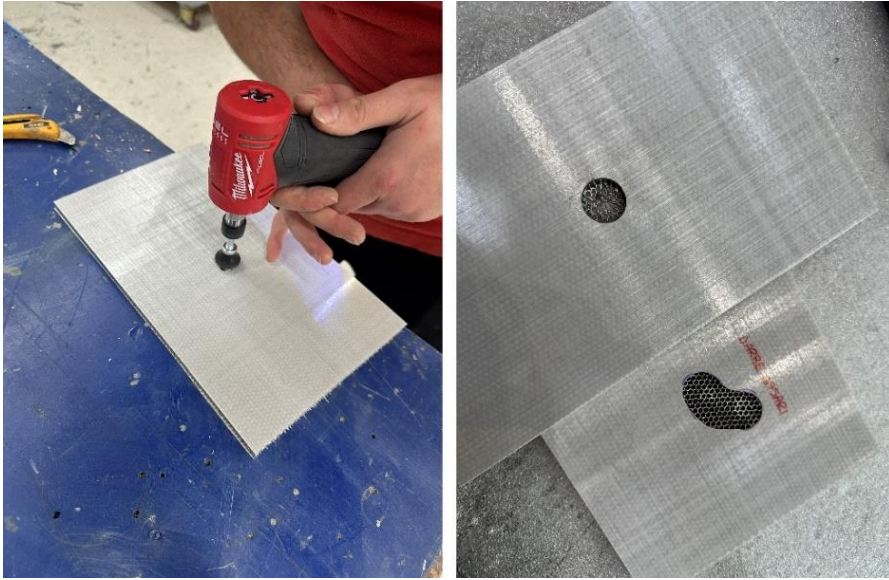


Fig. 6. Removal of the damaged area.

After the damaged area has been removed, the surface is carefully cleaned to remove burrs and dust. A template is then created on the damaged region using tape, which will serve as a fabric pattern for subsequent stages of the repair process. To address the core deficiency in the damaged area, the procedure involves filling the void with BMS 5-28, Type 19 filler material, as specified in the repair manual. This filler material can cure either in 7 days at room temperature or in 5 hours at 52 °C, depending on the chosen curing conditions. The filler material consists of two components that must be mixed in the prescribed ratio of approximately 20:1 (base material to activator). It is crucial to ensure that the entire damaged area is completely filled, and the filler level should be leveled with the surface of the sample. Once the filler material is applied, it is allowed to cure until it hardens. Following the curing process, the surface is shaved to achieve a smooth and level finish. During the shaving operation, safety precautions must be followed: safety goggles should be worn to prevent exposure to dust, or a vacuum device should be employed to minimize airborne particles. The shaving process continues until the filler material is even and flush with the surface of the sample. These steps are illustrated in Figure 7.



Fig. 7. Template creation, filler material application, and shaving process.

Following these procedures, fabric dimensions are measured based on the size of the damage, as previously outlined

in the template. According to the repair protocol, three layers of fabric will be applied. The dimensions of each fabric layer should be 0.50 inches wider than the previous one. The BMS 9-3 repair fabrics are used in accordance with the measurements specified by the template. Since these fabrics are not preimpregnated, an impregnation process is required. The impregnation is carried out using BMS 8-201 resin, which is composed of two chemicals that must be mixed in the appropriate proportions as per the application instructions. Each fabric layer is individually impregnated with epoxy in an approximately 1:1 ratio (Figure 8).

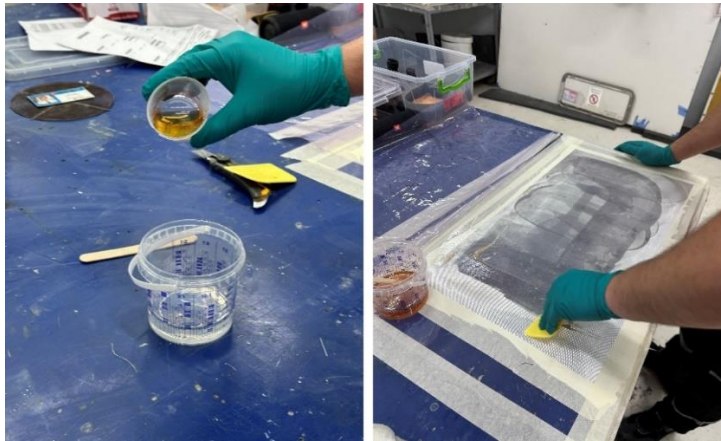


Fig. 8. Epoxy impregnation of the fabric and template creation for the fabric layers.

After the impregnation process, the templates are carefully cut from the fabric, and the laying process begins immediately. Prior to initiating the laying process, resin is applied to the surface to be treated. The fabric layers are then applied sequentially, one at a time, to complete the repair. These procedure steps are illustrated in Figure 9.



Fig. 9. Removal of fabric templates and fabric laying process.

After completing the laying process, the vacuum process is initiated immediately. The first step involves placing the vacuum bag over the sample. The sample is then positioned on the blanket with the untreated surface facing down. Once the sample is placed, fabrics are applied to prevent the blanket from adhering to the sample while allowing air to pass through. A flat plate is employed to ensure more uniform pressure distribution across the sample. The vacuum bag is sealed tightly using double sided tape to prevent air from entering. Subsequently, the vacuum bag is carefully cut to accommodate the insertion of the vacuum probe, which is then positioned. The sample is then subjected to the

vacuum process in accordance with the procedure. The vacuum process is carried out at room temperature as specified in the procedure. The vacuum device is equipped with a warning system that detects any pressure loss or temperature variation. It is capable of adjusting the temperature if necessary. According to the procedure, the sample must cure for 24 hours. After curing, the vacuum probes are removed. The double sided tape is carefully taken off, and the sample undergoes an initial visual inspection by authorized personnel. During this inspection, the sample is checked for bubble formation or any other unusual conditions. For a more detailed assessment, non-destructive testing methods, as outlined in the procedure, are applied to the sample. These process steps are illustrated in Figure 10.



Fig. 10. The vacuum process implementation.

2.3. Non-Destructive Testing Procedure

To detect any invisible defects in a composite sandwich structure that has been repaired, a non-destructive testing (NDT) method is applied. This method enables the identification of discontinuities within the material without causing any damage, thereby allowing a decision to be made about whether the structure is fit to return to service. According to the Boeing procedure, the repaired sample undergoes a non-destructive inspection in accordance with the relevant control procedures. The procedure specifies that, at the repair site, delamination, separation between layers, and any voids in the filler material must be checked. For this purpose, ultrasonic testing, a detailed acoustic inspection method, is performed. The tests were carried out in the non-destructive testing laboratory, under the supervision of authorized personnel.

Two types of techniques were used for the acoustic testing method: the bond test and the transmission path test. The bond test procedure is employed to detect core damage and separations between the core and the surface layers. A low frequency testing device is utilized for this test. The relevant procedure specifies the suitable devices for this type of testing. The sensitivity of the device must be adjusted based on the material thickness. Since low frequency is used, there is no requirement for a liquid medium between the sensor and the structure. Prior to testing, both the sample and the surrounding environment were thoroughly cleaned. The appropriate procedure for material thickness was determined, and Bondmaster 600 and Olympus devices were used for the test. To calibrate the device, either an undamaged sample with the same thickness or calibration packs made from the same material can be used. The probe is slowly moved over the undamaged sample to obtain a clean signal. Figure 11 illustrates how the device generates response signals for both undamaged and damaged areas.

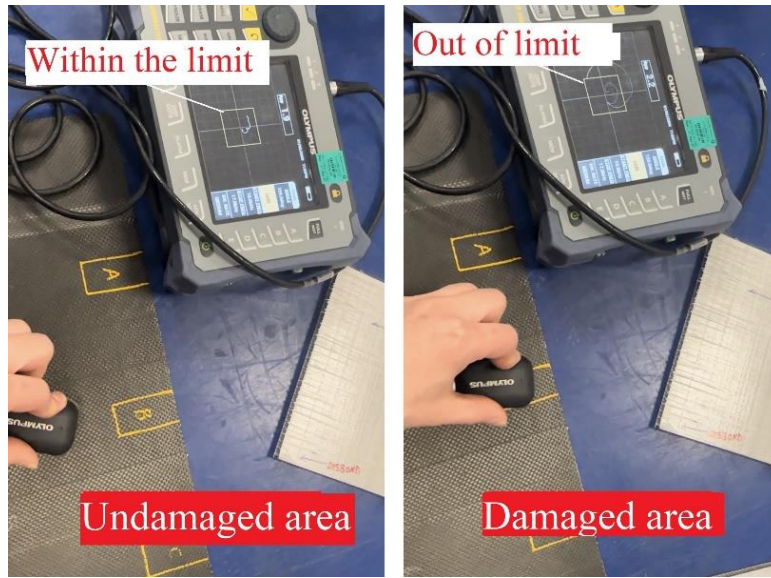


Fig. 11. It illustrates how the device generates response signals for both undamaged and damaged areas.

After the device is calibrated, the test is conducted on both specimens (Figure 12). During the test, no signal distortion is detected in either specimen. It is observed that there are no defects in the filler material or its adhesion to the surface layer.

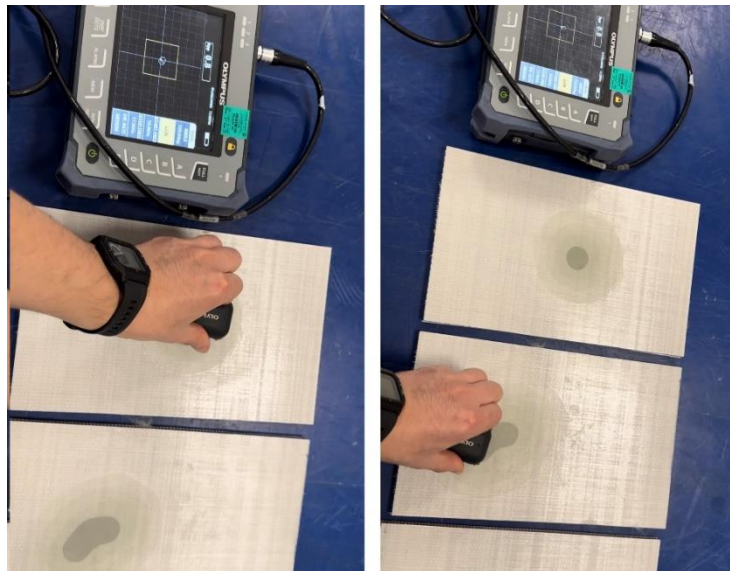


Fig. 12. A bond test is performed on the specimens.

In the transmission test, interlayer delaminations and separations between the core and the surface layer are detected. The test is conducted using sound transmission sensitivity. The sound wave striking the ramp is subsequently

received by the probe, with detections made based on the intensity of the sound. Different ramps with varying angles can be employed, making the test applicable for angular structures. Both the environment and the specimen must be clean prior to testing. To eliminate air contact, gel is applied between the probe and the structure.

For this test, the Sonatest D-70 device, which complies with the procedure, was used. Initially, the device is calibrated. Unlike the bond test, this test can detect separations between fabric layers, making the number of fabric layers repaired a critical factor. Therefore, a calibration plate is used during the calibration process. Based on the repair performed, the device is calibrated according to Region B of the plate shown in Figure 13.

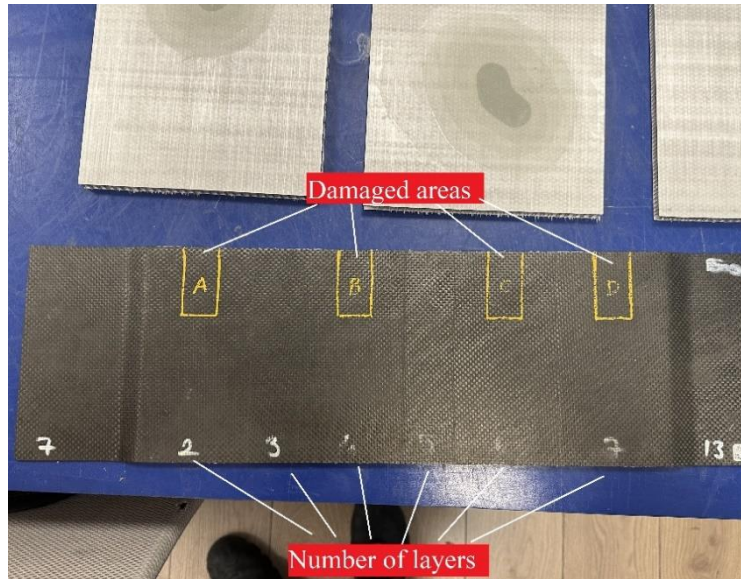


Fig. 13. A device calibration plate.

During calibration and testing, the probes must be perfectly aligned. No signal should be received when the probe is positioned over the damaged area. Signals should only be detected outside the damaged areas. The resulting signals are clearly shown in Figure 14.

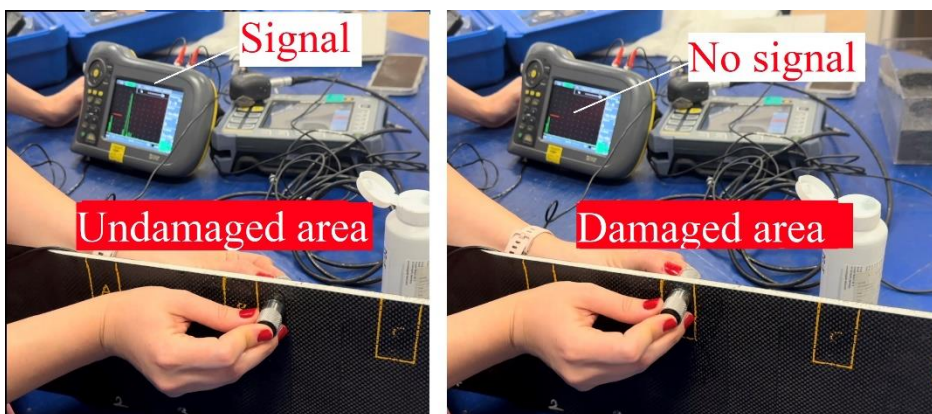


Fig. 14. The display of signals on the calibration plate.

After the device is calibrated, the test is applied to the specimens. Since the areas where filling has been done are

not suitable for the transmission test, the test is only applied to areas without filler material. The test is conducted over the entire repair area. According to the procedure, to determine whether the repair is suitable, the signal must be transmitted with a minimum efficiency of 40%. The signals for the specimen are shown in Figure 15. It has been determined by authorized personnel that the specimens successfully passed the transmission test.



Fig. 15. The signals for the specimen.

2.4. Bending Test Implementation

A bending test of a material allows for the determination of its ductility, bending strength, fracture strength, and resistance to fracture. If a material begins to crack or fracture during the testing phase, it can be assumed that the material would similarly fail in active use, potentially leading to failure. The testing procedure was conducted by authorized personnel in accordance with the relevant standard. The bending operation was performed on an Instron brand three point bending device, which is equipped with an adjustable mandrel and has a capacity to apply a load of up to 100 kN. Real time data can be monitored through the device's display.

The bending process was applied sequentially to the unblemished specimen, the damaged specimen with renewed surface coating, and the specimen with both surface and core repair. During all three tests, the following parameters were maintained: the support span was set to 100 mm, the mandrel width was 77 mm, the mandrel diameter was 10 mm, and the compression force speed was 2 mm/min. The test points were positioned at the center of the specimen for the original specimen and aligned with the center of the damage area for the repaired specimens. The setup for the bending operation is shown in Figure 16.

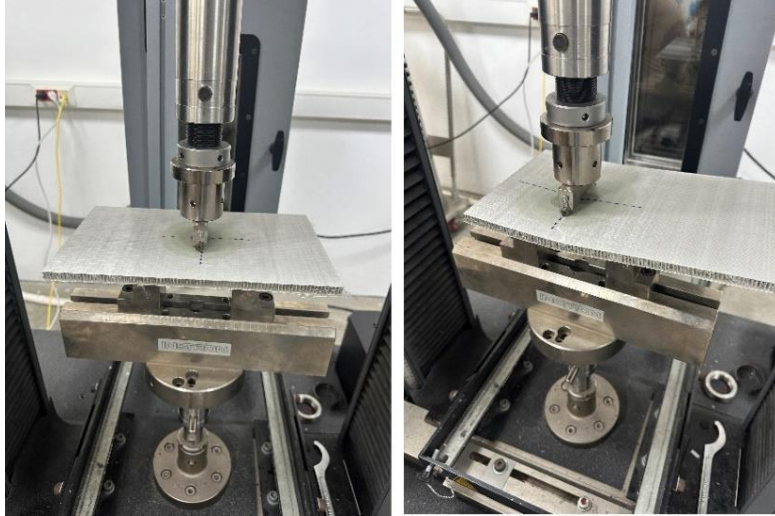


Fig. 16. The setup for the bending operation.

The test continued until the material fractured and for a period following the fracture. Upon examining the final condition of the specimens, it was observed that the fracture point passed through the center of the repaired areas, as desired, as shown in Figure 17.

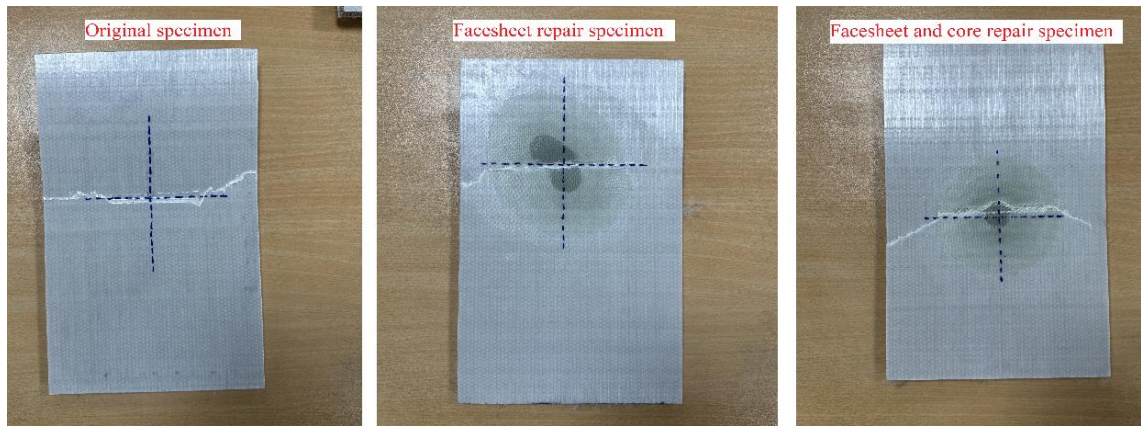


Fig. 17. The post-bending test appearance of the specimens.

3. Conclusion and Discussion

The study proposes a new repair technique applied to aluminum honeycomb structures, which are widely used in aviation and aerospace engineering applications, subjected to artificial damage. The repair procedures were executed in accordance with the maintenance protocols established by the manufacturing companies, with the objective of restoring the material's original strength characteristics. During the repair phase, the latest revision of the Structural Repair Manual (SRM) provided by Boeing was utilized as a reference. Following the repair, various non-destructive testing (NDT) methods were employed to assess the presence of discontinuities. Firstly, a three point bending test was conducted on an undamaged glass fiber reinforced aluminum sandwich material in accordance with ASTM standards. Upon analysis of the results, it is evident that the material initially exhibited a linear increase within the elastic region, where stress and strain maintained a proportional relationship. Following approximately 2.5 mm of elongation, plastic

deformation commenced beyond the yield point, which was represented as a peak in the graph. After this point, permanent shape changes occurred.

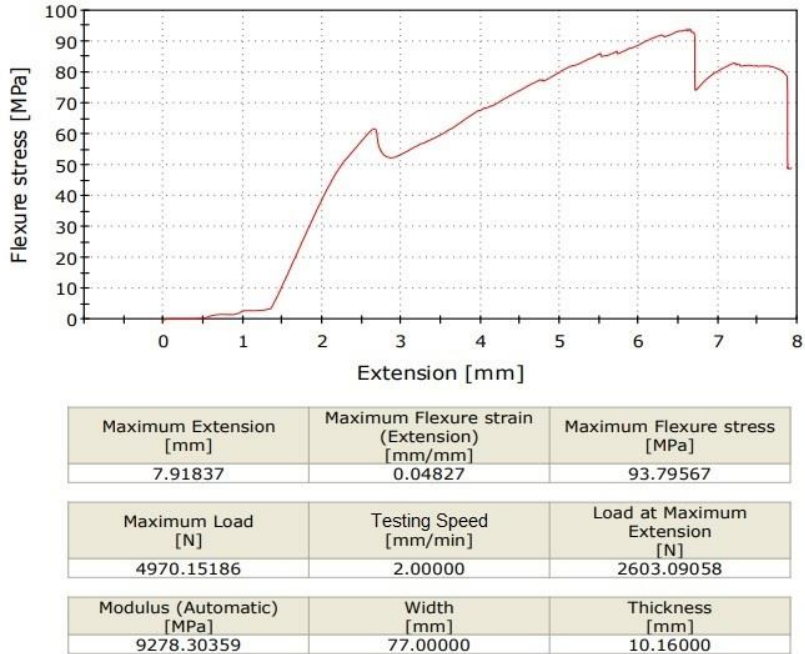
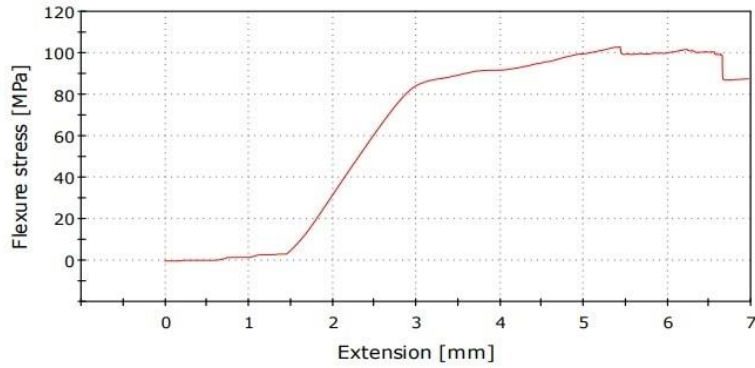


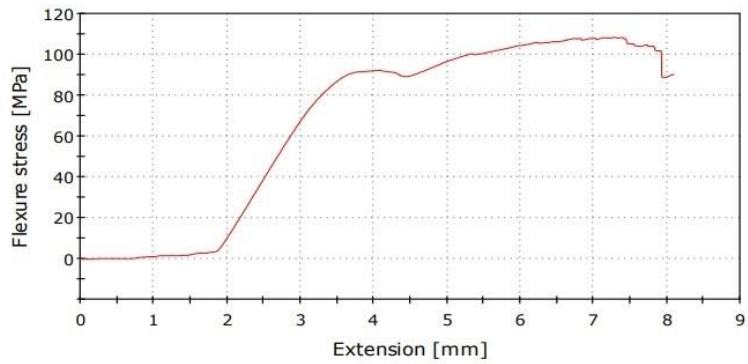
Fig. 18. The bending test result of the undamaged specimen.

Secondly, conducting the three point bending tests on the surface repaired and both surface and core repaired glass fiber reinforced aluminum sandwich materials (Figure 19 and 20), it was proved that repaired specimens displayed bending stress and elongation behavior comparable to that of the undamaged specimen. However, a closer examination of the curves at the yield points revealed a sharp drop in the original specimen, while no such abrupt decrease was observed in the repaired specimens. It was deduced that the presence of filler material may contribute to this observed difference. The results presented in the study shows that the repaired specimens achieved values similar to those of the original specimen. Additionally, the graphs indicate that composite sandwich structures retain resistance to applied forces even following fracture. As a reviewer of this manuscript, it is evident that this research may provide valuable insights for future investigations and contribute to the advancement of repair methodologies for similar structures and to the development of safe and effective repair processes in the aerospace applications by enhancing the quality of maintenance repair applications.



Maximum Extension [mm]	Maximum Flexure strain (Extension) [mm/mm]	Maximum Flexure stress [MPa]
6.96142	0.04244	102.94234
Maximum Load [N]	Testing Speed [mm/min]	Load at Maximum Extension [N]
5454.82617	2.00000	4638.45068
Modulus (Automatic) [MPa]	Width [mm]	Thickness [mm]
9700.80211	77.00000	10.16000

Fig. 19. The bending test result of the specimen with facesheet repair.



Maximum Extension [mm]	Maximum Flexure strain (Extension) [mm/mm]	Maximum Flexure stress [MPa]
8.08741	0.04930	108.37933
Maximum Load [N]	Testing Speed [mm/min]	Load at Maximum Extension [N]
5742.92725	2.00000	4782.02490
Modulus (Automatic) [MPa]	Width [mm]	Thickness [mm]
9524.30724	77.00000	10.16000

Fig. 20. The bending test result of the specimen with both facesheet and core repairs.

This research examined the repair and inspection methods of glass fiber reinforced aluminum sandwich composite materials tested according to aerospace standards and evaluated the conclusions derived from the flexure test. The base material is heavily structured, significantly advancing the understanding of how composites behave under stress, their response to damage, and the repair processes. However, certain aspects of the repair process can still affect

damage detection and mechanical test results for composite materials and require further investigation. These factors include:

➤ **Comparison of Repair Approaches:** Various repair options are available for composite materials, each offering distinct advantages under specific conditions. While mechanical repair is typically fast and cost effective, it has been observed to result in a gradual loss of strength over time. In contrast, methods such as resin injection, while more permanent and cost effective in the long term, are time consuming and expensive. Studies by Préau and Hubert [6] have demonstrated similar repair approaches, achieving promising results in terms of both structural integrity and durability. Therefore, selecting an appropriate repair method requires careful consideration and a balance of factors based on the specific priorities of the situation. Establishing a standardized approach to repair in aircraft maintenance manuals could help mitigate these challenges and ensure more consistent outcomes.

➤ **Inspection Method Effectiveness:** NDT (Non-Destructive Testing) methods are vital for composite safety. Ultrasonic inspection and thermography have been a couple of methods to achieve that of the early damage detection highly accurately. But the accuracy of these tests varies depending on environmental conditions. High temperature and humidity can cause these tests to lose their sensitivity, highlighting the importance of taking them into account across the inspection process.

➤ **The Human Factor Effect:** Non-destructive testing operation reduces the risk of human error effect and improves the success of aerospace repair. Nonetheless, the human factor is significant in both the repair phase and non-destructive test. In repair procedures, the human factor is human responsibility that determines whether it will reach the result or not; sincerity with an operator's experience and knowledge makes or breaks the throughput of that process. It is noted that better results, especially in the manual repair operations (experienced and trained operators), have been observed. This implies that procuring human factors support for composite repair efforts can result in an improved average success of the procedure. In the literature study [5], six different repair scenarios were applied. These scenarios achieved results based on the quality of the repairs and highlighted the importance of the human factor.

➤ **Environmental Factors Play a Role:** Environmental conditions are the direct influence of repair and inspection success processes. Temperature, humidity, and dust are very essential, especially in resin repairs. High humidity, in particular, will shorten the life of repairs, and dealing with temperature fluctuation is a difficult repair process. Those results reveal issues of environmental control during repair procedures.

➤ **Sustainability and Cost Analysis:** The analysis of sustainability and cost associated with repair methods highlights an essential aspect of long term operational efficiency. While some repair methods may appear cost effective initially, as noted in reference [9], the long term financial impact can be compromised due to environmental consequences arising from the materials and methods used. For instance, environmentally harmful repair procedures can lead to higher maintenance costs over time, as the need for more frequent repairs or replacements increases. Witik et al. [10] discusses how these costs can accumulate, particularly when the durability and performance of repairs are adversely affected by improper handling of environmental factors. Moreover, as highlighted by Khalil [11], the use of advanced materials and improved repair techniques, which consider environmental impact, offers significant advantages in terms of both economic viability and ecological responsibility. These approaches ensure a longer service life for the repaired components, reducing the frequency of costly repairs and minimizing waste generation. Thus, the findings from this study reinforce that integrating sustainability into repair practices provides both environmental benefits and long term financial savings, making eco-friendly solutions a favorable option for the aerospace industry.

➤ **Importance of Mechanical Testing:** The mechanical tests of data in this study were essential to assess the strength and durability of repaired composite materials. For diagnosis, specifically tensile, compression, and bending tests are essential to evaluate the repair success. The objective of these tests is to look at how close the strength can be made to approaching the repair test result, which testifies to the validity of resin reparability. Examining the deviation rates in the repaired areas of mechanical tests provides rich data in terms of the effectiveness of reliability on these tests in order to judge the performance of the material. As an example study conducted by Tunca and Kafalı [21], it was found that the three point bending test is an effective testing method for the use of composite materials in aircraft.

Acknowledgements

Origin of this study is master thesis.

Author Contributions

A.C. and O.T. contributed to the design and implementation of the research, to the analysis of the results and to the writing of the manuscript.

References

- [1] M. Mrazova, “Advanced composite materials of the future in aerospace industry.” *Incas Bulletin* 5, no. 3, 6 September 2013: 139–50. <https://doi.org/10.13111/2066-8201.2013.5.3.14>.
- [2] B. Parveez et al., “Scientific advancements in composite materials for aircraft applications: A review.” *Polymers* 14, no. 22, 18 November 2022: 5007. <https://doi.org/10.3390/polym14225007>.
- [3] M. Kalanchiam and M. Chinnasamy. “Advantages of Composite Materials in Aircraft Structure.” *World Academy of Science*, Vol:6, No:11, 2012.
- [4] P. D. Mangalgi, “Composite materials for aerospace applications.” *Bulletin of Materials Science* 22, no. 3, May 1999: 657–64. <https://doi.org/10.1007/BF02749982>.
- [5] S. Pantelakis, and K. I. Tserpes, “Adhesive bonding of composite aircraft structures: Challenges and recent developments’.” *Science China Physics, Mechanics and Astronomy* 57, no. 1, January 2014: 2–11. <https://doi.org/10.1007/s11433-013-5274-3>.
- [6] M. Préau and P. Hubert, “Bonded repairs of honeycomb sandwich structures: Process monitoring and quality assessment.” 20th International Conference on Composite Materials Copenhagen, 19–24th July 2015.
- [7] C. Soutis, “Fibre reinforced composites in aircraft construction.” *Progress in Aerospace Sciences* 41, no. 2, February 2005: 143–51. <https://doi.org/10.1016/j.paerosci.2005.02.004>.
- [8] Z. Wang et al., “On the influence of structural defects for honeycomb structure.” *Composites Part B: Engineering* 142, June 2018: 183–92. <https://doi.org/10.1016/j.compositesb.2018.01.015>.
- [9] A. J. Timmis et al., “Environmental impact assessment of aviation emission reduction through the implementation of composite materials.” *The International Journal of Life Cycle Assessment* 20, no. 2, February 2015: 233–43. <https://doi.org/10.1007/s11367-014-0824-0>.
- [10] R. A. Witik et al., “Economic and environmental assessment of alternative production methods for composite aircraft components.” *Journal of Cleaner Production* 29–30, July 2012: 91–102. <https://doi.org/10.1016/j.jclepro.2012.02.028>
- [11] Y. F. Khalil, “Eco-efficient lightweight carbon-fiber reinforced polymer for environmentally greener commercial aviation industry.” *Sustainable Production and Consumption* 12, October 2017: 16–26. <https://doi.org/10.1016/j.spc.2017.05.004>.
- [12] M.H. Hassan et al., “A review on the manufacturing defects of complex-shaped laminate in aircraft composite structures.” *The International Journal of Advanced Manufacturing Technology* 91, no. 9–12, August 2017: 4081–94. <https://doi.org/10.1007/s00170-017-0096-5>.
- [13] M. K. Hagnell et al., “From aviation to automotive a study on material selection and its implication on cost and weight efficient structural composite and sandwich design.” *Heliyon* 6, no. 3, March 2020: e03716. <https://doi.org/10.1016/j.heliyon.2020.e03716>.
- [14] A. Anderson, C. Longo and P. Teufel, “New composite design and manufacturing methods for general aviation aircraft structures.” Toyota Aviation Business Development Office Toyota Motor Sales, USA Inc. 19001 South Western Avenue, MS32 Torrance, CA 90509.
- [15] V. Birman and G. A. Kardomateas, “Review of current trends in research and applications of sandwich structures.” *Composites Part B: Engineering* 142, June 2018: 221–40. <https://doi.org/10.1016/j.compositesb.2018.01.027>.
- [16] X. Wei et al., “New advances in fiber-reinforced composite honeycomb materials.” *Science China Technological Sciences* 63, no. 8, August 2020: 1348–70. <https://doi.org/10.1007/s11431-020-1650-9>.
- [17] N. Takeda et al., “Smart composite sandwich structures for future aerospace application - damage detection and suppression-: A review.” *Journal of Solid Mechanics and Materials Engineering* 1, no. 1, 2007: 3–17. <https://doi.org/10.1299/jmmp.1.3>.
- [18] X. Zhao et al., “Composite Aircraft Components Maintenance Cost Analysis.” Delft University of Technology, Kluyverweg 1, Delft, The Netherlands, 2629 HS.
- [19] B. He et al., “Damage resistance of honeycomb sandwich composites under low-energy impact.” *Applied Composite Materials*, 29 October 2024. <https://doi.org/10.1007/s10443-024-10278-1>.
- [20] B. Castanie et al., “Review of composite sandwich structure in aeronautic applications.” *Composites Part C: Open Access*, 2020. <https://doi.org/10.1016/j.jcomc.2020.100004>
- [21] E. Tunca and H. Kafalı, “Compression and three-point bending analyzes of aerospace sandwich composites produced with polymeric core materials using ansys.” *European Journal of Science and Technology*, (31), 553-561. <https://doi.org/10.31590/ejosat.1012658>.
- [22] I. Bozkurt, “Investigation of low velocity impact behavior of aluminum honeycomb sandwich structures with gfrp face sheets by finite element method.” *Düzce University Journal of Science & Technology*, 2024, 2159-2184. <https://doi.org/10.29130/dubited.1477434>.

- [23] H. A. Hegazi and A. H. Mokhtar, "Optimum design of hexagonal cellular structures under thermal and mechanical loads." *International Journal of Engineering Research & Technology (IJERT)*, Vol. 9 Issue 06, June-2020.
- [24] A. Kausar et al., "State of the art of sandwich composite structures: manufacturing to high performance applications." *J. Compos. Sci.* 2023, 7, 102. <https://doi.org/10.3390/jcs7030102>.



Contents lists available at *Dergipark*

Journal of Scientific Reports-A

journal homepage: <https://dergipark.org.tr/pub/jsr-a>



E-ISSN: 2687-6167

Number 59, December 2024

REVIEW ARTICLE

Receive Date: 09.06.2024

Accepted Date: 19.09.2024

Cellulose and its derivatives as biodegradable materials: A review

Muhammed Zakir Tufan^{a*}, Cengiz Özel^b

^a*Isparta University of Applied Sciences, Department of Forest Products Engineering, Isparta 32200, Turkey, ORCID:0000-0002-6110-7018*

^b*Isparta University of Applied Sciences, Department of Civil Engineering, Isparta 32200, Turkey, ORCID:0000-0002-2715-1680*

Abstract

From ancient times to the present day, human beings have carried out many studies to make their lives easier. As a result of these studies, they aimed to discover something new. With the industrial revolution, petrochemical materials began to be produced. The fact that these materials have gone through various chemical stages has become a threat to human health. In addition, the fact that petroleum-derived materials remain in nature for centuries without degrading, and the parallel increase in environmental problems has led humanity to search for different resources. In this work, general information is given about the types of derivatives obtained from cellulose, which is the most common in nature.

© 2023 DPU All rights reserved.

Keywords: Cellulose; Cellulose Derivatives; Cellulose Ether Derivatives; Cellulose Ester Derivatives

1. Cellulose

Plants synthesize cellulose, a polymer that forms in a linear structure [1-4]. Currently, it stands as the most prevalent polysaccharide globally, serving as the primary reservoir of sustainable polymers [2, 5, 6, 7, 8]. Cellulose forms the fundamental structure of both wood and cotton, comprising a substantial 94% of cotton fibers. The wood of trees contains a high proportion of cellulose, exceeding 50%, while its lignin content is comparatively low. Bacteria are capable of producing cellulose, which is referred to as microbial or bacterial cellulose. In contrast to cellulose sourced

* Corresponding author.

E-mail address: zakir_65@hotmail.com

<http://dx.doi.org/10.1016/j.cviu.2017.00.000>

from cotton and wood, which is produced through photosynthesis, bacterial cellulose is not formed through this process and is obtained in a more purified form. [9-10].

Cellulose is comprised of numerous monosaccharide molecules [11]. The arrangements of these monosaccharide units shape the structure of cellulose. Cellulose molecules are created by linking anhydroglucose units, with the chemical formula $(C_6H_{10}O_5)_n$, in a linear chain. The number of anhydroglucose units is referred to as the degree of polymerization (DP, typically averaging between 10,000 and 15,000). These units are linked by 1,4- β -glucosidic bonds, with one of the two anhydroglucose units rotated 180 degrees in relation to the other. The arrangement of cellulose is depicted in Figure 1. As a result, a tension-free linear cellulose structure emerges [1, 3, 6, 7, 12, 13, 14].

Each D-anhydroglucopyranose unit that makes up the cellulose molecule contains hydroxyl groups at the C2, C3, and C6 positions, which can participate in typical reactions of primary and secondary alcohols. Because of its configuration, cellulose 1 can exhibit various characteristics including hydrophobicity, chirality, degradability, and chemical diversity. These collectives establish numerous hydrogen bonds with hydroxyl groups in neighboring chains. The complex network of hydrogen bonds both within and between cellulose chains provides the polymer with stability, increasing the stiffness of cellulose fibrils along their axes. The chains are also stacked regularly in places where the crystal zone will form. In amorphous regions, they form a dispersed stacking. These properties were effective in the formation of the current properties of cellulose [9, 13, 14, 15, 16, 17].

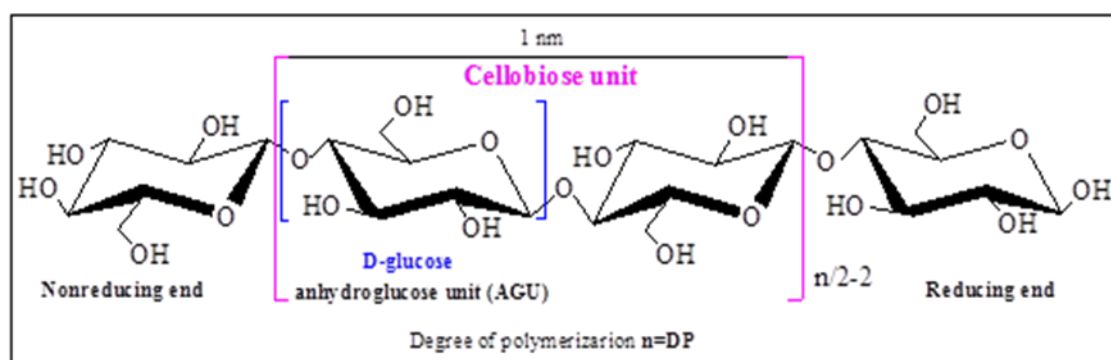


Fig 1. Structure of the cellulose molecule [6].

Cellulose, a polymeric raw material, is primarily utilized in two main fields: the first is the production of materials derived from wood and cotton, and the second is the manufacture of paper and cardboard. Furthermore, cellulose serves as a primary substrate for chemical transformations in the production of cellulose-derived goods, which find utility across diverse fields. The cellulose molecule has been subjected to various reactions to obtain these products, which we call cellulose derivatives. The most important duo of these reactions is etherification and esterification [9, 13, 18].

2. Cellulose ether derivatives

Cellulose ethers are macromolecules derived from cellulose in which the hydroxyl groups of the hydrogen atoms in the anhydroglucose units are replaced by alkyl or substituted alkyl groups. The assessment of key properties of cellulose ethers, such as their molecular weight, chemical composition, distribution of substituent groups, degree of substitution, and molar substitution characteristics, depends on their specific application. These characteristics typically encompass dissolvability, fluid thickness in solutions, surface behavior, qualities of thermoplastic films, and resistance to decomposition by organisms, high temperatures, water breakdown, and oxygen exposure. The viscosity of cellulose ether solutions increases in proportion to their molecular weight. Cellulose ethers, frequently used in

various applications, include methyl cellulose (MC), ethyl cellulose (EC), hydroxyethyl cellulose (HEC), hydroxypropyl cellulose (HPC), hydroxypropylmethyl cellulose (HPMC), carboxymethyl cellulose (CMC), and sodium carboxymethyl cellulose [18-20]. Despite the wide variety of cellulose derivatives produced, The primary factors behind the excessive use of cellulose ethers worldwide are their availability in the market, economic functionality, ease of use, and almost no toxic effects. Therefore, there is a constant expansion in its use. Cellulose ethers offer functionalities such as flow regulation, stabilization, moisture retention, and the formation of protective films. Combining properties such as these cannot generally be achieved when fully synthetic polymers are used [21]. Etherification of cellulose is given in Figure 2

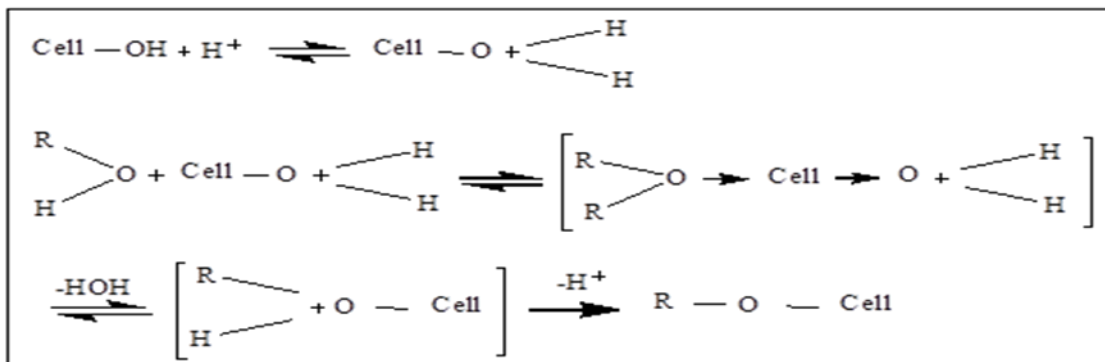


Fig 2. Etherification reaction of cellulose [12].

2.1. Methyl cellulose (MC)

Methyl cellulose (MC) is a key cellulose derivative extensively used in numerous industrial fields due to its diverse applications [22]. MC, was first synthesized as a result of Suida's studies, and it was first named as cellulose ether in 1905 [23]. Methyl cellulose, which is abundant in nature and is expected to stand out as an alternative raw material in the future thanks to its low cost and environmentally friendly properties, is similar to cotton with its neutral, odourless, tasteless and inert structure. MC, is not digested and also has no toxic effects. It swells in water and becomes a light color, making the colloidal solution clear and insoluble in most common organic solvents. It's possible to weaken it by mixing it with ethanol. MC solutions maintain their stability across a broad pH spectrum, from 2 to 12, with negligible alterations in viscosity [11, 24, 25, 26].

MC obtained using iodomethane, chloromethane and dimethyl sulfate is synthesized using the Williamson etherification method. The degree of displacement (DS) of methyl cellulose varies according to its usage areas and purposes. The DS value is determined by the average count of hydroxyl groups (OH) on the anhydroglucose unit that have undergone reaction with the desired substitute group. Since each anhydroglucose unit in the cellulose molecule contains three hydroxyl groups, the highest degree of substitution possible is three, represented as DS = 3 [27].

Methyl cellulose (MC) is extensively utilized as a binder or thickening agent in pharmaceutical chemistry, the food industry, and ceramic processing. It is also employed in electrochemical supercapacitors and electrolyte applications. Methyl cellulose finds extensive application in the food and pharmaceutical sectors owing to its remarkable attributes like superior film-forming capacity, effectiveness as a barrier against lipids, and its ability to minimize permeability to oxygen and moisture vapor [23, 26, 28, 29, 30]. When placed in water, it forms a gel between 60 and 80 degrees Celsius, which dissolves upon cooling. MC is a cellulose derivative with extended chains, encompassing roughly 27 to 32% of hydroxyl groups within its methyl ether framework. The level of polymerization in different classes of

methyl cellulose is between 50-1000 and their molecular weight (average number) is between 10.000 and 220.000 [31-32].

MC undergoes heat-recoverable gelation in aqueous solution by heating in water, and it is also a polymer soluble in water. Cellulose, the base component of methyl cellulose, exhibits an affinity for water. Cellulose fibers resist dissolution in water due to the presence of structured crystalline regions formed through both intra- and intermolecular hydrogen bonding. The formation of crystalline regions in cellulose varies according to its source, yet when a specific quantity of hydroxyl groups undergo substitution with methoxyl groups, it disrupts certain hydrogen bonds, resulting in the solubility of methyl cellulose in water. This change is defined as the number of methoxyl groups separated by the numbers of glucose units and is expressed as the level of substitution (DS). If the degree of displacement (DS) is very low, a sufficient number of hydrogen bonds ensure that methyl cellulose remains undissolved, whereas methyl celluloses with a high degree of displacement (DS) have a hydrophobic and at the same time insoluble structure. Therefore, DS values of products to be used commercially are selected as moderate (1.7-2.0). At colder temperatures, water molecules arrange themselves into "cage-like" formations that encase the hydrophobic methoxyl groups, leading to the solubility of methyl cellulose in water. Above the specified temperature values, these structures deteriorate and break to reveal hydrophobic structures. This phenomenon causes clustered structures to form. Therefore, the gelation phenomenon shows that the hydrophobic effect occurs and also reduces the gel temperature in common solvents that are easily dissolved in water, such as strong electrolytes [25, 30, 33]. The molecular configuration of methyl cellulose is depicted in Figure 3.

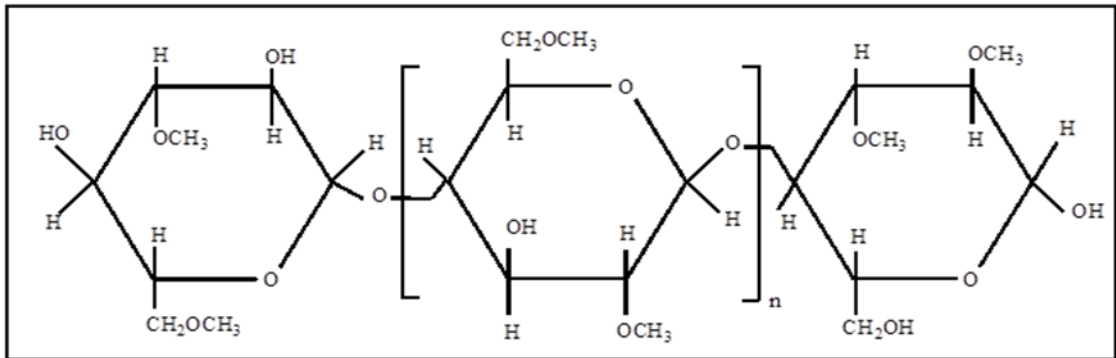


Fig 3. Molecular structure of methyl cellulose [34].

2.2. Ethyl cellulose (EC)

Ethyl cellulose (main source cotton and wood), which is widely used in the pharmaceutical industry [35-36], contains three reactive OH sites in repeating anhydroglycose units. Some of these hydroxyl groups can react partially or completely with various chemicals, leading to the formation of different cellulose derivatives. As a result of these reactions, ethyl cellulose (one of the most expensive cellulose derivatives), which is obtained by converting cellulose into ethyl ether groups called non-ionic ethyl ether, is partially ethylated and has an ethoxy content ranging from 44% to 51%. It is also a non-ionic and pH insensitive cellulose ether [24, 37, 38, 39]. Thanks to its versatile properties, ethyl cellulose is widely used in optical materials, film forming, packaging, coating material, tablet binder and microencapsulation. We can exemplify these properties as follows [38, 40, 41, 42]: (1) it is white to light skin colored and is in the form of a tasteless, odorless powder or granular material; (2) the melting point is in the range of 240-255°C; (3) its specific density is between 1.07-1.18, its degradation point is between 135 and 155°C, and its combustion temperature is between 330-360°C; (4) insoluble in water but dissolves in various organic solvents, such as ether, ketone, alcohol, and ester; (5) biocompatible, working well with the majority of celluloses, resins, and

plasticizers; (6) is not biodegradable, so it can only be used orally; (7) It is resistant to light, heat, oxygen, moisture and chemicals [40] (8) it is non-toxic [43-44]; (9) has no irritating properties; (10) used as a mold binder to impart plasticity to the flow of particles; (11) possesses the capacity to take pressure, so it protects the coating from breaking during compression [40]; (12) It does not swell or dissolve in water, but it does dissolve in numerous organic solvents [24], so the density and porosity of ethyl cellulose play a key role in drug release from such hydrophobic substances [45]; (13) Despite its lack of solubility in water, it can absorb water. The interaction results from the attraction between water molecules and hydrogen atoms, influenced by the difference in polarity between the oxygen atom and the ethyl group in ethyl cellulose [45-46]; (14) the viscosity of ethyl cellulose varies based on the length of its chains, polymerization degree, or the quantity of anhydroglucose units. At the same time, existing viscosity can also be considered an indirect measure of molecular weight [40]; (15) The glass transition temperature is 120°C; (16) It is physiologically inert, its pH level is between 3 and 11 and does not change. The degree of substitution (DS) for its solubility in water is in the range of 1-1.5, while in organic solvents this value is in the range of 2.4-2.5 [11, 47]. Figure 4 depicts the molecular arrangement of ethyl cellulose.

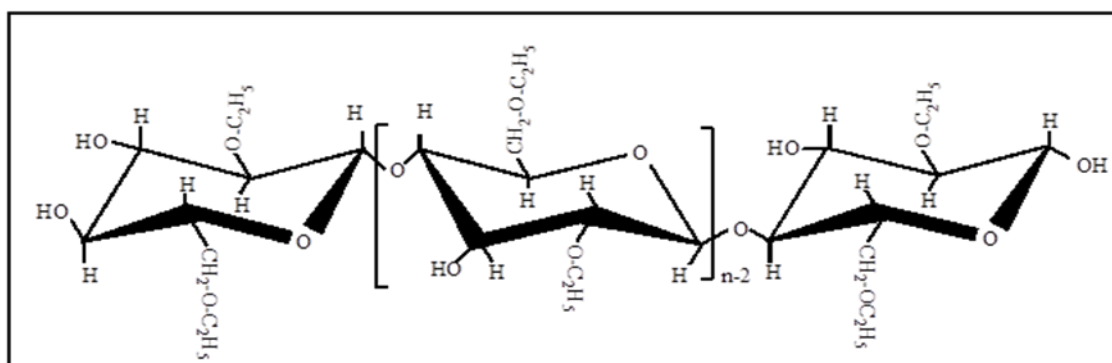


Fig 4. Molecular structure of ethyl cellulose [40].

2.3. Hydroxyethyl cellulose (HEC)

Hydroxyethyl cellulose (HEC) is among the most commonly utilized cellulose derivatives and is a water-soluble and low-density hydrophilic polymer obtained by etherification of alkaline cellulose with ethylene oxide or ethylene chlorohydrin, replacing the H atoms in cellulose with hydroxyethyl groups. Cationic polymers, especially biopolymers, are used as stabilisers and thickeners in paint mixtures and hair and eye care products. With its greatest hydrophilic property, hydroxyethyl cellulose is the most often utilized cellulose ether. Together with other non-ionic, protective colloidal qualities, this soluble cellulose ether has the ability to thicken, suspend, disperse, emulsify, create films, and protect against water. HEC is widely used in many industrial fields such as polymer chemistry, cosmetics, agriculture, building materials, textiles and paper, paints, aerogel production, synthetic resins, ceramic industry, etc [11, 48, 49, 50, 51, 52, 53, 54, 55]. HEC powder can have a high viscosity in aqueous media, which varies depending on temperature and shear rate, and shows pseudoplastic behaviour. Aqueous solutions of hydroxyethyl cellulose are highly viscous and their viscosity varies depending on DS and molecular weight. It is also insoluble in most organic solvents [31, 56]. Figure 5 illustrates the molecular configuration of hydroxyethyl cellulose.

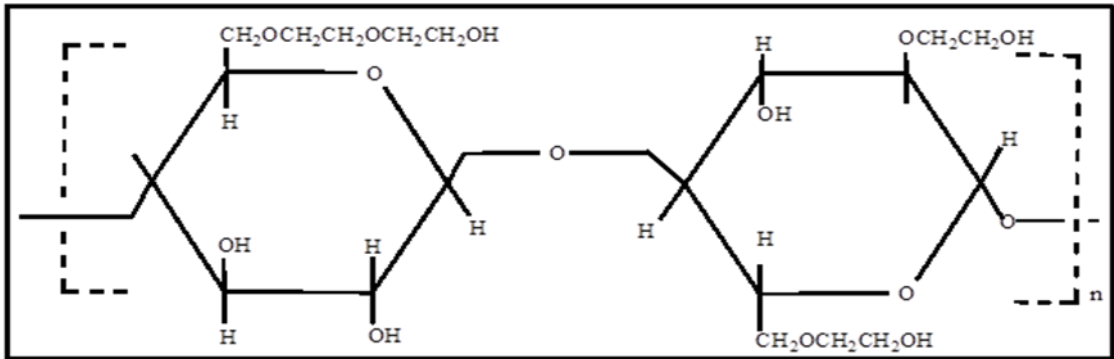


Fig 5 Molecular structure of hydroxyethyl cellulose [57].

2.4. Hydroxypropyl cellulose (HPC)

Sodium cellulose (Na-cellulose) is created when cellulose reacts with sodium hydroxide (NaOH). Hydroxypropyl cellulose (HPC) is produced by reacting sodium cellulose (or alkaline cellulose) with propylene oxide under high temperature and pressure. Propylene oxide with one or more of the three reactive hydroxyl groups present in each glucose monomer in the cellulose chain may create ether bonds under these circumstances. The degree of substitution (DS) varies in the range 1-3. However, if the second hydroxy group in the side chains reacts with propylene oxide, the DS value can be higher than 3. The obtained HPC is used in various industrial applications as colloidal stabiliser, flow regulator and surfactant. HPC exhibits heterogeneity because of the widely scattered arrangement of raw cellulose and the dispersion and allocation of propylene oxide throughout the polymer chain [58-61].

Hydroxypropyl cellulose is the most important cellulose derivative due to its easy production, complex phase behavior and hydrophilic properties [62]. Hydroxypropyl cellulose has a slightly yellowish white color and is a non-toxic, odorless and tasteless powder [48, 63]. As an application area, extruded films are widely used in food, pharmaceutical formulations and cosmetic products [48, 64, 65, 66]. It is used especially as a precipitant in many materials such as coating, encapsulation, bonding materials, foam carrier, protected colloids and foods, paper, ceramics and plastics [67]. Hydroxypropyl cellulose is a semi-crystalline polymer that is hydrophilic and soluble in non-ionic water and polar organic solvents and pH insensitive [24, 65]. In particular, when dissolved in water, they can be used as thickeners, binders, emulsifiers and stabilizers [65, 68]. It decomposes in water at temperatures below 40°C and in specific polar organic solvents such as methanol, ethanol, and isopropanol [59]. Figure 6 illustrates the molecular arrangement of hydroxypropyl cellulose.

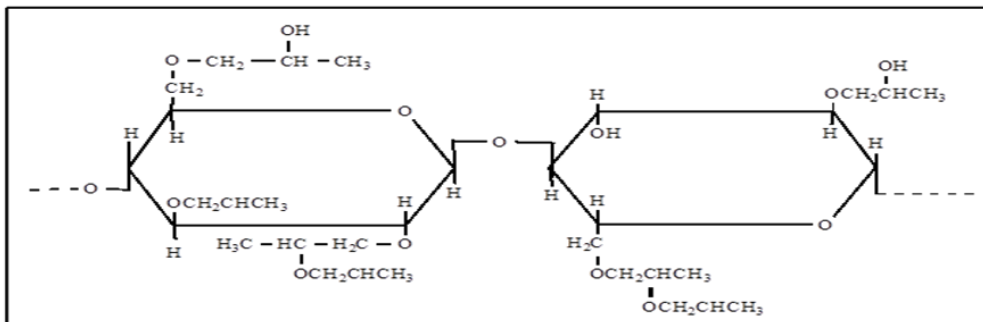


Fig 6. Molecular structure of hydroxypropyl cellulose [34].

2.5. Hydroxypropylmethyl cellulose (HPMC)

HPMC, a derivative of cellulose, is achieved through the reaction of alkaline cellulose with chloromethane and propylene oxide, resulting in partial *o*-methylation and *o*-(2-hydroxypropylation). HPMC is shown as the formula $C_8H_{15}O_8-(C_{10}H_{18}O_6)_n-C_8H_{15}O_8$ and its molecular weight is approximately 86000 [32, 69, 70, 71]. The term "molar substitution" (MS) in HPMC refers to the amount of hydroxypropyl groups each repeating unit, whereas "degree of substitution" (DS) refers to the number of methyl groups per unit [72-73.]

This cellulose derivative is a non-ionic polymer, soluble in cold water (below 40°C) but thermally reversible when heated in the range 50-80°C and turns into a relatively hard gel. It has a creamy or white hue, odourless, transparent, stable, oil-resistant and tasteless granular or fibrous powder. The solubility of HPMC, which has no toxic effect, is independent of pH (in the range of 1-10) and ionic strength, because there are no groups or permanent charges that can turn into ions in its structure. The lower the viscosity, the higher the solubility. At low temperatures, HPMC becomes more soluble in water, whereas at high temperatures, it becomes less soluble. This is due to the fact that water molecules and HPMC's hydroxypropyl groups may establish hydrogen bonds. The hydrogen bonds that hold water molecules together are more stiff on hydrophobic surfaces. The HPMC/water combination is transparent at low temperatures, and water molecules near hydrophobic methyl groups are arranged in a highly organized fashion. The system's kinetic energy grows with temperature, causing the hydrogen bonds to progressively weaken until the water molecules' lattice structures collapse and methyl groups emerge. At this point, the methyl groups' hydrophobic interactions start to encourage the development of a physical network with hydrophobic junctions. The gelation point of HPMC varies between 50 °C and 90 °C [69-74].

HPMC, among cellulose ethers, is commonly employed as the primary active component in hydrophilic matrix tablets designed for sustained release. At the same time, their roles as gelling agents hold significant importance in formulation procedures, as they contribute to the creation of a gel layer that resists diffusion and erosion through hydration, a crucial aspect in regulating drug release [43]. It also has a high swelling capacity, which significantly affects the release kinetics of the combined drug. It expands on contact with water or biological fluids and causes the polymer chains to relax, leading to an increase in its volume [75].

HPMC has several functions in the food industry as a film-forming, emulsifying, foaming, solubilising, stabilising, suspending and thickening agent. At the same time, HPMC serves as a semi-synthetic, viscoelastic polymer, inert and lacking in electrical charge, and is extensively employed as a lubricant in formulations related to ocular care, pharmaceuticals, medicine, food, and cosmetics [69, 74, 76, 77, 78]. Figure 7 depicts the molecular arrangement of hydroxypropylmethyl cellulose.

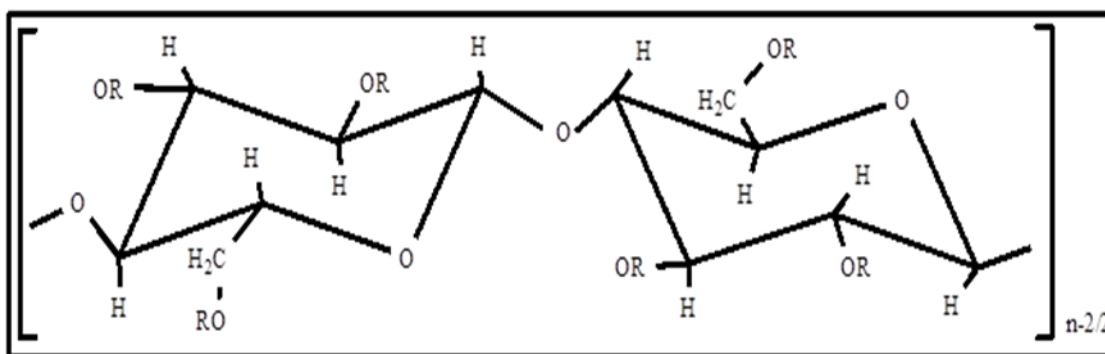


Fig 7. Molecular structure of hydroxypropyl methyl cellulose [79].

2.6. Carboxymethyl cellulose (CMC)

Carboxymethyl cellulose (CMC), a cellulose derivative, is a linear polysaccharide made up of anhydroglucose units that is both water-soluble and anionic. The repeating units are linked by β -1,4-glycosidic bonds. At the molecular scale, CMC and cellulose differ primarily in that CMC incorporates anionic carboxymethyl groups (CH_2COOH) within its structure, substituting certain hydroxyl groups found in pure cellulose. CMC was initially synthesized in 1918. According to the Williamson ether synthesis, the production of CMC involves two main stages: i) the alkaline cellulose process and ii) the esterification reaction. Initially, cellulose is treated with sodium hydroxide to produce active alkaline cellulose. This alkaline cellulose is then reacted with monochloroacetic acid. During this step, carboxymethyl groups replace the three hydroxyl groups in the cellulose molecules, with the degree of substitution ranging from 0.4 to 1.5. As a result of this substitution range, CMC can have molecular weights varying from 90,000 to 2,000,000 g/mol. However, the commercial production of these significant polymeric materials began in Germany in the early 1920s [80-81].

CMC is a crucial industrial polymer with diverse applications, such as entrainment reduction in sedimentation processes, in detergents, textiles, smart packaging industry, industrial construction and agricultural soil improvement, paper, food, pharmaceutical products, paint, pharmaceuticals and oil well drilling. It is also known as a viscosity increasing agent, widely used in pharmaceuticals, foods and cosmetics [21, 80, 82, 83, 84, 85] CMC forms through the interaction between alkaline cellulose and either monochloroacetic acid or Na-monochloroacetate via the Williamson ether synthesis process [12, 80, 86].

CMC stands as a paramount cellulose derivative, holding immense significance across industrial sectors and within our everyday routines. CMC, an anionic polysaccharide, exhibits water solubility and chemical reactivity owing to its elongated linear structure, featuring polar carboxyl groups derived from cellulose [11, 21, 87]. Moreover, refined cellulose exhibits a neutral flavor, lacks scent, and appears as a smooth ivory powder that flows freely. In addition to these properties, they have high molecular weight properties because they are water-soluble heteropolysaccharides. As a result, blending CMC with starch is frequently done to achieve the preferred consistency, enhance product excellence and durability, manage moisture levels, and guarantee optimal water movement [21, 87].

The characteristics of CMC change based on the level of substitution (DS, indicating the quantity of carboxymethyl groups in each anhydroglucose unit), the arrangement, and the polymerization extent. DS has the most significant influence on the solubility of the CMC solution, shear force, rheological characteristics, and resilience to temperature variations and the presence of low molecular weight additives [21]. The structural arrangement of carboxymethyl cellulose is depicted in figure 8.

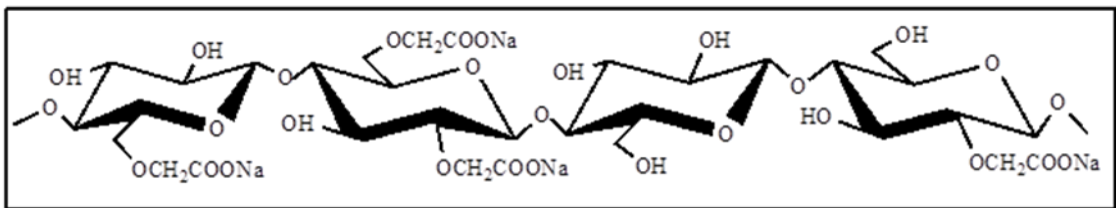


Fig 8. Molecular structure of carboxymethyl cellulose [87].

2.7. Sodium carboxymethyl cellulose (NaCMC)

NaCMC, a derivative of cellulose, which is the abundant polysaccharide composing the structural tissue of plants, is known as sodium carboxymethyl cellulose [88]. NaCMC is an anionic, linear cellulose derivative created through the reaction of cellulose with an alkali and chloroacetic acid. In this reaction, the H atom in the hydroxyl group of cellulose is replaced by the carboxymethyl group. As a result, the natural CH_2OH group in the glucose unit of cellulose

is easily replaced by the carboxymethyl group, thus obtaining sodium carboxymethylcellulose (NaCMC) [88-91]. This change is determined by the degree of displacement (DS). At the same time, the chain length of both DS and polymer determines the solubility, viscosity and gelation power of NaCMC [88].

NaCMC is used in many fields such as coatings, laminates, optical films and pharmaceuticals, as well as in the paper industry due to its high modulus, hardness, durability, thickening and stabilising properties. It is also one of the most important derivatives of cellulose, widely used in the food and cosmetics industries due to its moisturising, anti-caking, foaming, volumising, gelling and brightening properties. Nowadays, it is becoming increasingly popular as a soil conditioner [89]. Their high viscosity at low concentrations is the key characteristic that makes them valuable for these applications. Furthermore, the most important disadvantages of cellulose and derivative films are their mechanical properties, brittleness and low vapour permeability [24, 93, 94, 95, 96, 97] This polymer has become one of the most preferred cellulose derivatives due to its thickening, suspending, stabilizing, binding and film-forming properties [24, 98].

NaCMC is a derivative of cellulose in powder form, which is white to off-white in color, straight-chain, non-toxic, odorless, biodegradable and abundantly available, soluble in hot or cold water [23, 93, 94, 99, 100]. The molecular structure of NaCMC is illustrated in Figure 9.

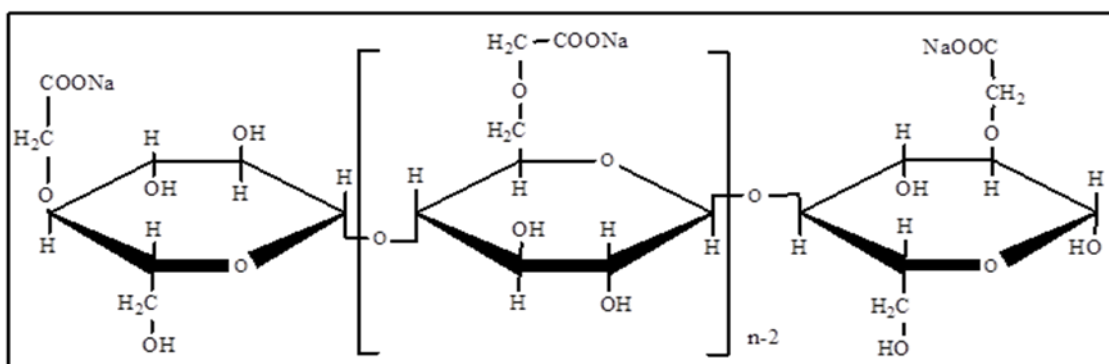


Fig 9. Molecular structure of sodium carboxymethyl cellulose [101].

The etherification and esterification derivatives of cellulose have many different uses and stand out as sustainable materials. These derivatives can show significant differences in their physical, chemical and mechanical properties depending on their environment and application conditions. The properties of various cellulose derivatives examined in detail within the scope of the study are presented comparatively in Table 1 and Table 2. In these tables, the properties of each cellulose derivative are summarized and their common applications are emphasized.

Table 1. Important properties of cellulose ethers considered in the study.

CELLULOSE ETHERS	PROPERTIES
Methylcellulose	<ul style="list-style-type: none"> ✓ pH value is between 2 and 12 ✓ Neutral, odourless, tasteless, inert and non-toxic and insoluble in water. ✓ Insoluble in most organic solvents. ✓ It is cost-effective and beneficial to the environment. ✓ It is synthesised by Williamson etherification method. ✓ It is used in pharmaceutical, chemical, ceramic, electrochemical supercapacitors and electrolyte applications. ✓ It gels in the range of 60-80 ° C temperatures. ✓ Polymerisation degree is in the range of 50-1000.

Ethyl cellulose	<ul style="list-style-type: none"> ✓ pH value is between 3 and 11. ✓ It is anionic and insensitive to pH. ✓ Insoluble in water. Dissolvable in organic solvents like alcohol, ether, ketone, and ester. ✓ Non-toxic and resistant to external factors. ✓ Its colour is white to light tan, odourless, tasteless powder and granular. ✓ It is used in areas such as optics, film formation, packaging, coating material and micro-encapsulation. ✓ Melting point is between 240 and 255 degrees Celsius. ✓ The transition temperature of glass is 120°C. ✓ Specific density is between 1.07-1.18, decomposition point 135-155°C and combustion temperature 330-360°C.
Hydroxyethyl cellulose	<ul style="list-style-type: none"> ✓ It is water soluble and has low density. ✓ Insoluble in most organic solvents. ✓ It is the most hydrophilic cellulose ether. ✓ It is an anionic substance with the ability to thicken, suspend, disperse, emulsify, create films, and protect against water.. ✓ It is used in polymer chemistry, ceramic industry, cosmetics, agriculture, construction materials, textiles, paper, paints, aerogel production, synthetic resins, etc.
Hydroxypropyl cellulose	<ul style="list-style-type: none"> ✓ It is anionic and semi-crystalline, soluble in most polar organic solvents and pH insensitive. ✓ It has a slightly yellow coloured white appearance. ✓ It is a non-toxic, odourless, tasteless powder. ✓ It is used in food, pharmaceuticals and cosmetics ✓ Used in industry as colloidal stabiliser, flow modifier and surface activator. ✓ It is used in coating, encapsulation, foam carrier, preserved colloid and food, paper, ceramics and plastics.
Hydroxypropylmethyl cellulose	<ul style="list-style-type: none"> ✓ Its solubility does not depend on pH value and ionic strength. ✓ It is a white or creamy white, odourless, transparent, stable, inert, oil resistant, non-toxic, anionic and tasteless granular or fibrous powder. ✓ Soluble in cold water below 40°C. ✓ It becomes a hard gel in the range of 50-80 °C. ✓ It is used in pharmaceutical, food and cosmetic fields. ✓ It has functions such as emulsifying, foaming, solubilising, stabilising, suspending and thickening agent.
Carboxymethyl cellulose	<ul style="list-style-type: none"> ✓ Anionic and soluble in water. Synthesised according to Williamson ether synthesis. ✓ It is a cream-coloured white, tasteless, odourless powder. ✓ It is used in detergents, textiles, smart packaging, construction, soil improvement, paper, food and paint.
Sodium carboxymethyl cellulose	<ul style="list-style-type: none"> ✓ It is odorless, non-toxic, soluble in both hot and cold water, and comes in powder form. It can decompose naturally. ✓ It is used in coatings, laminates, optical films, pharmaceutical and paper industry. ✓ It is widely used in food and cosmetics industry due to its moisturising, anti-caking, foaming, volumising, gelling and brightening properties.

3. Cellulose ester derivatives

Esterification, a common equilibrium reaction, involves the combination of an alcohol and an acid to produce an ester and water. Cellulose can undergo esterification with various acids, including acetic acid, nitric acid, sulfuric acid, and phosphoric acid [24]. Cellulose esters typically exhibit low solubility in water and possess excellent capabilities for forming films. Cellulose esters are widely used in pharmaceutical formulations for controlled release, such as in osmotic and enteric-coated drug delivery systems. These polymers are often used in combination with cellulose ethers to create microporous distribution membranes. Cellulose esters are divided into two distinct categories: one organic and the other inorganic. Cellulose esters derived from organic sources hold greater significance within the pharmaceutical sector. Different forms of organic cellulose esters find application in both commercial products and

pharmaceutical research. Organic cellulose esters like cellulose acetate (CA), cellulose acetate phthalate (CAP), cellulose acetate butyrate (CAB), cellulose acetate trimellitate (CAT), and hydroxypropylmethyl cellulose phthalate (CATM) exemplify this group. Organic cellulose esters hold greater significance in the pharmaceutical sector compared to their inorganic counterparts like cellulose nitrate and cellulose sulfate. Cellulose nitrate, also known as pyroxylin, possesses transparency and excellent film-forming properties. However, its infrequent utilization in pharmaceutical formulations stems from its minimal flammability in contemporary pharmaceutical solvents [19].

The presence of three hydroxyl (OH) groups in each glucose unit allows for the formation of mono-, di-, and tri-ester compounds. The mutual bonding of hydrogen bonds and OH- groups within the large molecular structure of cellulose causes this structure to be partially or completely broken during esterification. As the cellulose groups attack the cellulose chain in pieces, the chain structure of the cellulose either transforms into another structure or degradation occurs [12]. The esterification reaction of cellulose is shown in figure 10.

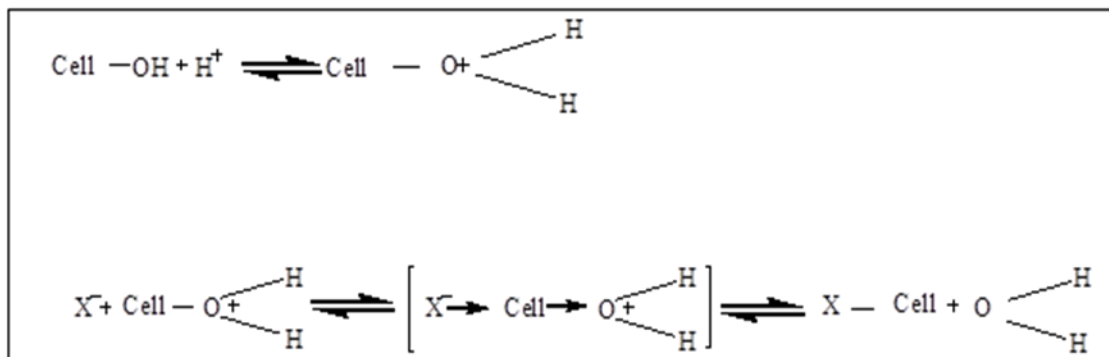


Fig 10. Esterification reaction of cellulose [12].

3.1. Cellulose acetate (CA)

Cellulose acetate (CA) is a widely used derivative of cellulose, the main component of plant cell walls. It can be produced from diverse natural resources including cotton, recycled newsprint, sugarcane pulp and straw, rice husk, sorghum straw, and Babassu coconut shells [102-103].

Cellulose acetate (CA) is a significant cellulose ester produced by reacting cellulose with acetic anhydride and acetic acid in the presence of sulfuric acid. This process facilitates the replacement of cellulose's hydroxyl groups with acetyl groups [23, 102, 104]. The degree of substitution (DS) significantly influences the material's properties, including its thermal behavior, hydrophobicity, transparency, processability, and solubility. Notably, hydrophobicity and processability distinguish cellulose acetate (CA) from natural cellulose, which is insoluble in most solvents. Additionally, as the DS increases, the glass transition temperature of cellulose acetate generally decreases [105]. The molecular structure of cellulose acetate is given in figure 11.

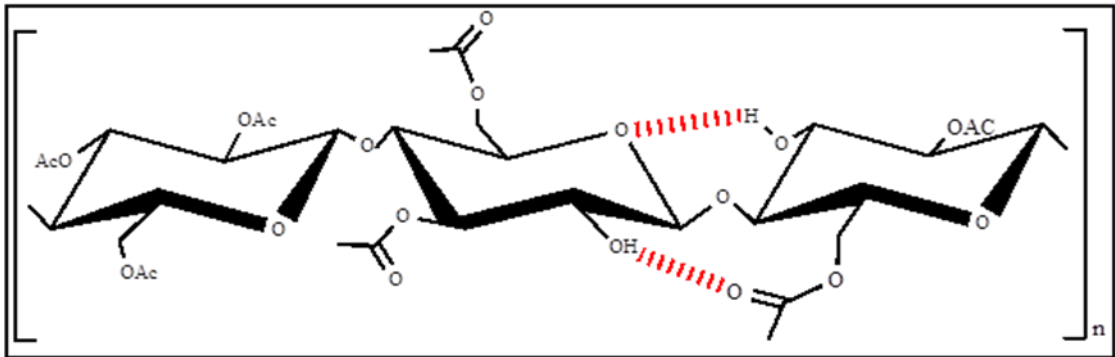


Figure 11. Chemical structure of cellulose acetate [106].

Cellulose acetate stands out as the most important biopolymer cellulose derivative obtained from organic acids. Thanks to its superior physical, chemical and biological properties, it finds wide application in many fields; varnishing, textiles, photographic films, active food packaging, removal of pollutants from waste water, plastic materials, membranes, cigarette filters, medical applications, film and fibre production [12, 105, 107, 108, 109, 110, 111, 112]. Compared to cellulose nitrate, its flammability and combustion properties are quite low. At the same time, film strips made of cellulose acetate can remain intact for many years [12]. CA is a biocompatible, biodegradable, and non-toxic biomaterial. It is relatively inexpensive, has low hygroscopicity, and exhibits excellent resistance to chemicals and heat [102, 113, 114]. Application areas that benefit from cellulose acetate are given in figure 12.

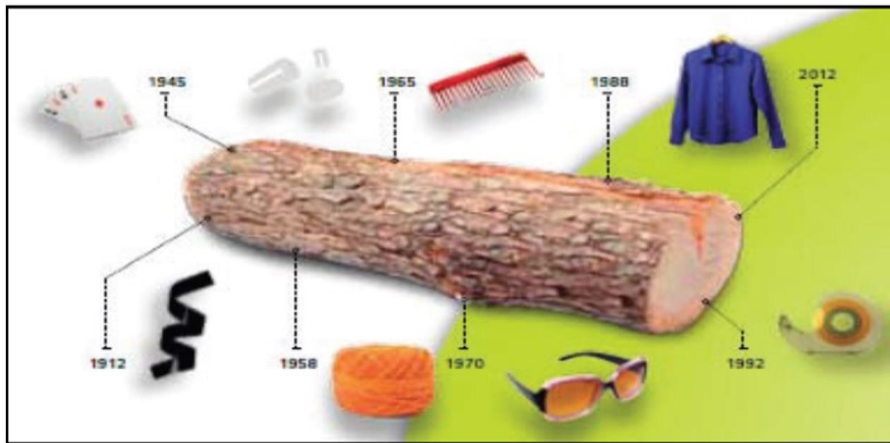


Fig 12. Application areas that benefit from cellulose acetate from past to present [106].

The mechanical strength, superior abrasion resistance, transparency, heat resistance, low water absorption, dyeability, simplicity of processing, moldability, and high dielectric strength of cellulose acetate are among its noteworthy qualities [12, 111, 121]. Cellulose ester derivatives like cellulose acetate-butyrate and cellulose acetate propionate hold more significance compared to standard cellulose acetate owing to their attributes, including minimal moisture absorption, heightened dimensional stability, exceptional resistance to atmospheric conditions, superior abrasion resistance, dyeing capabilities, and enhanced finishing techniques [12].

Technical properties determined by the degree of substitution are very important for cellulose acetate in terms of determining its solubility in organic solvents, its behavior in areas of use such as plastic material production and varnish resin production. At the same time, the structure responsible for the mechanical and processability properties of cellulose is called viscosity, that is, the degree of polymerization [12].

3.2. Cellulose nitrate (NC)

Cellulose nitrate (cotton powder) is an important cellulose derivative, a semi-synthetic plastic produced by the reaction of cellulose with inorganic acids. This polymer, produced through the nitration process involving a mixture of nitric acid, sulfuric acid, and water, is made up of d-glucopyranose units connected by β (1-4) glucosidic bonds. As a cellulose derivative, its structural distinction comes from the substitution of hydroxyl groups (-OH) in cellulose with nitrate groups (-ONO₂) [12, 115, 116]. Cellulose nitrate is used in various fields depending on its nitrogen content. These include plastics (celluloid), varnishes, energy binders, rocket propellants, smokeless gunpowder, civil and military applications, paints, production of new filter membranes, composite coatings, adhesives and explosive making. In particular, cellulose nitrate with a nitrogen content of less than 12% is used in the production of photographic films, inks and paints, while those with a nitrogen content of more than 12% are used as propellants in explosive formulations [12, 117, 118, 119, 120].

The degree of substitution of NC can be determined depending on the degree of polymerisation (DP) or nitrogen content of the cellulose. Differences in this degree of substitution also lead to variations in the products obtained. Furthermore, the different rates of substitution of cellulose nitrate also affect its solubility in organic solvents. [12]. Cellulose acetate (NC) is considered one of the most appealing and promising energetic materials for both current and future uses, thanks to its remarkable characteristics, including low cost, high flammability, explosive potential, and high enthalpy of combustion. [120]. However, cellulose nitrate poses a serious risk to museum and archive collections. This cellulose derivative can degrade substantially over time, leading to yellowing, brittleness, and cracking, which may eventually cause the material to disintegrate completely. It can also be dangerous as it releases nitric acid, a strong oxidiser and corrosive in its environment [119].

In addition to the previously mentioned applications of cellulose nitrate, it is also valued for its thermoplastic properties. Its ability to melt easily when heated makes it different from rubber. Another distinguishing characteristic of cellulose nitrate, compared to rubber, is its elastomeric property. Thanks to its elastomer feature, it prevents the shape from deteriorating easily, thus preserving the shape. While the nitration process for commercial purposes is carried out using sulfuric acid and aqueous nitric acid, the raw material of cellulose is obtained chemically from wood or pure cotton or cotton threads. To prevent issues like delignification and degradation caused by alkaline extraction during the cellulose extraction process and to achieve high degree of polymerization (DP) values, cellulose is sourced from wood that has undergone a nitration process. As a result of this application, the polymerization degree (DP) of different wood types was found to be between 5000 - 10,000. In studies conducted on this subject, it has been determined that mixtures rich in HNO₃ have a low degradation effect on cellulose. It has been observed that treating cellulose for a long time and the high temperature effect increases the yield obtained from extraction [112].

Table 2. Important properties of cellulose esters considered in the study.

CELLULOSE ESTERS	PROPERTIES
Cellulose acetate	✓ Used in varnishing, textiles, photographic films, active food packaging, waste water cleaning, plastics, membranes, cigarette filters, medical applications, film and fibers.
	✓ It has low ignition and combustion properties.
	✓ Non-toxic, low cost, chemical and heat resistant.
	✓ Mechanical durability, high abrasion resistance, low water absorption, dyeability and processability.

Cellulose nitrate	✓	It is a semi-synthetic plastic.
	✓	It is used in plastics, varnishes, rocket propellant formulations, smokeless gunpowder, civil and military applications, paints, composite coatings, adhesives and explosives.
	✓	Its low cost, high flammability and explosive properties make it attractive for future applications.
	✓	It is not recommended for use in museum and archive applications as it will deteriorate over time, causing yellowing, brittleness and cracking.
	✓	It is dangerous in environments where it releases nitric acid.
	✓	The degree of polymerization is between 5000-10000.

4. Conclusion

In the 1970s, with the industrial revolution, steam engines began to be used, and this caused a simultaneous increase in the use of synthetic products. The use of these unnatural products has started to have negative effects on the environment over time. Among these negative effects, the fact that the materials used remain intact in nature for many years after their useful life has ended has begun to be seen as the most important problem. As a result of these developments, searches have begun to use renewable and clean raw materials. One of the results of these searches is the use of cellulose raw material. Cellulose derivatives produced from cellulose raw material can also be considered in this context. It seems that they have significant advantages compared to petrochemical products, especially in terms of their rapid decomposition in nature after their use. At the same time, Cellulose derivatives, created through the modification of cellulose, possess robust, cost-effective, reproducible, recyclable, and environmentally friendly qualities.

Conflict Declaration

As the authors of this study, we declare that we have no declaration of conflict.

Acknowledgements

This review study received no specific grants from any funding agency in public, commercial, or non-profit organizations.

References

- [1] M. Granstrom, Cellulose Derivatives: "Synthesis, properties and applications," [dissertation], University of Helsinki, Helsinki, Finland, 2009.
- [2] L. Kuutti, "Cellulose, starch and their derivatives for industrial applications," VTT Technical Research Centre of Finland, 2013, <http://www.vtt.fi/publications/index.jsp>.
- [3] M. Poletto, V. Pistor and A. J. Zattera, "Structural characteristics and thermal properties of native cellulose," *Cellulose-fundamental aspects*, 2, 45-68, 2013, doi: 10.5772/50452.
- [4] A. K. Rana, E. Frollini and V. K. Thakur, "Cellulose nanocrystals: Pretreatments, preparation strategies, and surface functionalization," *International Journal of Biological Macromolecules*, 182, 1554-1581, 2021, doi:10.1016/j.ijbiomac.2021.05.119.
- [5] D. Ciolacu, F. Ciolacu and V. I. Popa, "Amorphous cellulose—structure and characterization," *Cellulose chemistry and technology*, 45(1), 13, 2011.
- [6] S. Coseri, "Cellulose: To depolymerize or not to?," *Biotechnology advances*, 35(2), 251-266, 2017, doi:10.1016/j.biotechadv.2017.01.002.
- [7] A. Etale, A. J. Onyianta, S. R. Turner and S. J. Eichhorn, "Cellulose: A review of water interactions, applications in composites, and water treatment," *Chemical reviews*, 123(5), 2016-2048, 2023, doi:10.1021/acs.chemrev.2c00477.
- [8] M. Gericke, A. J. Amaral, T. Budtova, P. De Wever, T. Groth, T. Heinze and P. Fardim, "The European Polysaccharide Network of Excellence (EPNOE) research roadmap 2040: Advanced strategies for exploiting the vast potential of polysaccharides as renewable bioresources," *Carbohydrate polymers*, 326, 121633, 2024, doi:10.1016/j.carbpol.2023.121633.
- [9] B. Magnus, "Absorbent cellulose based fibers Investigation of carboxylation and sulfonation of cellulose," Master of Science Thesis in the International Master's Program Chemical Engineering. Department of Chemical and Biological Engineering, Division of Materials Science, Chalmers University of Technology, Sweden, 2011.

- [10] Z. Hussain, W. Sajjad, T. Khan and F. Wahid, "Production of bacterial cellulose from industrial wastes: a review," *Cellulose*, 26, 2895-2911, 2019, doi: 10.1007/s10570-019-02307-1.
- [11] D. Lavanya, P. K. Kulkarni, M. Dixit, P. K. Raavi and L. N. V. Krishna, "Sources of cellulose and their applications—a review," *International Journal of Drug Formulation and Research*, 2, 2, 2011.
- [12] H. Kırıcı, S. Ateş and M. Akgül, "Selüloz türevleri ve kullanım yerleri," *Fen ve Mühendislik Dergisi*, 4(2), 119-130, 2001.
- [13] T. Aziz, A. Farid, F. Haq, M. Kiran, A. Ullah, K. Zhang and S. K. Al Jaouni, "A review on the modification of cellulose and its applications," *Polymers*, 14(15), 3206, 2022, doi:10.3390/polym14153206.
- [14] W. Cheng, Y. Zhu, G. Jiang, K. Cao, S. Zeng, W. Chen and H. Yu, "Sustainable cellulose and its derivatives for promising biomedical applications," *Progress in Materials Science*, 101152, 2023, doi:10.1016/j.pmatsci.2023.101152.
- [15] R. A. Festucci-Buselli, W. C. Otoni and C. P. Joshi, "Structure, organization, and functions of cellulose synthase complexes in higher plants," *Brazilian Journal of Plant Physiology*, 19(1), 1-13, 2007, doi:10.1590/S1677-04202007000100001.
- [16] R. J. Moon, A. Martini, J. Nairn, J. Simonsen and J. Youngblood, "Cellulose nanomaterials review: structure, properties and nanocomposites," *Chemical Society Reviews*, 40(7), 3941-3994, 2011, doi: 10.1039/c0cs00108b.
- [17] D.R. Bogati, "Cellulose based biochemicals and their applications," Bachelor's Thesis, Saimaa University of Applied Sciences, Lappeenranta, Finland, 2011.
- [18] H. Seddiqi, E. Oliaei, H. Honarkar, J. Jin, L. C. Geonzon, R. G. Bacabac and J. Klein-Nulend, "Cellulose and its derivatives: towards biomedical applications," *Cellulose*, 28(4), 1893-1931, 2021, doi:10.1007/s10570-020-03674-w.
- [19] J. Shokri and K. Adibkia, "Application of cellulose and cellulose derivatives in pharmaceutical industries," In *Cellulose-medical, pharmaceutical and electronic applications*. IntechOpen, 2013, doi: 10.5772/55178.
- [20] S. Zuppolini, A. Salama, I. Cruz-Maya, V. Guarino and A. Borriello, "Cellulose amphiphilic materials: Chemistry, process and applications," *Pharmaceutics*, 14(2), 386, 2022, doi:10.3390/pharmaceutics14020386.
- [21] B. Tosh, "Synthesis and sustainable applications of cellulose esters and ethers: A review," *International Journal of Energy, Sustainability and Environmental Engineering*, 1, 2, 2014.
- [22] P. L. Nasatto, F. Pignon, J. L. Silveira, M. E. R. Duarte, M. D. Nosedá and M. Rinaudo, "Methylcellulose, a cellulose derivative with original physical properties and extended applications," *Polymers*, 7(5), 777-803, 2015, doi:10.3390/polym7050777.
- [23] A. M. Hamad, S. Ates and E. Durmaz, "Evaluation of the possibilities for cellulose derivatives in food products," *Cellulose*, 45(2), 42-2, 2016.
- [24] S. Kamel, N. Ali, K. Jahangir, S. M. Shah and A. A. El-Gendy, "Pharmaceutical significance of cellulose: A review," *Express Polym Lett*, 2(11), 758-778, 2008, doi: 10.3144/expresspolymlett.2008.90.
- [25] T. Ahlfeld, V. Guduric, S. Duin, A. R. Akkineni, K. Schütz, D. Kilian and M. Gelinsky, "Methylcellulose—a versatile printing material that enables biofabrication of tissue equivalents with high shape fidelity," *Biomater Sci* 8: 2102–2110, 2020, doi: 10.1039/d0bm00027b.
- [26] C. Hopson, M. M. Villar-Chavero, J. C. Domínguez, M. V. Alonso, M. Oliet and F. Rodríguez, "Cellulose ionogels, a perspective of the last decade: A review," *Carbohydrate Polymers*, 274, 118663, 2021, doi: 10.1016/j.carbpol.2021.118663.
- [27] M. Dolaz, K. O. Ç. Ali, C. A. Ziba, S. Akarsu and B. Orhan, "Tekstil atıklarından selüloz eldesi, metil selüloz sentezi, karakterizasyonu ve çimento pastasında kullanımı," *Kahramanmaraş Sütçü İmam Üniversitesi Mühendislik Bilimleri Dergisi*, 19(3), 115-123, 2016.
- [28] S. Kalkan, E. Ünal and Z. Erginkaya, "Nisin ilave edilmiş metil selüloz filmlerin antimikrobiyel etkilerinin belirlenmesi," *Gıda ve Yem Bilimi-Teknolojisi Dergisi*, 14, 1-7, 2014.
- [29] M. K. Trivedi, A. Branton, D. Trivedi, G. Nayak, R. Mishra and S. Jana, "Characterization of physicochemical and thermal properties of biofield treated ethyl cellulose and methyl cellulose," *International Journal of Biomedical Materials Research*, 3(6), 83-91, 2015, doi: 10.11648/j.ijbmr.20150306.12.
- [30] M. L. Coughlin, L. Liberman, S. P. Ertem, J. Edmund, F. S. Bates and T. P. Lodge, "Methyl cellulose solutions and gels: Fibril formation and gelation properties," *Progress in Polymer Science*, 112, 101324, 2021, doi: 10.1016/j.progpolymsci.2020.101324.
- [31] F. D. Marques-Marinho and C. D. Vianna-Soares, "Cellulose and its derivatives use in the pharmaceutical compounding practice," In *Cellulose-medical, pharmaceutical and electronic applications*. IntechOpen, 2013, doi: 10.5772/56637.
- [32] S. Jain, P. S. Sandhu, R. Malvi and B. Gupta, "Cellulose derivatives as thermoresponsive polymer: an overview," *Journal of Applied Pharmaceutical Science*, 3(12), 139-144, 2013, doi: 10.7324/JAPS.2013.31225.
- [33] H. Jeong, J. Lee, Y. J. Jo and M. J. Choi, "Thermo-irreversible emulsion gels based on deacetylated konjac glucomannan and methylcellulose as animal fat analogs," *Food Hydrocolloids*, 137, 108407, 2023, doi: 10.1016/j.foodhyd.2022.108407.
- [34] R. L. Feller and M. H. Wilt, "Evaluation of cellulose ethers for conservation," The Getty Conservation Institute, Los Angeles, CA, USA, 1990.
- [35] H. Jin, W. Zhou, J. Cao, S. D. Stoyanov, T. B. Blijdenstein, P. W. De Groot and E. G. Pelan, "Super stable foams stabilized by colloidal ethyl cellulose particles," *Soft Matter*, 8(7), 2194-2205, 2012, doi: 10.1039/c1sm06518a.
- [36] D. Hegyesi, "Study of the widely used ethylcellulose polymer as film forming and matrix former agent," [dissertation], University of Szeged Faculty of Pharmacy, Hungary, 2016.
- [37] Jr. G. Regdon, D. Hegyesi and K. Pintye-Hódi, "Thermal study of ethyl cellulose coating films used for modified release (MR) dosage forms," *Journal of thermal analysis and calorimetry*, 108(1), 347-352, 2012, doi: 10.1007/s10973-011-1918-6.
- [38] T. Mahnaj, S. U. Ahmed and F. M. Plakogiannis, "Characterization of ethyl cellulose polymer," *Pharmaceutical development and technology*, 18(5), 982-989, 2013, doi:10.3109/10837450.2011.604781.
- [39] K. Wu, Q. Zhu, H. Qian, M. Xiao, H. Corke, K. Nishinari and F. Jiang, "Controllable hydrophilicity-hydrophobicity and related properties of konjac glucomannan and ethyl cellulose composite films," *Food Hydrocolloids*, 79, 301-309, 2018, doi:10.1016/j.foodhyd.2017.12.034.
- [40] G. Murtaza, "Ethylcellulose microparticles: A review," *Acta Poloniae Pharmaceutica*, 69(1), 11-22, 2012.
- [41] X. Su, Z. Yang, K. B. Tan, J. Chen, J. Huang and Q. Li, "Preparation and characterization of ethyl cellulose film modified with capsaicin," *Carbohydrate polymers*, 241, 116259, 2020, doi: 10.1016/j.carbpol.2020.116259.

- [42] Y. Zhou, Y. Hu, Z. Tan and T. Zhou, "Cellulose extraction from rice straw waste for biodegradable ethyl cellulose films preparation using green chemical technology," *Journal of Cleaner Production*, 439, 140839, 2024, doi: 10.1016/j.jclepro.2024.140839.
- [43] R. Enayatifard, M. Saeedi, J. Akbari and Y. H. Tabatabaee, "Effect of hydroxypropyl methylcellulose and ethyl cellulose content on release profile and kinetics of diltiazem HCl from matrices," *Tropical Journal of Pharmaceutical Research*, 8(5), 2009, doi:10.4314/tjpr.v8i5.48086.
- [44] P. Ahmadi, A. Jahanban-Esfahlan, A. Ahmadi, M. Tabibiazar and M. Mohammadifar, "Development of ethyl cellulose-based formulations: A perspective on the novel technical methods," *Food Reviews International*, 38(4), 685-732, 2022, doi:10.1080/87559129.2020.1741007.
- [45] M. O. Emeje, O. O. Kunle and S. I. Ofoefule, "Compaction characteristics of ethylcellulose in the presence of some channeling agents," *AAPS PharmSciTech*, 7(3), E18-E21, 2006, doi:10.1208/pt070358.
- [46] A. M. Agrawal, R. V. Manek, W. M. Kolling and S. H. Neau, "Studies on the interaction of water with ethylcellulose: effect of polymer particle size," *AAPS PharmSciTech*, 4(4), 469-479, 2003.
- [47] M. Davidovich-Pinhas, S. Barbut and A. G. Marangoni, "Physical structure and thermal behavior of ethylcellulose," *Cellulose*, 21, 3243-3255, 2014, doi: 10.1007/s10570-014-0377-1.
- [48] R. C. Rowe, P. Sheskey and M. Quinn, "Handbook of pharmaceutical excipients," Libros Digitales-Pharmaceutical Press, 2009.
- [49] N. Arfin and H. B. Bohidar, "Concentration selective hydration and phase states of hydroxyethyl cellulose (HEC) in aqueous solutions," *International journal of biological macromolecules*, 50(3), 759-767, 2012, doi:10.1016/j.ijbiomac.2011.11.028.
- [50] E. Kargı, "Sondaj çamuru uygulamaları için kil-polimer etkileşimlerinin belirlenmesi," [dissertation], İstanbul Teknik Üniversitesi, Fen Bilimleri Enstitüsü, İstanbul, Türkiye, 2015.
- [51] Z. Lu, J. Huang, E. Songfeng, J. Li, L. Si, C. Yao and M. Zhang, "All cellulose composites prepared by hydroxyethyl cellulose and cellulose nanocrystals through the crosslink of polyisocyanate," *Carbohydrate polymers*, 250, 116919, 2020, doi:10.1016/j.carbpol.2020.116919.
- [52] S. Basu, S. Malik, G. Joshi, P. K. Gupta and V. Rana, "Utilization of bio-polymeric additives for a sustainable production strategy in pulp and paper manufacturing: A comprehensive review," *Carbohydrate Polymer Technologies and Applications*, 2, 100050, 2021, doi:10.1016/j.carpta.2021.100050.
- [53] C. Cen, F. Wang, Y. Wang, H. Li, L. Fu, Y. Li and Y. Wang, "Design and characterization of an antibacterial film composed by hydroxyethyl cellulose (HEC), carboxymethyl chitosan (CMCS), and nano ZnO for food packaging," *International Journal of Biological Macromolecules*, 231, 123203, 2023, doi:10.1016/j.ijbiomac.2023.123203.
- [54] K. Ulutas, S. Yakut, D. Bozoglu, M. I. Tankul and D. Deger, "Thickness dependent glass transition temperature of hydroxyethyl cellulose thin films based on dielectric properties," *Journal of Applied Polymer Science*, 141(14), e55185, 2024, doi:10.1002/app.55185.
- [55] M. F. Abou Taleb and K. Alzidan, "Multifunctional applications of seaweed extract-infused hydroxyethyl cellulose-polyvinylpyrrolidone aerogels: Enhanced mechanical reinforcement, antibacterial, and antibiofilm proficiency for water decontamination," *International Journal of Biological Macromolecules*, 135021, 2024, doi:10.1016/j.ijbiomac.2024.135021.
- [56] K. Benyounes, S. Remli and A. Benmounah, "Rheological behavior of hydroxyethylcellulose (HEC) solutions," In *Journal of Physics: Conference Series*, Canada, (Vol. 1045, p. 012008). IOP Publishing, 2018, doi: 10.1088/1742-6596/1045/1/012008.
- [57] F. H. Zulkifli, F. S. J. Hussain, M. S. B. A. Rasad and M. M. Yusoff, "Nanostructured materials from hydroxyethyl cellulose for skin tissue engineering," *Carbohydrate polymers*, 114, 238-245, 2014, doi:10.1016/j.carbpol.2014.08.019.
- [58] E. Marsano and G. Fossati, "Phase diagram of water soluble semirigid polymers as a function of chain hydrophobicity," *Polymer*, 41(11), 4357-4360, 2000, doi:10.1016/S0032-3861(99)00795-8.
- [59] S. Mezdour, G. Cuvelier, M. J. Cash and C. Michon, "Surface rheological properties of hydroxypropyl cellulose at air-water interface," *Food Hydrocolloids*, 21(5-6), 776-781, 2007, doi:10.1016/j.foodhyd.2006.09.011.
- [60] M. H. Godinho, D. G. Gray and P. Pieranski, "Revisiting (hydroxypropyl) cellulose (HPC)/water liquid crystalline system," *Liquid Crystals*, 44(12-13), 2108-2120, 2017, doi:10.1080/02678292.2017.1325018.
- [61] A. Berardi, D. R. Perinelli, H. A. Merchant, L. Bisharat, I. A. Basheti, G. Bonacucina and G. F. Palmieri, "Hand sanitisers amid CoViD-19: A critical review of alcohol-based products on the market and formulation approaches to respond to increasing demand," *International journal of pharmaceuticals*, 584, 119431, 2020, doi:10.1016/j.ijpharm.2020.119431.
- [62] S. G. Hirsch and R. J. Spontak, "Temperature-dependent property development in hydrogels derived from hydroxypropylcellulose," *Polymer*, 43(1), 123-129, 2002, doi:10.1016/S0032-3861(01)00608-5.
- [63] M. El-Hag, M. W. Moselhey and O. Guirguis, "Extensive study of the mechanical properties of poly(vinyl alcohol)/ hydroxypropyl cellulose copolymer blends," *British Journal of Applied Science & Technology*. 21. 1-8, 2017, doi:10.9734/BJAST/2017/34114.
- [64] M. Bercea and P. Navard, "Viscosity of hydroxypropylcellulose solutions in non-entangled and entangled states," *Cellulose Chemistry and Technology*, 52, 603-608, 2019, https://hal.science/hal-02439814.
- [65] P. Talik, P. Moskal, L. M. Proniewicz and A. Weselucha-Birczyńska, "The Raman spectroscopy approach to the study of Water-Polymer interactions in hydrated hydroxypropyl cellulose (HPC)," *Journal of Molecular Structure*, 1210, 128062, 2020, doi:10.1016/j.molstruc.2020.128062.
- [66] J. Zhang, M. Guo, M. Luo and T. Cai, "Advances in the development of amorphous solid dispersions: The role of polymeric carriers," *Asian Journal of Pharmaceutical Sciences*, 100834, 2023, doi:10.1016/j.ajps.2023.100834.
- [67] G. Şengül, S. Demirci, S. Çörekçi and T. Caykara, "Annealing effect on surface segregation behavior of hydroxypropylcellulose/polyethylenimine blend films," *Applied surface science*, 255(17), 7703-7707, 2009, doi:10.1016/j.apsusc.2009.04.141.
- [68] C. Carotenuto and N. Grizzuti, "Thermoreversible gelation of hydroxypropylcellulose aqueous solutions," *Rheologica acta*, 45(4), 468-473, 2006, doi: 10.1007/s00397-005-0075-x.
- [69] K. Ghosal, S. Chakrabarty and A. Nanda, "Hydroxypropyl methylcellulose in drug delivery," *Der pharmacia sinica*, 2(2), 152-168, 2011.
- [70] W. Huichao, D. Shouying, L. Yang, L. Ying and W. Di, "The application of biomedical polymer material hydroxy propyl methyl cellulose (HPMC) in pharmaceutical preparations," *Journal of Chemical and Pharmaceutical Research*, 6(5), 155-160, 2014.

- [71] T. Majumder, G. R. Biswas and S. B. Majee, "Hydroxy propyl methyl cellulose: different aspects in drug delivery," *J. Pharm. Pharmacol.*, 4(8), 381-5, 2016, doi: 10.17265/2328-2150/2016.08.003.
- [72] L. L. Tundisi, G. B. Mostaço, P. C. Carricondo and D. F. S. Petri, "Hydroxypropyl methylcellulose: Physicochemical properties and ocular drug delivery formulations," *European Journal of Pharmaceutical Sciences*, 159, 105736, 2021, doi:10.1016/j.ejps.2021.105736.
- [73] E. S. Khater, A. Bahnasawy, B. A. Gabal, W. Abbas and O. Morsy, "Effect of adding nano-materials on the properties of hydroxypropyl methylcellulose (HPMC) edible films," *Scientific Reports*, 13(1), 5063, 2023, doi:10.1038/s41598-023-32218-y.
- [74] D. Phadtare, G. Phadtare and M. Asawat, "Hypromellose—a choice of polymer in extended release tablet formulation," *World J Pharm Pharm Sci*, 3(9), 551-566, 2014.
- [75] J. Siepmann and N. A. Peppas, "Modeling of drug release from delivery systems based on hydroxypropyl methylcellulose (HPMC)," *Advanced drug delivery reviews*, 64, 163-174, 2012, doi:10.1016/j.addr.2012.09.028.
- [76] F. D. Marques-Marinho and C. D. Vianna-Soares, "Cellulose and its derivatives use in the pharmaceutical compounding practice," In *Cellulose-Medical, Pharmaceutical and Electronic Applications*. IntechOpen, 2013, doi: 10.5772/56637.
- [77] C. Ding, M. Zhang and G. Li, "Preparation and characterization of collagen/hydroxypropyl methylcellulose (HPMC) blend film," *Carbohydrate polymers*, 119, 194-201, 2015, doi:10.1016/j.carbpol.2014.11.057.
- [78] R. Ghadermazi, S. Hamdipour, K. Sadeghi, R. Ghadermazi and Asl. A. Khosrowshahi, "Effect of various additives on the properties of the films and coatings derived from hydroxypropyl methylcellulose—A review," *Food science & nutrition*, 7(11), 3363-3377, 2019, doi: 10.1002/fsn3.1206.
- [79] J. Siepmann and N. A. Peppas, "Modeling of drug release from delivery systems based on hydroxypropyl methylcellulose (HPMC)," *Advanced drug delivery reviews*, 64, 163-174, 2012, doi:10.1016/j.addr.2012.09.028.
- [80] V. Kanikireddy, K. Varaprasad, T. Jayaramudu, C. Karthikeyan and R. Sadiku, "Carboxymethyl cellulose-based materials for infection control and wound healing: A review," *International Journal of Biological Macromolecules*, 164, 963-975, 2020, doi:10.1016/j.ijbiomac.2020.07.160.
- [81] M. S. Rahman, M. S. Hasan, A. S. Nitai, S. Nam, A. K. Karmakar, M. S. Ahsan and M. B. Ahmed, "Recent developments of carboxymethyl cellulose," *Polymers*, 13(8), 1345, 2021, doi:10.3390/polym13081345.
- [82] V. Pushpamalar, S. J. Langford, M. Ahmad and Y. Y. Lim, "Optimization of reaction conditions for preparing carboxymethyl cellulose from sago waste," *Carbohydrate Polymers*, 64(2), 312-318, 2006, doi:10.1016/j.carbpol.2005.12.003.
- [83] S. Jain, P. S. Sandhu, R. Malvi and B. Gupta, "Cellulose derivatives as thermoresponsive polymer: an overview," *Journal of Applied Pharmaceutical Science*, 3(12), 139-144, 2013, doi: 10.7324/JAPS.2013.3.1225.
- [84] R. Ramakrishnan, J. T. Kim, S. Roy and A. Jayakumar, "Recent advances in carboxymethyl cellulose-based active and intelligent packaging materials: a comprehensive review," *International Journal of Biological Macromolecules*, 129194, 2024, doi:10.1016/j.ijbiomac.2023.129194.
- [85] F. Shao, H. Yan, S. Lin, Q. Wang, W. Tao, J. Wu and L. Su, "Magnetically treated water drip irrigation combined with carboxymethyl cellulose (CMC) application: A regulating strategy for enhancing the jujube yield and quality in southern Xinjiang of China," *Scientia Horticulturae*, 326, 112723, 2024, doi:10.1016/j.scienta.2023.112723.
- [86] T. Heinze and A. Koschella, "Carboxymethyl ethers of cellulose and starch—A review," *Macromolecular Symposia*, 223(1), 13–40, 2005, doi: 10.1002/masy.200550502.
- [87] M. H. Koh, "Preparation and characterization of carboxymethyl cellulose from sugarcane bagasse," [dissertation], Universiti Tunku Abdul Rahman, Petaling Jaya, Malaysia, 2013.
- [88] A. P. Rokhade, S. A. Agnihotri, S. A. Patil, N. N. Mallikarjuna, P. V. Kulkarni and T. M. Aminabhavi, "Semi-interpenetrating polymer network microspheres of gelatin and sodium carboxymethyl cellulose for controlled release of ketorolac tromethamine," *Carbohydrate polymers*, 65(3), 243-252, 2006, doi:10.1016/j.carbpol.2006.01.013.
- [89] F. He, D. Zhao, J. Liu and C. B. Roberts, "Stabilization of Fe–Pd nanoparticles with sodium carboxymethyl cellulose for enhanced transport and dechlorination of trichloroethylene in soil and groundwater," *Industrial & Engineering Chemistry Research*, 46(1), 29-34, 2007, doi: 10.1021/ie0610896.
- [90] T. Shui, S. Feng, G. Chen, A. Li, Z. Yuan, H. Shui and C. Xu, "Synthesis of sodium carboxymethyl cellulose using bleached crude cellulose fractionated from cornstark," *Biomass and Bioenergy*, 105, 51-58, 2017, doi:10.1016/j.biombioe.2017.06.016.
- [91] S. Li, Y. M. Liu, Y. C. Zhang, Y. Song, G. K. Wang, Y. X. Liu and X. D. Guo, "A review of rational design and investigation of binders applied in silicon-based anodes for lithium-ion batteries," *Journal of Power Sources*, 485, 229331, 2021, doi:10.1016/j.jpowsour.2020.229331.
- [92] G. Li, Y. Shan, W. Nie, Y. Sun, L. Su, W. Mu and Q. Wang, "Application of carboxymethyl cellulose sodium (CMCNa) in maize–wheat cropping system (MWCS) in coastal saline-alkali soil," *Science of The Total Environment*, 912, 169214, 2024, doi:10.1016/j.scitotenv.2023.169214.
- [93] X. H. Yang and W. L. Zhu, "Viscosity properties of sodium carboxymethylcellulose solutions," *Cellulose*, 14(5), 409-417, 2007, doi: 10.1007/s10570-007-9137-9.
- [94] C. G. Lopez, S. E. Rogers, R. H. Colby, P. Graham and J. T. Cabral, "Structure of sodium carboxymethyl cellulose aqueous solutions: A Sans and rheology study," *Journal of Polymer Science Part B: Polymer Physics*, 53(7), 492-501, 2015, doi: 10.1002/polb.23657.
- [95] B. Wang, X. Yang, C. Qiao, Y. Li, T. Li and C. Xu, "Effects of chitosan quaternary ammonium salt on the physicochemical properties of sodium carboxymethyl cellulose-based films," *Carbohydrate polymers*, 184, 37-46, 2018, doi:10.1016/j.carbpol.2017.12.030.
- [96] A. Baran, E. Sulukan, M. Türkoğlu, A. Ghosigharehagaji, S. Yildirim, M. Kankaynar and S. B. Ceyhun, "Is sodium carboxymethyl cellulose (CMC) really completely innocent? It may be triggering obesity," *International Journal of Biological Macromolecules*, 163, 2465-2473, 2020, doi:10.1016/j.ijbiomac.2020.09.169.
- [97] E. Cherif and H. Moumni, "The properties on a polysaccharide of Sodium carboxymethylcellulose (CMC) in dimethylacetamide+ acetone by Conductometric study," *Physics and Chemistry of Liquids*, 60(3), 442-451, 2022, doi:10.1080/00319104.2021.2012776.

- [98] G. O. Akalin and M. Pulat, "Preparation and characterization of nanoporous sodium carboxymethyl cellulose hydrogel beads," *Journal of Nanomaterials*, 2018, Volume 2018, doi:10.1155/2018/9676949.
- [99] C. Xiao and Y. Gao, "Preparation and properties of physically crosslinked sodium carboxymethylcellulose/poly (vinyl alcohol) complex hydrogels," *Journal of applied polymer science*, 107(3), 1568-1572, 2008, doi: 10.1002/app.27203.
- [100] W. Lan, L. He and Y. Liu, "Preparation and properties of sodium carboxymethyl cellulose/sodium alginate/chitosan composite film," *Coatings*, 8(8), 291, 2018, doi:10.3390/coatings8080291.
- [101] F. He, D. Zhao, J. Liu and C. B. Roberts, "Stabilization of Fe–Pd nanoparticles with sodium carboxymethyl cellulose for enhanced transport and dechlorination of trichloroethylene in soil and groundwater," *Industrial & Engineering Chemistry Research*, 46(1), 29-34, 2007.
- [102] M. A. Wsoo, S. Shahir, S. P. M. Bohari, N. H. M. Nayan and S. I. Abd Razak, "A review on the properties of electrospun cellulose acetate and its application in drug delivery systems: A new perspective," *Carbohydrate research*, 491, 107978, 2020, doi:10.1016/j.carres.2020.107978.
- [103] A. Bouftou, K. Aghmih, F. Lakhdar, N. Abidi, S. Gmouh and S. Majid, "Enhancing cellulose acetate film with green plasticizers for improved performance, biodegradability, and migration study into a food simulant," *Measurement: Food*, 15, 100180, 2024, doi:10.1016/j.meafao.2024.100180.
- [104] S. Fischer, K. Thümmler, B. Volkert, K. Hettrich, I. Schmidt and K. Fischer, "Properties and applications of cellulose acetate," *Macromol. Symp.* 262, 89–96, 2008, doi: 10.1002/masy.200850210.
- [105] S. C. Teixeira, N. O. Gomes, T. V. de Oliveira, P. Fortes-Da-Silva, N. D. F. F. Soares and P. A. Raymundo-Pereira, "Review and Perspectives of sustainable, biodegradable, eco-friendly and flexible electronic devices and (Bio) sensors," *Biosensors and Bioelectronics*: X, 14, 100371, 2023, doi:10.1016/j.biosx.2023.100371.
- [106] C. Bao, "Cellulose acetate/plasticizer systems: structure, morphology and dynamics," [dissertation], Université Claude Bernard, Lyon I, France, 2015.
- [107] H. Liu and Y. L. Hsieh, "Ultrafine fibrous cellulose membranes from electrospinning of cellulose acetate," *Journal of Polymer Science Part B: Polymer Physics*, 40(18), 2119-2129, 2002, doi:10.1002/polb.10261.
- [108] G. Rodrigues Filho, D. S. Monteiro, C. da Silva Meireles, R. M. N. de Assunção, D. A. Cerqueira, H. S. Barud and Y. Messadeq, "Synthesis and characterization of cellulose acetate produced from recycled newspaper," *Carbohydrate Polymers*, 73(1), 74-82, 2008, doi:10.1016/j.carbpol.2007.11.010.
- [109] H. S. Barud, A. M. de Araújo Júnior, D. B. Santos, R. M. de Assunção, C. S. Meireles, D. A. Cerqueira and S. J. Ribeiro, "Thermal behavior of cellulose acetate produced from homogeneous acetylation of bacterial cellulose," *Thermochimica Acta*, 471(1-2), 61-69, 2008, doi:10.1016/j.tca.2008.02.009.
- [110] J. Puls, S. A. Wilson and D. Hölder, "Degradation of cellulose acetate-based materials: a review," *Journal of Polymers and the Environment*, 19(1), 152-165, 2011, doi: 10.1007/s10924-010-0258-0.
- [111] N. A. Bahmid, K. Syamsu and A. Maddu, "Production of cellulose acetate from oil palm empty fruit bunches cellulose," *Chemical and Process Engineering Research*, 17, 2013, <https://www.iiste.org/Journals/index.php/CPER/J>.
- [112] M. P. Egot and A. C. Alguno, "Preparation and characterization of cellulose acetate from pineapple (Ananas comosus) leaves," *Key Eng. Mater.* 772, 8-1, 2018, doi: 10.4028/www.scientific.net/KEM.772.8.
- [113] N. Nikoomeh, M. Zandi and A. Ganjloo, "Development of eco-friendly cellulose acetate films incorporated with Burdock (Arctium lappa L.) root extract," *Progress in Organic Coatings*, 186, 108009, 2024, doi:10.1016/j.porgcoat.2023.108009.
- [114] G. V. Carballo, H. L. Yang, Y. X. Hsu, R. B. Leron, H. A. Tsai and K. R. Lee, "Incorporation of zwitterionic carbon quantum dots in cellulose acetate tubular membrane for oil/water separation," *Separation and Purification Technology*, 337, 126301, 2024, doi:10.1016/j.seppur.2024.126301.
- [115] A. L. M. Neves, "Cellulose Nitrate Objects In Collections: History Of Science And Technology Hand In Hand With Conservation Of Cultural Heritage," [dissertation], NOVA University Lisbon, Portugal, 2023.
- [116] E. Kim, C. Longo, E. C. Docking, C. Gallupe, R. Langmuir and C. Magarro, "Treatment Case Studies in the Consolidation and Adhesion of Cellulose Nitrate," *Studies in Conservation*, 1-16, 2024, doi:10.1080/00393630.2024.2345422.
- [117] S. Berthumeyrie, S. Collin, P. O. Bussiere and S. Therias, "Photooxidation of cellulose nitrate: New insights into degradation mechanisms," *Journal of Hazardous Materials*, 272, 137-147, 2014, doi:10.1016/j.jhazmat.2014.02.039.
- [118] Y. Gismatulina, A. Korchagina, V. Budaeva and G. Sakovich, "Highly soluble cellulose nitrates from unconventional feedstocks," MATEC Web of Conferences Bandung, Indonesia, (Vol. 243, p. 00005). EDP Sciences, 2018, doi:10.1051/mateconf/201824300005.
- [119] A. Neves, E. M. Angelin, É. Roldão and M. J. Melo, "New insights into the degradation mechanism of cellulose nitrate in cinematographic films by Raman microscopy," *Journal of Raman Spectroscopy*, 50(2), 202-212, 2019, doi: 10.1002/jrs.5464.
- [120] S. Bekhouche, D. Trache, A. Abdelaziz, A. F. Tarchoun, S. Chelouche, A. Boudjellal and A. Mezroua, "Preparation and characterization of MgAl-CuO ternary nanothermite system by arrested reactive milling and its effect on the thermocatalytic decomposition of cellulose nitrate," *Chemical Engineering Journal*, 453, 139845, 2023, doi:10.1016/j.cej.2022.139845.
- [121] V. Vatanpour, M. E. Pasaoglu, H. Barzegar, O. O. Teber, R. Kaya, M. Bastug and I. Koyuncu, "Cellulose acetate in fabrication of polymeric membranes: A review," *Chemosphere*, 295, 133914, 2022, doi:10.1016/j.chemosphere.2022.133914.



Contents lists available at *Dergipark*

Journal of Scientific Reports-A

journal homepage: <https://dergipark.org.tr/en/pub/jsrc>



E-ISSN: 2687-6167

Number 59, December 2024

REVIEW ARTICLE

Receive Date: 08.07.2024

Accepted Date: 09.09.2024

The golden discovery of *camelina sativa*: a pivotal study of its unique components and its multiple uses in various applications in science and industry

Rayane Mahious^a, Ebru Halvacı^b, Aysenur Aygun^b, Fatih Sen^{b*}

^aDepartment of Biology, Kutahya Dumlupinar University, 43000, Kutahya, Turkiye, ORCID: 0009-007-9443-1934

^bDepartment of Biochemistry, Sen Research Group, Kutahya Dumlupinar University, 43000, Kutahya, Turkiye, ORCID: 0009-0003-2343-0046

^bDepartment of Biochemistry, Sen Research Group, Kutahya Dumlupinar University, 43000, Kutahya, Turkiye, ORCID: 0000-0002-8547-2589

^bDepartment of Biochemistry, Sen Research Group, Kutahya Dumlupinar University, 43000, Kutahya, Turkiye, ORCID: 8449363400

Abstract

The increase in the global population causes a rapid increase in environmental pollution and energy consumption. Countries aim to increase the use of alternative energy sources as fossil fuels are limited and not universally accessible when generating their energy. In addition, research in the biofuels industry is expanding to include research on the use of vegetable oils as fuel. Camelina serves as a perfect illustration because of its abundant nutrients. Camelina, known as *Camelina sativa* L. Crantz, is a member of the cruciferous family and has been grown for its valuable characteristics for many centuries. Camelina seeds contain high levels of both protein (27-32%) and oil (38-43%). Camelina oil is rich in various components like phytosterols, phenolic compounds, tocopherols, and fatty acids, with omega-3 and omega-6 being the key ones. In the field of agriculture, growing this crop is appealing because it has a brief growing period and requires little water and fertilizers. Camelina is well-suited for arid regions because of its ability to withstand dry conditions and low temperatures. Due to its economic importance and easy cultivation in recent years, Camelina has many applications such as biofuel, food, agriculture, animal feed, cosmetics, and medicine. For example, Camelina is grown in the United States and Europe as a valuable crop that can be used to replace existing fuels. Future research aims to enhance its agricultural characteristics and view it as a substitute for existing fuels. This review focuses on the camelina plant, its oil, components, and properties, as well as its use in areas such as food, biofuels, animal feed, and agrochemicals.

© 2023 DPU All rights reserved.

Keywords: Brassicaceae; *Camelina sativa*; fatty acids; fuels; phenolic compounds.

* Corresponding author.

E-mail address: fatihsen1980@gmail.com

1. Introduction

Plant extracts have been used in many application areas such as medicine, cosmetics, and food since ancient times due to their aromatic and healing properties [1], [2], [3]. The structure of plant extracts includes flavonoids, steroids, phenolics, alkaloids, enzymes, amino acids, proteins, and saponins [4], [5], [6], [7]. All parts of plants such as seeds, stems, leaves, flowers, and fruits are used in the production of plant extracts. Filtering, microwave, Soxhlet, and boiling are the most important methods to obtain plant extracts [8], [9], [10], [11]. Several seed-bearing plants, including Camelina (*Camelina sativa*), groundnut (*Arachis hypogaea*), mustard (*Brassica* spp), and soybean (*Glycine max*), are excellent sources of oil. A few of these species are commonly utilized in the production of edible oil. However, Camelina stands apart from the rest due to its versatility [12]. Camelina oil is produced for a variety of uses, including food, medicine, and industry. Biodiesel is one application for this plant oil in the industry. One of the remarkable traits of Camelina is its minimal fertilizer requirements and its ability to flourish in marginal and impoverished soils. It has a short growth cycle of 85 to 100 days [13], [14], [15], [16]. Camelina is more resilient than other oil crops under abiotic stress, and studies have indicated that it may compete with other members of the Brassicaceae family, such as *Brassica napus* and *Brassica juncea* [17], [18].

2. History of the camelina species

Camelina is an old plant native to Central Asia and Europe [19]. Humans have cultivated and used it since the Iron Age in various daily activities. During the Iron and Bronze Ages, inhabitants of Scandinavia and Western Europe domesticated the camelina plant for use as food, cooking oil, and cattle feed, while its wild ancestors almost completely covered Europe and Central Asia. Additionally, some research suggests that it was present in eastern Turkey between the years 700 and 900 BCE [20], [21]. Although research on genetic diversity suggests that the origins of many species are likely in either Russia or Ukraine [22]. After being grown for centuries in Europe and North America, canola, a higher-yielding oil seed crop, replaced *Camelina sativa* in the 1950s [20], [21]. Currently, only a small amount of land in Germany, Poland and Russia is used for production [15].

3. Botanical features

Camelina sativa is a flowering plant and an oilseed source belonging to the Camelinae tribe of the Brassicaceae family [23], [24]. *Camelina sativa* goes by several names, including gold of pleasure and false flax [16], [23], [25], [26], [27]. Camelina is grown throughout Europe and Central Asia, as well as in Russia, where it is considered native. Its cultivation was stopped after World War II for economic and other benefits [19], [25], [28]. There are four species within the Camelina genus: *Camelina alyssum*, *Camelina microcarpa*, *Camelina rumelica*, and *Camelina sativa*. Among these species, *Camelina sativa* is one of the most used types [17]. Although the chromosome number of *Camelina* has been reported to be $n = 6$, $n = 14$, $2n = 12$, $2n = 26$, or $2n = 40$, $2n = 40$ is the most widely accepted, researchers from many regions of the world have reported varying numbers of chromosomes [21], [29]. Natural variation within populations may be the cause of variations in chromosome numbers [29], [30]. Camelina has simple hairy leaves arranged alternately on a straight, slightly rough stem [17]. The lance-shaped leaves have margins that are either smooth or lobed. It may have smooth or dichotomous bristles, typically 2-10 mm wide and 2-8 cm long [24], [29]. Leaves without petioles are arranged in an alternative position, usually touching each other. Camelina plants have a height ranging from 30 to 80 cm at maturity [29]. Camelina plants yield diminutive yellow flowers measuring 5-7 mm in diameter, featuring four petals arranged in a racemose configuration [31]. These floral structures bear resemblance to other Brassica flowers, yet are distinguished by the presence of delicate, lance-shaped leaflets. Camelina is mostly self-pollinating, characterized by its perfect anther flowers housing medium-sized pollen grains, which range from spherical to prolate in shape [17], [29]. The camelina fruit is shaped like a pear, orange-to-brown pod that is 10 to 25 mm wide and 5 mm long and is around one-fourth to one-half the size of canola seeds [17], [32]. Camelina has 8 to 15 seeds with color ranging from golden to brown [32]. Camelina has short roots, which allows it to draw water from shallow soil layers and is well adapted to fallow wheat production systems in arid regions [29].

Camelina seeds (Fig. 1) are quite tiny, measuring 2 to 3 mm in length [17], [32], and the weight of 1000 seeds is between 0.8 and 1.8 g [21], [29]. Camelina seed pods are siliques; globular and rounded, divided by a septum and typically contain 10 to 25 seeds at maturity. Seed pod changes their colour from green to yellow-reddish and then completely dry at full maturity [17], [24], and [29]. Camelina seeds contain 27 to 32% protein and 38 to 43% oil [16], [33], [34]. At harvest, the grain moisture level should be about 11%, and during storage, it should be around 8%. Unfavourable weather during harvest might result in a decrease in grain production. The germination period is 4 to 6 weeks, depending on the prevailing weather conditions [23].

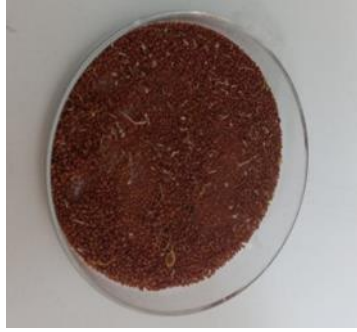


Fig 1. Camelina seeds.

4. Plant camelina and agricultural practices

Camelina is gaining an increase in economic importance in the field of the agricultural sector due to its different attributes [31], [35]. Its oil content in dry weight ranges between 30 and 48% [31], [35], [36]. These values are twice that of soybeans, which contain between 18 and 22% oil [37]. Because of its short growth cycle and minimal water and fertilizer requirements, interest in this crop has surged [14], [21]. Camelina contains many phytochemicals that increase its resistance to pests and diseases, which is another reason why it is a resilient crop [38]. Camelina can grow in hot and cold climate conditions, and this is what led to heightened attention in the agricultural sector [21], [39]. Compared to other oilseed crops, camelina seeds can germinate at 0°C, as their plants can tolerate very low temperatures [40], [41]. These features enable it to thrive in cold climates [42]. During seed growth, temperature rises more than 25°C may cause a significant drop in the amount of unsaturated fatty acid [43]. Camelina is usually sown in spring, but winter sowing is also possible. It is best to plant them in late October. Seeding rate, soil preparation, planting method, and seeding depth all influence seed yield and plant growth [44], [45]. Camelina might improve soil quality when grown in rotation with grains. Seeds are sown at a short depth with good soil contact. This can be performed by drilling seeds with packing wheels or disseminating seeds with a roller harrow [46]. The recommended planting rate is 3 to 7 kg/ha (250 to 600 seeds/m²), with a stand density of 125 to 200 plants/m². Increased seeding rates can reduce the time to maturity and increase yield competitiveness. Row spacing is suggested for camelina production. The ideal row spacing for camelina cultivation is 20–30 cm, while 15 cm row spacing might be advised to prevent weed infestation [17]. Camelina emergence rates range from 12% to 70%, with a 40% average. Because of its limited growth season, it is advised that it be planted no more than once every three to four years. Camelina may be used in multiple cropping systems, particularly in warmer areas [34]. Camelina seeds react well to fertilizers high in nitrogen, sulphur, and phosphorus [47]. The application of nitrogen fertilizer enhances crop yield but diminishes oil content. The nitrogen response of *Camelina sativa* is like that of *Brassica juncea* on Canadian prairies, so cultivators can use *Brassica juncea*'s soil recommendations for *Camelina sativa* production [48]. Camelina, a short-season crop, requires little nitrogen fertilizer, with suggested rates ranging from 60 to 100 kg N/ha [49]. Phosphorus and sulphur may potentially increase yield, although the ideal treatment rate is uncertain. Camelina can tolerate dry soil, minimal rainfall, and cold temperatures, ripening 21 days earlier than flaxseed. It requires few fertilizers and has a sensitivity to nitrogen, phosphate, and potassium. In Montana, the highest yield was obtained with 78.5 to 100.9 kg N ha⁻¹. In

Romania, the yield of seeds rose by 14% and 27% with 40 and 60 kg P ha⁻¹, respectively. Phosphor increases oil content, but nitrogen decreases it. Nitrogen treatment enhanced plant height, total nitrogen content, and seed output, among other agronomic and quality metrics [34]. In new studies conducted by Hazrati and his friends on camelina crop, activated biochar can enhance soil quality for crop production under rainfed conditions. A split plot experiment with nine treatments and three replicates has been conducted to study the effects of supplementary irrigation and activated biochar on camelina growth. The results showed that Activated Biochar 10 and Activated Biochar at flowering stage increased seed and oil yield, unsaturated fatty acid content, seed yield (2751.8 kg/ha), 1000 seed weight (1.16 g), and oil yield (991.50 kg/ha) [50].

5. Camelina's most important applications

Many culinary and health items are made with camelina oil, where its usage rate reaches 80%. In addition, about 14% of camelina oil is used in industrial materials such as plastic softening compounds, cosmetics, detergents, lubricants, eco-fuels, phytochemicals, and adhesives [12]. Although the use of camelina as a cooking oil is largely limited, it plays an essential role in meeting the needs of increasing demand for bio-oils, especially in the biofuel industry. Camelina is characterized by a unique fatty acid profile, which allows it to be used in multiple industries such as medical, agricultural, nutrition, and the biofuel industry. Therefore, camelina has gained a good reputation in recent years due to its multiple usage and effectiveness in a variety of industries [14], [15], [34], [51].

5.1 Biodiesel

5.1.1 Biofuel manufacturing

Environmental pollution is mostly caused by the continued use of traditional non-renewable fuels. It results in the release of greenhouse gases, which have a detrimental effect on the environment. More generally, greenhouse gases such as carbon dioxide and nitrogen oxide cause climate change and increase global temperatures. Moreover, these high emissions lead to many other environmental problems, and therefore a lack of biodiversity [52]. Consequently, we should consider using renewable and sustainable energy sources as alternatives to traditional fuels to preserve the environment and reduce the effects of pollution. As a result, there is a growing interest in the manufacture of renewable fuels such as biodiesel, ethanol, and biomet fuel [53], [54]. Many feedstocks for biofuel production are being investigated, including seed oils, animal fats, algae, and low-value waste products (such as grease, cooking oil, and soap) [55], [56]. Although not all oilseeds are appropriate for production, some desirable qualities of vegetable oils in biofuel preparation include high seed yield, high oil content, unique fatty acids, consistent seed maturation rate, and flexibility in the local growing environment. In addition, it is especially desired to employ non-edible oilseed crops in the creation of biofuel to preserve the balance within the generation of food products and biofuel [20]. Many studies have examined the benefits of using Camelina oil extracts to produce diesel fuel [57]. Based on their previous research, scientists have emphasized the nutritional importance of camelina oil [36], [58], and on the other hand, they have emphasized its economic importance in the industrial sector due to its short life cycle compared to canola and soybean [59].

Camelina oil is transformed into methyl or ethyl esters of long-chain fatty acid by the alcohol esterification process. Low-emission biofuels have been created using these esters as a substitute for conventional fuels. The researchers found that adding camelina oil, which produces a high-iodine methyl ester similar to rapeseed, improved biodiesel fuel. For usage in diesel engines, transformed biodiesel's fatty acids profile must equal that of the original oil, and the pure form must adhere to the American Society for Testing and Materials D6751 (ASTM D6751) in North America and the European Standard 14214 (EN14214) in the European Union. Certain factors, such as cetane number, kinematic viscosity, distillation temperature, oxidative stability, and cold flow qualities, influence the fatty acid makeup of the original oil. The degree of unsaturation and the chain length of the original oil fatty acid esters have an

impact on the characteristics of biodiesel. Checking the fatty acid profile is therefore essential for achieving the best biodiesel production [14], [60].

Various alcohols were mixed at 10% ratio with Camelina biodiesel for fuel analysis. Improvements in viscosity, density, calorific value, and cold flow properties were observed in all blends. Heptane, hexane, ethanol, and butanol blends have low flash points, while n-pentanol and iso-pentanol mixtures have higher flash points. High flash points are important for safe fuel transportation and storage. Blending camelina biodiesel with n-pentanol produced the most favourable results among the alcohols tested [61].

5.1.2. Hydroprocessed renewable jet fuel (HRJ)

The American Society for Testing and Materials (ASTM) International considers the Hydrotreated Esters and Fatty Acid (HEFA-SPK) or Hydrotreated Renewable Jet (HRJ) pathway as one of the most approved pathways for aviation biofuel production. Diversifying aviation fuel sources serves to achieve different goals; This includes reducing aviation emissions and reducing the cost of aviation fuel due to fluctuations in crude oil prices [61], [62]. These objectives are met with sustainable raw materials and production techniques. By utilizing sustainable, environmentally friendly materials and methods, HEFA-certified biofuels have the potential to lower operational expenses associated with fuel usage. Camelina presents itself as a potential raw material for hydrotreated renewable jet fuel. Camelina is being considered as a potential alternative to conventional jet fuel [58]. Agriculture and oil conversion operations demand a lot of energy and emit a lot of pollutants. Except in organic soils and heavy clay soil conditions, camelina matures in 80 to 100 days, depending on the soil type, making it a valuable plant [14], [63]. Camelina-derived jet fuel offers multiple environmental benefits for aviation, including substantial decrease in greenhouse gas emissions and energy utilization, and improved engine performance [64], [65]. The use of Camelina biofuel blends can lead to decreased emissions of carbon monoxide, unburnt hydrocarbons, and soot, although there may be a slight increase in nitrogen oxides [66]. Camelina-derived jet fuel can deliver 70% life cycle emission savings and improved thermodynamic behaviour in an operational gas turbine engine, resulting in 3-3.8% fuel savings [67].

5.2. Chemical byproducts

5.2.1. Bioadhesive

Recently, there has been an increased interest in producing ecologically friendly and renewable adhesives to replace formaldehyde-based resins which include Phenol-Formaldehyde (PF) and Urea Formaldehyde (UF), which are generated from non-renewable petrochemical sources [68]. Researchers investigated a variety of alternatives, including bio-based substances such as Camelina protein [26] and soybean-derived adhesives [69]. Canola and camelina proteins have the potential to replace conventional petroleum-based adhesives in several applications [26]. Globulin's compact shape results in weaker adhesion qualities and increased protein aggregation, whereas glutelin from defatted Camelina meal were reported to have superior adhesive strength than globulin [26]. Applications for pressure-sensitive adhesives include graphics, medical supplies, tapes, and labels, among others [70].

5.2.2. Alkyd resin

Polymeric alkyd resins are widely utilized in composites, adhesives, and coatings, among other industrial applications. These resins are synthesized from polyols and renewable vegetable oils. A novel source to produce these resins is camelina oil [14], [71]. In 2015, Nosal and associates developed an alkyd resin by alcoholizing oligomerized glycerol with camelina oil, employing renewable camelina oil and polyglycerol. The resins were produced by polycondensing the alcoholysis products of camelina oil with anhydrides of phthalic and maleic acids at temperatures ranging between 230°C and 250°C. The resulting resins exhibited drying periods and flexibility comparable to those derived from pentaerythritol and camelina oil. Additionally, alkyd resins were synthesized using camelina oil as a raw material and glycerol as a polyol, and their properties were compared to linseed oil-based products. The alkyd resins demonstrated characteristics like those of linseed oil-based polymers, highlighting their potential for a variety of applications [72].

5.2.3. Cosmetics and soaps

Oilseed crops are becoming increasingly important in the biorefinery industry due to their renewable and valuable feedstocks, particularly for pharmaceuticals, nutraceuticals, fine chemicals, cosmetics, agrochemicals, and biomaterials [16], [73]. Notably, vegetable oils have emerged as crucial ingredients in the cosmetic industry, particularly amidst a growing consumer inclination towards "Clean Beauty." This trend has led to a substantial increase, reportedly by 75%, in the utilization of "natural" raw materials in the cosmetic market [35]. In addition to industrial uses, camelina oil is useful in the manufacture of soap and cosmetics [74], [75]. Camelina oil's significant antioxidant capacity makes it suitable for usage in a range of cosmetic compositions. There are already a lot of commercial cosmetic goods, such as face and body lotions, shampoos, and other hair care items, that contain camelina oil in their formulation. Some companies, such as Springfield and Siberian Tiger Naturals, produce camelina oil-based soaps and distribute them in small markets. Cosmetics containing camelina oil are specially chosen by people who prefer to use vegetable oils in their beauty products [75].

5.2.4. Agrochemicals

Agricultural chemicals are important tools used to protect crops and enhance their growth and fertility. However, due to its irregular use, many problems such as pest resistance, health problems, and soil pollution have emerged [76]. The risks connected with synthetic pesticide usage have led to the use of organic pesticides (biopesticides), which are less expensive, environmentally friendlier, and more sustainable. Therefore, it is possible to replace these chemicals with plant-derived pesticides, which are considered a "green" alternative, as they decompose naturally and do not harm the environment [77]. Plant-derived insecticides are available in different forms, such as powders, pure plant materials, and extracts [78]. In field crops, camelina is a powerful insecticide, pesticide, and antifungal. It has been reported that when Camelina is applied to the soil at a rate of 5% and 1%, it inhibits the sclerotial germination and hyphae development of the *Phymatotrichopsis omnivorous* (Duggar) fungus, which causes cotton root rot and problems in cotton and alfalfa production. Secondary metabolites, such as Glucosinolates (GSLs), convert into nitrile, thiocyanate, and isothiocyanate, which help protect plants [12], [21]. *Camelina sativa* has been revealed to exhibit allelopathic properties, which restrict weed development while indirectly affecting pathogen dynamics [31], [79]. It is discovered that the effects of varying concentrations of aqueous extracts from Brassicaceae cover crops on *Ambrosia artemisiifolia* L varied depending on the species and concentration. *Camelina sativa* had the greatest ability to restrict shoot, radicle length, germination, and fresh seedling weight. The study discovered 15 phenolic compounds in the Brassicaceae, with Camelina containing the most vanillin, chlorogenic acid, vanillic acid, caffeic acid, and syringic acid. These data indicate that Camelina is the most allelopathic species employed in the study, and its seeds are particularly high in allelochemical content [31], [80].

5.3. Therapeutic medicinal applications

Camelina Sativa has gained a prominent position among nutritional materials due to its components, which have a biological activity that plays an important role in preserving human health and protecting it from diseases [73]. Fatty acids such as Alpha linoleic acids and Linolic are the most important omega-3 fatty acids. In its natural state, our body cannot produce these acids, and therefore we must obtain them externally to prevent negative effects on nutrition and body health, such as poor growth and neurological disfunction. Docosahexaenoic acids and eicosapentaenoic acids are the most important alpha linoleic products, which have proven effective in preventing heart diseases [81], [82]. Camelina's richness in biological compounds gives it a very distinctive characteristic among natural oil plants. These compounds give it several activities, such as anti-viral, anti-cancer, and antioxidant activity. Tocopherol and eicosenoic acids are among the most important contents of Camelina, as they are present in varying proportions in the human body and contribute to its protection [83], [84]. Due to its distinctive activity against infections, it is included among the effective medicines for treating burns of various degrees and eye irritation [12], [85].

Phytosterols and tocopherols are fatty acids that are present in varying proportions in oil plants. Researchers have proven the effectiveness of these substances in preventing heart diseases caused by high levels of cholesterol in the blood. Camelina contains good amount of these acids, especially phytosterols, making it an important product that

contributes to reducing harmful cholesterol levels in the body [86].

5.3.1. Edible camelina oil

Since ancient times, humans have relied on collecting plants and including them in their meals because of their advantages. Oil plants are one of these plants that have occupied a prominent position due to their richness in beneficial fatty acids such as Omega 3-6-9. These fatty acids constitute a large percentage of camelina oil, which is considered an alternative to current oils used in cooking [87], [88].

5.3.2. Camelina meal and cake

Camelina contains many organic substances, the most important of which are proteins, vitamins, and essential fatty acids. Camelina is used as a plant-based protein source in animal feed [89], [90]. Camelina meal can reduce thyroid activity in some animals, according to previous research [91]. Experiments investigating the effect of *camelina sativa* oil on blood metabolism characteristics in broiler chickens have shown that dietary intake containing camelina can affect plasma lipid profile. In a study published by Anca, the plasma lipid profile of broiler chickens fed a diet containing camelina oil have shown various levels of cholesterol decrease, as well as other changes in blood lipid content. In comparison, other studies have shown a tangible impact on plasma lipid levels when camelina oil is added to the diet. The results of the studies indicate that *camelina sativa* oil can contribute to reducing lipid levels, including cholesterol, in the blood [92], [93].

6. Camelina's bioactive components

Oil plants contain many active substances, such as phenolic acids, tocopherols, and others, in addition to essential fatty acids, which have many roles in the human body. These compounds play a role in enhancing the activity of the mind and protecting the body from cardiovascular diseases and other diseases [39], [94], [95]. Camelina also occupies an important position among these oils [39]. The principal product of the *Camelina sativa* plant is the oil produced by crushing and pressing the seeds, which comprises roughly 30 to 40% oil on a dry matter basis. 90% are unsaturated fatty acids. Camelina oil is a bright yellow liquid with a slightly nutty aroma and a distinct mustard odor. Camelina oil's physical qualities include a refractive index of 1.4756, a density of 0.92 g/cm² measured at 25°C, an iodine value of 105 (g I₂/100 g oil), and a saponification value of 187.8 (mg KOH/g oil) [88].

6.1. Content of essential amino acids

Camelina is an excellent source of protein. The protein content of various camelina feed components varies. Camelina seed has 24.78% protein, whereas seed byproducts such as cake have more protein. Camelina cake has a crude protein level similar to rapeseed meal (29.69-39.89%) but lower than soybean meal (43.0-56.3%) [96], [97]. It is well recognised that the essential amino acids composition of proteins indicates their biological importance. In camelina cake, the necessary amino acids range from 15.09 to 18.39%. Where it contains a minimum of 17 amino acids. The principal amino acids contents are isoleucine, leucine, lysine, phenylalanine, and valine. Protein in camelina seeds is abundant in non-essential amino acids such as glutamic and aspartic acids, serine, proline, and arginine, in addition to essential amino acids [98]. Camelina seeds contain many essential amino acids, especially arginine [99]. The fact that Camelina meal, which is extracted from its seeds, contains high levels of proteins makes it the best source of protein and energy for animals [91], [100]. The corresponding table shows the contents of *Camelina Sativa's* essential amino acids (Table 1).

Table 1. Essential amino acids profile of *Camelina sativa* [35], [42], [101].

Amino acids	Content (g/100 g)
Aspartic acids	8.71–9.04
Phenylalanine	4.19–5.22
Cystine	1.94–2.12
Alanine	4.61–6.14

Glutamic acids	14.98–16.12
Glycine	5.25–6.06
Histidine	2.60–4.06
Isoleucine	3.96–4.62
Arginine	8.15–8.57
Leucine	6.63–7.12
Methionine	1.72–2.85
Lysine	4.46–4.52
Proline	5.09–6.07
Serine	5.04–5.96
Threonine	2.75–2.89
Tryptophan	1.21–1.32
Tyrosine	3.04–3.64
Valine	5.42–6.34

6.2. Composition of fatty acids

Recently, researchers have shown interest in *Camelina sativa* in various sectors, especially industry and agriculture, thanks to its chemical contents [52]. Camelina seeds are a raw source of essential oils, especially fatty acids, where they contain varying percentages of them. Camelina oil consists predominantly of saturated fatty acids, accounting for 64% of its composition, with low percentages of polyunsaturated and monounsaturated fatty acids, at 30% and 6%, respectively. The quality of fatty acids in camelina seeds is affected by climatic conditions and the quality of the crop [16], [39], [99]. Camelina oil contains elevated concentrations of alpha linoleic acid (18:3, 31–40%), oleic (18:1, 14–16%), linoleic (18:2, 15–23%), and eicosenoic (20:1, 12–15%) acids. Minor fatty acids such as palmitic (16:0), stearic (18:0), and erucic (22:1) acids. Camelina meal contains 0.17% myristic acids (C14:0), 7.19–9.12% palmitic acids (C16:0), 2.27–2.9% stearic acids (C18:0), 28.6–36.77% linolenic acids (C18:3), 13.5–28.5% linoleic acids (C18:2) and 14.4–19.9% oleic acids (C18:1) are among its constituents. Camelina seed contains significant amounts of palmitic acids (C16:0), myristic acid (C14:0), and stearic acids (C18:0). The fatty acids inside of camelina grains are 14.4–19.9% oleic acids (C18:1) and 13.5–28.5% linoleic acids (C18:2) [102], [103]. The ranges of camelina cake myristic acids (C14:0) ranges from 0.1 to 0.2%, whereas palmitic acids (C16:0) 7.19 to 9.46%. The percentage ranges of oleic acids (C18:1), linoleic acids (C18:2), and linolenic acids (C18:3) in camelina meal are 17.8–21.7, 24.35–28.8%, and 24.2–46.3%, respectively. One of the best natural sources of n-3 PUFA, especially alpha linoleic acids. The range of Camelina seed's polyunsaturated fatty acids (PUFA) content is 55.2–57.1%, monounsaturated fatty acids content is 32.1–36.16% and its Saturated Fatty Acids (SFA) content is 9.04–13.3%. Camelina oil consists of 55.2 % PUFA, 10.2 % SFA, and 34.6 % MUFA [51], [102]. The corresponding table displays the various percentages of fatty acids found in Camelina seeds (Table 2.)

Table 2. The various percentages of fatty acids found in Camelina seed [103], [104].

Fatty acids (%)	[105]	[106]	[107]	[108]
Arachidic acids	1.3	1.5	1.8	1.7
Behenic acids	-	0.3	0.8	0.4
Clupanodinic acids	-	0.2	0.4	-
Arachidonic acids	1.4	1.4	-	-
Docosatrienoic acids	-	0.4	-	-
Erucic acids	2.3	3.1	4.2	3.5
Eicosadienoic acids	1.8	2.2	1.9	1.8
Gadoleic acids	14	15	11.9	15.1

Lignoceric acids	-	0.2	-	-
Linoleic acids	18.5	19.1	18.7	18.5
Linolenic acids	35.8	33.5	28.6	32.8
Myristic acids	-	0.1	0.2	-
Nervonic acids	-	0.6	-	0.7
Oleic acids	16.1	14.4	17.6	15.7
Palmitic acids	6.1	5.5	5.1	5.7
Palmitoleic acids	0.1	0.1	0.3	-
Stearic acids	2.6	2.4	2.4	2.4

6.3. Phenolic compounds

Plant oils, particularly cold-pressed varieties, are an abundant source of biologically active compounds like the hydroxylated derivatives of cinnamic and benzoic acids coumarins, lignin and flavonoid compounds [109], [110], [111]. There are few investigations on the existence of natural phenolic compounds and antioxidant activity in *Camelina sativa* extracts [108], [111]. Camelina oil contains 760 mg of tocopherols, which are important antioxidants for the oxidative stability of vegetable oils. Other tocopherols include α -tocopherol (28.07–41.8 mg/kg) and delta-tocopherol (12.3–20.47 mg/kg). Pure camelina oil had a higher total tocopherol concentration (751–687 mg/kg) than rapeseed and flax oil [112]. Fresh camelina oil contains 123 mg of polar phenolic molecules, which are also known as chlorogenic acids. Camelina cake includes phenolic substances such as tocopherols, sinapine, and sinapic acids [111]. Several phenolic compounds were identified in camelina cake that may be responsible for the antioxidant effect. Tocopherols, sinapic and sinapine acids are the main antioxidants found in camelina cake, while flavanols also play a role in its antioxidant properties [113], [114]. Camelina contains large amounts of phenolic acids and flavonoids. The phenolic acids quantity in camelina in oil is from 681.89 to 892.12 mg/L and in seed ranges between 2043.6 to 3704.7 mg/kg, in the cake from 1148.67 to 1413.76 mg/kg dry matter. Flavonoids in camelina seed from 329.49 to 526.4 mg/kg, oil from 266.01 to 435.32 mg/L, and cake range from 37.69 to 73.13 mg/g [39].

6.4. vitamins, macroelements, and microelements in camelina

Camelina contains a significant amount of vitamin B1 (thiamine), B3 (niacin), and B5 (pantothenic acids). *Camelina Sativa* generally has higher levels of B-series vitamins when compared to the other seeds, except for pyridoxine (B6) [85], [115]. Vitamin B3 is the most abundant vitamin in camelina seed (194 μ g/g) [94], twice as much as flaxseed's (91 μ g/g) [85]. Camelina contains 18 μ g/g of vitamin B1 and 11.3 μ g/g of vitamin B5. Camellina has much more thiamine than flaxseed (6 μ g/g) and rapeseed (8 μ g/g). Pantothenic acids concentration in camelina is similar to flaxseed (11 μ g/g) but lower than rapeseed (16 μ g/g) [87], [116].

Camelina seed contains a trace of macrominerals. Potassium (K) (1.6%), phosphor (P) (1.4%) and calcium (Ca) (1.0%) are among the greatest concentrations. Additionally, camelina seed includes sulphur (S) (0.24%), magnesium (Mg) (0.51%), sodium (Na) (0.06%), and chlorine (Cl) (0.04%). The iron amount of camelina seed is substantial (329 μ g/g), and it also contains large amounts of zinc (Zn) (69 μ g/g). It includes 1.9 μ g of nickel (Ni) and 9.9 μ g of copper (Cu) per gram [87].

Camelina meals are composed of carbohydrates such as disaccharides, monosaccharides, polysaccharides, oligosaccharides, and fibre. Monosaccharides and disaccharides are easily digested and provide rapidly metabolizable energy in the human body. Camelina is characterized by a low concentration of carbohydrates. It contains 5.5% sucrose, which is twice the percentage of flaxseed (2.8%) but less than rapeseed (6.8%). Camelina contains very small amounts of oligosaccharides, such as stachyose and raffinose (less than 1%) [34]. For polysaccharides, which include starch, pectin, and mucilage, the percentage of starch and pectin does not exceed (1%). The mucilage content in camelina is 6.7%, less than flaxseed (8%) [87]. Camelina meal includes different secondary metabolites such as

sinapine, inositol phosphates, glucosinolates, and condensed tannins, which are common antinutritional chemicals found in oilseeds. Sinapine and GSLs are often connected with Brassicaceae plants [116].

7. Conclusion

Recent studies have shown the importance of the *Camelina sativa* plant as a rich source of nutrients and active substances. According to available research, camelina seed oil has a special combination of vital fatty acids, making it beneficial for human health and many industrial applications. With further research and developments in agriculture and biotechnology, camelina are expected to have a significant impact in improving human food and improving environmental sustainability. Therefore, future research is important to discover the full potential of the camelina plant and make the most of its potential benefits.

Acknowledgements

We extend our sincere thanks to the researchers, scientists and experts whose previous studies and results laid the foundation for our research. Their valuable ideas and contributions have influenced our understanding of *Camelina sativa* and its many benefits. We appreciate the support and encouragement from our teachers, advisors, and colleagues who provided guidance, feedback, and motivation throughout the research process.

References

- [1] B. Şahin *et al.*, "Cytotoxic Effects Of Platinum Nanoparticles Obtained From Pomegranate Extract By The Green Synthesis Method On The MCF-7 Cell Line," *Colloids Surfaces B Biointerfaces.*, vol. 163, pp. 119-124, Mar. 2018, doi: 10.1016/j.colsurfb.2017.12.042.
- [2] A. Aygün, S. Özdemir, M. Gülcan, K. Cellat, and F. Şen, "Synthesis and characterization of Reishi mushroom-mediated green synthesis of silver nanoparticles for the biochemical applications," *J. Pharm. Biomed. Anal.*, vol. 178, pp. 112970, Jan. 2020, doi: 10.1016/j.jpba.2019.112970.
- [3] A. Aygun *et al.*, "Biogenic platinum nanoparticles using black cumin seed and their potential usage as antimicrobial and anticancer agent," *J. Pharm. Biomed. Anal.*, vol. 179, pp. 112961, Feb. 2020, doi: 10.1016/j.jpba.2019.112961.
- [4] F. Göl, A. Aygün, A. Seyrankaya, T. Gür, C. Yenikaya, and F. Şen, "Green Synthesis and Characterization of Camellia Sinensis Mediated Silver Nanoparticles for Antibacterial Ceramic Applications," *Mater. Chem. Phys.*, vol. 250, pp. 123037, Aug. 2020, doi: 10.1016/j.matchemphys.2020.123037.
- [5] B. Şahin, E. Demir, A. Aygün, H. Gündüz, and F. Şen, "Investigation of the effect of pcranate extract and monodisperse silver nanoparticle combination on MCF-7 cell line," *J. Biotechnol.*, vol. 260, pp. 79-83, Oct. 2017, doi: 10.1016/J.JBIOTEC.2017.09.012.
- [6] R. N. E. Tiri, F. Gulbagca, A. Aygun, A. Cherif, and F. Sen, "Biosynthesis of Ag-Pt bimetallic nanoparticles using propolis extract: Antibacterial effects and catalytic activity on NaBH₄ hydrolysis," *Environ. Res.*, vol. 206, pp. 112622, Apr. 2022, doi: 10.1016/J.ENVRES.2021.112622.
- [7] A. Aygun, G. Sahin, R. N. E. Tiri, Y. Tekeli, and F. Sen, "Colorimetric sensor based on biogenic nanomaterials for high sensitive detection of hydrogen peroxide and multi-metals," *Chemosphere.*, vol. 339, pp. 139702, Oct. 2023, doi: 10.1016/j.chemosphere.2023.139702.
- [8] Y. Kocak *et al.*, "Eco-friendly production of platinum nanoparticles: physicochemical properties, evaluation of biological and catalytic activities," *Int. J. Environ. Sci. Technol.*, vol. 1, pp. 51-62, Oct. 2024, doi: 10.1007/s13762-023-05232-w.
- [9] F. Karimi, E. E. Altuner, A. Aygun, R. Bayat, S. Rajendran, and F. Sen, "Synthesis of Silver Nanoparticles by Biogenic Methods: Characterization and Development of a Sensor Sensible to Pharmaceutical Medicine Paracetamol," *Top. Catal.*, vol. 9, pp. 585- 593, Oct. 2024, doi: 10.1007/s11244-023-01887-4.
- [10] R. N. E. Tiri *et al.*, "Environmental Energy Production and Wastewater Treatment Using Synthesized Pd Nanoparticles with Biological and Photocatalytic Activity," *Top. Catal.*, vol. 67, no.9, pp. 714-724, Feb. 2024, doi: 10.1007/s11244-024-01912-0.
- [11] I. Meydan *et al.*, "Chitosan/PVA-supported silver nanoparticles for azo dyes removal: fabrication, characterization, and assessment of antioxidant activity," *Environ. Sci. Adv.*, vol. 2, no. 1, pp. 129-142, Mar. 2023, doi: 10.1039/d3va00224a.
- [12] S. Chaturvedi, A. Bhattacharya, S. K. Khare, and G. Kaushik, *Camelina sativa: An Emerging Biofuel Crop*, pp. 265-282. 2018. doi: 10.1007/978-3-319-58538-3_110-1.
- [13] M. K. Walia *et al.*, "Winter camelina seed yield and quality responses to harvest time," *Ind. Crops Prod.*, vol. 111, pp. 22- 29, Jan. 2018, doi: 10.1016/j.indcrop.2018.08.025.

- [14] M. Arshad *et al.*, “Valorization of camelina oil to biobased materials and biofuels for new industrial uses: a review,” *RSC Advances*. vol. 12, no. 42, pp. 22- 29, Jan. 2022. doi: 10.1039/d2ra03253h., 27230-27245.
- [15] K. A. Mcvay and P. F. Lamb, “Camelina Production in Montana (*Report*),” Bull. MT200701AG, 2008.
- [16] I. Montero-Muñoz, D. Mostaza-Colado, A. Capuano, and P. V. Mauri Ablanque, “Seed and Straw Characterization of Nine New Varieties of *Camelina sativa* (L.) Crantz,” *Land.*, vol. 12, no. 2, pp. 328, Jan. 2023, doi: 10.3390/land12020328.
- [17] B. Bakhshi, H. R. Ahmadvandi, and H. R. Fanaei, “Camelina, an adaptable oilseed crop for the warm and dried regions of Iran,” *Cent. Asian J. Plant Sci. Innov.*, vol. 1, no. 1, pp. 39-45, Mar. 2021, doi 10.22034/CAJPSI.2021.01.05.
- [18] R. K. Gugel and K. C. Falk, “Agronomic and seed quality evaluation of *Camelina sativa* in western Canada,” *Can. J. Plant Sci.*, vol. 86, no. 4, pp. 1047–1058, Oct. 2006, doi: 10.4141/P04-081.
- [19] M. Campbell, “Camelina- An alternative oil crop,” in *Biokerosene: Status and Prospects.*, pp. 259-275. 2017 doi: 10.1007/978-3-662-53065-8_12.
- [20] B. R. Moser, “Camelina (*Camelina sativa* L.) oil as a biofuels feedstock: Golden opportunity or false hope” *Lipid Technol.*, vol. 22, no. 12, pp 270-273, Dec. 2010, doi: 10.1002/lite.201000068.
- [21] D. Neupane, R. H. Lohaus, J. K. Q. Solomon, and J. C. Cushman, “Realizing the Potential of *Camelina sativa* as a Bioenergy Crop for a Changing Global Climate”, *Plants.*, vol. 11, no. 6, pp. 131, 2022, doi: 10.3390/plants11060772.
- [22] K. Ghankhar, J. Croser, N. Aryamanesh, M. Campbell, N. Konkova, and C. Francis, “Camelina (*Camelina sativa* (L.) Crantz) as an alternative oilseed: molecular and ecogeographic analyses”, *Genome.*, vol. 53. no. 7, pp. 558-56, Jul. 2010, doi: 10.1139/G10-034.
- [23] J. Vollmann, T. Moritz, C. Kargl, S. Baumgartner, and H. Wagentristl, “Agronomic evaluation of camelina genotypes selected for seed quality characteristics”, *Ind. Crops Prod.*, vol. 26, no. 3, pp. 270-277, Oct. 2007, doi: 10.1016/j.indcrop.2007.03.017.
- [24] A. Guendouz, A. Hannachi, M. Benidir, Z. E. A. Fellahi, and B. Frih, “Agro-biochemical Characterisation of *Camelina sativa*: A Review”, *Agric. Rev.*, vol.43, no. 3, pp. 278-287, Oct. 2022, doi: 10.18805/ag. Rf-230.
- [25] M. Ghidoli, E. Ponzoni, F. Araniti, D. Miglio, and R. Pilu, “Genetic Improvement of *Camelina sativa* (L.) Crantz: Opportunities and Challenges”, *Plants.*, vol. 12, no. 3, pp. 118, Oct. 2023, doi: 10.3390/plants12030570.
- [26] Y. Li and X. S. Sun, “Camelina oil derivatives and adhesion properties”, *Ind. Crops Prod.*, vol. 30, no.73, pp. 73-80, Oct. 2015, doi: 10.1016/j.indcrop.2015.04.015.
- [27] J. J. Delver and Z. K. Smith, “Opportunities for Camelina Meal as a Livestock Feed Ingredient, Agriculture (Switzerland)”, vol. 71, no. 3, 371-383. 2024, doi: 10.3390/agriculture14010116.
- [28] M. Berti, R. Gesch, C. Eynck, J. Anderson, and S. Cermak, “Camelina uses, genetics, genomics, production, and management”, *Ind. Crops Prod.*, vol. 94, no. 2016, pp. 690710, 2016, doi: 10.1016/j.indcrop.2016.09.034.
- [29] U. Sevilmiş, M. E. Bilgili, Kahraman, S. Seydoğlu, and D. Sevilmiş, “Ketencik (*Camelina sativa*) Tarımı”, *Uluslararası Doğu Akdeniz Tarımsal Aratırma Enstitüsü Dergi.*, vol. 2, no.2, pp.36-62, Dec. 2016, pp. 2019.
- [30] G. A. Mulligan, “Weedy introduced mustards (Brassicaceae) of Canada, *Can. Field-Naturalist*”, Mar. 2004, doi: 10.5962/p.363514.
- [31] M. Ghidoli, M. Pesenti, F. Colombo, F. F. Nocito, R. Pilu, and F. Araniti, “*Camelina sativa* (L.) Crantz as a Promising Cover Crop Species with Allelopathic Potential”, *Agronomy.*, vol. 13, no.8, pp. 2187, Jun. 2023, doi: 10.3390/agronomy13082187.
- [32] M. Mondor and A. J. Hernández-Álvarez, “*Camelina sativa* Composition, Attributes, and Applications: A Review,” *European Journal of Lipid Science and Technology.*, vol. 124, no. 3, pp. 2100035, Aug.2022, doi: 10.1002/ejlt.202100035.
- [33] W. F. Schillinger, D. J. Wysocki, T. G. Chastain, S. O. Guy, and R. S. Karow, “Camelina: Planting date and method effects on stand establishment and seed yield”, *F. Crop. Res.*, vol. 130, no. 138, pp. 138-144, Mar. 2012, doi: 10.1016/j.fcr.2012.02.019.
- [34] F. M. Ibrahim and S. F. El Habbasha, “Chemical composition, medicinal impacts and cultivation of camelina (*Camelina sativa*): Review”, *Int. J. PharmTech Res.*, vol. 8, no. 10, pp. 114-122.2015.
- [35] F. Zanetti *et al.*, “Camelina, an ancient oilseed crop actively contributing to the rural renaissance in Europe. A review”, *Agronomy for Sustainable Development.*, vol. 41, no. 2, pp. 1-18, Jan. 2021, doi: 10.1007/s13593-020-00663-y.
- [36] A. Obour K, “Oilseed Camelina (*Camelina sativa* L Crantz): Production Systems, Prospects and Challenges in the USA Great Plains”, *Adv. Plants Agric. Res.*, vol. 2, no. 2, pp. 1-10, Mar. 2015, doi: 10.15406/apar.2015.02.00043.
- [37] U. Iskandarov, H. J. Kim, and E. B. Cahoon, “Camelina: An emerging oilseed platform for advanced biofuels and bio-based materials”, in *Plants and BioEnergy.*, vol. 41, no. 2, pp. 1-18, Jan. 2014. doi: 10.1007/978-1-4614-9329-7_8.
- [38] J. Zubr and B. “Matthaus, Effects of growth conditions on fatty acids and tocopherols in *Camelina sativa* oil”, *Ind. Crops Prod.*, vol. 15, no. 2, pp. 155-162, Mar. 2002, doi: 10.1016/S0926-6690(01)00106-6.
- [39] D. Kurasiak-Popowska, B. Rynska, and K. Stuper-Szablewska, “Analysis of distribution of selected bioactive compounds in *camelina sativa* from seeds to pomace and oil,” *Agronomy.*, vol. 9, no. 4, pp. 168, Feb. 2019, doi: 10.3390/agronomy9040168.
- [40] R. Kirakosyan, I. Kapristova, and E. Kalashnikova, “Influence of coherent light on seed quality of *Camelina sativa* L”, in *BIO Web of Conferences.*, vol. 9, pp. 00065, Nov. 2020, doi: 10.1051/bioconf/20202700065.
- [41] B. L. Allen, M. F. Vigil, and J. D. Jabro, “Camelina growing degree hour and base temperature requirements”, *Agron. J.*, vol. 106, no. 3,

pp. 940-944, May. 2014, doi: 10.2134/agronj13.0469.

- [42] J. Zubr, "Dietary fatty acids and amino acids of *Camelina sativa* seed", *J. Food Qual.*, vol. 26, no. 6, pp. 451-462, May. 2007, doi: 10.1111/j.1745-4557.2003.tb00260.x.
- [43] Z. Mozghan and Z. Ergun, "The Effect of Storage Temperature on the Composition of Fatty Acids in Crimson Sweet (*Citrullus lanatus* var. *lanatus*) Watermelon Cultivar Seeds", *Iğdır Üniversitesi Fen Bilim. Enstitüsü Dergi.*, vol. 11, no. 2, pp. 839-845, May. 2021, doi: 10.21597/jist.830878. 11.2: 839-845
- [44] M. Berti, R. Wilckens, S. Fischer, A. Solis, and B. Johnson, "Seeding date influence on camelina seed yield, yield components, and oil content in Chile", *Ind. Crops Prod.*, vol. 26, no. 6, pp. 451-462, Jun. 2011, doi: 10.1016/j.indcrop.2010.12.008.
- [45] L. G. Angelini, L. A. Chehade, L. Foschi, and S. Tavarini, "Performance and potentiality of camelina (*Camelina sativa* L. Crantz) genotypes in response to sowing date under mediterranean environment", *Agronomy.*, vol. 10, no. 12, pp. 1929, Nov. 2021, doi: 10.3390/agronomy10121929.
- [46] F. Angelopoulou et al., "Influence of Organic Fertilization and Soil Tillage on the Yield and Quality of Cold-Pressed Camelina [*Camelina sativa* (L.) Crantz] Seed Cake: An Alternative Feed Ingredient", *Appl. Sci.*, vol. 13, no. 6, pp. 3759, Feb. 2023, doi: 10.3390/app13063759.
- [47] A. Solis, I. Vidal, L. Paulino, B. L. Johnson, and M. T. Berti, "Camelina seed yield response to nitrogen, sulfur, and phosphorus fertiliser in South Central Chile," *Ind. Crops Prod.*, vol. 44, pp. 132-138, Jan. 2013, doi: 10.1016/j.indcrop.2012.11.005.
- [48] K. J. Jankowski, M. Sokólski, and B. Kordan, "Camelina: Yield and quality response to nitrogen and sulfur fertilization in Poland", *Ind. Crops Prod.*, vol. 141, pp. 111776, Dec. 2019, doi: 10.1016/j.indcrop.2019.111776.
- [49] S. S. Malhi, E. N. Johnson, L. M. Hall, W. E. May, S. Phelps, and B. Nybo, "Effect of nitrogen fertilizer application on seed yield, N uptake, and seed quality of *Camelina sativa*", *Can. J. Soil Sci.*, vol. 94, no. 1, pp. 35-47, Dec. 2014, doi: 10.4141/CJSS2012-086.
- [50] R. Riaz, I. Ahmed, O. Sizmaz, and U. Ahsan, "Use of *Camelina sativa* and By-Products in Diets for Dairy Cows: A Review", *Animals.*, vol. 12, no. 9, pp. 1082, Apr. 2022. doi: 10.3390/ani12091082.
- [51] I. Manisalidis, E. Stavropoulou, A. Stavropoulos, and E. Bezirtzoglou, "Environmental and Health Impacts of Air Pollution: A Review", *Frontiers in Public Health.*, vol. 8, no.14, Feb.2020, doi: 10.3389/fpubh.2020.00014.
- [52] N. L. Panwar, S. C. Kaushik, and S. Kothari, "Role of renewable energy sources in environmental protection: A review", *Renewable and Sustainable Energy Reviews.*, vol. 15, no. 3, pp. 1513-1524, Apr. 2011, doi: 10.1016/j.rser.2010.11.037.
- [53] R. Zahedi, A. Zahedi, and A. Ahmadi, "Strategic Study for Renewable Energy Policy, Optimizations and Sustainability in Iran," *Sustainability.*, vol. 14, no. 4, pp. 2418, Feb. 2022, doi: 10.3390/su14042418.
- [54] Ý. Ekin, "Quality and composition of lipids used in biodiesel production and methods of transesterification: A review", *Int. J. Chem. Technol.*, vol. 3, no. 2, pp. 77-91, Dec. 2019, doi: 10.32571/ijct.623165.
- [55] R. Sawangkeaw and S. Ngamprasertsith, "A review of lipid-based biomasses as feedstocks for biofuels production", *Renewable and Sustainable Energy Reviews.*, vol. 25, pp. 97-108, Sep. 2013, doi: 10.1016/j.rser.2013.04.007.
- [56] O. S. Stamenkoviã et al., "Biodiesel production from camelina oil: Present status and future perspectives", *Food and Energy Security.*, vol. 12, no. 1, pp. 340, Nov. 2023, doi: 10.1002/fes3.340.
- [57] B. R. Moser and S. F. Vaughn, "Evaluation of alkyl esters from *Camelina sativa* oil as biodiesel and as blend components in ultra low-sulfur diesel fuel", *Bioresour. Technol.*, vol. 101, no.2, pp. 646-653, Jan. 2010, doi: 10.1016/j.biortech.2009.08.054.
- [58] A. Bernardo et al., "Camelina oil as a fuel for diesel transport engines," *Ind. Crops Prod.*, vol. 17, no. 3, pp. 191-197, May. 2003, doi: 10.1016/S0926-6690(02)00098-5.
- [59] Şahin, S "., Determination of Some Physicochemical Properties of Camelina Biodiesel Blends with Different Alcohols", *MAS Journal of Applied Sciences.*, vol.9, no. 1, pp. 43-99, Mar.2024, doi: org/10.5281/zenodo.10613853.
- [60] Y. Sun et al., "Transesterification of *camelina sativa* oil with supercritical alcohol mixtures", *Energy Convers. Manag.*, vol. 101, pp. 402-409, Sep. 2015, doi: 10.1016/j.enconman.2015.05.056.
- [61] A. L. Duly, J. A. Harris, A. M. Khatchadourian, R. T. Ulics, and M. C. Wolter, "Price and expenditure measures of petroleum products: A comparison," *Mon. Labor Rev.*, vol. 129, pp. 56. 2006.
- [62] J. Shila and M. E. Johnson, "Techno-economic analysis of Camelina-derived hydroprocessed renewable jet fuel within the US context," *Appl. Energy.*, vol. 287, pp. 116525, Jan. 2021, doi: 10.1016/j.apenergy.2021.116525.
- [63] J. Zubr, "Oil-seed crop: *Camelina sativa*", *Ind. Crops Prod.*, vol. 6, no. 2, pp. 113-119, May. 1997, doi: 10.1016/S0926-6690(96)00203-8.
- [64] D. R. Shonnard, L. Williams, and T. N. Kalnes, "Camelina-derived jet fuel and diesel: Sustainable advanced biofuels", *Environ. Prog. Sustain. Energy.*, vol. 29, no. 3, pp. 382-392, Sep. 2010, doi: 10.1002/ep.10461.
- [65] C. D. Klingshirn et al., "Hydroprocessed renewable jet fuel evaluation, performance, and emissions in a T63 turbine engine", *J. Eng. Gas Turbines Power.*, vol. 134, no.5, pp. 8, May. 2012, doi: 10.1115/1.4004841.
- [66] R. H. Sundararaj et al., "Combustion and emission characteristics from biojet fuel blends in a gas turbine combustor", *Energy.*, vol. 182, pp. 689-705, Sep. 2019, doi: 10.1016/j.energy.2019.06.060.

- [67] K. Lokesh, V. Sethi, T. Nikolaidis, E. Goodger, and D. Nalianda, "Life cycle greenhouse gas analysis of biojet fuels with a technical investigation into their impact on jet engine performance", *Biomass and Bioenergy.*, vol. 77, pp. 26-44, Jun. 2015, doi: 10.1016/j.biombioe.2015.03.005.
- [68] S. Chen, Y. Chen, Z. Wang, H. Chen, and D. Fan, "Renewable bio-based adhesive fabricated from a novel biopolymer and soy protein", *RSC Adv.*, vol. 11, no.19, pp. 11724-11731, Nov. 2021, doi: 10.1039/d1ra00766a.
- [69] D. M. Fitzgerald, Y. L. Colson, and M. W. Grinstaff, "Synthetic pressure sensitive adhesives for biomedical applications", *Progress in Polymer Science.*, vol. 142, pp. 101692, Jul. 2023, doi: 10.1016/j.progpolymsci.2023.101692.
- [70] H. Nosal, J. Nowicki, M. Warzaa, E. Nowakowska-Bogdan, and M. Zarębska, "Synthesis and characterization of alkyd resins based on *Camelina sativa* oil and polyglycerol", *Prog. Org. Coatings.*, vol. 86, pp. 59-70, Sep. 2015, doi: 10.1016/j.porgcoat.2015.04.009.
- [71] S. Tavarini, M. De Leo, R. Matteo, L. Lazzeri, A. Braca, and L. G. Angelini, "Flaxseed and camelina meals as potential sources of health-beneficial compounds", *Plants.*, vol. 10, no. 1, pp.156, Jan. 2021, doi: 10.3390/plants10010156.
- [72] N. Codina-Pascual, J. Torra, B. Baraibar, and A. Royo-Esnal, "Weed suppression capacity of camelina (*Camelina sativa*) against winter weeds: The example of corn-poppy (*Papaver rhoeas*)", *Ind. Crops Prod.*, vol. 184, pp. 115063, Sep. 2022, doi: 10.1016/j.indcrop.2022.115063.
- [73] S. Tavarini et al., "Evaluation of chemical composition of two linseed varieties as sources of health-beneficial substances", *Molecules.*, vol. 24, no. 20, pp. 3729, Oct. 2019, doi: 10.3390/molecules24203729.
- [74] A. Majeed, "Application of Agrochemicals in Agriculture: Benefits, Risks and Responsibility of Stakeholders, Cit. Majeed A J Food Sci Toxicol.", vol. 2, no.1, pp. 3, Jan. 2018.
- [75] M. S. Ayilara et al., "Biopesticides as a promising alternative to synthetic pesticides: A case for microbial pesticides, phytopesticides, and nanobiopesticides", *Frontiers in Microbiology.*, vol. 14, pp. 1040901, Feb. 2023. doi: 10.3389/fmicb.2023.1040901.
- [76] J. Pernak et al., "Ammonium bio-ionic liquids based on camelina oil as potential novel agrochemicals", *RSC Adv.*, vol. 8, pp. 28676-28683, Agu.2018, doi: 10.1039/c8ra03519a.
- [77] A. Abbas et al., "Application of allelopathic phenomena to enhance growth and production of camelina (*Camelina sativa* (L.))", *Appl. Ecol. Environ. Res.*, vol. 19, no. 1, pp. 453-469, Jul. 2021, doi: 10.15666/aer/1901_453469.
- [78] M. aepanovia et al., "Inhibitory effects of brassicaceae cover crop on ambrosia artemisiifolia germination and early growth", *Plants.*, vol. 10, no.9, pp. 28676-28683, Agu. 2021, doi: 10.3390/plants10040794.
- [79] M. Yue, H. Lambert, E. Pahon, R. Roche, S. Jemei, and D. Hissel, "Hydrogen energy systems: A critical review of technologies, applications, trends and challenges", *Renewable and Sustainable Energy Reviews.*, vol. 146, pp. 111180, Agu. 2021. doi: 10.1016/j.rser.2021.111180.
- [80] P. Trumbo, S. Schlicker, A. A. Yates, and M. Poos, "Dietary reference intakes for energy, carbohydrate, fiber, fat, fatty acids, cholesterol, protein and amino acids", *J. Am. Diet. Assoc.*, vol. 102, no. 11, pp. 1621-1631, Nov. 2002, doi: 10.1016/S0002-8223(02)90346-9.
- [81] V. Musazadeh, P. Dehghan, and S. Azadmard-Damirchi, "Effectiveness of Co-Administration of Camelina Oil and Caloric Restriction on Cardiometabolic Risk Factors, Liver Function and Mental Health in Patients with Non-Alcoholic Fatty Liver Disease: A Blinded Randomized Controlled Trial Protocol", *J. Nutr. Food Secur.*, vol. 7, no. 3, pp. 379-387. 2022, doi: 10.18502/jnfs.v7i3.10204.
- [82] D. Kurasiak-Popowska and K. Stuper-Szablewska, "The phytochemical quality of *Camelina sativa* seed and oil", *Acta Agric. Scand. Sect. B Soil Plant Sci.*, vol. 70, no. 1, pp. 39-47, May. 2020, doi: 10.1080/09064710.2019.1665706.
- [83] J. Rode, "Study of autochthon *Camelina sativa* (L.) Crantz in Slovenia", *J. Herbs, Spices Med. Plants.*, vol. 9, no. 4, pp. 313-318, Oct. 2002, doi: 10.1300/J044v09n04_08.
- [84] H. M. Karvonen, A. Aro, N. S. Tapola, I. Salminen, M. I. J. Uusitupa, and E. S. Sarkkinen, "Effect of α -linolenic acid-rich *Camelina sativa* oil on serum fatty acid composition and serum lipids in hypercholesterolemic subjects", *Metabolism.*, vol. 51, no. 10, pp. 1253-1260, Oct. 2002, doi: 10.1053/meta.2002.35183.
- [85] H. Abramovie and V. Abram, "Physico-chemical properties, composition and oxidative stability of *camelina sativa* oil, Food Technol". *Biotechnol.*, vol. 43, no .1, pp. 63-70, Sep. 2005.
- [86] J. Zubr, "Carbohydrates, vitamins and minerals of *Camelina sativa* seed", *Nutr. Food Sci.*, vol. 40, no. 5, pp. 523-531, Sep. 2010, doi: 10.1108/00346651011077036.
- [87] V. L. N. Brandao et al., "Effects of replacing canola meal with solvent-extracted camelina meal on microbial fermentation in a dual-flow continuous culture system", *J. Dairy Sci.*, vol. 101, no. 10, pp. 9028-9040, Oct. 2018, doi: 10.3168/jds.2018-14826.
- [88] Hajjazi, F., Sadeghi, A., & Ibrahim, S. (2024). *Camelina sativa* (L. Crantz) products; an alternative feed ingredient for poultry diets with its nutritional and physiological consequences. *Tropical Animal Health and Production*, 56(2), 59.
- [89] Anca, G., Hăbeanu, M., Lefter, N. A., & Ropotă, M. (2019). Performance parameters, plasma lipid status, and lymphoid tissue fatty acid profile of broiler chicks fed camelina cake. *Brazilian Journal of Poultry Science*, 21, eRBCA-2019.
- [90] P. Moriel et al., "Camelina meal and crude glycerin as feed supplements for developing replacement beef heifers", *J. Anim. Sci.*, vol. 89, no. 12, pp. 4314-4324, Dec. 2011, doi: 10.2527/jas.2010-3630.
- [91] E. M. Paula, L. G. da Silva, V. L. N. Brandao, X. Dai, and A. P. "Faciola, Feeding canola, camelina, and carinata meals to ruminants",

Animals., vol. 9, no. 10, pp. 704, Agu. 2019, doi: 10.3390/ani9100704.

[92] M. A. Rahim et al., "Essential Components from Plant Source Oils: A Review on Extraction, Detection, Identification, and Quantification", *Molecules.*, vol. 28, no. 19, 6881, Sep. 2023, doi: 10.3390/molecules28196881.

[93] J. M. Song et al., "Oil plant genomes: current state of the science", *Journal of Experimental Botany.*, vol. 73, no. 9, pp. 2859-2874, May. 2022, doi: 10.1093/jxb/erab472.

[94] R. Juodka et al., "Camelina (*Camelina sativa* (L.) Crantz) as Feedstuffs in Meat Type Poultry Diet: A Source of Protein and n-3 Fatty Acids", *Animals.*, vol. 12, no. 3, pp. 295, Jan. 2022, doi: 10.3390/ani12030295.

[95] A. Y. Pekel, J. I. Kim, C. Chapple, and O. Adeola, "Nutritional characteristics of camelina meal for 3-week-old broiler chickens", *Poult. Sci.*, vol. 94, no. 3, pp. 371-378, Mar. 2015, doi: 10.3382/ps/pew066.

[96] R. K. Kahindi, T. A. Woyengo, P. A. Thacker, and C. M. Nyachoti, "Energy and amino acid digestibility of camelina cake fed to growing pigs", *Anim. Feed Sci. Technol.*, vol. 193, pp. 93-101, Jul. 2014, doi: 10.1016/j.anifeeds.2014.03.012.

[97] F. N. Almeida, J. K. Htoo, J. Thomson, and H. H. Stein, "Amino acid digestibility in camelina products fed to growing pigs", *Can. J. Anim. Sci.*, vol. 93, no. 3, pp. 335-343, Agu. 2013, doi: 10.4141/CJAS2012-134.

[98] T. A. Woyengo, R. Patterson, B. A. Slominski, E. Beltranena, and R. T. Zijlstra, "Nutritive value of cold-pressed camelina cake with or without supplementation of multi-enzyme in broiler chickens", *Poult. Sci.*, vol. 95, no. 10, pp. 2314-2321, Oct. 2016, doi: 10.3382/ps/pew098.

[99] Ş. L. Bâtrina et al., "Camelina sativa: A study on amino acid content", *Rom Biotechnol Lett*, vol. 25, no. 1, pp. 1136-1142, Jul. 2020, doi: 10.25083/rbl/25.1/1136.1142.

[100] J. Zubr, "Camelina oil in human nutrition", *Agro Food Ind. Hi. Tech.*, vol. 12, no. 4, pp. 22-28. 2009.

[101] C. Hurtaud and J. L. Peyraud, "Effects of feeding camelina (seeds or meal) on milk fatty acid composition and butter spreadability", *J. Dairy Sci.*, vol. 90, no. 11, pp. 5134-5145, Nov. 2007, doi: 10.3168/jds.2007-0031.

[102] C. Christodoulou et al., "Assessing the optimum level of supplementation with camelina seeds in ewes diets to improve milk quality", *Foods.*, vol. 10, no. 9, pp. 2076, Agu. 2021, doi: 10.3390/foods10092076.

[103] Z. Piravi-vanak et al., "Physicochemical properties of oil extracted from camelina (*Camelina sativa*) seeds as a new source of vegetable oil in different regions of Iran", *J. Mol. Liq.*, vol. 345, pp. 117043, Jan. 2022, doi: 10.1016/j.molliq.2021.117043.

[104] H. R. Ahmadvandi, A. Zeinodini, R. Ghobadi, and M. Gore, "Benefits of Adding Camelina to Rainfed Crop Rotation in Iran: A Crop with High Drought Tolerance", *Agrotechniques Ind. Crop.*, vol. 1, no. 2, pp. 91-96, Jun. 2021, doi: 10.22126/atic.2021.6410.1007

[105] P. G. Ergönül and Z. A. Özbek, "Cold pressed camelina (*Camelina sativa* L.) seed oil, in *Cold Pressed Oils: Green Technology, Bioactive Compounds, Functionality, and Applications.*, pp. 28676-28683. 2020, doi: 10.1016/B978-0-12-818188-1.00021-9.

[106] M. Raczkyk, E. Popis, B. Kruszewski, K. Ratusz, and M. Rudzińska, "Physicochemical quality and oxidative stability of linseed (*Linum usitatissimum*) and camelina (*Camelina sativa*) cold-pressed oils from retail outlets", *Eur. J. Lipid Sci. Technol.*, vol. 118, no. 5, pp. 834-839, Jul. 2016, doi: 10.1002/ejlt.201500064.

[107] X. Wu and D. Y. C. Leung, "Optimization of biodiesel production from camelina oil using orthogonal experiment", *Appl. Energy.*, vol. 88, no. 11, pp. 3615-3624, Nov. 2011, doi: 10.1016/j.apenergy.2011.04.041.

[108] J. Yang, C. Caldwell, K. Corscadden, Q. S. He, and J. Li, "An evaluation of biodiesel production from *Camelina sativa* grown in Nova Scotia", *Ind. Crops Prod.*, vol. 81, pp. 162-168, Mar. 2016, doi: 10.1016/j.indcrop.2015.11.073.

[109] N. Mikoajczak, M. Tańska, and D. Ogródowska, "Phenolic compounds in plant oils: A review of composition, analytical methods, and effect on oxidative stability", *Trends in Food Science and Technology.*, vol. 113, pp. 110-138, Jul. 2021, doi: 10.1016/j.tifs.2021.04.046.

[110] Y. Kocak et al., "Microwave-Assisted Fabrication of AgRuNi Trimetallic NPs with Their Antibacterial vs Photocatalytic Efficiency for Remediation of Persistent Organic Pollutants", *Bionanoscience.*, vol. 14, no. 1, pp. 93-101, Nov. 2024, doi: 10.1007/s12668-023-01237-4.

[111] B. Matthäus, "Antioxidant activity of extracts obtained from residues of different oilseeds", *J. Agric. Food Chem.*, vol. 50, no. 12, pp. 3444-3452, May. 2002, doi: 10.1021/jf011440s.

[112] P. Terpinc, T. Polak, D. Makuc, N. P. Ulrih, and H. Abramovič, "The occurrence and characterisation of phenolic compounds in *Camelina sativa* seed, cake and oil", *Food Chem.*, vol. 131, no. 2, pp. 580-589, Mar. 2012, doi: 10.1016/j.foodchem.2011.09.033.

[113] H. Abramovič, B. Butinar, and V. Nikolič, "Changes occurring in phenolic content, tocopherol composition and oxidative stability of *Camelina sativa* oil during storage", *Food Chem.*, vol. 104, no. 3, pp. 903-909. 2007, doi: 10.1016/j.foodchem.2006.12.044.

[114] H. Salminen, M. Estévez, R. Kivikari, and M. Heinonen, "Inhibition of protein and lipid oxidation by rapeseed, camelina and soy meal in cooked pork meat patties", *Eur. Food Res. Technol.*, vol. 223, pp. 461-468, Jan. 2006, doi: 10.1007/s00217-005-0225-5.

[115] M. Zajc, B. Kiczorowska, W. Samolińska, and R. Klebaniuk, "Inclusion of camelina, flax, and sunflower seeds in the diets for broiler chickens: Apparent digestibility of nutrients, growth performance, health status, and carcass and meat quality traits", *Animals.*, vol. 10, no. 2, pp. 321, Feb. 2020, doi: 10.3390/ani10020321.

[116] R. Russo and R. Reggiani, "Antinutritive Compounds in Twelve *Camelina sativa* Genotypes", *Am. J. Plant Sci.*, vol. 3, no. 10, pp. 4, Jul. 2012, doi: 10.4236/ajps.2012.310170.